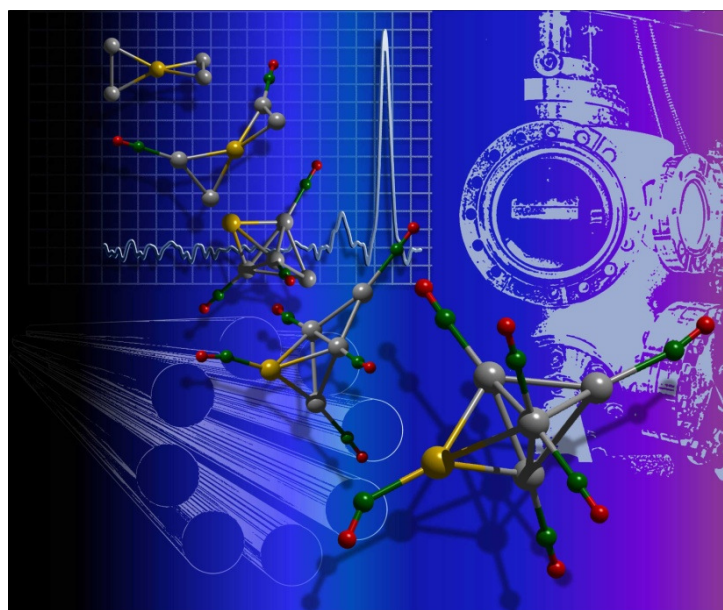




ulm university universität  
**uulm**

# **Size and composition dependent reaction kinetics and femtosecond photodissociation dynamics of noble metal cluster complexes**



Dissertation  
zur Erlangung des Doktorgrades  
Dr. rer. nat.  
der Fakultät für Naturwissenschaften  
der Universität Ulm

vorgelegt von  
Denisia Maria Popolan  
aus Brad, Rumänien

2010



Amtierender Dekan: Prof. Dr. Axel Groß

1. Gutachter: Prof. Dr. Thorsten M. Bernhardt
2. Gutachter: Prof. Dr. Harold Jones

Tag der Promotion: 28.01.2011





In loving memory of my beloved mommy ...



# Abstract

The aim of the present work was the investigation of the size and composition dependent chemistry of free, mass-selected gold, silver, and binary silver-gold clusters. It had been demonstrated previously that these clusters display unexpected size-dependent catalytic activity when deposited on metal oxide substrates. These observations raised questions about the intrinsic properties of these clusters and how they interact with catalytically relevant ligands. This thesis approaches these issues from two fronts: (i) by probing the reactivity of mass-selected  $\text{Ag}_n^+$ ,  $\text{Au}_m^+$ , and  $\text{Ag}_n\text{Au}_m^+$  nanoclusters in the gas phase under well defined reaction conditions and (ii) by studying the femtosecond-laser photodissociation of their complexes with molecular ligands.

Temperature dependent reactivity measurements were performed to determine the binding energies of carbon monoxide to the triatomic binary silver-gold clusters. The binding energies of the first CO molecule to the trimer clusters was found to increase with increasing gold content and with changing the charge from negative to positive. Thus, the reactivity of the binary clusters could be sensitively tuned by varying charge state and composition. Also multiple CO adsorption on the clusters was investigated. The maximum number of adsorbed CO was found to strongly depend on cluster charge and composition as well. Most interestingly, the cationic carbonyl complex  $\text{Au}_3(\text{CO})_4^+$  was formed at cryogenic temperatures whereas for the anion at maximum two CO were adsorbed, leading to  $\text{Au}_3(\text{CO})_2^+$ . All other trimer clusters adsorbed three CO in the case of the cations and were completely inert toward CO in our experiment in the case of the anions.

The investigations were further extended to larger cluster sizes. Temperature dependent equilibrium methods were applied to determine the binding energies for the sequential adsorption of CO ligands to five-atom silver-gold cluster cations. The CO binding energies to  $\text{Ag}_n\text{Au}_m^+$  ( $n+m = 5$ ) clusters were found to decrease with increasing number of silver atoms. More strikingly, after the adsorption of the fourth CO to  $\text{Au}_5^+$  and third CO to  $\text{Ag}_5^+$ , respectively, a pronounced decrease in the binding energies of further CO molecules was observed. In conjunction with theoretical simulations, it could be demonstrated that this observation can be explained by a CO-induced structural transformation yielding more compact metal clusters geometries. For all investigated systems, the structure calculations were performed using density functional theory (DFT) by Professor Vlasta Bonačić-Koutecký and coworkers.

While gold and silver cluster cations were found to be completely inert towards molecular oxygen under our experimental conditions, it was possible to produce metal-oxide clusters through the reaction with nitrous oxide. In particular, the reaction of the triatomic silver cation clusters with  $\text{N}_2\text{O}$  was investigated in detail and exhibited a very sophisticated temperature dependent reaction mechanism, which manifested itself in an increase in reactivity with decreasing temperature and in unexpected fragmentation channels in the temperature range between 270 and 230 K. Experimental evidence was obtained for the occurrence of a complete catalytic CO oxidation cycle promoted by silver and gold oxide,

which was generated by reaction with  $\text{N}_2\text{O}$ . For the silver oxide clusters such a catalytic cycle was described in this work for the first time.

Furthermore, the reactions of size-selected gold and silver clusters cations  $\text{Ag}_n^+$  and  $\text{Au}_n^+$  ( $n = 3, 5$ ) with  $\text{C}_6\text{H}_6$  and with a mixture of  $\text{C}_6\text{H}_6$  and  $\text{CO}$  were investigated. While benzene was found to react with all investigated metal clusters exhibiting size dependent adsorbate coverages, the coadsorption of  $\text{C}_6\text{H}_6$  and  $\text{CO}$  was only observed on the investigated gold clusters. Moreover, in the case of silver clusters photodissociation experiments at 353 and 393 nm, respectively, provided indications for a charge transfer induced fragmentation. In particular, for  $\text{Ag}_5(\text{C}_6\text{H}_6)^+$  the femtosecond time resolved fragmentation dynamics could be measured. The charge state dependent reactivity of potential coadsorbates of  $\text{C}_6\text{H}_6$  on the small noble metal clusters might open a new promising route to the real-time investigation of reactions on metal clusters initiated by laser-induced charge transfer as demonstrated in the present work.

In a final series of experiments the gas phase reactions of gold cluster cations, in this case with  $\text{CH}_3\text{Br}$ , could be directly compared to similar experiments with metal oxide supported gold clusters that were obtained in the same apparatus. This direct comparison provided valuable support for the notion that complementary information can be obtained from free cluster studies that may help to elucidate reactions on clusters at surfaces.

# Contents

<b>Abstract.....</b>	<b>I</b>
<b>List of figures.....</b>	<b>VII</b>
<b>List of tables.....</b>	<b>XI</b>
<b>Abbreviations .....</b>	<b>XIII</b>
<b>1 General introduction .....</b>	<b>1</b>
1.1 Cluster science .....	1
1.2 Experimental techniques in cluster ion chemistry .....	4
1.3 Concepts in cluster ion chemistry and femtochemistry .....	7
1.4 Motivation and objective of the thesis .....	8
1.5 Outline of the thesis .....	10
<b>2 Experimental setup .....</b>	<b>13</b>
2.1 Cluster production and analysis .....	14
2.1.1 Ion source .....	14
2.1.2 Phase space compressor .....	17
2.1.3 Triple quadrupole mass spectrometer .....	19
2.1.4 Octopole ion trap .....	21
2.2 Laser system.....	24
2.2.1 Generation and characterization of the fs-laser pulses: oscillator and amplifier .....	25
2.2.1.1 Ti:Sapphire active medium .....	25
2.2.1.2 Femtosecond oscillator.....	26
2.2.2 Pulse amplification .....	29
2.2.3 Optical parametric amplifier .....	32
2.2.4 Third harmonic generation .....	34
2.2.5 Pulse characterization.....	35
2.2.5.1 Spectral measurements .....	35
2.2.5.2 Temporal pulse profile .....	36
<b>3 Data acquisition and evaluation methods.....</b>	<b>39</b>
3.1 Kinetic data acquisition method.....	40
3.2 Kinetic data evaluation procedure .....	43
3.2.1 Low-pressure reaction kinetics.....	44
3.2.2 Langevin theory.....	46
3.2.3 RRKM theory .....	48
3.2.4 Fitting procedure. <i>MassKinetics</i> input .....	51
3.2.5 Energized molecule and transition-state model .....	52
3.2.6 Error analysis.....	53
3.3 Equilibrium thermodynamics evaluation method.....	54

3.4	Computational methods .....	57
3.5	Femtosecond photodissociation processes and data acquisition method .....	57
<b>4</b>	<b>CO binding energies to <math>\text{Ag}_n\text{Au}_m^{+/-}</math> (<math>n+m = 3</math>). Tuning cluster reactivity by charge state and composition .....</b>	<b>63</b>
4.1	Introduction .....	64
4.2	Results .....	65
4.2.1	Gas phase reaction kinetics and CO binding energies .....	65
4.2.2	Temperature dependent CO coverage .....	69
4.3	Discussion .....	70
4.4	Conclusion .....	74
4.5	Outlook.....	74
4.6	Supplementary information .....	75
<b>5</b>	<b>Composition dependent adsorption of multiple CO molecules on binary silver-gold clusters <math>\text{Ag}_n\text{Au}_m^+</math> (<math>n+m = 5</math>) .....</b>	<b>93</b>
5.1	Introduction .....	94
5.2	Results and discussion .....	95
5.2.1	Temperature dependent CO coverage .....	95
5.2.2	Experimental CO binding energies .....	97
5.2.3	Theoretical structures and binding energies.....	98
5.2.3.1	$\text{Au}_5(\text{CO})_q^+$ ( $q = 1-5$ ) .....	100
5.2.3.2	$\text{Ag}_2\text{Au}_3(\text{CO})_q^+$ ( $q = 1-5$ ) .....	101
5.2.3.3	$\text{Ag}_3\text{Au}_2(\text{CO})_q^+$ ( $q = 1-5$ ) .....	101
5.2.3.4	$\text{Ag}_4\text{Au}(\text{CO})_q^+$ ( $q = 1-6$ ) .....	103
5.2.3.5	$\text{Ag}_5(\text{CO})_q^+$ .....	105
5.3	Conclusions .....	108
5.4	Supporting information .....	110
<b>6</b>	<b>Reactions of free <math>\text{Ag}_3^+</math> clusters with <math>\text{N}_2\text{O}</math> and mixtures of <math>\text{N}_2\text{O}</math> and CO .....</b>	<b>117</b>
6.1	Reactions of $\text{Ag}_3^+$ with nitrous oxide: Mass spectra and kinetics .....	118
6.1.1	Introduction .....	118
6.1.2	Results and discussion.....	120
6.2	Indication of two distinct kinds of oxygen atoms involved in the CO oxidation by silver clusters .....	128
<b>7</b>	<b>Formation and femtosecond photodissociation of <math>\text{Ag}_n^+</math> and <math>\text{Au}_n^+</math> complexes with benzene and carbon monoxide .....</b>	<b>131</b>
7.1	Introduction .....	132
7.2	Results and discussion .....	133
7.2.1	Reactions of silver and gold cluster cations with $\text{C}_6\text{H}_6$ and $\text{C}_6\text{H}_6/\text{CO}$ .....	133
7.2.2	Photodissociation spectroscopy of $\pi$ -complexes: $\text{Ag}_3\text{bz}_3^+$ and $\text{Ag}_5\text{bz}_2^+$ .....	135
7.2.3	Femtosecond time resolved fragmentation dynamics .....	138
7.3	Conclusions .....	140

<b>8 Interaction of gold and silver cluster cations with CH<sub>3</sub>Br: Thermal and photoinduced reaction pathways.....</b>	<b>141</b>
8.1 Introduction.....	142
8.2 Results and Discussion .....	142
8.2.1 Thermal reactions of Au <sub>n</sub> <sup>+</sup> (n=1-3, 5, 7) clusters with CH <sub>3</sub> Br .....	142
8.2.2 Photodissociation of Au <sub>3</sub> (CH <sub>3</sub> Br) <sub>n</sub> Br <sub>3-n</sub> <sup>+</sup> (n = 1-3) product complexes .....	145
8.2.3 Thermal reaction of Ag <sub>3</sub> <sup>+</sup> with CH <sub>3</sub> Br .....	146
8.2.4 Photodissociation of Ag <sub>3</sub> (CH <sub>3</sub> Br) <sub>n</sub> Br <sub>3-n</sub> <sup>+</sup> (n = 1-3) product complexes.....	148
8.3 Summary and comparison to the supported clusters data.....	148
<b>9 Conclusions and outlook .....</b>	<b>151</b>
<b>Zusammenfassung.....</b>	<b>155</b>
<b>Bibliography .....</b>	<b>157</b>
<b>List of publications.....</b>	<b>173</b>
<b>Poster and oral contributions .....</b>	<b>177</b>
<b>Curriculum Vitae .....</b>	<b>181</b>
<b>Acknowledgments .....</b>	<b>183</b>
<b>Erklärung.....</b>	<b>185</b>





# List of figures

<b>Figure 1.1:</b> Typical evolution of a physical quantity ( $\chi(n)$ ) as a function of the cluster size....	2
<b>Figure 2.1:</b> Experimental setup for the investigation of reaction kinetics and catalytic activity of free mass-selected metal clusters .....	15
<b>Figure 2.2:</b> (a) Schematic representation of the ion sputter cluster source. (b) SimION simulation illustrating the electrical fields in a longitudinal cross-section image of the cluster production chamber together with the Xe and the metal cluster ion trajectories .....	16
<b>Figure 2.3:</b> Numerical simulation of an ion trajectory inside of a gas filled ion guide .....	18
<b>Figure 2.4:</b> Principle of quadrupole mass filter, acting as a mass band-pass filter: depending on their mass, ions react differently to the modulated $V_{rf}$ field.....	20
<b>Figure 2.5:</b> (a) Thermalization efficiency of trimer cluster ions inside the helium filled coolable octopole ion trap; (b) Thermalization of $Pd_{13}$ clusters through collision with helium atoms .....	22
<b>Figure 2.6:</b> Layout of the femtosecond laser system. Indicated in the figure are the most important laser parameters together with the corresponding wavelengths.....	25
<b>Figure 2.7:</b> (a) Energy level structure of $Ti^{3+}$ in sapphire. (b) Absorption and emission spectra of Ti:Sapphire.....	26
<b>Figure 2.8:</b> The mode-locking principle. (a) The net gain curve (gain minus losses); (b) Cavity longitudinal modes structure in the resonator; (c) The amplified modes.....	27
<b>Figure 2.9:</b> Configuration of the Ti:sapphire oscillator cavity.....	28
<b>Figure 2.10:</b> Illustration of the principle of the CPA method .....	30
<b>Figure 2.11:</b> Schematic principle of a regenerative amplifier cavity.....	31
<b>Figure 2.12:</b> Schema of the optical parametric amplifier employed for the production of the probe pulses.....	32
<b>Figure 2.13:</b> Top view of the optical scheme of the home-built THG employed for the production of the pump laser pulse .....	34
<b>Figure 2.14:</b> Spectra of the 353 and 393 nm laser beams recorded by the optical spectrometer .....	35
<b>Figure 2.15:</b> Schematic sketch of the autocorrelator .....	36
<b>Figure 2.16:</b> AC snapshot illustrating a typical autocorrelation curve at the amplifier output .....	37
<b>Figure 3.1:</b> Schematic representation of the experimental setup .....	40

<b>Figure 3.2:</b> Cluster cation distributions generated by the CORDIS sputter source from different target materials .....	41
<b>Figure 3.3:</b> Schematic representation of the data acquisition method.....	43
<b>Figure 3.4:</b> Diagram of the energies in the RRKM theory .....	49
<b>Figure 3.5:</b> The cross-correlation trace of the pump and the probe pulse measured by recording the photoemission from a gold plate .....	58
<b>Figure 3.6:</b> Upper part: Scheme of the gas phase apparatus. Center: Illustration of the cluster cooling trapping inside the octopole ion trap, as well as the laser interaction during the photodissociation CT experiment. Lower part: View into the rf-ion trap chamber.....	60
<b>Figure 4.1:</b> Temperature dependent kinetics of the reactions of CO with $\text{Ag}_3^+$ (a, b) and $\text{Ag}_2\text{Au}^+$ (c, d) as a function of the reaction time $t_R$ at 300 K (a, c) and at 250 K (b, d), respectively .....	66
<b>Figure 4.2:</b> Experimental and RRKM decomposition rate constants $k_d$ as a function of the temperature .....	67
<b>Figure 4.3:</b> (a) Average number of adsorbed CO molecules after a reaction time of $t_r = 0.5$ s as a function of the reaction temperature $T_R$ for (a) the cationic cluster trimers, $\text{Ag}_3^+$ , $\text{Ag}_2\text{Au}^+$ , and $\text{Au}_3^+$ , and (b) for the anionic cluster trimers $\text{Ag}_3^-$ , $\text{Ag}_2\text{Au}^-$ , $\text{AgAu}_2^-$ , and $\text{Au}_3^-$ .....	69
<b>Figure 4.4:</b> Plot of experimental (exptl.) and theoretical (theoret.) binding energies of CO to the cluster trimers as a function of the cluster charge and composition .....	71
<b>Figure 4.5:</b> Schematic Kohn-Sham-MO energy diagrams for $\text{Ag}_3^-$ , $\text{Ag}_2\text{Au}^-$ , $\text{AgAu}_2^-$ and $\text{Au}_3^-$ showing the closing of the s-d energy gap with increasing gold content.....	72
<b>Figure 4.6:</b> Plot of the calculated DFT binding energies as a function of the number of adsorbed CO molecules. Also shown are the calculated lowest energy structures of selected carbonyl complexes .....	73
<b>Figure 5.1:</b> Product ion mass spectra recorded after a reaction time of $t_R = 0.1$ s and at different reaction temperatures, $T_R$ , as indicated, for (a) $\text{Au}_5^+$ , (b) $\text{Ag}_3\text{Au}_2^+$ , and (c) $\text{Ag}_5^+$ .....	96
<b>Figure 5.2:</b> Average number of adsorbed CO molecules after a reaction time of $t_R = 0.1$ s as a function of the reaction temperature, $T_R$ , for all investigated clusters .....	97
<b>Figure 5.3:</b> Plots of the Gibbs free energy, $\Delta G_T^\circ$ , vs. temperature for the CO adsorption reactions on (a) $\text{Ag}_3\text{Au}_2^+$ , (b) $\text{Ag}_4\text{Au}^+$ , and (c) $\text{Ag}_5^+$ . $q$ denotes the number of adsorbed CO molecules.....	99
<b>Figure 5.4:</b> Calculated geometries of the $\text{Au}_5(\text{CO})_q^+$ cluster complexes ( $q = 0-5$ ). The depicted geometries have been obtained employing DFT at the B3LYP/TZVP level.....	100

- Figure 5.5:** Computed structures of the binary silver-gold cluster carbonyls  $\text{Ag}_2\text{Au}_3(\text{CO})_q^+$  ( $q = 0-5$ ),  $\text{Ag}_3\text{Au}_2(\text{CO})_q^+$  ( $q = 0-5$ ), and  $\text{Ag}_4\text{Au}(\text{CO})_q^+$  ( $q = 0-6$ ) illustrating the sequential adsorption of carbon monoxide onto the lowest energy metal cluster isomer..... 102
- Figure 5.6:** Ground state geometries of  $\text{Ag}_5(\text{CO})_q^+$  carbonyl complexes obtained by employing DFT with different functionals and basis sets as well as by using coupled cluster SD theory..... 105
- Figure 5.7:** CO binding energies as a function of the number of CO molecules. The calculated values that have been obtained employing the different theoretical methods are compared to the experimentally deduced values ..... 107
- Figure 6.1:** Product ion mass spectra obtained after the reaction of mass selected  $\text{Ag}_3^+$  with  $\text{N}_2\text{O}$  in the rf-ion trap for  $t_R = 1$  s (left column) and  $t_R = 5$  s (right column), respectively. The spectra were recorded at (a) 300 K, (b) 270 K, (c) 250 K, (d) 230 K, and (e) 200 K and well defined amount of He buffer gas and  $\text{N}_2\text{O}$  reactive gas ..... 119
- Figure 6.2:** The lowest energy isomers of (a)  $\text{Ag}_3\text{O}_x^+$  ( $x = 1-3$ ) (b)  $\text{Ag}_3\text{ON}_2\text{O}^+$ , (c)  $\text{Ag}_3\text{O}(\text{N}_2\text{O}_2)^+$ , and (d)  $\text{Ag}_3(\text{N}_2\text{O})_x^+$  ( $x = 1-3$ ), obtained from DFT with B3LYP functional and TZVP atomic basis set by Bonačić-Koutecký et al. .... 121
- Figure 6.3:** Product ion concentrations of the reaction  $\text{Ag}_3^+ + \text{N}_2\text{O}$  as a function of the reaction time  $t_R$  for: (a-c)  $T = 270$  K, (d-f)  $T = 250$  K and (g-i)  $T = 230$  K, respectively ..... 123
- Figure 6.4:** Product ion concentrations as a function of reaction time for a reaction temperature of 250 K..... 124
- Figure 6.5:** Proposed reaction mechanism of the reaction between  $\text{Ag}_3^+$  and  $\text{N}_2\text{O}$ ..... 125
- Figure 6.6:** Product ion mass spectra obtained after trapping of  $\text{Au}_3^+$  and  $\text{Ag}_3^+$ , respectively, inside the octopole ion trap pre-filled with 1 Pa of helium buffer gas and defined quantities of reactant gases..... 129
- Figure 7.1:** Product ion mass spectra obtained after reaction ( $t_R = 200$  ms) of  $\text{Ag}_{3,5}^+$  and  $\text{Au}_{3,5}^+$  with  $\text{C}_6\text{H}_6$  and  $\text{C}_6\text{H}_6/\text{CO}$  ( $p_{\text{He}} = 1$  Pa; (a)-(d)  $p_{\text{bz}} = 0.1$  Pa; (e)-(f)  $p_{\text{bz}} = p_{\text{CO}} = 0.1$  Pa) ..... 134
- Figure 7.2:** Upper frame: Photodissociation mass spectra of the  $\text{Ag}_3\text{-bz}_3^+$  complex; Lower frame: Photodissociation mass spectra of the  $\text{Ag}_5\text{-bz}_2^+$  complex. .... 136
- Figure 7.3:** Femtosecond time dependent signal intensity of (a)  $\text{Ag}_5\text{-bz}_2^+$  and of (b)  $\text{Ag}_3\text{-bz}_3^+$  ..... 139
- Figure 8.1:** Product ion mass spectra of the reaction of (a) - (e)  $\text{Au}_n^+$  ( $n = 1 - 3, 5, 7$ ) with  $\text{CH}_3\text{Br}$  ( $t_R = 10$  ms), (f) - (j)  $\text{Au}_3^+$  with  $\text{CH}_3\text{Br}$  after different reaction times between 10 ms and 5 s (300 K,  $p(\text{He}) = 1$  Pa,  $p(\text{CH}_3\text{Br}) = 0.1$  Pa) ..... 144
- Figure 8.2:** Photodissociation of  $\text{Au}_3(\text{CH}_3\text{Br})_n\text{Br}_{3-n}^+$  ( $n = 1 - 3$ ) product complexes. (a) Thermal reaction products of  $\text{Au}_3^+$  after 5 s reaction time. (b) Product ion mass spectrum obtained

under similar reaction conditions after 5 s laser irradiation (266 nm). (c) Difference spectrum (b - a)..... 145

**Figure 8.3:** Proposed mechanism for the photocatalytic methyl elimination reaction. .... 146

**Figure 8.4:** Product ion mass spectra of the reaction of  $\text{Ag}_3^+$  with  $\text{CH}_3\text{Br}$  at various reaction temperatures: (a) 300 K, (b) 250 K, (c) 240 K, and (d) 230 K ( $p(\text{He}) = 1 \text{ Pa}$ ,  $p(\text{CH}_3\text{Br}) = 0.1 \text{ Pa}$ ,  $t_R = 5 \text{ s}$ ). .... 147

**Figure 8.5:** Photodissociation mass spectrum of the  $\text{Ag}_3(\text{CH}_3\text{Br})_n\text{Br}_{3-n}^+$  ( $n = 1 - 3$ ) product complexes at a laser wavelength of 266 nm (230 K,  $t_R = 5 \text{ s}$ ,  $p(\text{CH}_3\text{Br}) = 0.1 \text{ Pa}$ )..... 148

**Figure 8.6:** TPD spectra of  $\text{CH}_3\text{Br}$  from (a) bare 10 ML MgO on Mo(100); (b-g) MgO supported gold nano-particles generated by depositing different gold coverages..... 149

# List of tables

<b>Table 2.1:</b> Output characteristic of the Ti:Sapphire oscillator. ....	28
<b>Table 2.2:</b> Output characteristic of the amplifier. ....	31
<b>Table 2.3:</b> Output characteristic of the OPA tuned to 353 nm .....	33
<b>Table 2.4:</b> Output characteristic of the home-build frequency tripler.....	35
<b>Table 2.5:</b> Autocorrelation width and spectral bandwidth for different transform-limited pulses.....	37
<b>Table 3.1:</b> The vibrational energy $E_{\text{vib}}$ , the free energy $E_{\text{free}}$ , and the energy of the activated complex $E^*$ according to the model proposed by Cox et al.. $n$ denoted the number of atoms contained in the molecular complex.....	51
<b>Table 3.2:</b> Calculated frequencies for the energized complexes $(M_nL^{+/-})^*$ and the “loose” TS $(M_nL^{+/-})^\ddagger$ .....	53
<b>Table 4.1:</b> Experimental and theoretical binding energies of CO to anionic and cationic cluster trimers as deduced by employing RRKM theory for “tight” and “loose” TSs, thermodynamic equilibrium method, and DFT ab initio simulations. The corresponding theoretical complex structures are given in the supplementary information.....	68
<b>Table 5.1:</b> Binding energies (in eV) of the $q^{\text{th}}$ CO in the complexes $\text{Ag}_n\text{Au}_m(\text{CO})_q^+$ for all investigated metal cluster cations. Experimental values (exptl.) are compared to theoretical data (calculated according to Equation (8)) obtained via the different methods as indicated (cf. also Section 2.2). The error of the experimental thermochemical equilibrium data is estimated to be within $\pm 0.1$ eV. ....	104



# Abbreviations

<i>ac</i>	alternating current
<b>AOM</b>	Acousto-Optical Modulator
<b>BBO</b>	$\beta$ -Barium Borate
<b>B3LYP</b>	A hybrid method, a mixture of Hartree-Fock exchange with density functional exchange correlation
<b>bz</b>	Benzene
<b>CCD</b>	Charge Coupled Device
<b>CC-SD</b>	Coupled Clusters Singles Doubles method
<b>CORDIS</b>	Cold Reflex Discharge Ion Source
<b>CPA</b>	Chirped Pulse Amplification
<b>CT</b>	Charge Transfer
<i>cw</i>	continuous wave
<b>2D</b>	Two Dimensional
<i>dc</i>	direct current
<b>DFT</b>	Density Functional Theory
<b>fs</b>	femtosecond
$E_b$	Binding Energy
<b>19e-RECP</b>	19-electron Relativistic Effective Core Potential
<b>FWHM</b>	Full Width at Half Maximum
<b>HOMO</b>	Highest Occupied Molecular Orbital
<i>k</i>	pseudo first-order rate constant
$k^{(3)}$	termolecular rate constant
$k_a$	association rate constant
$k_d$	decomposition rate constant
$k_s$	stabilization rate constant
<b>LUMO</b>	Lowest Unoccupied Molecular Orbital
<b>ML</b>	Monolayer equivalent
<b>NeNePo</b>	Negative-to-Neutral-to-Positive
<b>OPA</b>	Optical Parametric Amplifier
<b>RF</b>	Radio Frequency
<b>RGA</b>	Residual Gas Analyzer
<b>RRK</b>	Rice-Ramsperberg-Kassel theory
<b>RRKM</b>	Rice-Ramsperberg-Kassel-Marcus theory

## *Abbreviations*

---

<b>SFG</b>	Sum Frequency Generation
<b>SFM</b>	Sum Frequency Mixing
<b>SHG</b>	Second Harmonic Generation
<b>THG</b>	Third Harmonic Generation
<b>TPD</b>	Temperature Programmed Desorption
<b>TS</b>	Transition State
<b>TZVP</b>	Triple-Zeta-Valence-plus-Polarization atomic basis set
<b>UHV</b>	Ultra-High Vacuum



# 1

## General introduction

---

### 1.1 Cluster science

*“I would like to describe a field, in which little has been done, but in which an enormous amount can be done in principle. This field is not quite the same as the others in that it will not tell us much of fundamental physics (in the sense of, “What are the strange particles?”) but is more like solid-state physics in the sense that it might tell as much of great interest about the strange phenomena that occur in complex situations. Furthermore, a point that is most important is that it will have an enormous number of technical applications. What I want to talk about is the problem of manipulating and controlling things on a small scale.”*

Richard P. Feynman

In **“There’s Plenty of Room at the Bottom”**

An Invitation to Enter a New Field of Physics<sup>1</sup>

The field of nanoscience can be said to derive from a visionary article by Richard P. Feynman. In this often-quoted article, entitled **“There’s Plenty of Room at the Bottom”**,<sup>1</sup> Feynman challenged scientists to develop a new field of study where devices and machines could be constructed from components consisting of a small number of atoms. This article has inspired generations of physicists and chemists to try to make Feynman’s vision a reality. Thus, the world of small particles has burgeoned during the past decades motivated also by the growing interest in the unexpected evolution of physical and chemical properties from the atom to the bulk solid, a progression passing through the cluster domain.

*Clusters* are defined as aggregates of atoms or molecules, generally intermediate in size between individual atoms and aggregates large enough to be called bulk matter. Clusters differ from conventional molecules in composition and structure. Basically, molecules

have a definite, highly restricted number of atoms and specific composition. Moreover, they almost always have unique structures. Clusters may be composed of any number  $n$  of component particles, and, for most kinds of clusters, as the number of particles becomes larger, the number of stable structures grows rapidly. Thus, clusters of a given composition may exhibit a variety of structures but they generally cannot be distinguished as different chemical species.<sup>2</sup>

Clusters may be characterized by many factors such as size, composition, charge, structure, as well as by the type of force which holds them together. Thus, considering the number of atoms  $n$  in a cluster, different size regimes can be distinguished: small clusters ( $n \leq 10^2$ ), medium-size clusters ( $10^2 \leq n \leq 10^3$ ) and large clusters ( $10^3 \leq n$ ).<sup>3</sup> This classification is however arbitrary, since depending on their composition, clusters may exhibit a size-selective behavior, where each atom counts, or already a bulk-like behavior. Small clusters are those whose properties vary with size and shape such that no simple, smooth function

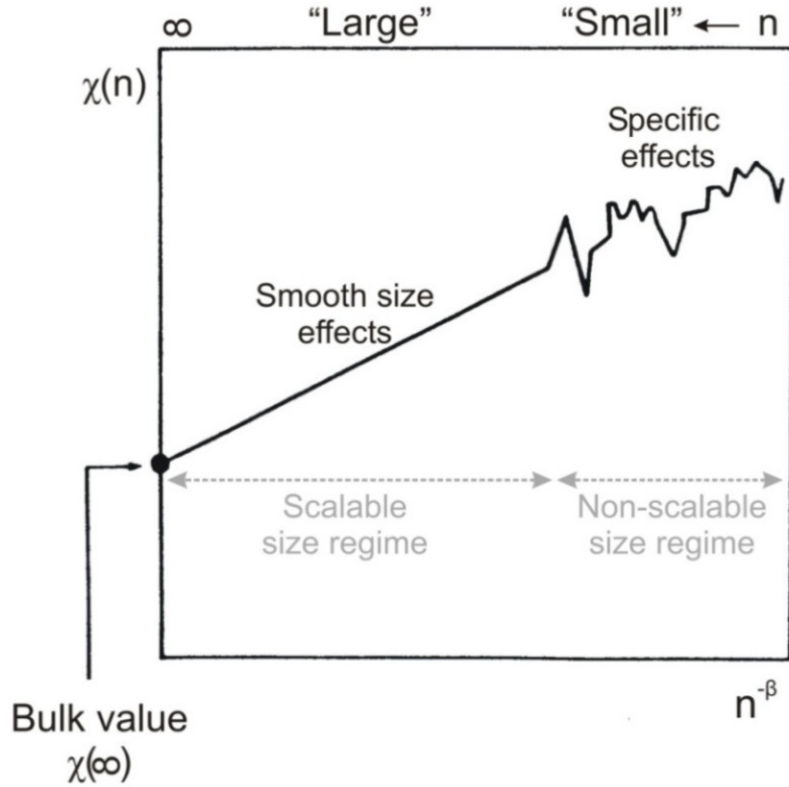


**Figure 1.1:** Typical evolution of a physical quantity ( $\chi(n)$ ) as a function of the cluster size ( $n$ : number of clusters constituents). The data are plotted vs.  $n^{-\beta}$  where  $0 \leq \beta \leq 1$ . Small clusters reveal specific size effects, while large clusters are expected to exhibit for many properties a “smooth” size dependence of  $\chi(n)$  which converges for  $n \rightarrow \infty$  to the bulk value  $\chi(\infty)$ . The scalable and non-scalable regime are denoted by the grey arrows.<sup>4</sup>

can be given for their dependence on number of composing particles. If the cluster properties are smoothly varying functions of the number of component particles, the cluster is medium size or large.

Based on their composition the clusters can be homogeneous (consisting of only one type of atoms or molecules) or heterogeneous (consisting of more than one kind of atoms or molecules). On the other hand, depending on their charge state, the clusters are classified in neutral and charged (positive or negative). Taking into account the type of forces which hold them together we can consider covalent-, metallic-, ionic-, van der Waals-, and hydrogen-bonded clusters.

For a long time it has been assumed that the properties of small metal clusters can be obtained by down-scaling the properties of the bulk material. In the case of large clusters, the specific physical quantities typically emerge as a smooth function of the size of the clusters because of the changes in the average coordination of the constituents as a function of cluster size.

However, when the particle size is reduced below a few nanometers, unexpected new properties and functionalities arise and the evolution of the physical quantities becomes less predictable. Typically, adding or removing a single atom or molecule from a cluster may result in very significant changes, i.e. their structural, electronic, and electromagnetic observables vary irregularly with cluster size and can exhibit strong variations from one size to the other (as schematically illustrate the Figure 1.1). In addition, small clusters have the advantage that they represent tractable systems for sophisticated high-level theoretical treatments. They also constitute an ideal playground to test theoretical models against experimental results.

The chemistry of small metal clusters has received considerable attention over the last several years,<sup>5-7</sup> especially due to their important role in a number of catalytic reactions. The fascination for metals in the cluster state of matter is not new. The glaziers of the Middle Aged discovered how to produce beautiful stained glasses by special treatments of metal-containing glasses. Rayleigh was the first who recognized that the colors of stained glasses were due to the scattering of the light by small metal particles embedded in the glass. His work was followed by an extensive electrodynamic treatment by Mie,<sup>8</sup> which is even now relevant.

Today, the metal clusters are no longer only delightfully beautiful for the “eyes and heart”, but they represent valuable model systems and provide new types of materials. They are particularly useful to learn how bulk properties emerge from properties of atoms, as the clusters become larger and larger.

Cluster science is not only a fascinating field in its own right; it enriches the fields around it and offers tantalizing possibilities for new materials and processes. The present knowledge on stabilities, quantum size effects, electronic and optical properties of metal clusters has been summarized in a number of detailed review articles.<sup>9-19</sup>

## 1.2 Experimental techniques in cluster ion chemistry

For almost three decades, isolated mass-selected metal clusters have been considered important model systems for the understanding of chemical reactions, in particular catalytic processes. Since there is no universal cluster source yet capable to satisfy simultaneously all experimental requirements needed for the gas phase studies, a variety of cluster sources have been developed during the last period. Depending on the nature and conditions of the source, different size distributions of clusters may be generated. The list below summarizes the characteristics of the most commonly used cluster sources:

(i) *Seeded supersonic nozzle sources* are mostly used to produce intense cluster beams of low-melting-point metals, such as alkali metals.<sup>20-22</sup> These sources produce continuous beams with reasonably narrow energy spread. Clusters with up to several hundreds of atoms per cluster may be produced in adequate abundance.

In the seeded supersonic nozzle source the material is heated in an oven and a mixture of gaseous material and a seed gas expands through a nozzle into the vacuum. The expansion into the vacuum proceeds adiabatically and causes cooling of the mixture. The cooled metal vapor becomes supersaturated, condensing in the form of clusters. Cluster production continues until the expanding vapor density becomes too low to promote further growth, typically within a few nozzle diameters from the nozzle exit.

(ii) *Gas-aggregation sources* are particularly efficient in the production of large clusters ( $N < 10000$ ). The intensities are generally much lower than those of the nozzle sources. The overall cluster size distributions can be adjusted within rather broad limits. These sources are used for low-to-medium-boiling-point materials ( $< 2000$  K). Low cluster temperatures ( $< 100$  K) can be achieved.

In the gas-aggregation source, the metal is vaporized and introduced into a flow of cold inert gas. The metal vapor becomes in that way highly supersaturated. Due to the low temperature of the inert gas, cluster production proceeds primarily by successive single-atom addition. Since the reverse process, i.e., reevaporation is insignificant, the cluster abundances are insensitive to the thermodynamic stabilities of the clusters and, consequently, the clusters abundance are relatively smooth functions of the cluster size determined mainly by collision statistics. The cluster size distribution is determined by the parameters of the source, such as the metal-vapor density and the gas flow rate.

Several versions of this source have been developed over the years, e.g., by Rayane et al.,<sup>23</sup> Schulze et al.,<sup>24</sup> and Limberger et al.<sup>25</sup> following the prototype by Sattler et al..<sup>26</sup>

(iii) *Laser vaporization sources* are cluster sources used to produce small- and medium-sized clusters in the size range from the atom to typically several hundreds of atoms per cluster.<sup>27-29</sup> These sources are pulsed and, although the time-average flux is low compared with the seeded supersonic nozzle sources, intensities within a pulse are much higher. In principle, these sources can be used for all metals to produce neutral, positively and nega-

tively charged clusters. In the laser vaporization source, vapor is produced by pulsed-laser ablation of a rod (of any metal) using an intense pulsed Nd:YAG or excimer lasers. The vaporized metal is introduced into a pulse of cold helium, which rapidly cools the vapor and induces cluster formation. The cluster temperatures are expected to be near or below the source temperature, depending on the supersonic expansion conditions. Closely related to the laser vaporization source is the pulsed-arc cluster ion source (PACIS).

(iv) *Pulsed-arc cluster-ion sources* (PACIS) are basically similar to laser vaporization sources, instead that the cluster material is vaporized by an intense electrical discharge.<sup>30-32</sup> The resulting cluster beams generated in this way are significantly more intense than when using laser vaporization. This cluster source generates ionized clusters directly but suffers from significant pulse-to-pulse variation in the beam intensity.

(v) *Ion sputtering sources* are used primarily to produce intense continuous beams with high stability of small singly ionized clusters of most metals. But as the beam intensity falls off rapidly with size, these sources are not suitable to produce medium to large clusters in large enough quantities. Nevertheless, and in spite of a relative large energy spread of the generated clusters, sputter sources are widely used for the production of small size-selected clusters. Cluster-ion beams are produced by bombarding a metal surface with high energy inert-gas ions. For the best performance, heavier inert gases (Kr and Xe) are typically used. The bombardment energies range are between 10 and 20 keV with currents up to 10 mA.<sup>33-35</sup> The produced clusters are hot, typically near to the evaporation limit, so that the abundance spectra reflect the thermodynamic stabilities of the clusters, determined by their binding energies.

(vi) *Liquid-metal ion sources* are used to produce singly and multiply ionized clusters of low-melting-point metals. They are often used in experiments involving multiply charged small clusters. Thus, cluster mass spectra have been analyzed to explain shell structure in rubidium and cesium clusters<sup>36</sup> as well as sodium clusters.<sup>37</sup>

In the liquid-metal ion source, very high electric fields are generated at the tip of the needle which has been wetted with the metal to be investigated and heated above the melting point of the metal<sup>38-40</sup> The high electric fields at the tip of the needle cause a spray of very small droplets to be emitted from the tip. The initially very hot and often multiply ionized clusters undergo evaporative cooling and cluster fission to generate smaller sizes.

As a consequence of the multiple ways of producing clusters, a variety of techniques for studying clusters in an interaction-free environment have been developed. The most important techniques presently used to investigate the chemical properties of mass selected free metal clusters will be summarized in the following.

(i) *Flow tube reactors* are one of the older methods to investigate metal cluster reactions. In its most simple form, an extender is attached to a cluster source (e.g., to a laser vaporization or discharge cluster source), which allows the downstream addition of reactive gases. Different variations of the basic principle have been realized.<sup>41-46</sup> Depending on the

exact design, relatively high reactant partial pressures might be reached in a flow tube reactor. This means that (a) multiple-collision conditions prevail, (b) thermal equilibration with the flow tube walls can be assumed, and (c) saturation coverage of adsorbates are expected to be observed at the highest reaction concentrations.

(ii) *Collision gas cells* represent a different approach to reveal the size-dependent cluster reactivity by investigating the individual collisions between clusters and reactive molecules. In this case, a beam of neutral clusters passes through one or more cells filled with only low pressures of reactive gas. Under such single-collision-like conditions, the determination of absolute numbers of the reaction probability in a collision is possible by evaluating the depletion of the pure metal clusters and the product formation employing statistical rate theory.<sup>47</sup> This method is claimed to be best suited for highly reactive systems, as the detection limit corresponds to a reaction probability of 0.01-0.05. However, cluster fragmentation is likely for small clusters as the reactions often proceed with high probability, but are also highly exothermic. Thus, the excess energy cannot be abducted during the reaction causing the reaction product analysis ambiguous.

(iii) *Low-energy ion guide*. Molecular beam experiments are strongly handicapped by fragmentation phenomena, which commonly occur during reactive collisions, electronic transitions, neutralization, or ionization processes. As a consequence, parent molecules and fragments can no longer be easily distinguished. In a typical low-energy guided ion beam experiment, this obstacle is circumvented by mass selection of the cluster ion beam prior to the reactive encounter. The reactions commonly take place in a radio frequency (rf) ion guide drift tube. The cluster ion confined by the rf field inside the ion guide have a defined low kinetic energy and experience multiple collision with the reactive gas added to the ion guide. Mass-selected detection of the product ions is accomplished by a quadrupole mass filter followed by signal amplification with a secondary electron multiplier.

(iv) *Ion traps*. Ion cyclotron resonance (ICR) mass spectrometry and also penning trap mass spectrometry have been demonstrated by several groups to be powerful tools to investigate metal cluster reactivity in the gas-phase under single-collision conditions.<sup>48-55</sup> An ICR cell is a small box or cylinder consisting of four isolated side plates and two isolated end plates. The cell is immersed in a homogeneous magnetic field. In order to investigate cluster reactions, the cluster ion packets entering the cell are excited by an rf pulse applied to one plate. Due to the homogeneous magnetic field traversing the ICR cell, the ions are thus led to perform a circular motion in the cell. The cyclotron frequency of the circular motion depends on the ion mass and the magnetic field strength. The image current induced on two opposite plates of the cell is amplified and analyzed by Fourier transformation. This method has a particular high mass resolution and sensitivity. The ICR instruments operate under UHV conditions and reactions are investigated under strict single-collision conditions.

Another approach to investigate metal clusters reactivity as well catalysis consist in storing the mass-selected cluster ions in a temperature variable rf multipole ion trap filled

with helium buffer gas and small partial pressure of reactant gases under multiple-collision conditions. The major advantage of this method for the investigation of gas-phase reactions is the precise control over reaction time, reactant concentrations, and reaction temperature inside the trap. This approach is employed in the present thesis and the octopole ion trap acts as a test tube for gas-phase reaction kinetics studies and is inserted into a standard guided ion beam apparatus.<sup>56-58</sup>

### 1.3 Concepts in cluster ion chemistry and femtochemistry

In this section, several aspects unique to the study of gas-phase metal cluster ions are introduced. These concepts are very important on one hand to ion cluster chemistry, particularly with respect to the analysis of catalytic reaction mechanisms, and on the other hand to cluster photochemistry.

(i) *Particle size-dependent reactivity* - Gas-phase investigations allow the application of mass spectrometric techniques to define the exact number of atoms that constitute the metal particle of interest. This is particularly important as in the non-scalable size regime below about 100 atoms per particle each atom is important to the catalytic reaction behavior and the chemical and physical properties of the particles often change by orders of magnitude when adding or removing a single atom (cf. Figure 1.1). Whereas small free metal clusters present fascinating new catalytic materials by themselves, mass-selective gas-phased methods also enable the study of size-dependent reaction behavior starting from the isolated atomic ions over small clusters and eventually reaching the regime of nanoparticles employed in condensed-phase heterogeneous catalysis.

(ii) *Charge state-dependent reactivity* - In particular in noble metal catalysis, charging of supported metal particles has been found to decisively determine the catalytic activity of the model catalyst materials.<sup>59,60</sup> However, the analysis of the influence and the extent of the charge transfer is difficult to evaluate experimentally in supported systems. In gas-phase systems, the charge state is exactly defined and the investigation of the chemical reaction behavior as a function of the charge state can provide important insight into the influence of electronic effects on catalytic reactions of small metal clusters like, e.g., the O<sub>2</sub> activation.

(iii) *Composition - dependent reactivity* - With respect to the influence of the electronic structure on the catalytic activity, the elemental composition of the metal cluster presents a further important aspect.<sup>59</sup> By changing the constituents of a cluster atom by atom, reactive behavior and important catalytic properties, like, e.g., the reaction selectivity, might be tuned to a maximum for a specific reaction system. In the majority of cases, mass spectrometric gas-phase techniques enable the precise control of the metal particle composition, which is in turn widely tunable with modern cluster sources. This versatile access to the influence of the particle composition on the catalytic behavior should provide important basic

information for systematic material design.

(iv) *Cooperative coadsorption effects* - Coadsorption phenomena in heterogeneous catalysis and surface chemistry quite commonly consider competitive effects between two reactants on a metal surface.<sup>61,62</sup> Also, cooperative mutual interaction in the adsorption behavior of two molecules has been reported.<sup>61</sup> Recently, this latter phenomenon was found to be very pronounced on small gas-phase cluster ions, too.<sup>63-66</sup> This is ascribed to be the above-mentioned fact that the metal cluster reactivity is often strongly charge state dependent and that an adsorbed molecule can effectively influence the electronic structure of the metal cluster by, e.g., charge transfer effects. This changed electronic complex structure in turn might foster (or also inhibit) adsorption and reaction of further reactant molecules that would otherwise not be possible.

(v) *Pump-probe spectroscopy* - Due to the advances in conceptual and technical aspects of the femtosecond pump-probe spectroscopy pioneered by Zewail,<sup>67-69</sup> ultrafast time-resolved studies of cluster dynamics became available in the last decades. In the typical pump-probe spectroscopy a first laser pulse (pump) initiates the chemical reaction, while a second (probe) pulse interrogates the system on the reaction path at different delay times after the pump pulse. Due to the broad frequency spectrum of femtosecond pulses several vibrational levels of a particular excited electronic state are coherently populated. Their coherent superposition is known as a wave packet. The propagation of the wave packet corresponds to the movement of the nuclei. By means of pump-probe spectroscopy the vibrational dynamics on bound states can be investigated, whereby a succession of minima and maxima of the measured signal is expected. Moreover, molecular dynamics on dissociative states can be also examined, whereby an exponential decay of the signal is expected.

(vi) *Charge-transfer interaction* - For a complex to demonstrate charge-transfer behavior one of its components must have electron-donating properties while the other component must be able to accept electrons. Adsorption of radiation then involves the transfer of the electron from the donor to a molecular orbital associated with the acceptor.

## 1.4 Motivation and objective of the thesis

Since the age of alchemy and the search for the philosopher's stone, people have searched for ways of controlling the transformation of matter. Today, scientists seek to control the outcome of chemical reactions, to suppress unwanted side products, and to create new reaction products. Metallic clusters were proven to be valuable systems for this purpose since their physical and chemical properties often change over orders of magnitude by mere addition or removal of one single atom. Therefore, playing with the cluster size, charge, and/or composition a chemical reaction can be guided along new, unexplored reaction pathways.



The experimental results of Haruta and coworkers first showed that highly disperse gold clusters are catalytically active when supported on metal-oxide surfaces<sup>70</sup> although gold is known to be chemically inert in the bulk phase.<sup>71</sup> This finding has prompted a sizeable experimental and theoretical effort in an attempt to fully understand these properties.<sup>72-76</sup> Much attention has also been paid to silver clusters, due in part to the fact that they, e.g., serve as epoxidation catalysts for ethene and propene.<sup>77-79</sup> There is currently a considerable interest in trying to understand the size-dependent catalytic activity<sup>60,80</sup> of these clusters and to develop robust theoretical models. Although the catalytic properties of nanoscale silver and gold were intensively studied, the intrinsic mechanisms of the heterogeneous catalysis at atomic and molecular level still remain elusive. In this context, model systems are required that are simple enough to be investigated experimentally at the molecular level and to be described theoretically in detail.

Detailed investigations of metal cluster reactivity in the gas-phase can provide important information, both as data for testing theoretical models and to establish structural, energetic, and reactive properties of size-selected clusters in the subnanometer range without any substrate or solvent influence.

An initial step that has been made to understand the properties of coinage metal clusters was to determine their gas-phase configuration. The geometrical structures of free gold, silver and binary silver-gold cluster ions have been investigated previously experimentally by means of ion mobility mass spectrometry<sup>81-84</sup>, ion trap electron diffraction,<sup>85-87</sup> photoelectron spectroscopy,<sup>88-91</sup> infrared multiphoton dissociation spectroscopy,<sup>53,92</sup> as well as theoretically via first principle calculations.<sup>81,82,84,93-101</sup>

The interaction between noble metal clusters and small, catalytically relevant molecules was the subject of extensive studies, as well. Systematic experiments have examined the properties of a variety of gas-phase noble metal complexes  $M_n^{+/-}L_m$  ( $M = Ag, Au$ ) with several ligands ( $L = O_2$ ,<sup>102-107</sup>  $CO$ ,<sup>108-114</sup>  $H_2$ ,<sup>102,115,116</sup>  $CH_4$ <sup>64,102,116,117</sup>). Recently even a full thermal catalytic gas phase oxidation cycle of CO on an anionic gold dimer could be demonstrated.<sup>118</sup> Furthermore, a joint experimental and theoretical study could show that  $Au_2^+$  was able to adsorb and activate methane and to selectively catalyze the formation of ethylene at temperature as low as 250 K.<sup>119</sup>

All these experiments in conjunction with theoretical calculations have broadened the understanding of the nature of noble metal ion bonding and have provided some of the fundamental information necessary to elucidate the complex factors involved in many catalytic processes. Although, gas-phase studies of metal clusters may never account for the precise mechanism in real catalysis, complemented by computational investigations, they can provide a conceptual framework and help to deduce reactivity patterns.<sup>120</sup>

The approach pursued in the present work consists in the investigation of small mass-selected pure and binary silver-gold cluster ions in the gas-phase under well defined reaction conditions. The main goal of this thesis is to study the chemical and photo-physical proper-

ties of these clusters in a range were each atom counts. The mixed silver-gold clusters are particularly interesting since their electronic properties can be tuned by changing the charge and the composition of the cluster.

An important initial step in combustion reactions is the adsorption of CO on the catalyst. Quantitative information concerning the binding of carbon monoxide to isolated clusters can thus be of great value and assist the understanding of the overall reaction mechanism. Therefore, a part of this thesis addresses the reactivity of size-selected pure and binary silver-gold clusters towards CO and delivers new insight into the binding mechanism and the number of adsorption sites for the reactants. A second task of this part is to learn how cluster reactivity is modified by playing with the cluster composition, changing the constituents atom by atom, or/and by varying the cluster charge state.

Another objective of the present investigation was to find a way to adsorb and activate oxygen on size selected silver and gold cluster cations, since both silver and gold clusters were found to be unreactive toward O<sub>2</sub> under our experimental conditions.<sup>121</sup> Therefore, our approach to produce silver- and gold-oxides was through reaction with N<sub>2</sub>O.

Pertinent to the size dependent physical and chemical properties of metal clusters in particular and to chemical reactions in general is the motion of the atomic nuclei in the course of the reactive transformation on the fundamental femtosecond ( $1\text{ fs} = 10^{-15}\text{ s}$ ) time scale. The recent developments of femtosecond laser technology in conjunction with pump-probe spectroscopic technique enables the study of the nuclear dynamics of a molecular system in real time<sup>68,69,122</sup> and represents the birth of a new scientific field referred to as femtochemistry. A major intent of this work therefore also aimed to cover the femtochemistry of metal clusters reactions with a special focus on the charge-transfer complexes in which charge state dependent photoinduced dynamics could be monitored in real time.

In the experiments presented in this work the pump-probe spectroscopic technique was applied to investigate the dynamics of silver-benzene and gold-benzene ion-molecule complexes on the femtosecond time-scale. Particularly, the silver cluster photodissociation experiments at 353 and 393 nm, respectively, provided indications for a charge transfer induced fragmentation. The Ag<sub>5</sub>(C<sub>6</sub>H<sub>6</sub>)<sup>+</sup> photofragmentation dynamics could be even resolved in real time.

## 1.5 Outline of the thesis

The present thesis contains contributions to two scientific fields, which are: (i) *cluster models* in the context of catalysis and (ii) *femtochemistry* of cluster-molecule complexes. The thesis is organized within nine chapters as follows. After the presentation of some fundamental concepts of cluster chemistry and photochemistry during the present chapter, the experimental setup consisting of an rf-octopole ion trap inserted into a multiple quadrupole

mass spectrometer arrangement in conjunction with a fs-laser system, which allows trapping, cooling and probing of mass selected gas phase ions, is described in detail in **Chapter 2**. Moreover, a short introduction into the world of femtosecond laser pulses is given here. Thus, the basics of their generation, amplification and measurement, together with elements of nonlinear optics are briefly described.

The experimental methods for data acquisition as well as the theoretical concepts of gas-phase reaction kinetics together with the computational method to deduce binding energies from the experimental data are presented in the **Chapter 3**. This chapter also provides the basis for understanding the subsequent temperature dependent reactivity study. Another approach to determine the binding energy by means of temperature-dependent equilibrium methods is also in detail described here. Finally, the data acquisition method for time-resolved photodissociation experiments together with some basics of charge-transfer processes closes the chapter.

The experimental results obtained from the systematic study of the reactivity of pure and binary silver-gold triatomic cluster ions towards carbon monoxide are presented in **Chapter 4**. The influence of the cluster charge as well as of the cluster chemical composition on their reactive behavior is discussed and the experimental obtained binding energies are compared to the values obtained by means of DFT *ab initio* calculations.

In **Chapter 5** temperature-dependent equilibrium measurements in conjunction with *ab initio* calculations were used to determine the experimental as well as theoretical binding energy of CO to pure and binary silver-gold cationic pentamers.

Since the cationic silver and gold clusters investigated in this work were found to be unreactive toward molecular oxygen, the reaction with nitrous oxide was used to produce metal oxide clusters. The obtained results are presented in **Chapter 6**. First evidence for a successful CO oxidation on triatomic silver- and gold-oxide cations are also presented here.

The second part of this work focuses on the formation and photodissociation dynamics of small cluster-molecule complexes. In **Chapter 7** the formation and femtosecond photodissociation of  $\text{Ag}_n^+$  and  $\text{Au}_n^+$  complexes with benzene and carbon monoxide was investigated. The presented photodissociation experiments deliver strong indications for charge-transfer induced fragmentation in the case of the silver cluster-benzene complexes. In particular, for  $\text{Ag}_5(\text{C}_6\text{H}_6)_2^+$  the femtosecond time resolved fragmentation dynamics could be measured.

Since gas-phase investigations of small clusters may provide valuable conceptual insights that support the understanding of surface experiments, the noble metal cluster reactivity toward  $\text{CH}_3\text{Br}$  as model system was studied. The formation and femtosecond photodissociation of  $\text{Au}_n(\text{CH}_3\text{Br})_m^+$  and  $\text{Ag}_n(\text{CH}_3\text{Br})_m^+$  complexes are reported in **Chapter 8** where the obtained results are subsequently compared to those obtained for  $\text{CH}_3\text{Br}$  molecule adsorbed on supported gold clusters as well as on gold surface.

The last chapter (**Chapter 9**) summarizes the results of this work and provides an outlook for possible future experiments.

# 2

## Experimental setup

---

*In this chapter, the details of the experimental setup employed to measure the cluster reactivity (reaction kinetics) as well as the fs-photodissociation dynamics of small noble metal cluster-molecule complexes are presented. The setup consists of a sputtering cluster ion source attached to a tandem quadrupole and octopole ion trap arrangement in conjunction with a commercial fs-laser system. After a detailed description of the cluster ion source, the basic principles of the ion optics, the quadrupole mass analyzers, and the radio frequency octopole ion trap are presented. Finally, the characteristics of the ultrafast laser system used in the present investigations are summarized.*

## 2.1 Cluster production and analysis

The vacuum setup shown in Figure 2.1 consists of two main parts. The first part (denoted with 1 in Figure 2.1) consists of the cluster ion source in conjunction with the rf-quadrupoles for cluster thermalization and mass selection. This part of the apparatus is mounted on a rail system and is connected to the second part by a flexible bellow. Its distance from the second chamber can be adjusted under operation conditions by a motor driven spindle. The second part (denoted with 2 in Figure 2.1) is composed of octopole ion trap, a quadrupole mass selector, and the ion detection unit. Details of the setup will be described below.

The vacuum system is differentially pumped by four roughing pumps ( $3 \times 16 \text{ m}^3/\text{h}$ ,  $1 \times 60 \text{ m}^3/\text{h}$ ) and six turbo-molecular pumps ( $4 \times 510 \text{ l/s}$ ,  $270 \text{ l/s}$  and  $2200 \text{ l/s}$ ). Four ion gauges monitor the pressure in the machine. The background pressure (all gas inlets closed) is about  $8 \times 10^{-9} \text{ mbar}$ .

Alternatively, for the investigation of soft-landed metal clusters, the produced cluster ions can be directed to the surface by means of a quadrupole deflector in conjunction with an ion guide arrangement. For this purpose the mobile part composed of the quadrupole ion guide  $Q_2$  and the source assembly can be retracted and the quadrupole deflector can be inserted by a translation mechanism under vacuum conditions in front of the exit lens of  $Q_2$ . Details concerning the new ion guide optics arrangement for cluster deposition can be found in Reference 123.

### 2.1.1 Ion source

A cold reflex discharge ion source (CORDIS)<sup>124</sup> is used for the production of metal cluster ions in both positive and negative charge state. As described in the Section 1.2, this type of cluster source is the best choice to produce intense continuous beams of small singly ionized clusters of most metals, as required by our experiment. In order to enhance the cluster signal, the initial original device constructed by R. Keller<sup>124</sup> was modified to obtain four primary Xe ion beams of typically 10 keV and about 2 mA. The basic principle of the cluster source is described in the following. An enlarged view of the cluster source together with the target chamber as well as the phase space compressor quadrupole ion guide is displayed in Figure 2.2a.

Six tantalum filaments supported on a tantalum holder are resistively heated (typically 170-180 A/6-7 V) to emit electrons which are further accelerated by a *dc*-field (around 60 V). The accelerated electrons ionize the rare gas atoms, Xe in the present case ( $p_{\text{Xe}} = 6 \times 10^{-2} \text{ mbar}$ ), and consequently a plasma is obtained. The produced plasma is magnetically confined in the center of the chamber by means of 18 radially placed cobalt-samarium permanent magnets. All parts which are in contact with the primary ion beam are machined from a tungsten-copper alloy and are water-cooled.

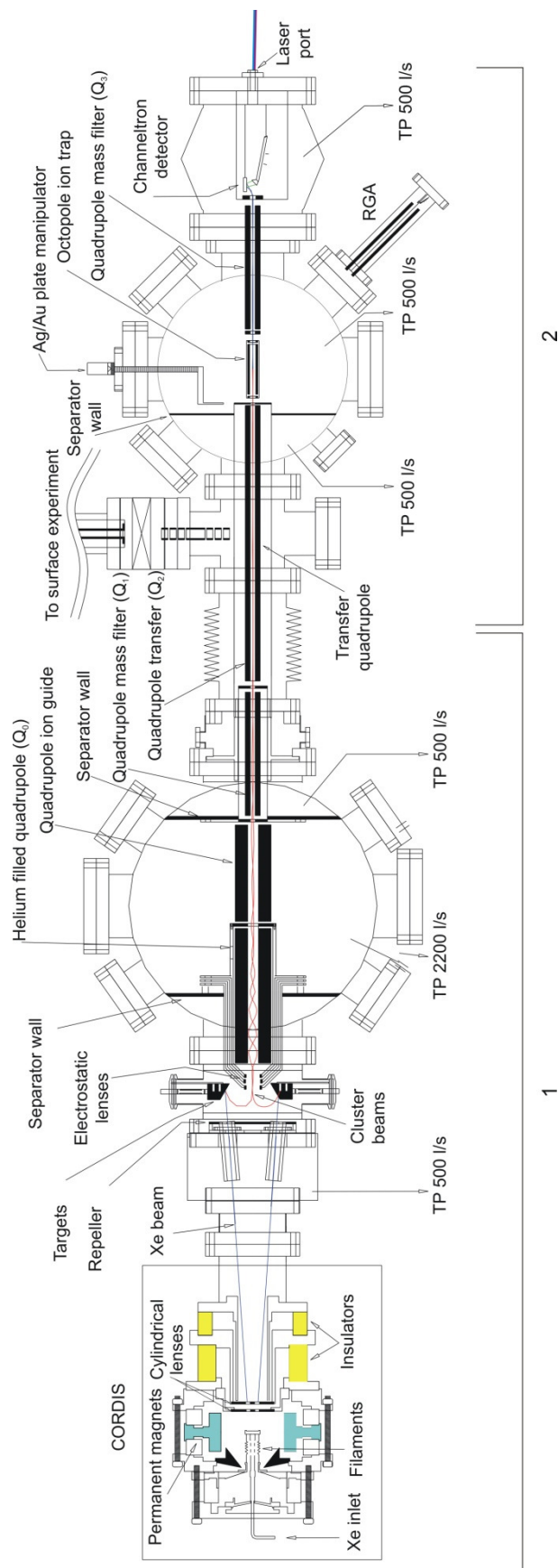


**Figure 2.1:** Experimental setup for the investigation of reaction kinetics and catalytic activity of free mass-selected metal clusters. The cluster ions are sputtered from solid targets with a cold reflex discharge ion source (CORDIS), mass-selected ( $Q_1$ ), and guided at low energies ( $Q_0$  and  $Q_2$ ) into the temperature controllable octapole ion trap. By means of appropriate switching of the octopole lenses, the reaction products are extracted and subsequently mass analyzed by another quadrupole mass filter ( $Q_3$ ).

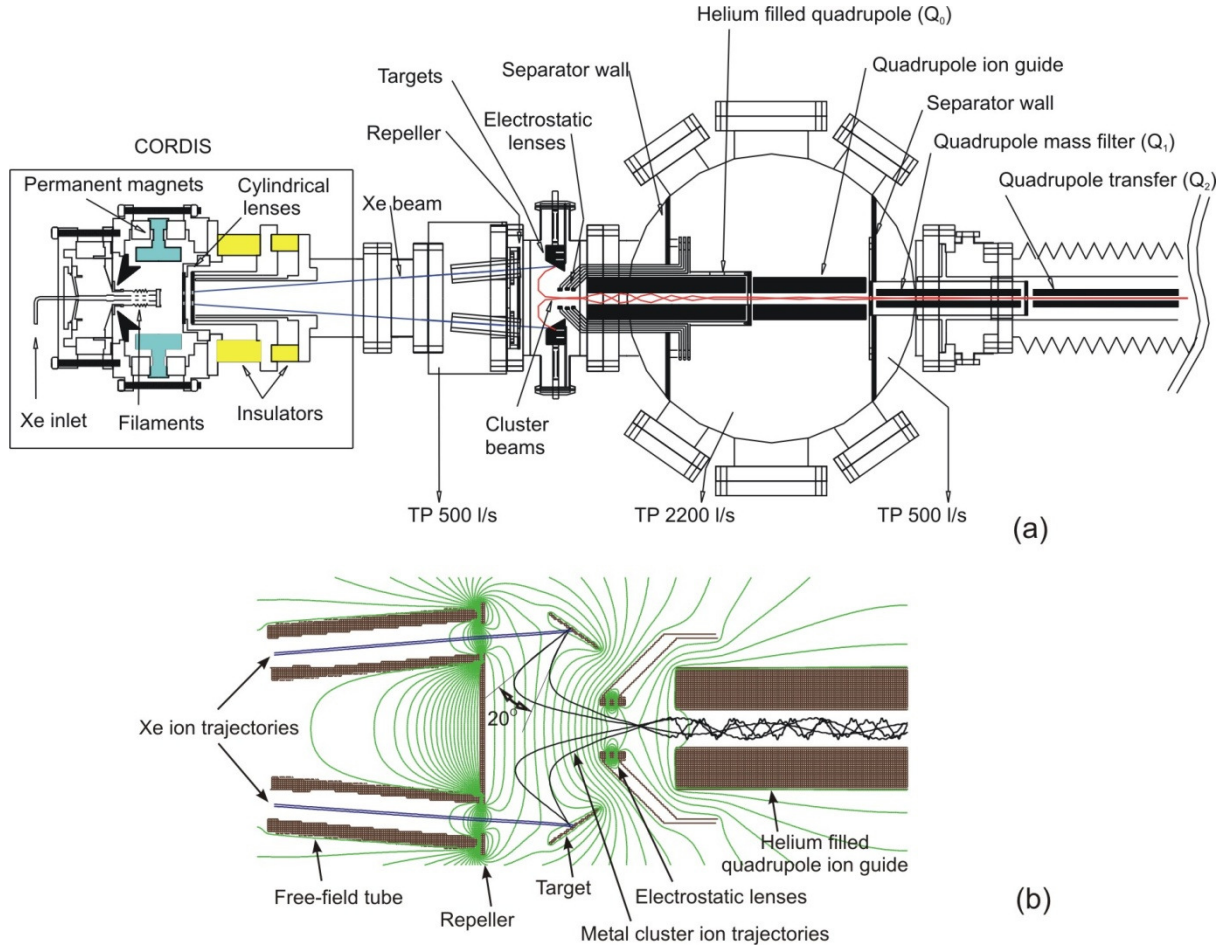


**Figure 2.2:** (a) Schematic representation of the ion sputter cluster source. The cross section schema shows two of the four primary Xe ion beams (blue lines) which are produced by the cold reflex discharge ion source (CORDIS)<sup>124</sup> assembly. These xenon ion beams are accelerated to kinetic energy of up to 15 keV before impinging onto four metal targets. In the sputtering process neutral as well as charged metal clusters are produced. The particular charge of interest is chosen by an appropriate bias voltage applied to the repeller plate opposite to the targets holders. The cluster ion beams (red lines) are deflected and subsequently focused into a quadrupole ion guide. This so-called phase space compressor is filled with helium buffer gas and serves to reduce the initial energy spread of the cluster beam and to collimate the beam to the center axis of the apparatus. (b) SimION<sup>125,126</sup> simulation illustrating the electric fields in a longitudinal cross-section image of the cluster production chamber together with the Xe and the metal cluster ion trajectories.<sup>127</sup>

The four primary Xe ion beams are directed onto four metallic targets by means of three cylindrical lenses. The first lens as well as the whole discharge chamber are at a potential of typically 10 kV which defines the Xe ion kinetic energy. A negative potential of typically -3 kV is applied to the second lens in order to extract and to collimate the Xe ion beams,



while the third lens is at ground potential. The metallic targets are located on four target holders 45 mm off the central axis. The target holders are water cooled and easily accessible for target replacement. The normal vector of the target surface forms an angle of  $55^\circ$  with the primary Xe ion beams. The trajectories of the cluster ions which emerge from the targets are bent back onto the central axis of the apparatus by a repeller plate and the metal cluster ions are extracted from the source region by an einzel lens.

Figure 2.2b presents a longitudinal cross-section image of a 3D-SimION<sup>125,126</sup> simulation of the electric fields and the ions trajectory in the cluster production chamber. The Xe ion beams produced by the CORDIS are guided toward the targets through four field free tubes arranged under a angle of  $5^\circ$  with respect to the symmetry axis. Following the collisions of the Xe ions with the targets two positively charged particles starting from each target have been simulated. They have the same mass and the same origin and emerge with an angle of  $20^\circ$  relative to each other. The kinetic energy of the particles differs by 5 eV. The ions are subsequently reflected by the potential applied to the repeller plate and are collimated by three electrostatic lenses at the input of the phase space compressor. Varying the origin and the starting angle (not shown in the presented simulation) a cluster beam with an energy spread larger than 25 eV can be steered into the phase space compressor. Note that the trajectories of the ions inside of the phase compressor were calculated without taking into consideration the interaction with the He buffer gas. Each collision with He atoms will change the trajectory and will diminish the kinetic energy of the clusters. After thermalization, a cluster energy spread of less than 2.5 eV is obtained.

The advantages of this type of cluster source consist in:

- (i) the adaptability to all solid materials, especially to those with high melting point;
- (ii) the production of charged particles, thus subsequent ionization of the clusters is not necessary;
- (iii) the production of a high intensity, very stable continuous cluster ion beam.

On the other hand, the exponential decrease of the signal intensity with increasing cluster size makes this source suitable only for small cluster production (up to 10-20 atoms/cluster).

### 2.1.2 Phase space compressor

Despite these advantages of the CORDIS cluster source, a major disadvantage is that the ion trajectories start from a large area (the total target area), and the momenta of the individual particles are broadly distributed.

Since all mass spectrometers have a limited acceptance, they are transmitting particles only from a limited volume in phase space. Therefore, most of the clusters produced by a sputtering ion source cannot be fed into a mass spectrometer. A crude estimation shows that for the case of a direct coupling between the cluster source and the quadrupole mass spectro-

meter used in our setup the ratio between the transmitted and the produced number of clusters would be only between  $10^{-4}$  and  $10^{-2}$  depending on the cluster size and the mass resolution of the quadrupole (the higher fraction applies for heavy clusters and low resolution).<sup>128</sup>

In order to collimate and thermalize the cluster ions a large gas filled quadrupole ion guide  $Q_0$ , similar to that used by Anderson and coworkers<sup>129</sup> but with a different geometry,<sup>130</sup> was employed (see Figure 2.1). The  $Q_0$  principle of operation is based on the friction the clusters experience on their way through the quadrupole. Here, their internal and kinetic energy is thermalized among the degrees of freedom of the collision gas. The clusters thereby lose momentum and are compressed simultaneously to the center of the effective potential well in the quadrupole ion guide. For proper performance, each single collision should affect the trajectory of the cluster only slightly because otherwise the cluster would dephase with respect to the driving field in the ion guide.

The  $Q_0$  quadrupole ion guide is located in the first vacuum chamber which is differentially pumped on both sides by a 2200 l/s turbo-molecular pump (see Figure 2.1). It has a large rod diameter of 20 mm, which results in a more than six times larger transversal area between the quadrupole rods compared to that of the mass selecting quadrupoles used in the present experiment ( $Q_1$  and  $Q_3$ ). Due to this large geometrical cross section of the quadrupole, its rf drive frequency was chosen to be 400 kHz in order to match the high mass range of the subsequent mass spectrometers. The  $Q_0$  quadrupole is enclosed in a gas cell filled with helium gas at a pressure of  $1.9 \times 10^{-2}$  mbar. The pressure inside of the gas cell is controlled by a Pirani pressure gauge and adjusted for optimal performance for each investigated cluster size. Under these conditions, the He pressure in the main chamber rises up to  $10^{-3}$  mbar. In the first mass selecting quadrupole region it reaches about  $10^{-5}$  mbar.

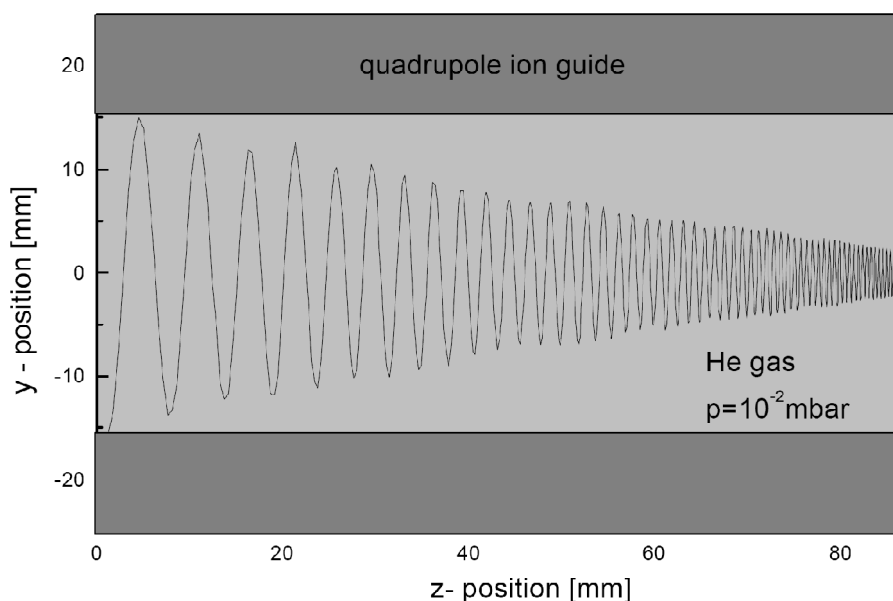


**Figure 2.3:** Numerical simulation of an ion trajectory inside of a gas filled ion guide.<sup>130</sup>

The trajectories of cluster ions in a gas filled quadrupole have been modeled using the SimION program and the typical trajectory of an  $\text{Ag}^+$  cluster is displayed in Figure 2.3. As can be seen, the amplitude of the oscillatory motion decreases by about a factor of three during the passage through the quadrupole. Simultaneously, the velocity of the clusters along the quadrupole axis is also strongly reduced. Therefore the ion guide serves as a compressor for the phase space occupied by the transmitted particles. The amount of compression that can be achieved theoretically depends on the mass of the clusters, the pressure and temperature of the He buffer gas, and the voltage applied at the quadrupole.

### 2.1.3 Triple quadrupole mass spectrometer

The subsequent triple quadrupole mass spectrometer ( $Q_1$ ,  $Q_2$ ,  $Q_3$ ) is a commercial EXTREL C50 setup. It offers continuous operation capability and a convenient possibility to choose between a high transmission and a high resolution mode. Two of the quadrupoles ( $Q_1$  and  $Q_3$ ) are operated in the mass selection mode while the third one ( $Q_2$ ) works as ion guide. The mass spectrometer uses rods of 9 mm diameter and operates at 880 kHz. It transmits masses up to  $m_{\text{max}} = 4000$  amu. The mass settings of the two spectrometers are controlled by an IBM compatible PC via a computer interface (Stanford Research SRS245).

In essence, a quadrupole mass analyzer operates through a combination of *dc* and *ac* potentials applied to the quadrupole rods which allow only a selected mass-to-charge ratio to pass the device. All other ions exhibit unstable trajectories through the quadrupole filter and will collide with the quadrupole rods. An “ideal” quadrupole field can be generated by using four parallel rods, with the two opposite rods being separated by  $2r_0$  ( $r_0$  is the distance from the center axis, the  $z$  axis). These are electrically coupled in pairs and a *dc* potential difference  $U$  is applied across the pairs. This generates a hyperbolic cross-section field in the interior of the quadrupole. An *ac* component  $V_{\text{rf}}$ , which oscillates at a radio frequency  $\omega$  is added to this *dc* field:

$$V_{\text{rf}} = V \cos(\omega t) \quad (2.1)$$

The combined potentials are applied to the two pairs of rods such that they are out of phase by  $\pi$ , as shown in the Figure 2.4a. As a result, the potential  $\Phi$  at each point in the quadrupole filter as a function of time is given by:

$$\Phi = [U + V \cos(\omega t)] \frac{x^2 - y^2}{r_0^2} \quad (2.2)$$

where  $x$  and  $y$  are the distance along the given coordinate axes,  $r_0$  is the distance from the center axis (the  $z$  axis) to the surface of the any rods,  $\omega$  is the angular frequency of the applied

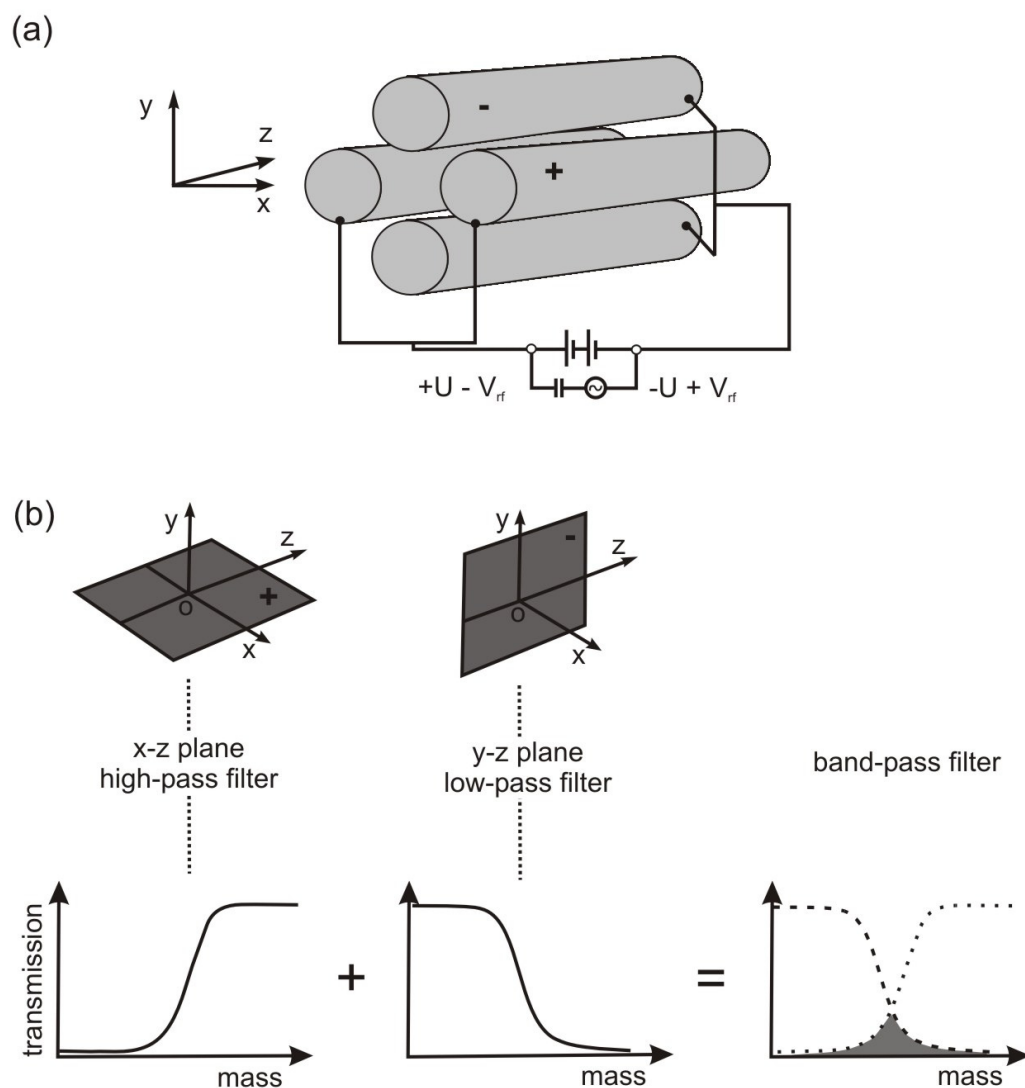


**Figure 2.4:** Principle of quadrupole mass filter, acting as a mass band-pass filter: depending on their mass, ions react differently to the modulated  $V_{rf}$  field. Adapted from Rouessac et al.<sup>131</sup>

$ac$  waveform,  $V$  is the magnitude of the applied  $ac$  of the rf waveform, and  $U$  is the magnitude of the applied  $dc$  potential.

The basic equation of motion for a ion with mass  $m$  and charge  $q$  during its flight through the quadrupole can be written in the form:

$$\frac{d^2x}{dt^2} = -\left(\frac{q}{m}\right) \frac{[U + V\cos(\omega t)]}{r_0^2} x \quad (2.3)$$

$$\frac{d^2y}{dt^2} = \left(\frac{q}{m}\right) \frac{[U + V\cos(\omega t)]}{r_0^2} y \quad (2.4)$$

$$\frac{d^2z}{dt^2} = 0 \quad (2.5)$$

The two equations (2.3-2.4) are recognized as the Mathieu equations. Their solutions describe the motion of the ion as an oscillation in the  $x$  and  $y$  directions while traveling in the  $z$  direction.

One may view the quadrupole filter's action as a combination of a "low-pass" and "high-pass" filter for masses, i.e. a "band-pass" filter as indicated Figure 2.4b. The transmission centre of a mass band-pass filter can be adjusted either by altering the modulation frequency, or by adjusting  $U$  and  $V_{rf}$  together, with their ratio at a constant value.

### 2.1.4 Octopole ion trap

The octopole ion trap used in the present work consists of eight metal rods (74 mm length and 3 mm diameter) arranged in a circular geometry with a diameter of 13 mm. They are embedded in an 80 mm long gold-plated copper housing in order to avoid thermal losses.<sup>54,132</sup> The trap space charge limit amounts to approximately 7 pC<sup>132</sup> corresponding to an ion density of about  $10^4$  ion/cm<sup>3</sup>. Two computer controlled electrostatic lenses mounted at the entrance and at the exit of the octopole enable the filling of the trap as well as the storage and extraction of the ions. In order to efficiently store the cluster ions, the octopole is pre-filled with helium as buffer gas prior to the cluster admission.

The temperature control inside the trap (in a range between 20 and 300 K) is achieved through resistive heating against a closed cycle helium-cryostat (APD Cryogenics Inc., Model HC-2D) attached to the ion trap enclosure. The trap temperature is monitored by two thermocouples (Gold/Iron and Chromel/Alumel) attached to the upper and lower part of the trap. During the measurements, a difference of less than 5 K between the readings of the two thermocouples was observed.

Since many physical and chemical cluster properties show a strong temperature dependence, the precise determination of the cluster ion temperature prior to the chemical reaction is of great importance. The buffer gas collisions ensure the thermal equilibration of the

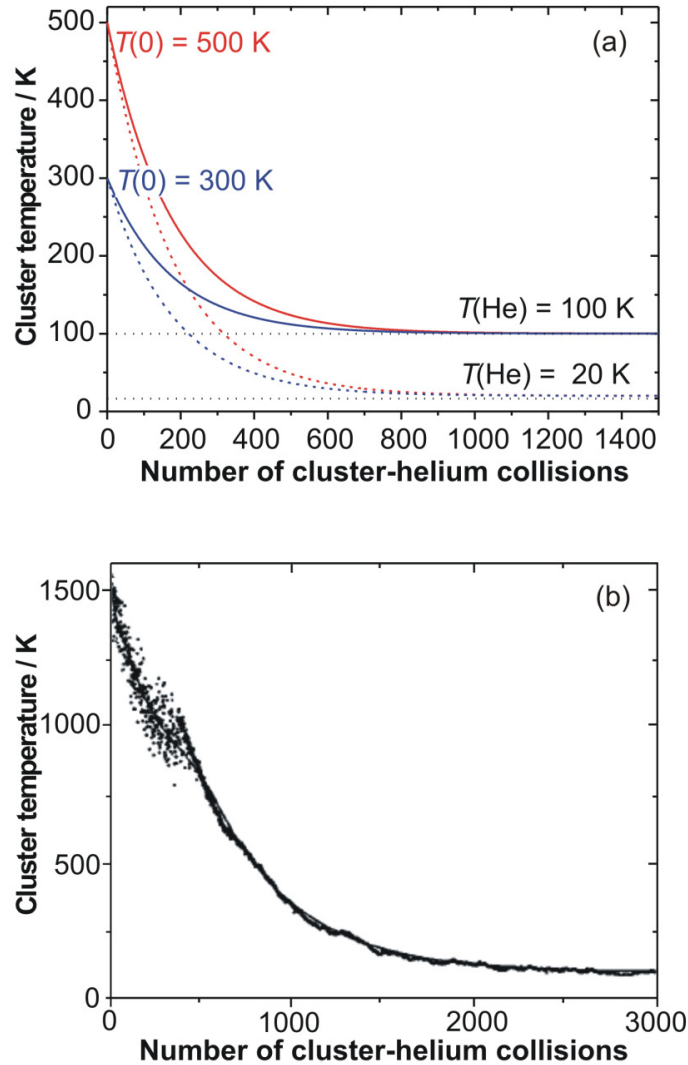


**Figure 2.5:** (a) Thermalization efficiency of trimer cluster ions inside the helium filled coolable octopole ion trap. The cluster temperature is plotted as a function of the number of cluster-helium collision. The blue and red colored solid lines represent collisions in which the buffer gas temperature is  $T(\text{He}) = 100$  K and the cooling process starts from an initial cluster temperature of  $T(0) = 500$  or  $300$  K, respectively. The dashed lines show the evolution starting from the same  $T(0)$  initial values, but approaching a final buffer gas temperature of  $T(\text{He}) = 20$  K. Thermal equilibrium is achieved in less than 1000 buffer gas collisions, which corresponds to less than a millisecond under the experimental conditions; (b) Thermalization of  $\text{Pd}_{13}$  clusters through collision with helium atoms, adapted from Westergren et al.<sup>133,134</sup> The initial cluster temperature has a value of  $1500$  K while the buffer gas temperature has value of  $100$  K.

clusters entering the trap within less than a few thousand collisions, i. e. in a few milliseconds, under our operating conditions. Figure 2.5a presents a simulation of the thermalization efficiency according to Westergren et al.,<sup>133,134</sup> where the temperature of a trimer cluster is plotted as a function of the number of cluster-helium collisions. As can be seen in Figure 2.5a the cluster assumes the trap temperature  $T(\text{He})$  within less than thousand buffer gas collisions, regardless of the initial cluster temperature  $T(0)$  (in this case 300 or 500 K) and also almost independent of the ion trap temperature  $T(\text{He})$  (20 or 100 K). The cluster size has also only a minor influence on the thermalization time. The simulation for a 13-atom cluster reveals that the cluster is thermalized within less than 3000 buffer gas collisions (Figure 2.5b).<sup>133,134</sup>

The complete and rapid thermalization of the clusters inside the ion trap was verified by temperature and pressure dependent real-time laser probing of the nuclear cluster dynamics. Variation of the buffer gas pressure between 0.2 and 0.9 Pa had no influence on the strongly temperature dependent time-resolved pump-probe signal that reflects very sensitively the nuclear cluster dynamics.<sup>54</sup> This confirms the complete cluster ion thermalization inside the ion trap. Whereas thermalization is thus accomplished within a few milliseconds, the cluster ions are stored in the trap for a considerably longer period of time, typically for several seconds, without significant ion loss.

In the collisional ion cooling process inside an rf-ion trap the field frequency, the geometry of the trap as well as the mass ratio between the ions and cooling atoms play a decisive role. Thus, an efficient cluster cooling requires:

- (i) rf-frequencies,
- (ii) the mass of the buffer gas atoms should be small with respect to the investigated ion mass,
- (iii) the trap should have a large field-free region with steep confining walls, i.e. the number of electrodes should be as large as possible.

In the present experiment all above mentioned conditions are accomplished.

Both, the buffer gas and the reactive gases, are admitted into the trap via a small Teflon tube (1 mm inner diameter). A similar tube attached to the interior of the trap housing allows the measurement of the absolute pressure inside the ion trap by means of a Baratron manometer (MKS, Typ 627B). The pressure measurement is based on the capacitive measurement of the deformation of a membrane which is accurately kept at 318 K. This type of manometer is suited for measuring small gas pressures ( $10^{-4}$  down to  $10^{-5}$  Torr), while the calibration is insensitive to the type of measured gases.

The behavior of gas molecules is determined by a pressure gradient in the viscous regime and by diffusion in the molecular regime. This can be rationalized considering that in viscous regime,<sup>135</sup> the interaction of the gas molecule with each other is dominant, whereas it can be neglected in the molecular regime. Thus, it is clear that in the viscous regime under equilibrium conditions, the pressures at the two openings of the tube (trap and Baratron sides) must be equal independent of the temperature; otherwise the motion of the gas molecules

would follow the pressure gradient. In the molecular regime, the pressure does not have to be homogeneous. If different regions are held at different temperatures, one will necessarily obtain different values for the pressure (thermal transpiration).

Since the trap is cooled down to temperatures as low as 20 K while the manometer head is constantly kept at 318 K, the effect of thermal transpiration has to be considered.<sup>136-139</sup> This effect has been described theoretically<sup>140,141</sup> and experimentally<sup>135,142,143</sup> in the molecular flow pressure regime below  $10^{-1}$  Pa. Thermal transpiration leads, in its simplest form, to a correction factor of:

$$\frac{p_{\text{trap}}}{p_{\text{gauge}}} = \sqrt{\frac{T_{\text{trap}}}{T_{\text{gauge}}}}, \quad (2.6)$$

applicable to the pressure read from the gauge  $p_{\text{gauge}}$  to obtain the true trap pressure  $p_{\text{trap}}$  at trap and gauge temperatures of  $T_{\text{trap}}$  and  $T_{\text{gauge}}$ , respectively. At higher pressures corresponding to the viscous flow regime, this phenomenon is, however, not observed.<sup>135</sup> The present experiment operates at pressures around 1 Pa and thus just in the transition range between molecular and viscous flow. Therefore, the termolecular rate constants of the reactions studied here have been calculated employing partial pressures both with and without correction for thermal transpiration. However, the deviations in the deduced binding energies were consistently within the errors bars.

For all experimental measurements presented in the following chapters the measured pressure  $p_{\text{measured}}$  are indicated, while for the calculation of the reaction rate constant the correction factor for thermal transpiration was taken into account.

## 2.2 Laser system

In order to monitor the photodissociation dynamics of small noble metal cluster-molecule complexes on an ultra-short time scale, an amplified femtosecond laser system generating ultra-short laser pulses was employed. Figure 2.6 displays a schematic representation of the laser system.

The femtosecond laser pulses were generated by a Ti:Sapphire oscillator (Spectra Physics Tsunami) continuously pumped by a 6 W Nd:YVO<sub>4</sub> laser (Spectra Physics Millennia). Pulse amplification was carried out by a Nd:YLF laser (Spectra Physics Empower) pumped Ti:Sapphire amplifier (Spectra Physics Spitfire XP).

In order to obtain the appropriate wavelength for each experiment 60% of the total intensity from the amplifier output was used to seed two optical parametric amplifiers (Spectra Physics OPA 800C). Just one OPA was employed in the present experiment. According to the



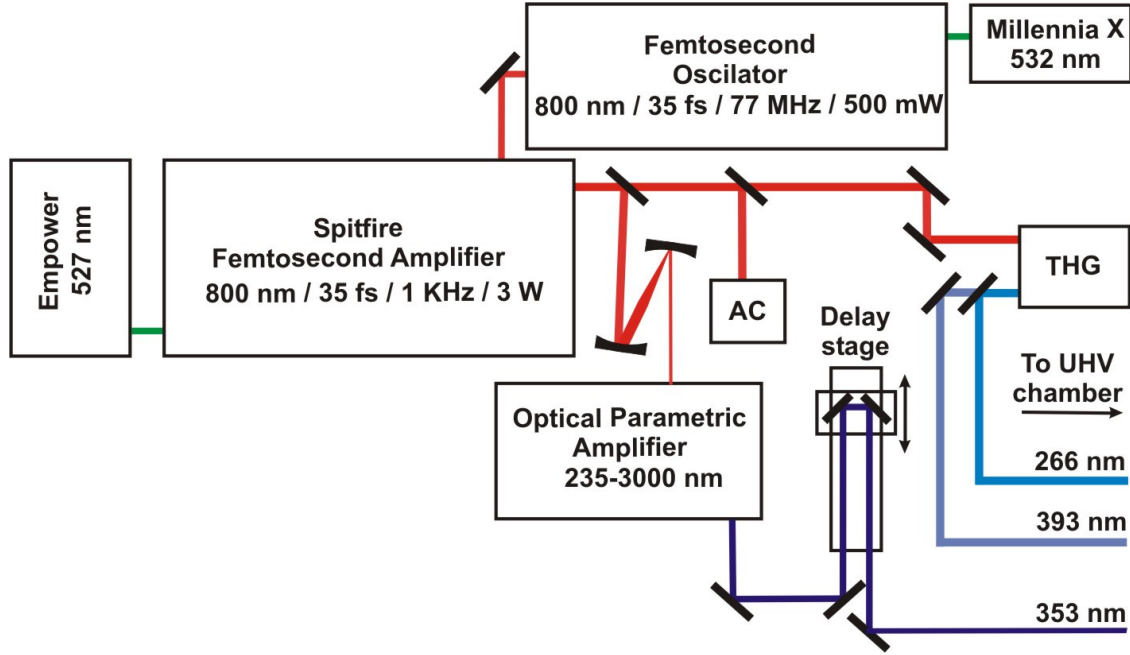


**Figure 2.6:** Layout of the femtosecond laser system. Indicated in the figure are the most important laser parameters together with the corresponding wavelengths. Notations: AC-autocorrelator; THG-third harmonic generator (trippler). Note that the wavelength of 393 nm was obtained when the fundamental wavelength was tuned to 786 nm.

technical requirements of the OPA, the infrared input beam diameter was reduced by a home built telescope. About 20% of the initial intensity from the amplifier output was used for the generation of the second and the third harmonic generation by means of a home built third harmonic generator. For the pump-probe experiments, a computer controlled delay stage was used to vary the length of a laser beam path, hence to control the delay between the pump and the probe laser pulses.

The wavelengths of the laser beams were measured with an optical spectrometer (Spectra Physics OSM100). For the measurement of the laser pulse duration a beam splitter reflecting  $< 1\%$  of the incident intensity was employed to deflect the amplified infrared laser pulses into an autocorellator (Spectra Physics PulseScout).

## 2.2.1 Generation and characterization of the fs-laser pulses: oscillator and amplifier

### 2.2.1.1 Ti:Sapphire active medium

The ultrashort laser pulses were generated by means of a femtosecond solid state laser system. Both the femtosecond oscillator as well as the femtosecond amplifier use a titanium doped sapphire crystal as active laser medium ( $\text{Ti:Al}_2\text{O}_3$ ). The spectroscopic and laser characteristics

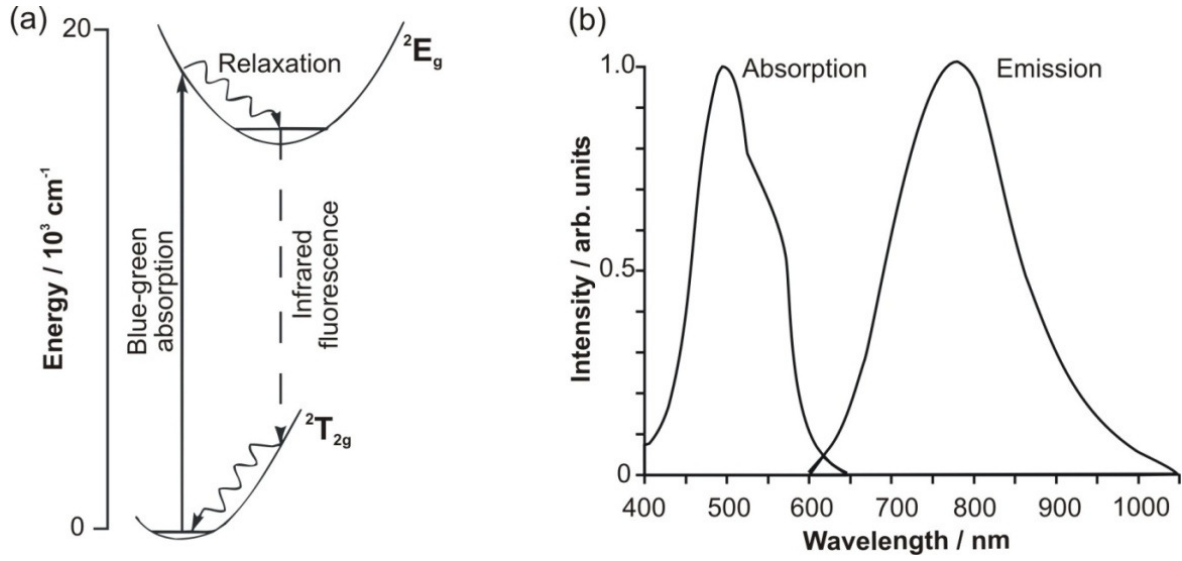


**Figure 2.7:** (a) Energy level structure of  $\text{Ti}^{3+}$  in sapphire. (b) Absorption and emission spectra of Ti:Sapphire.

of Ti:Sapphire ion were first reported by Moulton.<sup>144,145</sup> The Ti:Sapphire is a crystal with  $\text{Ti}^{3+}$  ions embedded in the sapphire ( $\text{Al}_2\text{O}_3$ ) host material replacing an  $\text{Al}^{3+}$  ion. Titanium, which is responsible for the laser transition in the material, is present in the crystal at up to 0.1% of the concentration by weight. The electronic ground state of the  $\text{Ti}^{3+}$  is split into a pair of vibrationally broadened levels as can be seen in the Figure 2.7a. Absorption transitions occur over a broad range of wavelengths from 400 nm to 600 nm. Fluorescence transitions occur from the lower vibrational levels of the excited state ( $^2E_g$ ) to the upper vibrational levels of the ground state ( $^2T_{2g}$ ). The fluorescence band extends from wavelengths as short as 600 nm to wavelengths greater than 1  $\mu\text{m}$ . This makes them suitable materials in constructing laser active media for generating femtosecond pulses. The laser action is restricted to the wavelength above 660 nm, since the long-wavelength side of absorption overlaps with the short wavelength end of the fluorescence spectrum, as can be seen in the Figure 2.7b. Additionally, the tuning range is affected by the mirror coating, losses in the laser cavity, pump mode quality, and the pump power.

### 2.2.1.2 Femtosecond oscillator

Basically, the generation of the fs-laser pulses consists in the coupling of the phase of different longitudinal modes within the laser cavity. This process is called mode-locking. Methods for producing mode-locking in a laser may be classified as either *passive* or *active*.

(i) *Passive mode-locking* is achieved by insertion of a saturable absorbing medium into the cavity. In the case of the passive Ti:Sapphire fs-laser oscillator, due to the non-uniform power density distribution of the Gaussian beam, the refractive index of the Ti-Sapphire changes

across the beam profile, being larger in the center than at the edge (known as optical Kerr-lens effect). By means of Kerr-lens effect the most strongly focused frequencies are higher amplified. Consequently the self-focusing of the seed beam favors the pulsed mode over *cw*.

To lock the laser modes implies to organize the competition between the modes in such a way that the relative phases stay constant. In this way all the waves of different frequencies will interfere constructively at one point, resulting in a very intensive and ultra short light pulse.<sup>146</sup>

For a simple plane mirror resonator the allowed modes are those for which the separation distance of the mirrors  $L$  is an exact multiple of the half the wavelength of the light (see Figure 2.8b),

$$\Delta\nu = \frac{c}{2L} \quad (2.7)$$

where  $\Delta\nu$  is the frequency separation between two adjacent modes, and  $c$  is the speed of light. The pulses of light produced in mode-locked regime when the laser modes constructively in-

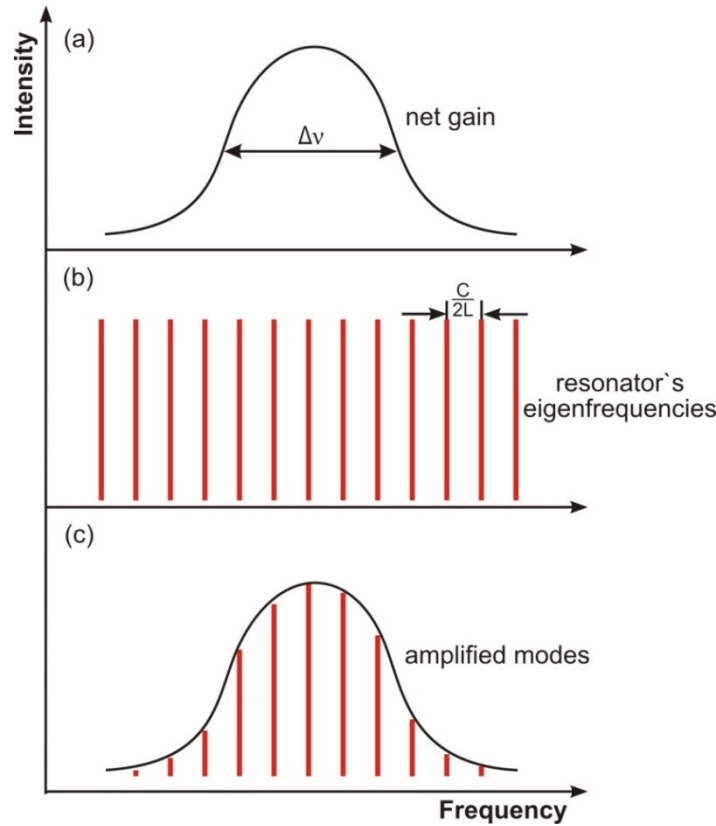


**Figure 2.8:** The mode-locking principle. The axial modes of a laser cavity are separated by the intermode frequency spacing  $\nu = c/2L$ . (a) The net gain curve (gain minus losses); (b) Cavity longitudinal modes structure in the resonator; (c) The amplified modes.<sup>147</sup>

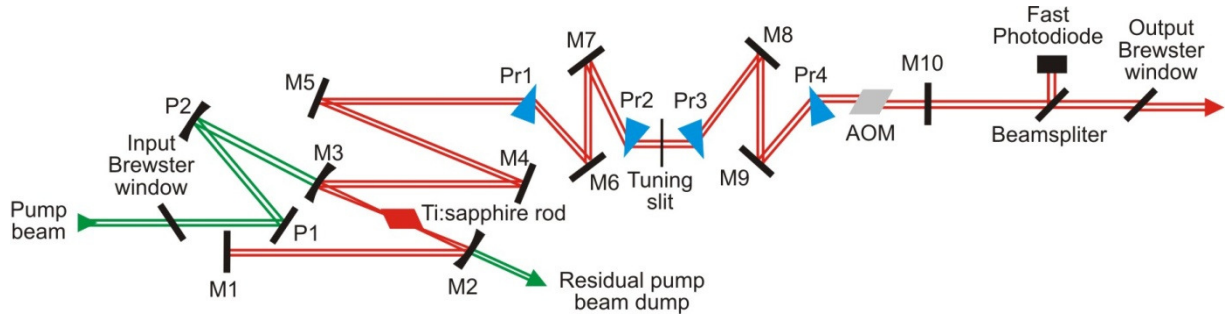


**Figure 2.9:** Configuration of the Ti:Sapphire oscillator cavity. Notations: P1, P2 pumping mirrors, M1-M10 infrared mirrors, Pr1-Pr4 prisms.

terfere (see Figure 2.8c) occur separated in time by:

$$\tau = \frac{2L}{c} \quad (2.8)$$

where  $\tau$  is the repetition rate, i.e. the time taken for light to make exactly one round trip in the laser cavity.

(ii) *Active mode-locking* resulting from an external modulation at frequency  $\Omega$  either of the cavity losses by inserting an acousto-optical modulator (AOM) inside the laser cavity or of the gain of the amplifying medium for example by pumping this medium with another mode-locked laser.

In the oscillator employed in the present work the modulation is performed by means of an AOM. The AOM modulates the modes at a frequency close to the intermode frequency interval  $c/2L$ . A competition for maximum gain inside the amplifying medium will result in a coupling between each mode and the side bands created by the modulation of its neighboring modes. The phases of the modes could then lock on to each other.

A detailed view of the fs-oscillator cavity employed in the experiments presented in this thesis is displayed in Figure 2.9 where the geometrical arrangement of the crystal, the prism pairs, and the mirrors can be seen.

The typical output parameters of the femtosecond oscillator are displayed in Table 2.1.

**Table 2.1:** Output characteristic of the Ti:Sapphire oscillator.

Characteristic / units	Value
Wavelength / nm	800
Bandwidth / nm	60
Pulse duration / fs	35
Repetition rate / MHz	77
Power / mW	500

### 2.2.2 Pulse amplification

The amplification of femtosecond laser pulses in the present setup was performed by means of a commercial amplifier (Spectra Physics Spitfire XP) system having a Ti:Sapphire crystal as laser active medium.

For femtosecond pulses the amplification process is complicated by the associated extremely high peak power intensities. Thus, a direct amplification of the fs-seed pulses would lead to the damaging of the amplifier optical components. The damage threshold of most optical materials, including Ti:Sapphire, is only a few gigawatts per square centimeter. However, laser pulses of up to a few terawatts per square centimeter are required in photochemistry experiments.

In order to overcome this problem a successful method of amplification called “chirped pulse amplification” (CPA) was devised by D. Strickland and G. A. Mourou.<sup>148</sup> This method, which is schematically illustrated in Figure 2.10a, consists of the following three steps. First, a short laser pulse to be amplified (produced by the oscillator) is stretched in time into its frequency components by means of a dispersive system such as a pair of diffraction gratings so that a chirped pulse is generated with the red components of the pulse preceding the blue ones (see Figure 2.10b top). This stretching in time of the pulse greatly reduces its peak intensity so that in the second step the frequency components of the chirped pulse are sent in succession through the amplifier without distortions and damage of the laser active medium and of the other optical components. In the third step, the amplified chirped pulse is compressed in time by another pair of diffraction gratings which recombine the dispersed frequencies, thus producing a short pulse with a very high peak intensity (see Figure 2.10 bottom). Finally, the resulting amplified short pulse is focused on a small area.

The main problem the compressor has to deal with is that it has to recover not only the pulse duration and quality, but it has to compensate the dispersion introduced in the amplification stage itself. To overcome this problem, the distance between gratings in the compressor has to be larger than in the stretcher. This will cancel over second-order dispersion and help in producing relatively short pulses, but also induces higher-order dispersion terms, which will result in pre-pulses and/or wings.

Two of the most widely used techniques for amplification of fs-laser pulses are the multipass and the regenerative amplification. The working principle of the multipass amplifier relies on the repetitive amplification of a laser pulse, which passes many times through the amplifying medium (Ti:Sapphire crystal). Thus, with every passage through the crystal, the stretched pulse depletes the population inversion generated by the green ns-pump pulse inside the crystal and is amplified. In the multipass amplification different passages through the crystal are geometrically separated. The number of passages (four to eight) is usually limited by the difficulties generated by focusing all the passes on a single spot of the crystal.

The pulse amplification in the present setup was performed by means of the regenera-

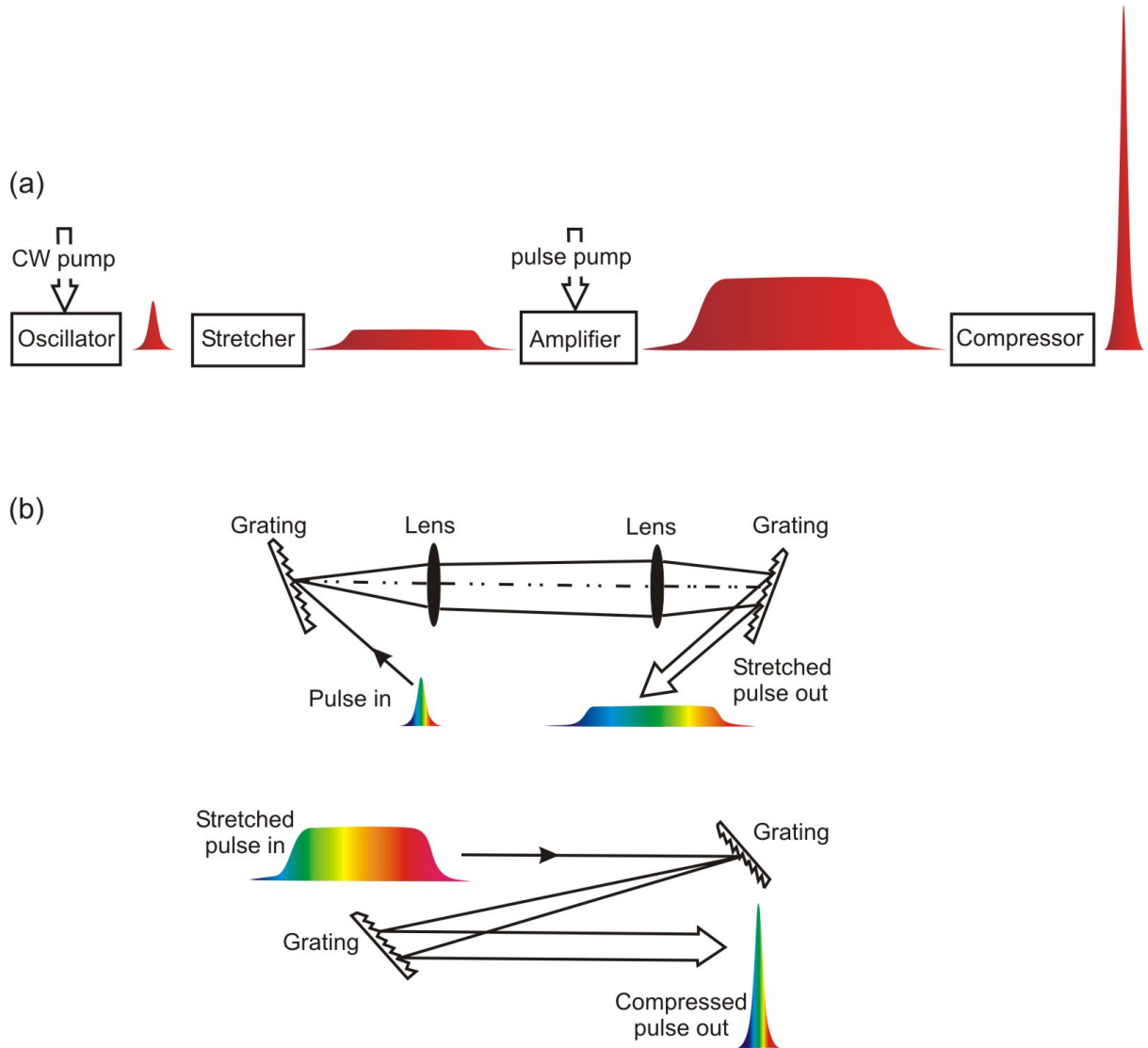


**Figure 2.10:** Illustration of the principle of the CPA method. (a) The short laser pulse to be amplified (produced by the oscillator) is stretched in time into its frequency components by a dispersive system such as a pair of diffraction gratings. Further, the frequency components of the chirped pulse are sent in succession through the amplifier without distortions and damage. The amplified chirped pulse is compressed in time by another pair of diffraction gratings which recombine the dispersed frequencies, thus producing a short pulse with very large peak intensity. (b) The matched stretcher (top) and compressor (bottom) of the CPA method. Both setups are part of femtosecond amplifiers. Adapted from G. A. Mourou et al.<sup>148</sup>

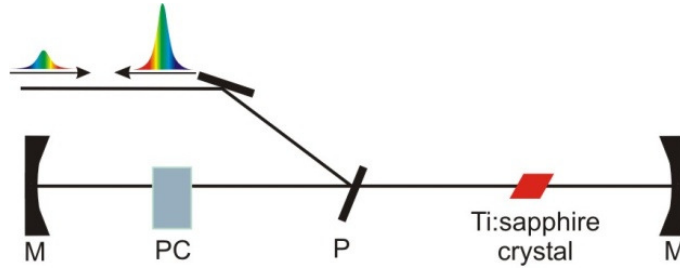


**Figure 2.11:** Schematic principle of a regenerative amplifier cavity. Notations: *M* – mirrors, *PC* – Pockels-cell, *P* – thin-film polarizer.

tive amplification technique. A schematic representation of a regenerative amplification principle can be seen in Figure 2.11. This involves the trapping of the laser pulses in the laser cavity until all the energy stored in the amplification crystal is extracted and laser pulse energy reaches the highest intensity. Trapping and dumping the pulse in and out of the resonator is performed by a Pockels-cell and a broad-band polarizer.<sup>147</sup> The Pockel-cell consists of a birefringent crystal, which can change the polarization of a traveling laser field by applying high voltage to the cell. When a pulse is inside the resonator, the voltage on the Pockels-cell is switched so that its optical properties become equivalent to a quarter wave plate. The pulse is kept in the cavity until it reaches saturation. Further, a second voltage step is applied so that the pulse can be extracted from the resonator.

The pumping of the regenerative amplifier is achieved in the present setup by means of the second harmonic (527 nm, up to 20 mJ) of a nanosecond, Q-switched neodymium-doped lithium yttrium fluoride (Nd:YLF) laser. The typical output parameters of the regenerative amplifier employed in the present work are displayed in Table 2.2.

In order to obtain the appropriate wavelengths required for the photodissociation experiments presented in this thesis, an optical parametric amplifier and a home-built third harmonic generator were used. These concepts are briefly outlined in the following sections.

**Table 2.2:** Output characteristic of the amplifier.

Characteristic / units	Value
Wavelength / nm	800
Bandwidth / nm	60
Pulse duration / fs	35
Repetition rate / kHz	1
Power / W	3.5

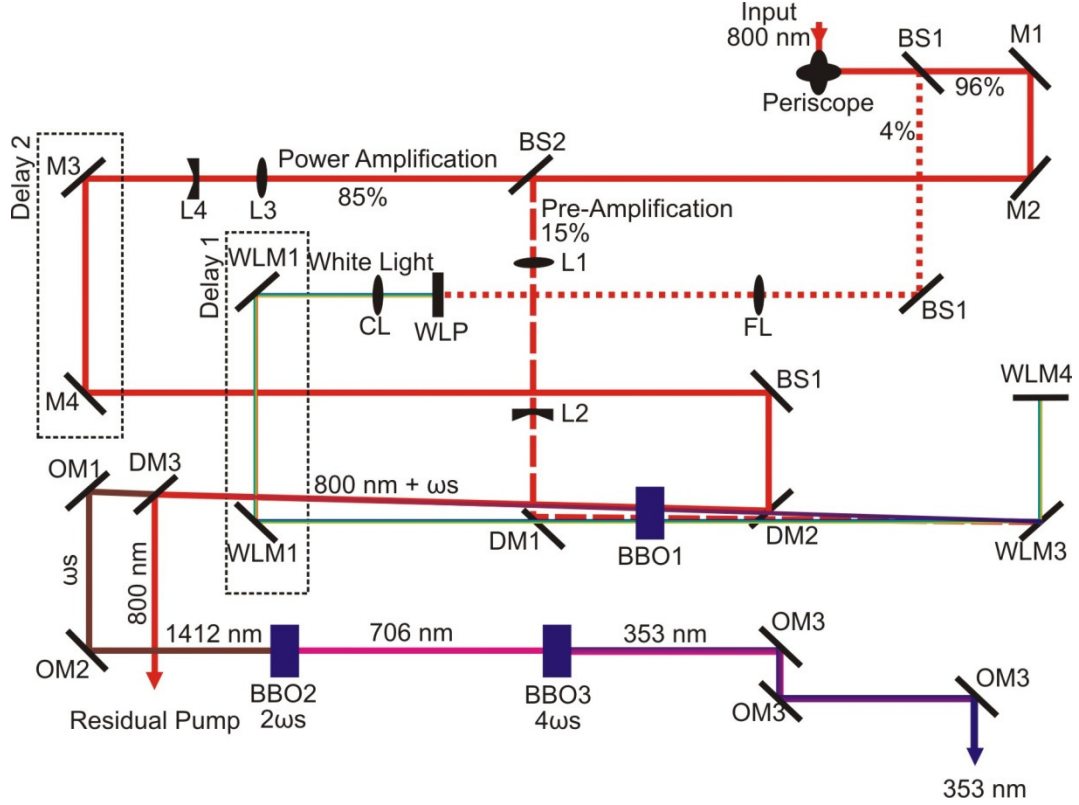


**Figure 2.12:** Schema of the optical parametric amplifier employed for the production of the probe pulses. Notations: BS – beam splitter, M – mirror, WLM – white light mirror, DM – dichroic mirror, OM – output mirror, L – lens, WLL – white light lens.

### 2.2.3 Optical parametric amplifier

The process of tuning the wavelength of a laser beam to a desired wavelength is based on the principle of frequency mixing.<sup>149</sup> Frequency mixing can be successfully obtained in anisotropic materials, which possess a high nonlinear second-order optical susceptibility ( $\chi > 0$ ). In this type of materials, nonlinear processes like second harmonic generation (SHG), sum frequency generation (SFG) or difference frequency generation (DFG) can be produced. The process of SHG involves that a photon with frequency  $2\omega$  can be generated from two incoming photons having an identical frequency  $\omega$ . The processes of SFG and DFG involve two incoming photons having different frequencies  $\omega_1$  and  $\omega_2$  that generate a third photon with the frequency  $\omega_3$  corresponding to the sum of the initial frequency, or the frequency difference.

The OPA involved in the present investigations has the capability to convert the fundamental wavelength of the Ti:Sapphire output into light with a wavelength ranging from 250 nm to 3  $\mu\text{m}$  by means of amplification with white light continuum generation and optical parametric amplification. In contrast to SHG, in parametric generation a photon having the frequency  $\omega_p$  (pump) “splits” to produce two photons one with the frequency  $\omega_s$  (signal) and



one with the frequency  $\omega_I$  (idler), and energy conservation determines the generated frequency or wavelength, i.e.,

$$\omega_P = \omega_S + \omega_I \quad (2.9)$$

or

$$\frac{1}{\lambda_P} = \frac{1}{\lambda_S} + \frac{1}{\lambda_I} \quad (2.10)$$

For an efficient conversion the best phase match is require, thus:

$$\Delta k \equiv k_P - k_S - k_I = 0 \quad (2.11)$$

or

$$\frac{n_P}{\lambda_P} = \frac{n_S}{\lambda_S} + \frac{n_I}{\lambda_I} \quad (2.12)$$

where  $k_P, k_S, k_I$  are the wave vectors of each beams while  $n_P, n_S, n_I$  are the refractive indices of the nonlinear crystal for each wavelength. By changing the crystal angle,  $n_P, n_S$ , and  $n_I$  are changed and consequently the wavelength can be tuned.

The amplification of the signal or idler intensity is realized through the interaction of one of these beams (seed beam) with the fundamental of the Ti:Sapphire in a type I BBO crystal. In Figure 2.12 the optical path in the OPA configured to produce 353 nm is presented. This wavelength is employed to induce charge transfer photodissociation of silver cluster-benzene complexes in the present work. A first beam splitter separates 4% of the total intensity from the 800 nm input beam to produce the seed beam through white light generation in a sapphire plate (white light plate - WLP).

The remaining intensity (96%) is split again in two beams used for the pre-amplification (15%) and amplification (85%) of the seed beam in a BBO1 crystal. Two mechanical delay stages accomplish the temporal overlap of the seed, pre-, and final amplification laser pulses in the first BBO1 crystal. The BBO1 is positioned to amplify the signal wave at 1412 nm. Subsequent to the separation from the pump beam by dicroic mirrors, the signal

**Table 2.3:** Output characteristic of the OPA tuned to 353 nm

Characteristic / units	Input value	Output value
Wavelength / nm	800	353
Bandwidth / nm	55	7.3
Pulse duration / fs	50	70*
Repetition rate / kHz	1	1
Power / mW	650	5

\* Value calculated taking into account the dispersion off all optical elements in the OPA.

wave beam is doubled in a second BBO2 crystal to produce 706 nm. This beam is doubled again in a third BBO3 crystal to produce 353 nm, which is further separated from the other wavelengths by using appropriate coated mirrors. The typical parameters of the OPA tuned to central wavelength of 353 nm are presented in Table 2.3.

### 2.2.4 Third harmonic generation

For third harmonic generation, the laser beam with the fundamental wavelength is split into two beams. One beam is frequency doubled (second harmonic generation) in a 0.3 mm thin BBO1 type I crystal having a diameter of 10 mm and the cutting angle  $\theta = 29.2^\circ$ . In the doubling crystal two photons having the same frequency are mixed together and give rise to a single photon with twice the original frequency. In type I crystals the two mixing photons should have the same polarization, whereas in type II crystals the photons to be mixed should be orthogonally polarized. The second harmonic conversion efficiency grows linearly with increasing pump intensity so that the intensity of the frequency doubled wave increases with the square of the pump intensity. In this experiment the second harmonic conversion efficiency is about 40%. For THG a second 0.3 mm thin BBO2 type I crystal with a diameter of 10 mm and the cutting angle  $\theta = 44.3^\circ$  is employed. The frequency tripling is realized by mixing the original pump wave and the frequency doubled part of it in the second BBO2 crystal (sum frequency mixing). The THG efficiency can reach up to 10% of the pump beam intensity. In Figure 2.13 the third harmonic generator is schematically represented. An 800 nm laser beam enters the tripler. Dicroic mirrors (DM1-DM3) separate/combine the laser beams having different wavelengths. After BBO1 the 400 nm laser beam has the polarization orthogonal to polarization of the 800 nm laser beam. A half wave plate rotates the polarization of the

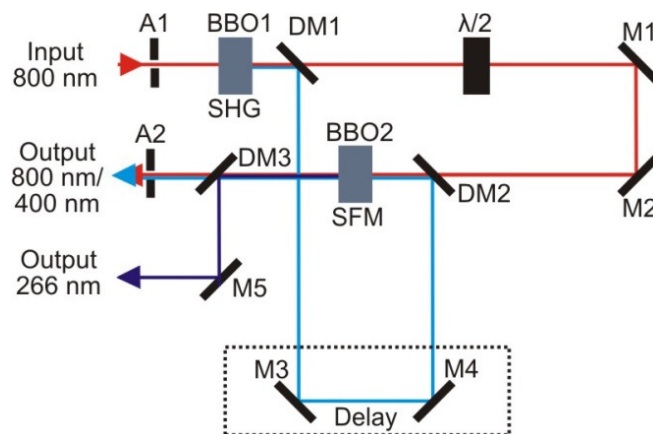


**Figure 2.13:** Top view of the optical scheme of the home-built THG employed for the production of the pump laser pulse. Notations: A1, A2 -, BBO1 - nonlinear crystal for second harmonic generation, BBO2 – nonlinear crystal for SFM, DM1-DM3-dicroic mirrors, M1-M5 mirrors.

**Table 2.4:** Output characteristic of the home-build frequency tripler.

Characteristic / units	Value
Wavelength / nm	266
Bandwidth / nm	1.5
Pulse duration / fs	70*
Repetition rate / kHz	1
Power / mW	up to 10% of the pump beam

800 nm laser beam prior to the THG in the BBO2 (type I). The temporal overlap of the 400 nm and the 800 nm laser pulses prior to sum frequency generation is accomplished by a mechanical delay stage. The typical output parameters of the tripler are listed in Table 2.4.

## 2.2.5 Pulse characterization

### 2.2.5.1 Spectral measurements

The central wavelength as well as the bandwidth of the employed laser pulses is determined by means of a commercial optical spectrometer (Newport OMS100). The light to be analyzed is directed into the spectrometer housing by means of an optical fiber. Further, it is spectrally decomposed by a diffraction grating (600 L/cm). The detection of the spectrum is performed

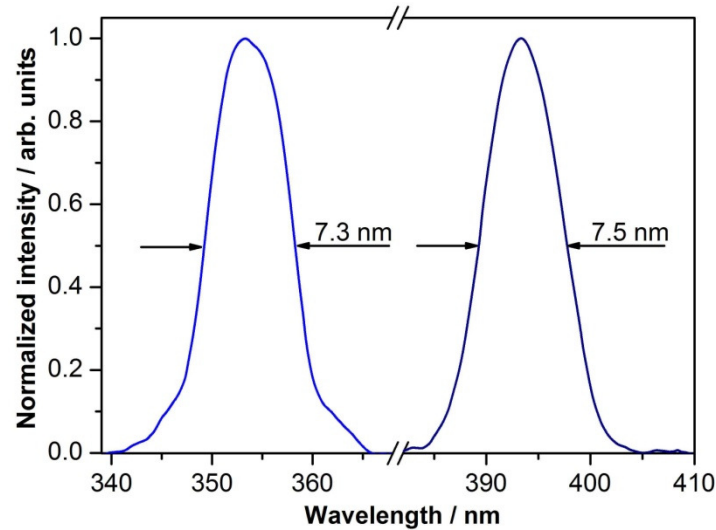


**Figure 2.14:** Spectra of the 353 and 393 nm laser beams recorded by the optical spectrometer.

\* Value calculated taking into account the dispersion of all optical elements between the amplifier output and the octopole ion trap.

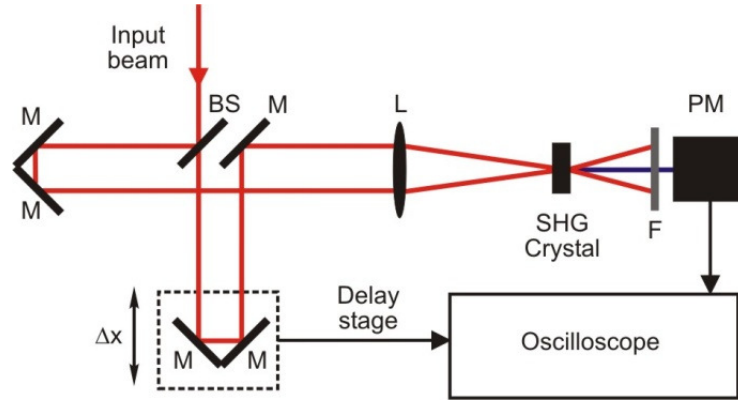


**Figure 2.15:** Schematic sketch of the autocorrelator. Notations: BS – beam splitter, M – moveable mirrors, L – lens, SHG – nonlinear crystal for SHG, F – filter, PM – photomultiplier.

by a linear CCD detector and visualized on a computer. The spectrometer has a spectral window from 250 to 850 nm, with a resolution of 0.3 nm.

Figure 2.14 displays the output wavelength spectra of the pump and probe laser beams employed in the photoinduced charge transfer (CT) experiments presented in Chapter 7 of this thesis.

### 2.2.5.2 Temporal pulse profile

In order to measure the time duration of the femtosecond laser pulses the autocorrelation technique was employed. The autocorrelation technique is one of the most common methods used for determining pulse width characteristics on a femtosecond timescale. Figure 2.15 displays the schematic sketch of the autocorrelator (AC). Its basic optical configuration is similar to that of a Michelson interferometer. The incoming femtosecond laser beam is split into two beams of equal intensity. On one arm an adjustable optical delay stage is used. As in the case of a Michelson interferometer, the beams are recombined into a BBO crystal for second harmonic generation. The intensity of the SHG signal resulting from the interaction of the two beams is proportional to the pulse overlap within the crystal. The resulting SHG autocorrelation trace is detected by a photo-multiplier as a function of the time delay  $\Delta t$  between the two pulses. The intensity of the SHG signal measured as a function of the delay time  $\Delta t$  between the pulses produces a correlation function which depends on the width of the incoming pulses  $\Delta v$ . If the incoming waves have the intensities  $I(t)$  and  $I(t-\tau)$ , then the autocorrelation function is:

$$A(\tau) = \int_{-\infty}^{\infty} I(t)I(t-\tau) dt \quad (2.13)$$

**Table 2.5:** Autocorrelation width and spectral bandwidth for different transform-limited pulses taken from Reference 147.

Shape	$I(t)$	$\Delta\nu \cdot \Delta t$	$\Delta\tau/\Delta t$
Gaussian	$\exp(-(4\ln 2)t^2/\Delta t^2)$	0.441	$\sqrt{2}$
Hyperbolic secant	$\text{sech}^2(1.76/\Delta t)$	0.315	1.55
Lorentian	$1/(1 + 2t/\Delta t)^2$	0.221	2

The autocorrelation function is always a symmetric function in time. Unfortunately, it gives very little information about the shape of the pulse, since an infinity of symmetric and asymmetric pulse shapes can have similar autocorrelation. The most widely used procedure to determine the pulse duration is to assume a pulse shape, usually a hyperbolic secant or a Gaussian shape for chirped pulses, and to calculate the pulse duration from the known ratio between the FWHM of the autocorrelation and of the pulse. Thus, the autocorrelation function depends on the assumed shape of the pulse. Table 2.5 lists the relevant parameters for various shapes.

A typical autocorrelation curve as measured by means of AC at the amplifier output can be seen in Figure 2.16. The measured FWHM of 58.5 fs is broadened due to the presence of a fused silica beam splitter located at the amplifier exit which splits the out-coming beam between the THG and OPA. Without the fused silica beam splitter an autocorrelation curve with a FWHM of 50 fs was measured (not shown here). Thus, an amplifier pulse duration around 35 fs is obtained assuming a Gaussian pulse shape.

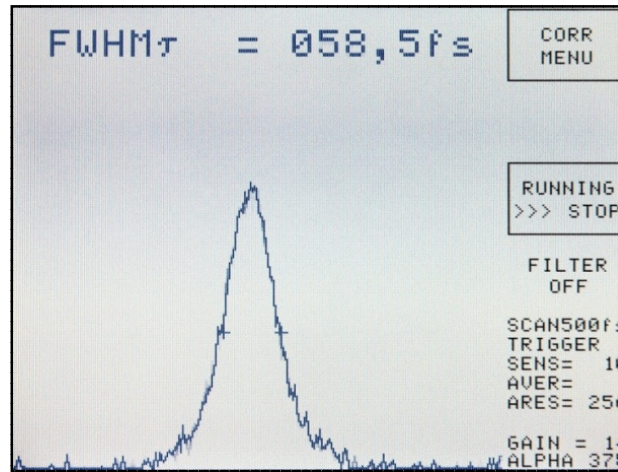


**Figure 2.16:** AC snapshot illustrating a typical autocorrelation curve at the amplifier output. Note that the FWHM of the autocorrelation curve is broadened (around 10 fs) due to a fused silica beam splitter used to split the amplifier beam between THG and OPA (see Figure 2.6).



# 3

## Data acquisition and evaluation methods\*

---

*In this chapter an overview over the experimental data acquisition methods as well as over the methods for data evaluation is presented. The theoretical concepts underlying the experimentally obtained reaction kinetics are explained, on the basis of which experimental binding energies of the neutral reactants to the ionic clusters can be deduced. The computational procedure employed to determine experimental binding energies  $E_b$  on the basis of RRKM theory is also presented and the possible sources of errors are analyzed in detail. In addition, temperature dependent equilibrium methods which have been used to determine the binding energies for the sequential ligands addition in conjunction with statistical mechanical calculations are also presented. Finally, details of the pump-probe setup and the cross correlation measurement procedure employed in the real time fs-photodissociation experiments are detailed.*

---

\* Parts of this chapter have been published in *The chemical physics of solid surfaces (Vol. 12): Atomic clusters: From gas phase to deposited*, edited by D. P. Woodruff, Elsevier, S. M. Lang, D. M. Popolan, T. M. Bernhardt, "Chemical reactivity and catalytic properties of size-selected gas-phase metal clusters", 53-90 (2007) and *The Journal of Physical Chemistry A*: T. M. Bernhardt, J. Hagen, S. M. Lang, D. M. Popolan, L. D. Socaciu-Siebert, L. Wöste, "Binding energies of O<sub>2</sub> and CO to small gold, silver, and binary silver-gold cluster anions from temperature dependent reaction kinetics measurements" **113**, 2724-2733 (2009).

### 3.1 Kinetic data acquisition method

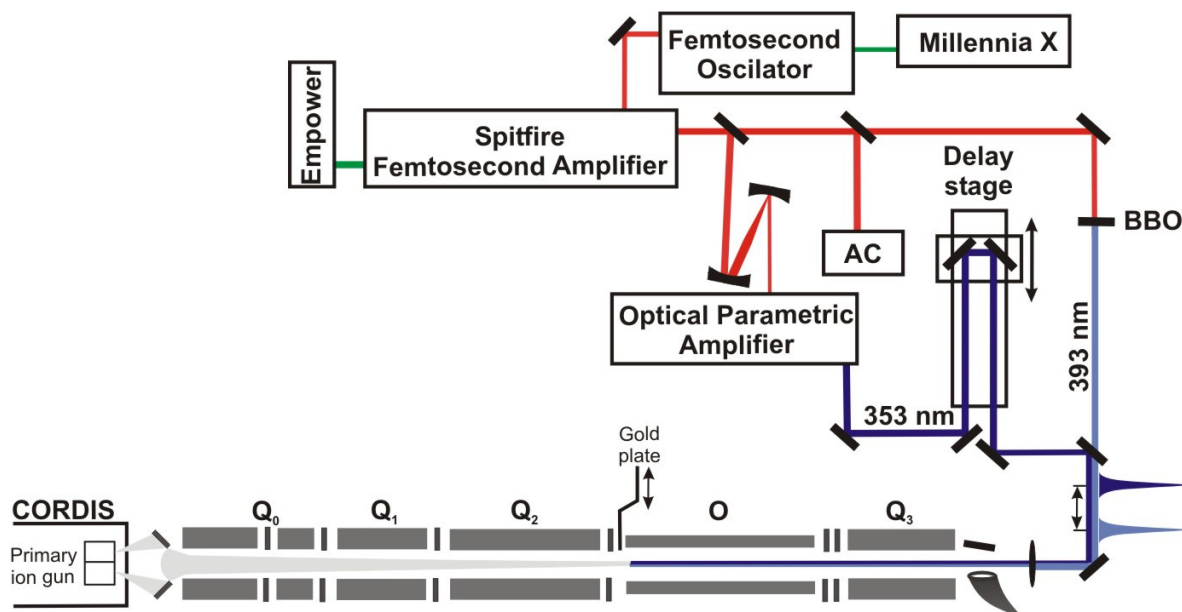


**Figure 3.1:** Schematic representation of the experimental setup. For details see text.

The schematic layout of the experimental setup consisting of the rf-octopole ion trap inserted into a multiple quadrupole mass spectrometer arrangement and the fs-laser system is displayed in Figure 3.1. Details concerning the pump & probe setup employed in the photodissociation experiments will be explained in Section 3.5.

The metal clusters were prepared by simultaneous sputtering of four metal targets with accelerated xenon ion beams generated by the CORDIS ion source<sup>124</sup> (for details see Section 2.1.1). The charged clusters sputtered from the targets were steered into the first helium filled quadrupole  $Q_0$ . Here, the cluster ions were cooled and thermalized to room temperature through collisions with the He background gas ( $p_{\text{He}} \approx 10^{-2}$  mbar). In this manner internal energy was removed from the clusters and the volume of the ion cloud was substantially compressed in both real and momentum spaces. The cluster ion beam was further guided through electrostatic lenses into a mass-selective quadrupole filter  $Q_1$  to record and to optimize the cluster ion distribution prepared by the sputter source and to select one particular mass for further analysis. A beam of well thermalized mass-selected metal clusters ions was created in this way. Typical mass spectra of distributions of positively charged cluster ions obtained from different target materials (silver, gold and gold-silver alloy) are displayed in Figure 3.2. The ion intensities in these experiments were optimized for the small clusters size regime.

Subsequently, the thermalized cluster ions were transferred into a home-built octopole ion trap O by means of a third quadrupole  $Q_2$ .<sup>54,150</sup> Prior to the cluster admission, the octopole ion trap was prefilled with about 1 Pa partial pressure of helium buffer gas. The entrance lens of the ion guide was kept at a potential slightly below the kinetic energy of the ions while the



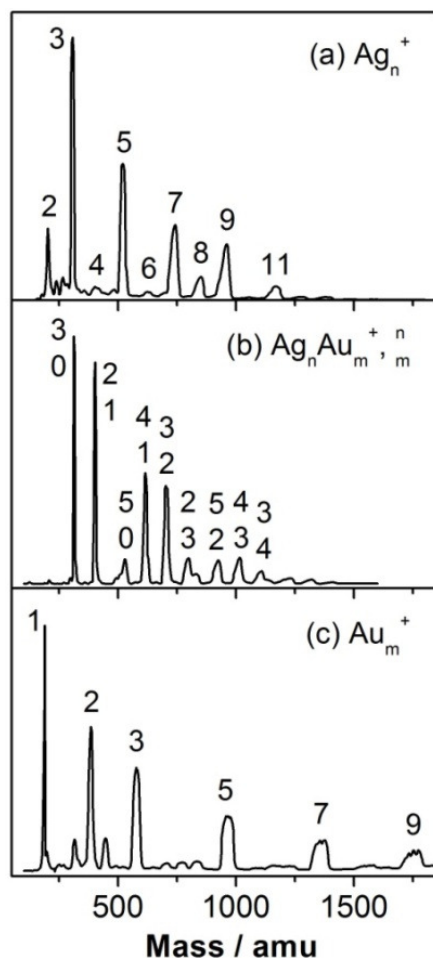


**Figure 3.2:** Cluster cation distributions generated by the CORDIS sputter source from different target materials. The mass spectra were obtained by scanning the mass-selective quadrupole filter  $Q_1$  and recording the ion currents on the rods of transfer quadrupole  $Q_2$  acting as a Faraday collector. The ion currents were optimized for the small cluster size regime. The cluster distributions were obtained by using pure silver (a) and pure gold (c) targets while for the binary silver-gold clusters (b) alloy targets with a composition of Ag 70% : Au 30% were used.

exit lens was at a higher potential. Hence, the cations could enter the octopole ion trap, but were reflected back at the exit lens. Travelling through the gas cell, the ions lose kinetic energy by collisions with the buffer gas (the collision frequency in our experiment was about  $3 \cdot 10^5 \text{ s}^{-1}$ ) and were no longer able to escape via the entrance lens. The ion trap was then filled with clusters up to the space charge limit, i.e. about  $10^4$  ions per  $\text{mm}^3$ . This value represents the initial concentration of the metal cluster reactants. After the trap was filled, the voltage applied to the entrance lens was switched to a hindered value that hinders new clusters to enter the trap. Thus, the voltage applied to the octopole entrance and exit lenses were chosen such that, when closed during the reaction time, no further clusters could enter or escape the

trap. The ion trap losses during the storage time were estimated to amounts to less than 10% after 10 s reaction time.

A closed cycle helium cryostat attached to the ion trap enclosure allows variable temperature adjustment in the range between 20 and 300 K by resistive heating against the cryostat. At the applied pressures (around 1 Pa He), the buffer gas collisions ensure that thermal equilibration of the clusters entering the trap within less than a few thousand collision. This corresponds to a few milliseconds under our operating condition, whereas the cluster ions were stored in the ion trap typically from 0.1 s up to few seconds (for details see Section 2.1.4). Prior to the admission into the octopole, the helium buffer gas is purified by flowing through a cold trap filled with liquid nitrogen.

To perform reaction experiments, a small well defined fraction of reactive gases is admitted into the trap. This is accomplished by a Teflon tube twisted around the cold finger of the cryostat and inserted into the trap housing. A similar tube (1 mm inner diameter) connects the interior of the trap housing to a capacitance monometer (Baratron gauge, MKS, Typ 672B) which measure the absolute partial pressures inside the trap. Since the trap can be cooled down to 20 K while the manometer is constantly kept at 318 K, for exact pressure determination inside the ion trap the thermal transpiration must be taken into account (for details see Section 2.1.4).

After the chosen reaction time, all ions, reactants, intermediates and products, are extracted by switching the voltage on the exit lens to a negative value, and the ion distribution is analyzed via the final quadrupole mass filter  $Q_3$ . The ion pulses are amplified by a channeltron/conversion dynode detector, digitalized and integrated by a LeCroy 9400A 175 MHz oscilloscope.

The trap operation in the filling, storing or extracting mode is computer controlled by a *LabView* program (National Instruments) developed for this purpose. A schematic view of data acquisition method and of the command stream controlled by the *LabView* program is presented in the Figure 3.3. The control sequence works as follows : (i) Through the computer interface (Scientific Research Instruments, SRS 245), the program commands two TTL-switches that change the voltages on the octopole entrance lens  $L_1$ , and exit lens  $L_2$ , respectively. In this way, the trapping cycle (filling, storing, and emptying of the trap) is initialized. (ii) The mass on  $Q_3$  is also set via the computer interface. The interface produces a *dc* voltage between 0 and 10 V (corresponding to the required mass) which in turn is converted into an appropriate high voltage in the  $Q_3$  power supply. (iii) The resulting ion signal is amplified by means of a channeltron detector and subsequently transferred to the oscilloscope. In order to increase the signal-to-noise ratio the oscilloscope averages the ion signal over ten trapping cycles prior to the transfer to the computer. The implemented *LabView* program then integrates the received signal and stores the final value. The above mentioned sequence (i)-(iii) is then repeated for each value of the parameter to be scanned, i.e. mass or reaction time.

The *LabView* program allowed, through the computer interface, the control of filling,

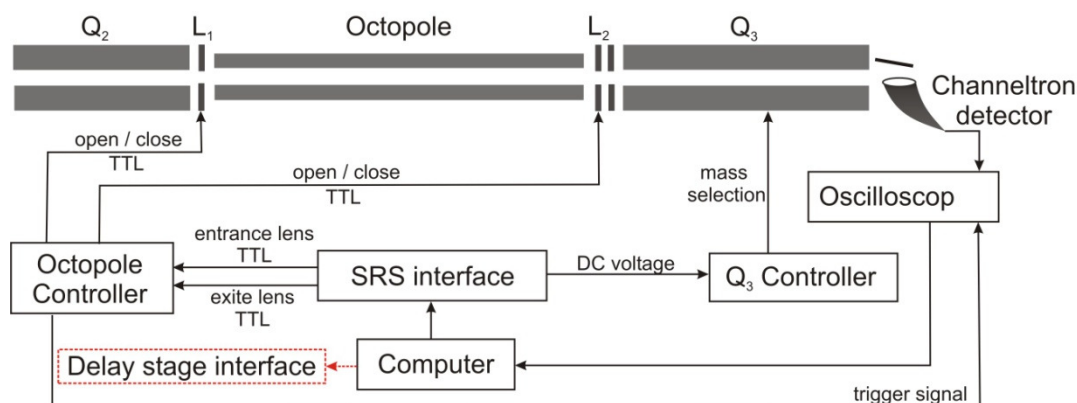


**Figure 3.3:** Schematic representation of the data acquisition method (see text for more details).

reaction, and extraction times, detection mass of  $Q_3$ , which parameter is to be scanned (mass or reaction time), starting and stopping value of the scanned parameter and the number of scanned points.

For all experiments presented in this thesis a filling time of 200 ms was chosen, which corresponds to an optimal filling of the ion trap. The extraction time was chosen to be 40 ms, so that, during the extraction process all the ions are expelled. Afterwards, the trap is empty and another cycle can begin.

With this experimental arrangement two types of measurements can be performed. Mass spectra can be recorded by keeping the reaction time constant and scanning the mass distribution of reaction products with the quadrupole mass spectrometer  $Q_3$ . When  $Q_3$  is set to select a specific mass and the reaction time is scanned, the time evolution of the concentration of a particular reaction product or educt is analyzed as a function of the reaction time (storage time) yielding the reaction kinetics.

## 3.2 Kinetic data evaluation procedure

The recorded ion signals (educts and products) are normalized to the total ion signal according to:

$$[X_i]_{\text{norm}} = \frac{[X_i]}{\sum_{j=1}^{j=n} [X_j]}, \quad (3.1)$$

where  $[X_i]$  represents the measured signal intensity of ion  $i$  and  $n$  is the total number of ionic reaction educts and products. This normalization of the cluster signal to the total ion signal was performed for every kinetic measurement presented in this thesis.

Possible reaction mechanisms were evaluated by fitting of the integrated rate equations to the measured kinetic data using the Detmech software.<sup>151</sup> This software allows for the determination of the likelihood of the proposed reaction mechanism and also the calculation of the corresponding rate constant  $k$  for each reaction step. Using this method the most simple reaction mechanism with the best fit to the experimental data is identified, discarding the more complex mechanisms with similar fit quality. In the fitting procedure, the differential equations derived from the proposed mechanistic model are solved numerically by using the fourth-order Runge-Kutta algorithm. The optimum set of rate constants is found by a least-squares minimum search for the deviations of the measured concentration versus the calculated ones.<sup>151</sup> When the simulated product and educt concentrations do not match with the measured data, the proposed reaction mechanism is modified and the procedure is repeated until the simulated data are in good agreement with the experiment. This procedure is very sensitive to the proposed reaction mechanism and a slight modification of the reaction mechanism, e.g., an optional equilibrium step, can lead to a significant mismatch between simulated and experimental data.

### 3.2.1 Low-pressure reaction kinetics

As an example, the generalized straightforward association reaction of the metal cluster ions  $M_n^{+/-}$  and the neutral reactant L will be examined in the following in detail.



Since the total pressure inside of ion trap was on the order of 1 Pa, we can conclude that the experiments were operated in the kinetic low-pressure regime. Therefore, an elementary inverse Lindemann-type mechanism has to be considered for reaction 3.2. Consequently, the reaction depends on the buffer gas pressure and becomes of third order. However, the concentrations of the reactive gas [L] and the helium buffer gas [He] in the ion trap were orders of magnitude larger than the cluster ion concentration  $[M_n^+]$  and a steady flow of the reactant was ensured. This permits the postulation of pseudo-first-order kinetics with the pseudo-first-order rate constant:

$$k = k^{(3)}[\text{He}][\text{L}] \quad (3.3)$$

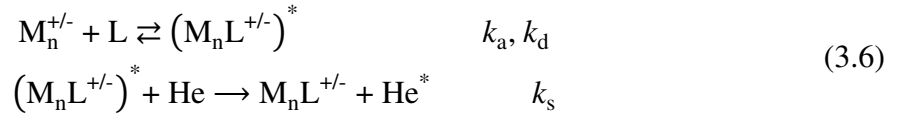
where  $k^{(3)}$  is the termolecular rate constant while [He] and [L] represent the concentration of the buffer gas and the reactant gas, respectively. Hence, the termolecular rate constant  $k^{(3)}$  can be directly obtained from the fitted pseudo-first-order rate constant  $k$  and the partial pressures of helium ( $p_{\text{He}}$ ) and of the reactant molecule L ( $p_{\text{L}}$ ) by applying the ideal gas law to calculate the concentrations [He] and [L] as follows:

$$[\text{He}] = \frac{p_{\text{He}}}{k_{\text{B}}T} \quad (3.4)$$

$$[\text{L}] = \frac{p_{\text{L}}}{k_{\text{B}}T} \quad (3.5)$$

where  $k_{\text{B}}$  is the Boltzmann constant and  $T$  the corresponding reaction temperature.

The details of reaction 3.2 and also of each reaction step of an overall mechanism proposed for more complex reactions are described by the Lindemann energy-transfer model for association reactions.<sup>152</sup> According to this model, an ion-molecule complex is formed first and stabilized by a collision with a third body (helium in our case) as follows:



where  $\text{M}_n^{+/-}$  represents the metal ion, L the ligand molecule, and the  $(\text{M}_n\text{L}^{+/-})^*$  designates the energized complex. The reaction model includes three elementary steps, (i) the formation of the energized complex  $(\text{M}_n\text{L}^{+/-})^*$  with the rate constant  $k_a$  and (ii) the possible unimolecular decomposition back to the reactants (rate constant  $k_d$ ) in competition with (iii) a stabilizing energy-transfer collision with helium buffer gas having the rate constant  $k_s$ . Assuming all these elementary reaction steps to be again of pseudo-first-order and additionally employing the steady-state assumption for the intermediate  $(\text{M}_n\text{L}^{+/-})^*$ , the overall third-order rate constant is obtained to be<sup>153</sup>

$$k_{\text{overall}}^{(3)} = \frac{k_a k_s}{k_d + k_s [\text{He}]}. \quad (3.7)$$

As the experiment is operating in the kinetic low-pressure regime, the decomposition rate constant can consequently be considered to be much larger than the stabilization rate constant,  $k_d \gg k_s [\text{He}]$ . This leads to a simplified expression for the termolecular rate constant which can be applied to the experimental conditions in the rf ion trap experiment:

$$k^{(3)} = \frac{k_a k_s}{k_d}. \quad (3.8)$$

In the present analysis, the values of the decomposition rate constant  $k_d$  were deduced from the experimental values of  $k^{(3)}$  using Langevin theory to determine the association rate constant  $k_a$  as well as the stabilization rate constant  $k_s$ . According to Langevin theory, ion-

molecule reactions are charge-induced dipole or charge-dipole interactions and exhibit no activation barrier, i.e., no temperature dependence.

### 3.2.2 Langevin theory

Developed by Langevin<sup>154</sup> in 1905, the Langevin theory in its simplest form describes the interaction between an ion and a non-polar molecule. It is assumed that the ion is a point charge and the molecule is a structure less sphere with polarizability  $\alpha$ . In the Langevin model, is further assumed that at the long range only the ion-induced dipole attractive term in the potential is important. The effective potential is given by:

$$V_{\text{eff}}(r) = U(r) + \frac{L^2}{2\mu r^2} = -\frac{1}{2} \frac{\alpha e^2}{r^4} + \frac{\mathcal{L}^2}{2\mu r^2}. \quad (3.9)$$

$U(r)$  represents the ion-induced dipole potential with the form  $U(r) = -\frac{1}{2}(\alpha e^2/r^4)$ , where  $\alpha$  is the polarizability of the neutral molecule,  $e$  represents the elementary electronic charge ( $4.8 \times 10^{-10}$  esu), and  $r$  is the relative distance between the ion  $M_n^+$  and the neutral molecule L. In the second term  $\mathcal{L}$  designates the classical angular momentum while  $\mu$  is the reduced mass. Considering the classical angular momentum  $\mathcal{L}$  with the form  $\mathcal{L} = \mu v b$ , with  $v$  as the relative velocity of the two particles and  $b$  as the impact parameter. The effective potential can be rewritten in term of the kinetic energy ( $E = 1/2 \mu v^2$ ) as:

$$V_{\text{eff}}(r) = -\frac{1}{2} \frac{\alpha e^2}{r^4} + E_{\text{rel}} \left( \frac{b}{r} \right)^2 \quad (3.10)$$

The effective potential has a maximum at the ion-molecule distance  $r_{\text{max}}$  along the reaction coordinate given by

$$V_{\text{max}}(r_{\text{max}}) = \frac{1}{2} \frac{E^2 b^4}{\alpha e^2} \quad (3.11)$$

with

$$r_{\text{max}} = \frac{\left( \frac{\alpha e^2}{E} \right)^{\frac{1}{2}}}{b} \quad (3.12)$$

where  $V_{\text{max}}(r_{\text{max}})$  represents the centrifugal barrier, which has to be overcome for the chemical reaction to take place. Whenever  $E < V_{\text{max}}$ , the centrifugal barrier cannot be penetrated, the ion-molecule critical distance  $r_c$  always remains greater than  $r_{\text{max}}$ , and reactions do not take

place. For  $E \geq V_{\max}$ , the reaction is supposed to occur with a probability of one. So the critical impact parameter at which the reaction can occur is found to be:

$$b_c = \left( \frac{2\alpha e^2}{E} \right)^{\frac{1}{4}} \quad (3.13)$$

and the Langevin rate constant is given by:

$$k_L = \left( \frac{4\pi^2 \alpha e^2}{\mu} \right)^{\frac{1}{2}} \quad (3.14)$$

The Langevin theory can also be extended to describe the interaction between an ion and a polar molecule but the simple Langevin rate constant (for non-polar molecules) must be corrected by an empirical expression ( $K_{\text{cap}}(T_R, I^*)$ ). The empirical expression found by T. Su et al. contains the permanent dipole moment of the ligand molecule  $L$ .<sup>155</sup> These authors found that the ratio between the capture rate constant  $k_{\text{cap}}(T)$  and Langevin rate constant  $k_L$  depends only on two reduced parameters, i.e. reduced temperature  $T_R = 2\alpha k_B T / \mu_D^2$  and the reduced moment of inertia  $I^* = \mu_D I / \alpha e \mu$  (with  $I$  as the moment of inertia of the neutral molecule):

$$k_{\text{cap}}(T) = k_L K_{\text{cap}}(T_R, I^*) \quad (3.15)$$

where  $k_{\text{cap}}(T)$  represents the rate constant for the reaction between an ion and the dipolar molecule. Empirical expressions found by Su et al.<sup>155,156</sup> for  $K(T_R, I^*)$  are given by:

$$K_{\text{cap}}(T_R, I^*) = \begin{cases} 0.4767x + 0.6200 & \text{for } 2 \leq x \leq 3 \\ \frac{(x + 0.5090)^2}{10.526} + 0.9754 & \text{for } x < 2 \end{cases} \quad (3.16)$$

with

$$x = \frac{1}{\sqrt{T_R}} = \frac{\mu_D}{(2\alpha k_B T)^{1/2}} \quad (3.17)$$

Introducing 3.16 in 3.15 the capture rate constant  $k_{\text{cap}}(T)$  for the reaction between an ion and a dipolar molecule can be calculated as follows:

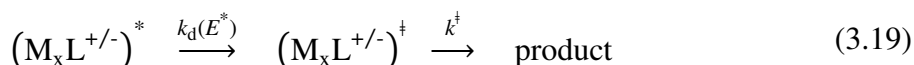
$$k_{\text{cap}}(T) = k_L \begin{cases} 0.4767x + 0.6200 & \text{for } 2 \leq x \leq 3 \\ \frac{(x + 0.5090)^2}{10.526} + 0.9754 & \text{for } x < 2 \end{cases} \quad (3.18)$$

The Equation 3.18 was employed for modeling of the reaction between cluster ions and carbon monoxide molecules presented in Chapter 4.

### 3.2.3 RRKM theory

Ion-molecule reactions can be described as interactions between a charge and an induced or permanent dipole and exhibit no activation barrier and, hence, no temperature dependence.<sup>157</sup> Therefore, any observed temperature dependence of reaction 3.2 must be contained in the unimolecular decomposition rate constant  $k_d$  (conform reactions 3.6).

The RRKM (Rice-Ramsperger-Kassel-Marcus) theory<sup>158,159</sup> was developed on the basis of the RRK (Rice-Ramsperger-Kassel) model to consider explicitly vibrational and rotational energies by using transition state theory to calculate the unimolecular decomposition rate constant  $k_d(E^*)$ . The decomposition reaction step is considered to proceed via



involving the transition state (TS)  $(M_n L^{+/-})^\ddagger$ . In the RRKM theory, it is very important to distinguish between the energized complex  $(M_n L^{+/-})^*$  and the TS  $(M_n L^{+/-})^\ddagger$ .

The energized complex  $(M_x L^{+/-})^*$  contains a total non-fixed energy  $E^* \geq E_0$  in its active degrees of freedom. In the course of the unimolecular process, the reaction path crosses a critical activated configuration at which the energy, as measured between the zero-point vibrational levels of the reactant and activated complex, is denoted  $E_0$ .  $E_0$  represents the critical energy which is necessary for the reaction to occur and which is assumed to be equal to the bond dissociation energy or the binding energy, respectively. In other words,  $E_0$  specifies the height of the energy barrier that has to be overcome to get from energized molecule to the transition state. In contrast, the subsequent decomposition ( $k^\ddagger$ ) is barrier free.

The transition state  $(M_x L^{+/-})^\ddagger$  is basically a species which is recognizable as being intermediate between reactants and products. The internal degrees of freedom of  $(M_x L^{+/-})^*$  and  $(M_x L^{+/-})^\ddagger$  are either active or adiabatic. Active modes are assumed to exchange energy freely, while an adiabatic mode is one that remains in the same quantum state during the reaction. Conservation of angular momentum usually requires the external rotation modes to be treated as adiabatic. By contrast, the vibrational and internal rotational modes are considered to be active.

The RRKM theory is closely related with the calculation of the number of ways of distributing a given amount of energy between various degrees of freedom in a molecule. Any energy that can be redistributed is called non-fixed, while any fixed energy that cannot be redistributed, as the zero-point energy and the translational energy, are of no interest and are neglected in the calculations.

Next, the decomposition of the complex with internal energies in the range from  $E^*$  to





$$k_d^{\text{RRKM}}(E^*) = L^\ddagger \frac{W(E_{\text{vr}}^\ddagger)}{h\rho(E^*)} \quad (3.22)$$

wherein  $L^\ddagger$  denotes the reaction path degeneracy,  $W(E_{\text{vr}}^\ddagger)$  the sum of vibrational-rotational quantum states of the TS,  $\rho(E^*)$  the density of quantum states of the energized complex, and  $h$  is Planck's constant. The evaluation of the density of states basically requires the knowledge of the total non-fixed energy  $E^*$ , the critical energy  $E_0$ , and the normal vibrational and rotational frequencies of the energized molecule as well as the transition state. The total non-fixed energy  $E^*$  of the complex  $(M_n L^{+/-})^*$  can be expressed as the sum of potential energy gained in forming the complex  $E_0$ , the vibrational energy of the reactants, which is the vibrational energy of the cluster  $E_{\text{vib}}(M_n L^{+/-})$  before reaction and energy  $E_{\text{free}}$  contained in the translational and rotational degree of freedom which is converted into internal energy of  $(M_n L^{+/-})^*$  upon reaction of  $M_n^{+/-}$  with L.<sup>161</sup>

$$E^* = E_0 + E_{\text{vib}}(M_n L^{+/-}) + E_{\text{free}} \quad (3.23)$$

The reactant molecules (L) can be considered vibrationally cold at the investigated reaction temperature and therefore in the following only vibrational levels of the clusters will be considered. The resulting values for  $E_{\text{vib}}(M_n L^{+/-})$ ,  $E_{\text{free}}$ , and  $E^*$  for different cluster sizes and geometries (linear or non-linear) are displayed in Table 3.1.

This model for molecular complexes with linear and non-linear structure proposed by Cox et al.<sup>161</sup> will be applied in Chapter 4 to calculate the reaction rate constants and binding energies of adsorbed molecules on clusters. Note that, since the total non-fixed energy  $E^*$  can be expressed by Equation 3.23 and both  $E_{\text{vib}}(M_n L^{+/-})$  and  $E_{\text{free}}$  are a function of the reaction temperature  $T$ , the expression  $k_d^{\text{RRKM}}(E^*)$  is equivalent to  $k_d^{\text{RRKM}}(T)$ .

A further, more subtle problem with respect to the total available energy is caused by the adiabatic rotational degrees of freedom, which have not been considered so far in Equation 3.23. Adiabatic rotations are those for which the angular momenta and thus the quantum states stay constant during the conversion of  $(M_n L^{+/-})^*$  to  $(M_n L^{+/-})^\ddagger$ . However, when the geometry and, with it, the moment of inertia changes, additional energy is released into other degrees of freedom and is contained in the energy of the transition state  $(E_{\text{vib}}(M_n L^{+/-}) + E_{\text{free}})$ . Hence, Equation 3.23 does not reflect the actually available total energy of the complex  $(M_n L^{+/-})^*$  which has to be rather denoted as  $E_{\text{act}}^* < E^*$ . Neglecting adiabatic rotations in the evaluation procedure therefore would result in a too low value of  $k_d$  and implicit for the binding energy. The treatment of the adiabatic rotations is detailed in the next section.

**Table 3.1:** The vibrational energy  $E_{\text{vib}}$ , the free energy  $E_{\text{free}}$ , and the energy of the activated complex  $E^*$  according to the model proposed by Cox et al..  $n$  denoted the number of atoms contained in the molecular complex.<sup>161</sup>

$n$	$E_{\text{vib}}$	$E_{\text{free}}$	$E^* = E_0 + E_{\text{vib}} + E_{\text{free}}$
$\geq 3$	$(3n - 6) k_B T$ (nonlinear)	$5/2 k_B T$	$E_0 + (3n - 7/2) k_B T$
$\geq 2$	$(3n - 5) k_B T$ (linear)	$2 k_B T$	$E_0 + (3n - 3) k_B T$
1	0	$3/2 k_B T$ (linear)	$E_0 + 3/2 k_B T$
1	0	$k_B T$ (bent)	$E_0 + k_B T$

### 3.2.4 Fitting procedure. *MassKinetics* input

The RRKM decomposition rate constant  $k_d$  and thus the binding energies  $E_0$  determined in this thesis have been calculated using the software package *MassKinetics* developed by Drahos et al.<sup>162</sup> This computational algorithm applies the harmonic oscillator model with internal rotations approximated by low-frequency vibrations. The density and the sum of state of Equation 3.22 are calculated by direct count employing the Beyer-Swinehart algorithm.<sup>159</sup> Furthermore, adiabatic rotations are taken into account by expressing them as a “rotational barrier”  $E_{\text{RB}}$ , that is, a correction factor to the too low binding energy and to the too high available energy  $E^*$  that would have been obtained by neglecting the adiabatic rotations.<sup>162</sup>

In order to calculate the decomposition rate constant  $k_d$  according to Equation 3.22, the *MassKinetics* program requires the specification of the following parameters:

- (i) the mass of the energized complex  $(M_n L^{+/-})^*$ ; The mass is given by the stoichiometry of the reaction product,
- (ii) the critical energy for dissociation (binding energy)  $E_0$ , which is a quantity in demand,
- (iii) the actual non-fixed energy  $E_{\text{act}}^*$ , which can be calculated according to formula<sup>159,161</sup>

$$E_{\text{act}}^* = E^* - E_{\text{RB}} = E_0 + E_{\text{vib}}(L_n^{+/-}) + E_{\text{free}} - E_{\text{RB}}, \quad (3.24)$$

- (iv) the “rotational barrier”  $E_{\text{RB}}$ ; Adiabatic rotations are considered in the following calculation by approximating  $E_{\text{RB}}$  according to the formula<sup>159,163</sup>

$$E_{\text{RB}} = \left( \frac{I^\ddagger}{I^*} - 1 \right) k_B T = \left( \frac{r_c^2}{r_e^2} - 1 \right) k_B T \quad (3.25)$$

where  $r_c$  represents the  $M_n-L^+$  distance in the transition state corresponding to capture radius of the long-range potential between  $M_n^+$  and  $L$  and  $r_e$  denotes the  $M_n-L^+$  distance of the energized molecule corresponding to the equilibrium radius.  $r_c$  can be calculated as follows:

$$r_c = \left( \frac{\alpha q^2}{2E} \right)^{\frac{1}{4}} = \left( \frac{\alpha q^2}{2k_B T} \right)^{\frac{1}{4}} \quad (3.26)$$

where  $\alpha$  is the polarizability of the neutral molecule (corresponding to CO, in this work),  $q$  is the elementary electronic charge,  $k_B$  is the Boltzmann constant and  $T$  is the corresponding temperature. Since the effect of the temperature dependence of  $E_{RB}$  on the resulting binding energy is negligible, a fixed mean  $E_{RB}$  value at  $T = 200$  K was chosen to be used for the fitting procedure,

- (v) the reaction path degeneracy  $L^\ddagger$ . For metal cluster reaction with one adsorbed ligand, the reaction path degeneracy is  $L^\ddagger = 1$ .

Additionally, the energized molecule  $(M_n L^{+/-})^*$  and the TS  $(M_n L^{+/-})^\ddagger$  are each characterized by its normal frequencies. Whereas for  $(M_n L^{+/-})^*$  vibrational frequencies can be obtained by DFT calculation or can be approximated, the transition state TS is usually unknown, and several assumptions must be made.

### 3.2.5 Energized molecule and transition-state model

For the complexes analyzed in the present thesis employing RRKM theory ( $(Ag_3CO^+)^*$ ,  $(Ag_2AuCO^+)^*$ ,  $(Au_3CO^+)^*$  and  $(Au_3CO^-)^*$ ) the normal frequencies have been calculated by Bonačić-Koutecký and coworkers using *ab initio* theory. All frequencies used to compute the binding energies are summarized in Table 3.2.

The binding energy  $E_b$  of CO in the investigated complexes is calculated by employing two different transition-state models, a “tight” TS and a more realistic “loose” TS. The “tight” transition-state, usually associated with rearrangement processes, has the same vibrational modes as the energized molecule, less one. This particular one is treated as internal translation along the reaction coordinate. This model represents the tightest reasonable transition state and gives a lower limit for the binding energy.<sup>164</sup> No “rotational barrier” exists for a “tight” TS ( $E_{RB} = 0$ ).

In contrast, the “loose” transition-state, common to the bond cleavage reactions, not only has one vibration removed and transformed into internal translation along the reaction coordinate but, in addition, also has the low-frequency bending vibration scaled by a factor of  $f < 1$ .<sup>165</sup> In this context, the TS can be tuned to be “tight” (lower limit for  $E_0$ ) or “loose” (upper limit for  $E_0$ ) just by varying this factor.

The vibrational frequencies of the reacting ions and the transition state give the entropy of activation  $S^\ddagger$ . The  $S^\ddagger$  is a convenient way to describe the nature of the reaction. Transition states that are less “ordered” (“loose”) than the reactant ion are characterized by positive  $S^\ddagger$  values,  $S^\ddagger \geq 0$ . Simple bond cleavage reactions typically have loose transition states. Transition states that are more “ordered” than the reactant ion have negative values for  $S^\ddagger$ ,  $S^\ddagger \leq 0$ .

**Table 3.2:** Calculated frequencies for the energized complexes  $(M_nL^{+/-})^*$  and the “loose” TS  $(M_nL^{+/-})^\ddagger$ .

Species	$(M_3CO^{+/-})^*$ vibrational frequencies [ $\text{cm}^{-1}$ ]	$(M_3CO^{+/-})^\ddagger$ (“loose” TS) vibrational frequencies [ $\text{cm}^{-1}$ ]
$\text{Ag}_3\text{CO}^+$	28, 36, 103, 114, 161, 202, 209, 227, 2287	28, 18, 101, 103, 105, 114, 161, 2170
$\text{Ag}_2\text{AuCO}^+$	33, 43, 106, 109, 163, 246, 268, 280, 2262	22, 33, 106, 109, 123, 134, 162, 2170
$\text{Au}_3\text{CO}^+$	34, 50, 76, 108, 159, 292, 311, 335, 2270	25, 34, 76, 108, 146, 155, 159, 2170
$\text{Au}_3\text{CO}^-$	25, 31, 58, 101, 165, 212, 263, 358, 2031	25, 31, 29, 101, 106, 132, 165, 2170

These “tight” transition states are usually associated with rearrangement processes, so, if the vibrational frequencies of the reactant ion and the transition state are known, the nature of the process can be surmised.<sup>165</sup> Generally, the bending vibrations are scaled by  $f = 0.5$ ,<sup>166,167</sup> which is also applied for all TSs under investigation in the present thesis and leads to  $S^\ddagger > 0$ .

### 3.2.6 Error analysis

To find out the error limits of the binding energy values determined in this thesis and thus to assess their accuracy, the uncertainties of the measured kinetic data and the uncertainties in the description of the  $(M_nL^{+/-})^*$  and  $(M_nL^{+/-})^\ddagger$  have to be considered.

As evaluative quantities, the error bars of the measured  $k_d$  valued include uncertainties in the fitting procedure to obtain  $k$  and errors in the measured gas pressure, which are considered to be  $\pm 0.01$  Pa according to the detection limit of the Baratron gauge.

The non-fixed energy  $E_{\text{act}}^*$  was determined from  $E_{\text{vib}}(M_n^{+/-})$  and  $E_{\text{free}}$ . In this calculation,  $E_{\text{free}}$  was assumed to amount to  $1/2k_B T$  for each translation and rotation degree of freedom that is lost by forming the complex  $(M_nL^{+/-})^*$  and is thus converted into internal energy. Additionally,  $E_{\text{vib}}(M_n^{+/-})$  contributes  $k_B T$  for each vibrational degree of freedom. These values represent the classical limits and are thus certainly upper limits at the low to moderate reaction temperature of the experiment.

Since “tight” TSs are usually associated with rearrangement processes and “loose” TSs are common for simple cleavage reactions, the “tight” TS model clearly represents a lower limit for the dissociation energy in the evaluation procedure described above. In contrast, the consideration of thermal transpiration and the rotational barrier  $E_{\text{RB}}$  as well as applying the upper classical limit for the determination of  $E_{\text{vib}}(M_n^{+/-})$  represent positive contributions to the obtained binding energies of the “loose” TS. Thus, the presented binding energies of the “loose” TSs correspond to the upper limit which can only be further increased by reducing the scaling factor  $f$  and hence marking the TS even “looser”.

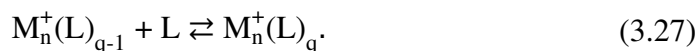
In order to illustrate the accuracy of the  $k_d$  fitting procedure employed to determine the binding energies, the experimental obtained reaction temperature dependent decomposition rate constants together with the calculated RRKM  $k_d(T)$  curves for both “tight” and “loose”

TSs were graphically compared (for details see Section 4.2). In addition to the best-fit RRKM  $k_d(T)$  curves determining the binding energy  $E_0$ , also error limits of the binding energy have been estimated by varying  $E_0$  (the upper and lower limits) to include all experimental  $k_d$  values. Their corresponding  $E_0$  values determine the reported uncertainty of the binding energy. Important to note is that these uncertainties of  $E_0$  include the errors in measuring  $k_d$  and fitting the RRKM rate constants, but do not, of course, account for possible deficiencies in the TS models or the RRKM model itself.

### 3.3 Equilibrium thermodynamics evaluation method

Due to a high reactivity of some cluster sizes towards some specific ligands, a comprehensive kinetic analysis of the cluster-molecule complexes was not always possible. Therefore, another approach to determine the binding of these molecules to pure and binary silver-gold clusters was employed.

For this purpose, after the trap reached a stable temperature, products/parent ion mass spectra was measured as a function of reaction time until no change in the recorded mass was found, so that the ions had sufficient time to attain equilibrium. Thus, for longer reaction time a steady state is reached, which can be parameterized by an equilibrium constant, which serves as an alternative approach to determine binding energies of the ligand molecule L to the metal clusters  $M_n^+$ , corresponding to the equation:



The product mass spectra were recorded at different temperatures between 90 and 310 K. The recorded product peaks areas in the mass spectra were then integrated and these values  $[M^+(L)_q]$  and  $[M^+(L)_{q-1}]$ , along with the partial pressure of the reactant molecule ( $p_L$ ) in mbar, were used to determine an equilibrium constant  $K_{eq}^0$  for each reaction according to:

$$K_{eq}^0 = \frac{[M^+(L)_q]}{[M^+(L)_{q-1}]} \frac{p^0}{p_L}, \quad (3.28)$$

wherein  $p^0$  represents the standard pressure and  $p_L$  the reactant gas partial pressure. The obtained equilibrium constant is then used to calculate the Gibbs free energy for the reactions in its standard state according to:

$$\Delta G_T^0 = -RT \ln(K_{eq}^0), \quad (3.29)$$

where  $R$  is the gas constant and  $T$  the reaction temperature. The experiment is then repeated at a series of temperatures in order to determine the temperature dependence of  $\Delta G_T^0$ . The values obtained for  $\Delta G_T^0$  are then plotted versus temperature, which is equivalent to a van't Hoff plot ( $\ln[K]_{\text{eq}}$  versus  $1/T$ ) but more convenient for our data analysis, to obtain  $\Delta S_T^0$  and  $\Delta H_T^0$  for each reaction according to Equation 3.30.

$$\Delta G_T^0 = \Delta H_T^0 - T\Delta S_T^0, \quad (3.30)$$

where  $\Delta H_T^0$  is the temperature dependent reaction enthalpy and  $\Delta S_T^0$  is the temperature dependent reaction entropy. Since all the resulting plots were to a good approximation linear over the experimental temperature range for all the systems investigated in this thesis, a least squares-fitting procedure was used to obtain the slopes and the intercepts of each line. The slopes are used to determine the association entropy for equation  $\Delta S_T^0$  and the intercepts give the corresponding  $\Delta H_0^0$  values at  $T = 0$  K. For simple association reaction the reaction enthalpy  $\Delta H_0^0$  represents the binding energy of the ligand to the cluster.<sup>168,169</sup>

Plotting the data this way allows a fairly accurate determination of  $\Delta H_0^0$  (binding energy). Especially for the cases when only few experimental points are available, in order to obtain highly accurate  $\Delta H_0^0$ , a more sophisticated extrapolation of  $\Delta G^0$  to 0 K is required; i.e., the temperature dependence of  $\Delta H_T^0$  and  $\Delta S_T^0$  must be included. This was done by using statistical mechanics calculations of  $\Delta G^0$ .<sup>169,170</sup> In this calculation the total reaction enthalpy (Kirchhoff's law) and entropy are given by

$$\Delta H_T^0 = \Delta H_0^0 + \int_0^T (\Delta C_{p,\text{trans}} + \Delta C_{\text{vib}} + \Delta C_{\text{rot}}) dT \quad (3.31)$$

and

$$\Delta S_T^0 = \Delta S_{\text{trans}}^0 + \Delta S_{\text{vib}} + \Delta S_{\text{rot}}. \quad (3.32)$$

$\Delta H_T^0$  or rather the heat capacity change  $\Delta C_p$  as well as  $\Delta S_T^0$  were determined by using translational, vibrational, and rotational partition functions  $q$  that require the knowledge of the structure of the complex (rotational contribution) and the vibrational frequencies of the reactants and products,

$$H = \int_0^T C_p dT = RT^2 \frac{d}{dT} \ln(q) \quad (3.33)$$

and

$$S = RT \frac{d}{dT} \ln(q) + R \ln(q). \quad (3.34)$$

Evaluating Equations 3.33 and 3.34 leads to the following translational, vibrational, and rotational contributions to the reaction enthalpy and reaction entropy,

$$H_{\text{trans}} = \frac{5}{2}RT \quad (3.35)$$

and

$$S_{\text{trans}} = R \ln \left[ \left( \frac{2\pi}{h^2} \right)^{3/2} \frac{(k_B T)^{5/2}}{p^0} e^{5/2} m^{3/2} \right]. \quad (3.36)$$

$S_{\text{trans}}$  is calculated for a gas in its standard state with the mass  $m$  of the gas in kilogram, the Boltzmann constant  $k_B$ , the Planck constant  $h$ , and the standard pressure  $p^0$ .

The vibrational reaction enthalpy and entropy are given by

$$H_{\text{vib}} = RT \sum_{i=1}^n \frac{\Theta_i}{T} \frac{\exp(-\Theta_i/T)}{[1 - \exp(-\Theta_i/T)]} \quad (3.37)$$

and

$$S_{\text{vib}} = -R \sum_{i=1}^n \ln[1 - \exp(-\Theta_i/T)] + R \sum_{i=1}^n \frac{\Theta_i}{T} \frac{\exp(-\Theta_i/T)}{[1 - \exp(-\Theta_i/T)]}, \quad (3.38)$$

where  $\Theta_i = hv_i/k_B$  contains the normal frequencies  $\nu_i$  of the molecule.

Finally, the rotational enthalpy and entropy for a linear and nonlinear molecule are

$$\begin{aligned} H_{\text{rot}}^{\text{linear}} &= RT, \\ H_{\text{rot}}^{\text{nonlinear}} &= \frac{3}{2}RT \end{aligned} \quad (3.39)$$

and

$$\begin{aligned} S_{\text{rot}}^{\text{linear}} &= R \left[ \ln \left( \frac{8\pi^2 I k_B T}{\sigma h^2} \right) + 1 \right], \\ S_{\text{rot}}^{\text{nonlinear}} &= R \left\{ \ln \left[ \frac{8\pi^2}{\sigma h^3} (2\pi k_B T)^{3/2} \sqrt{I_A I_B I_C} \right] + \frac{3}{2} \right\}, \end{aligned} \quad (3.40)$$

where  $I$  is the moment of inertia of a linear molecule,  $I_A$ ,  $I_B$ , and  $I_C$  are the moments of inertia of a nonlinear molecule and  $\sigma$  is the rotational symmetry number.

To obtain the reaction enthalpy  $\Delta H_T^0$  and entropy  $\Delta S_T^0$  of the reaction 3.27 the Equations 3.35-3.40 were applied for the reactants and products. As previously mentioned, this requires information about few molecular parameters as structure of reactants and products, moments of inertia, vibrational frequencies and bond lengths. The required parameters were available from first principles calculations for all systems investigated by this method in the



present work.

Finally, the calculated  $\Delta G^0$  vs  $T$  curve was varied until the line matched the experimental data points by adjusting the  $\Delta H_0^0$  value. The statistical mechanicals calculations of  $\Delta G^0$  was applied in this way in order to extract the binding energies of CO to pure and binary silver-gold cluster trimers presented and discussed in detail in the Chapter 4 of the present work.

### 3.4 Computational methods

The *ab initio* calculations presented in this thesis were carried out in the group of Prof. Bonačić-Koutecký. In this section just a few information concerning the functionals employed to extract structural and energetically information will be presented. For more details, see Reference.<sup>171</sup>

The structural properties of the cationic  $\text{Ag}_n\text{Au}_m(\text{CO})_q^+$  ( $n + m = 3, 5$ ) clusters were determined using density functional theory (DFT) with the hybrid B3LYP functional.<sup>172-175</sup> For gold and silver atoms a triple-zeta-valence-plus-polarization (TZVP) atomic basis sets combined with 19-electron relativistic effective core potential (19e-RECP) were employed.<sup>176,177</sup> For the carbon and oxygen they used the TZVP atomic basis sets.<sup>178</sup> All structures presented are fully optimized using gradient minimization technique and stationary points were characterized as minima by calculating the vibrational frequencies.

In order to find out whether the choice of the functional influences the results, in addition, the accuracy of B3LYP functional has been investigated by comparison with the non-hybrid BP86<sup>172,179</sup> and hybrid B3PW91<sup>172,173,180-184</sup> functional. Moreover, the single point calculations using DFT structures were carried out with the more accurate wave function based coupled cluster singles doubles (CC-SD) method. The latter can serve as a bench mark for DFT calculation.

### 3.5 Femtosecond photodissociation processes and data acquisition method

After the production and mass selection of the desired cluster size (for details see Section 3.1) the monodispersed cluster beam was further directed into the octopole ion trap where the clusters reacted with different reactive gases (here  $\text{C}_6\text{H}_6$  or  $\text{CH}_3\text{Br}$ ). During the storage time, the clusters and their reaction products continuously experienced the irradiation with a laser beam of an appropriate wavelength which was assumed to induce photodissociation of the cluster-molecule complexes. Alternatively, through a computer control mechanical shutter, the laser beam was admitted into the trap only for a defined time, i.e. smaller than the storage time. The resulting photodissociation reaction products were analyzed by the second quadrupole mass

selector ( $Q_3$ ) and detected by means of a channeltron detector as described in the Section 3.1. By measuring the product ion mass spectra with and without laser irradiation the possible photoinduced dissociation channels of the cluster-molecule complexes reaction were investigated.

In order to perform time resolved photodissociation investigations the amplified laser beam was split and 60% intensity was used to seed two OPAs (just one was used in the present experiments) to yield tunable light between 235-3000 nm, whereas the remaining 40% intensity was frequency-doubled in a beta barium borate (BBO) crystal. The two beams were time-delayed with respect to each other by guiding one beam on a computer-controlled delay stage. The recombined fs-laser beams were finally guided into the vacuum chamber in a direction collinear with the mass spectrometer and the ion trap axis (see Figure 3.1) and were slightly focused by a 1 m focal length lens mounted in front of the vacuum apparatus.

Cross-correlation of the pump and probe laser pulses was measured *in situ* by recording the two-photon photoemission current on a polycrystalline gold surface (gold plate) to determine the zero delay time of the experiment. The gold plate was positioned in front of the octopole entrance lens (see Figure 3.1) through a linear translator. By means of a picoammeter (Keithley Instruments, Model 617) connected to the gold plate the current of the positive charges on the gold plate was measured as a function of the delay time between the two laser pulses. Since gold has a work function of 5.2 eV,<sup>185</sup> a single ultraviolet photon having energy

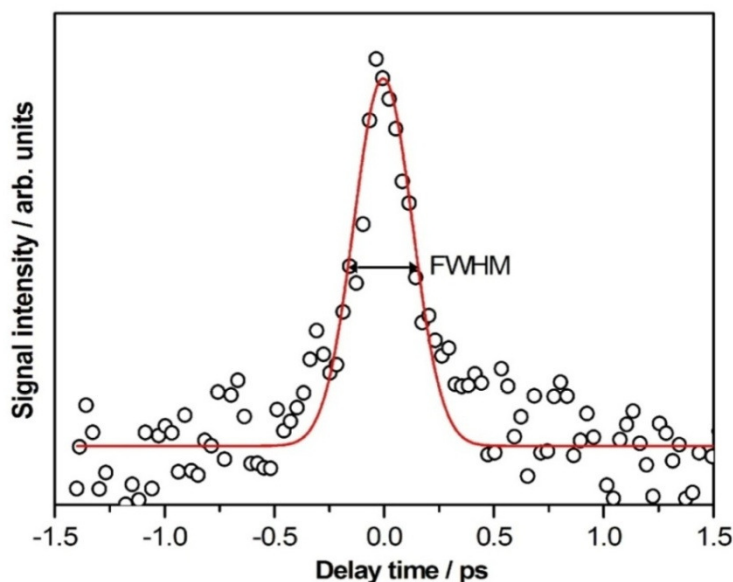


**Figure 3.5:** The cross-correlation trace of the pump and the probe pulse measured by recording the photoemission from a gold plate. The open circles represent the experimental data while the solid line represents a Gaussian fit to the measured signal. The experimental parameters were  $\lambda_{\text{Pump}} = 353 \text{ nm}$  ( $P_{\text{Pump}} = 4.4 \text{ mW}$ ) and  $\lambda_{\text{Probe}} = 393 \text{ nm}$  ( $P_{\text{Probe}} = 2.9 \text{ mW}$ ). The FWHM depicted in the figure by an arrow has a value of 330 fs

of about 3.5 eV is not sufficient in order to extract photoelectrons from the gold plate. In contrast, the contributions of the two laser pulses arriving simultaneously on the gold plate facilitate the photoelectron emission.

The zero delay time represents the temporal superposition of the two laser pulses, i.e. the time when the pump and the probe laser pulses arrive simultaneously on the sample.

The temporal dependence of the intensity of the positive charge current measured on the gold plate gave the autocorrelation function between the pump and the probe laser pulses:

$$I(\tau) = \int_{-\infty}^{+\infty} |E(t) + E(t - \tau)|^2 dt, \quad (3.41)$$

where  $I(\tau)$  represents the measured current intensity,  $\tau$  is the delay time between the two laser pulses,  $E(t)$  and  $E(t - \tau)$  represent the time-dependent profile of the electrical field of the pump and probe pulse, respectively. The correspondence between the full width at half maximum (FWHM) determined from the measured autocorrelation curve ( $\Delta\tau$ ) and the FWHM of the laser pulse ( $\Delta t$ ) is given by the expression:

$$\Delta t = \frac{\Delta\tau}{K} \quad (3.42)$$

where  $K$  represents the autocorrelation factor, and has for a Gaussian shape of the laser pulses a value of 1.414 (see Table 2.5).

Figure 3.5 shows the cross-correlation trace obtained by gold plate photoemission in the case of two-color pump-probe experiment. The wavelengths of the pump and probe pulses were 353 and 393 nm, respectively.

As can be seen in Figure 3.5, the measured full width at half maximum (FWHM) for this autocorrelation trace has a value of about 330 fs. Considering Equation 3.42, where  $\Delta\tau = 330$  fs and assuming a similar temporal length and a Gaussian shape ( $K = 1.414$ ) for both laser pulses, the duration of the laser pulse was calculated to be 233 fs. However, this cross correlation width is considerably larger than expected from the laser pulse width that was extrapolated from the amplifier output autocorrelation measurement to be about 80 fs (taking into account, certainly, the influence of all dispersive elements in the optical pathway). The temporal broadening can be attributed to two factors: (i) a power broadening due to the space charge repulsion effects induced by an excess in laser intensity used in this measurement, and (ii) the influence of the lifetime of the electronic state of the polycrystalline gold plate.<sup>186</sup>

Our experimental approach to investigate femtosecond reactions dynamics of metal cluster consisted in storing the mass-selected cluster ions in the rf-octopole ion trap prefilled with helium buffer gas and small partial pressures of reactant gases. The trap acted like a tube for gas phase reaction dynamics studies. The upper part of Figure 3.6 displays a schematic

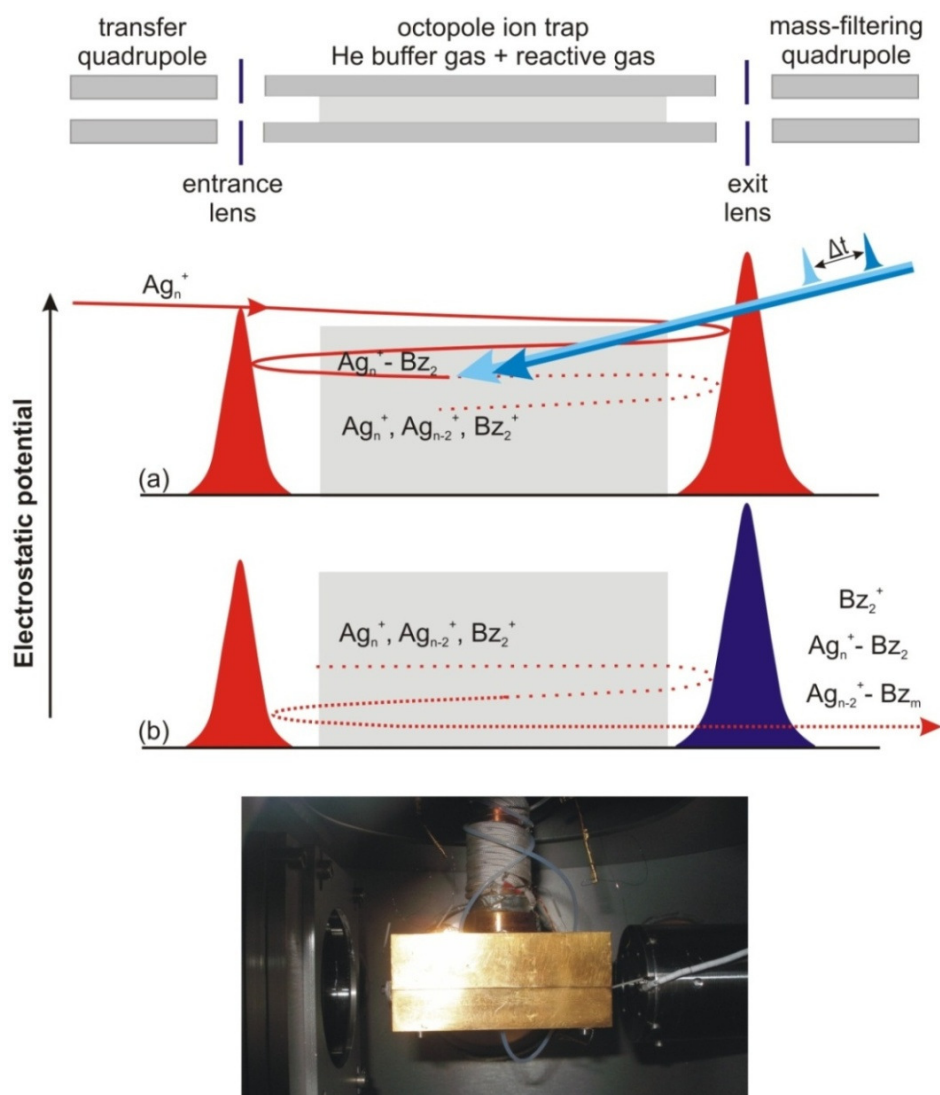


**Figure 3.6:** Upper part: Scheme of the gas phase apparatus. Center: Illustration of the cluster cooling trapping inside the octopole ion trap, as well as the laser interaction during the photodissociation CT experiment. (a) The silver clusters were admitted to the trap, reacted to form  $\text{Ag}_n\text{-Bz}_2^+$  cluster-molecule complexes and continuously experienced the interaction with the laser beam. The first laser pulse (pump pulse) was assumed to induce the excitation of the cluster-molecule complex in an excited CT electronic state. After a given delay time, the second laser pulse (probe pulse) ionized the neutral clusters. (b) The photo-products, initial cluster and their fragments, further reacted with the benzene molecule present in the trap and were then extracted by applying a negative potential on the exit octopole lens. Lower part: View into the rf-ion trap chamber.

sketch of the quadrupole, octopole device arrangements. The central part of the Figure 3.6 schematically illustrate the process of trapping inside the octopole ion trap, as well as the laser induced charge transfer process of the photodissociation CT experiment. During the storing time the cluster-molecule complexes continuously experienced the interaction with the laser beams. The first laser pulse (pump pulse) was assumed to induce the excitation of the cluster-molecule complex in an excited CT electronic state in which the metal cluster and its molecular ligand separate with the charge remaining on the neutral organic molecule (benzene dimer in the present case). After a certain delay time, the second laser pulse (probe pulse) ionized the neutral clusters. The positively charged products were expelled from the octopole ion trap by applying an electrostatic field, and the ion signals were measured as a function of the delay time between the pump and the probe pulse by using a picoammeter (Keithley Instruments, Model 617). A *LabView*-program, developed for this purpose, averaged ten values of the measured cluster current for every value of the delay time.

In the lower part of Figure 3.6 a view into the rf-ion trap chamber is presented. The octopole enclosure is visible in the center of the image.



# 4

## CO binding energies to $\text{Ag}_n\text{Au}_m^{+/-}$ ( $n+m = 3$ ). Tuning cluster reactivity by charge state and composition\*

---

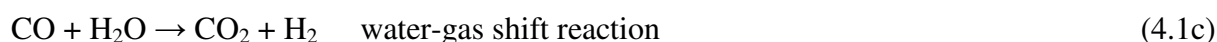
*Temperature dependent gas phase reaction kinetics measurements under multi-collision conditions and ab initio DFT calculations were employed to determine the binding energies of carbon monoxide to triatomic silver-gold binary cluster cations and anions. The binding energies of the first CO molecule to the trimer clusters increase with increasing gold content and with changing charge from negative to positive. Thus, the reactivity of the binary clusters can be sensitively tuned by varying charge state and composition. Also multiple CO adsorption on the clusters was investigated. The maximum number of adsorbed CO was found to strongly depend on cluster charge and composition as well. Most interestingly, the cationic carbonyl complex  $\text{Au}_3(\text{CO})_4^+$  is formed at cryogenic temperature whereas for the anion only two CO are adsorbed leading to  $\text{Au}_3(\text{CO})_2^-$ . All other trimer clusters adsorb three CO in case of the cations and are completely inert to CO in our experiment in case of the anions.*

---

\* The contents of this chapter have been accepted as a contribution to *The Journal of Physical Chemistry A*: D. M. Popolan, M. Nöbller, R. Mitrić, T. M. Bernhardt, V. Bonačić-Koutecký, "Tuning cluster reactivity by charge state and composition: Experimental and theoretical investigation of CO binding energies to  $\text{Ag}_n\text{Au}_m^{+/-}$  ( $n+m = 3$ )".

## 4.1 Introduction

The oxidation of carbon monoxide by molecular oxygen (reaction Equation 4.1a) is efficiently catalyzed at surprisingly low temperatures by gold nano-clusters supported on metal oxides<sup>70,72,80,187</sup> or support-free in the gas phase.<sup>66,118</sup> A great deal of research has been devoted to the revelation of molecular details of the gold cluster reaction mechanism, in order to be able to predict further potential catalytic reactions in which gold containing catalysts could be of use.<sup>188</sup> Equations 4.1b and 4.1c present two additional reactions of CO that are of enormous fundamental as well as economical interest.



One of the key quantities necessary to assess and to predict the reactivity of CO, if these reactions are to be catalyzed by nano-clusters, is the binding energy of CO molecules to small gold clusters as well as its dependence on cluster size, charge state and potential ‘dopant’ atoms in binary clusters (here silver-gold binary clusters). However, only very few quantitative experimental binding energy data and systematic charge state dependent investigations are available so far. Gas-phase studies of isolated metal clusters might presumably never account for the precise mechanisms, energetics, and kinetics operating in applied catalysis, as stated in a recent review.<sup>120</sup> Yet, such investigations can provide a valuable conceptual framework and an efficient tool to obtain direct insight into reactivity patterns.

Reactions of carbon monoxide with free gold, silver, and binary silver-gold clusters have been investigated by various groups, experimentally<sup>106,108,109,111,112,114,153,189-199</sup> as well as theoretically.<sup>200-207</sup> Experimental CO binding energy data have been obtained so far only for  $\text{Au}(\text{CO})^+$ ,<sup>208</sup>  $\text{Au}_n(\text{CO})^+$  ( $n = 5-65$ ),<sup>111</sup>  $\text{Au}_3(\text{CO})^-$ ,<sup>113</sup>  $\text{Ag}_n\text{Au}_m(\text{CO})^+$  ( $n + m = 5-6$ ,  $m \geq 3$ ),<sup>112</sup>  $\text{Ag}_n\text{Au}_m(\text{CO})_q^+$  ( $n + m = 5$ ,  $m < 3$ ,  $q = 1-5$ ),<sup>121</sup>  $\text{Ag}(\text{CO})_q^+$  ( $q = 1-4$ ),<sup>209</sup> and  $\text{Ag}_5(\text{CO})_q^+$  ( $q = 1-7$ ).<sup>121</sup>

In the present chapter we investigate the smallest cluster size that exhibits multiple vibrational degrees of freedom, the trimer. The focus of our joint experimental and theoretical investigation is on the influence of the charge state of the cluster and its composition in binary silver-gold clusters on the interaction with CO reflected in the binding energies. Interestingly, experimental studies of CO oxidation over Au-Ag alloy catalysts supported on mesoporous aluminosilicates, demonstrate the synergetic effect of combining Au and Ag; Ag was found to activate  $\text{O}_2$  while Au was found to adsorb CO.<sup>210</sup>

We employ gas phase reaction kinetic measurements in the ion trap in conjunction with Rice-Ramsperger-Kassel-Marcus (RRKM) statistical reaction rate theory as well as thermodynamic equilibrium method to obtain experimental binding energy values and com-



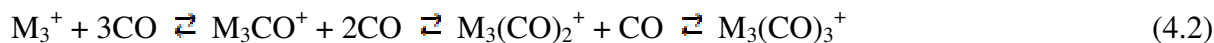
pare these to theoretical data resulting from *ab initio* Density Functional Theory (DFT) simulations. Furthermore, we discuss the implications of the observed trends in the binding energies on potential coadsorption mechanisms leading to reactions in Equations 4.1a to 4.1c.

## 4.2 Results

### 4.2.1 Gas phase reaction kinetics and CO binding energies

Figure 4.1 displays the reactant and product ion concentrations as a function of the reaction time for the positively charged trimers  $\text{Ag}_3^+$  and  $\text{Ag}_2\text{Au}^+$  at two different temperatures.  $\text{Au}_3^+$ , in contrast, reacted completely within the first 500 ms, even at room temperature, so that no reasonable reaction kinetics could be obtained in this case. For  $\text{AgAu}_2^+$ , our cluster source did not provide sufficient signal to obtain kinetic measurements. The anion clusters  $\text{Ag}_3^-$ ,  $\text{Ag}_2\text{Au}^-$ , and  $\text{AgAu}_2^-$  have been shown previously to be completely non-reactive toward CO under the reaction conditions in our ion trap.  $\text{Au}_3^-$  reacted with CO at cryogenic temperatures and the corresponding kinetics have been obtained in our experimental setup as reported in a recent contribution.<sup>113</sup>

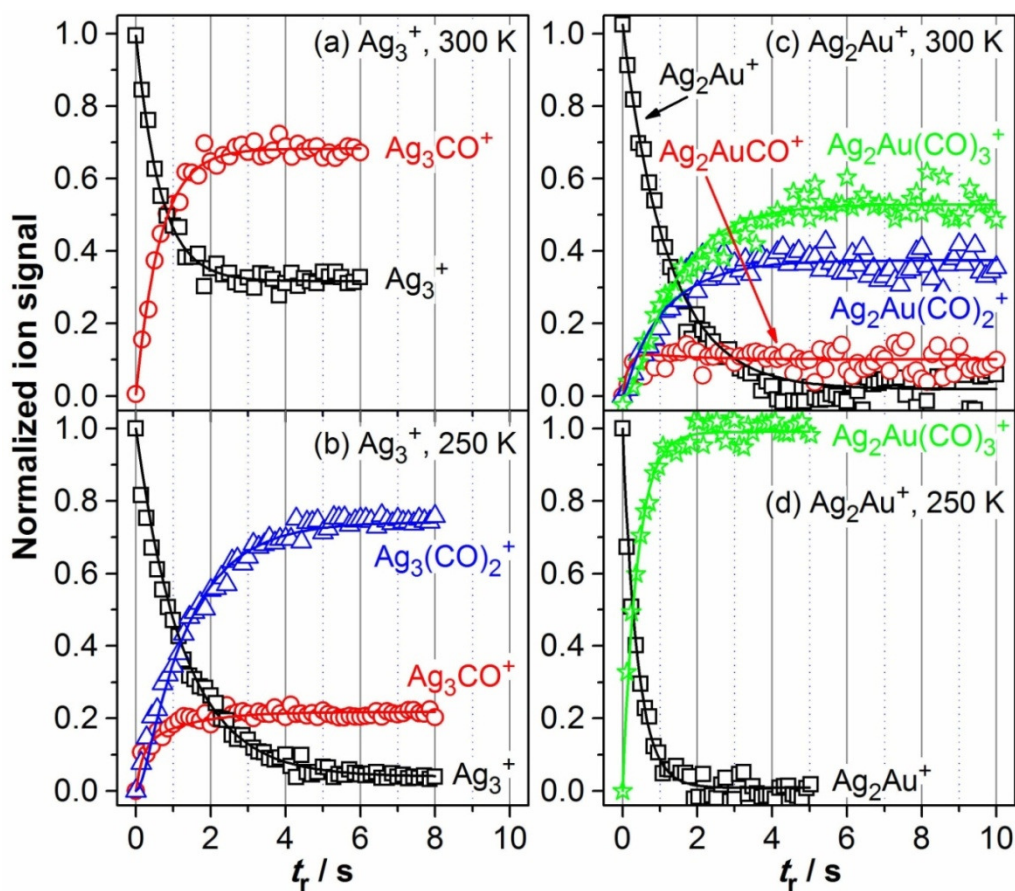
The solid lines in Figure 4.1 have been obtained for both trimers,  $\text{Ag}_3^+$  and  $\text{Ag}_2\text{Au}^+$ , by fitting of a sequential CO association reaction mechanism to the experimental data:



The rates of all observed association reactions increased with decreasing temperature in accordance with the Lindeman energy transfer mechanism for association reactions (see Section 3.2).

$\text{Ag}_3\text{CO}^+$  was the only detected reaction product of  $\text{Ag}_3^+$  at 300 K (see Figure 4.1a). At 250 K, the adsorption of a second CO could be observed (Figure 4.1b).  $\text{Ag}_2\text{Au}^+$  was considerably more reactive than  $\text{Ag}_3^+$ . Already at 300 K the reaction products  $\text{Ag}_2\text{AuCO}^+$ ,  $\text{Ag}_2\text{Au}(\text{CO})_2^+$ , and  $\text{Ag}_2\text{Au}(\text{CO})_3^+$  could be detected (Figure 4.1c). At a reaction temperature of 250 K (Figure 4.1d), the reaction proceeded already so fast that the intermediate products  $\text{Ag}_2\text{AuCO}^+$  and  $\text{Ag}_2\text{Au}(\text{CO})_2^+$  could not be resolved anymore on the time scale of our experiment, but only  $\text{Ag}_2\text{Au}(\text{CO})_3^+$  was detected. Nevertheless, the adsorption of the first CO molecule represented the rate-determining step. Thus, the rate constant obtained from the fitting procedure corresponds to the formation of  $\text{Ag}_2\text{AuCO}^+$ .

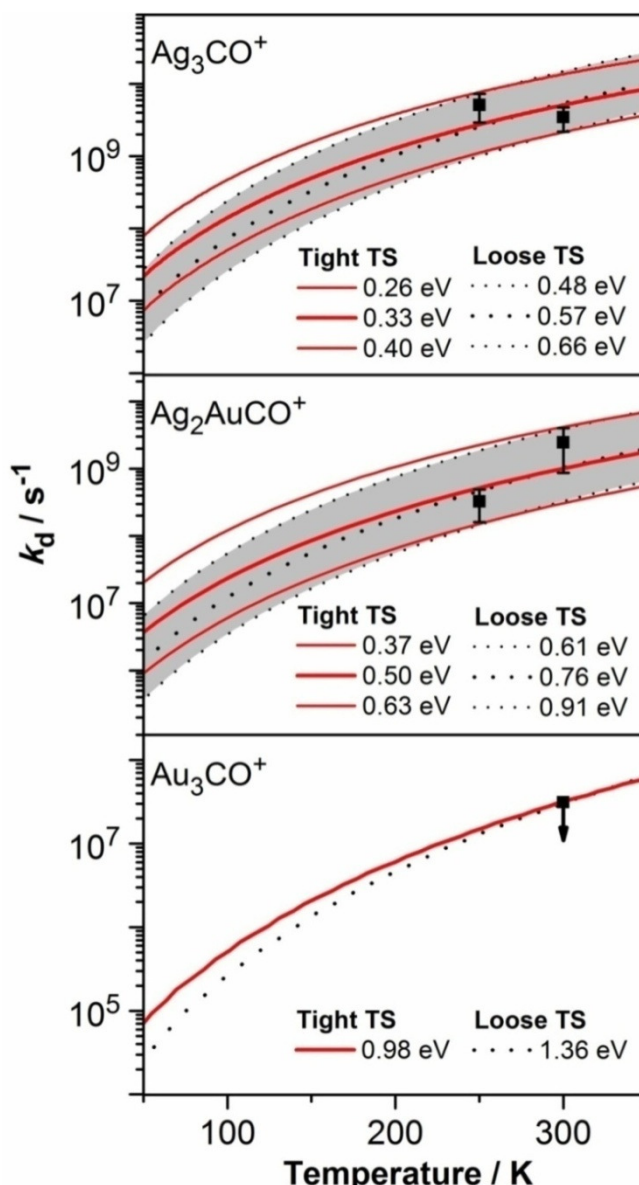
The unimolecular decomposition rate constants  $k_d$  of the CO adsorption reactions were calculated according to Equations 3.3 and 3.8 from the pseudo first-order rate constants  $k$ , which were obtained in the fitting procedure (cf. Section 3.2). To determine the binding energies, the unimolecular decomposition rate constants  $k_d$  were simulated as a function of the temperature employing RRKM theory (see Section 3.2). Figure 4.2 displays the experimental-



**Figure 4.1:** Temperature dependent kinetics of the reactions of CO with  $\text{Ag}_3^+$  (a, b) and  $\text{Ag}_2\text{Au}^+$  (c, d) as a function of the reaction time  $t_R$  at 300 K (a, c) and at 250 K (b, d), respectively. The open symbols represent the experimental data, normalized to the initial metal cluster concentration and to the total ion concentration in the trap (black squares:  $M_3^+$ , red circles:  $M_3\text{CO}^+$ , blue triangles:  $M_3(\text{CO})_2^+$ , green stars:  $M_3(\text{CO})_3^+$ ). The solid lines are obtained by fitting the integrated rate equations of the proposed reaction mechanism (Equation (4.2)) to experimental data.

ly obtained reaction temperature dependent decomposition rate constants  $k_d$  together with the RRKM simulated  $k_d(T)$  curves for the two (“tight” and “loose”) TS models for  $\text{Ag}_3\text{CO}^+$ ,  $\text{Ag}_2\text{AuCO}^+$ , and  $\text{Au}_3\text{CO}^+$ , respectively. In addition to the best-fit RRKM  $k_d(T)$  curves which determined the binding energy  $E_b$ , also error limits of the binding energies have been estimated by varying  $E_b$ , to include all experimental  $k_d$  values. The errors of  $k_d$  given in Figure 4.2 include the standard deviation resulting from the fitting procedure to obtain  $k$  and errors in the measured gas pressure, which are considered to be  $\pm 0.01$  Pa according to the detection limit of the Baratron gauge. For a detailed discussion of the error analysis, please refer to Section 3.2.6 and Reference.113 In the case of  $\text{Au}_3\text{CO}^+$ , only an upper limit for  $k_d$  value at room temperature could be obtained from the experiment (see above).

The resulting binding energies for both, the “tight” and the “loose” TSs, are listed in



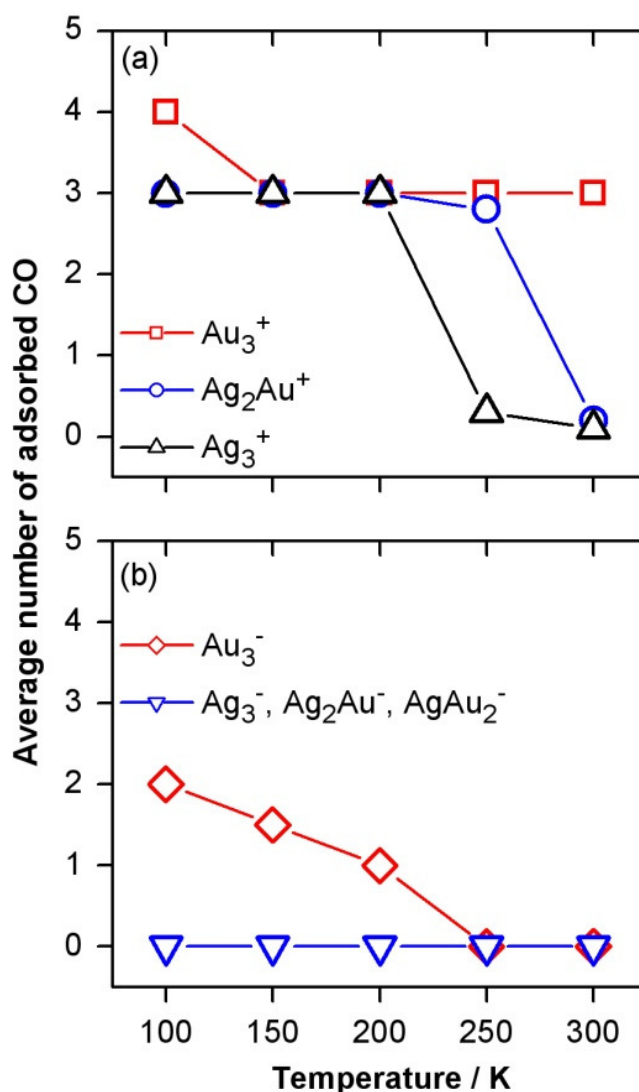
**Figure 4.2:** Experimental and RRKM decomposition rate constants  $k_d$  as a function of the temperature. Solid squares represent the experimentally obtained temperature dependent decomposition rate constants  $k_d$ . Red solid lines represent RRKM  $k_d(T)$  curves computed for different CO binding energies  $E_b$  for a “tight” transition state. Shown are the best fits to the experimental data (thick lines) and estimated upper and lower binding energy limits (thin solid lines). Black dotted lines represent RRKM  $k_d(T)$  curves computed for different CO binding energies  $E_b$  for a “loose” transition state. Shown are the best fit to the experimental data (thick dotted line) and estimated upper and lower binding energy limits (thin dotted lines, shaded area). The wiggles apparent in some of the RRKM  $k_d(T)$  curves are due to the stepwise calculation procedure required by the software and do not relate to a physical origin.

Table 4.1 together with the corresponding value of  $\text{Au}_3^-$  that had been reported previously.<sup>113</sup> Table 4.1 also displays experimental binding energies obtained from the thermodynamical equilibrium analysis (see Section 3.3) which are in good agreement with the RRKM-values and also with the theoretical binding energy data obtained by our *ab initio* calculations (also listed in Table 4.1 for all cluster compositions, charges, and CO coverages).

**Table 4.1:** Experimental and theoretical binding energies of CO to anionic and cationic cluster trimers as deduced by employing RRKM theory for “tight” and “loose” TSs, thermodynamic equilibrium method, and DFT *ab initio* simulations. The corresponding theoretical complex structures are given in the supplementary information.

Cluster complex	Theoretical binding energy $E_b$ (eV)	Experimental binding energy $E_b$ (eV)		Experimental binding energy $-\Delta H_0^0$ (eV)
		„tight“ TS	„loose“ TS	
$\text{Ag}_3\text{CO}^+$	0.69	$0.33 \pm 0.07$	$0.57 \pm 0.09$	$0.64 \pm 0.1$
$\text{Ag}_3(\text{CO})_2^+$	0.64	+	+	$0.58 \pm 0.1$
$\text{Ag}_3(\text{CO})_3^+$	0.58	+	+	
$\text{Ag}_2\text{AuCO}^+$	0.89	$0.50 \pm 0.13$	$0.76 \pm 0.15$	$0.81 \pm 0.1$
$\text{Ag}_2\text{Au}(\text{CO})_2^+$	0.78	+	+	$0.77 \pm 0.1$
$\text{Ag}_2\text{Au}(\text{CO})_3^+$	0.70	+	+	$0.73 \pm 0.1$
$\text{AgAu}_2\text{CO}^+$	1.25			
$\text{AgAu}_2(\text{CO})_2^+$	0.91			
$\text{AgAu}_2(\text{CO})_3^+$	0.84			
$\text{Au}_3\text{CO}^+$	1.34	$\geq 0.98$	$\geq 1.36$	
$\text{Au}_3(\text{CO})_2^+$	1.33	+	+	
$\text{Au}_3(\text{CO})_3^+$	0.98	+	+	
$\text{Au}_3(\text{CO})_4^+$	0.03	+	+	
$\text{Ag}_3\text{CO}$	0.47			
$\text{Ag}_2\text{AuCO}$	0.57			
$\text{AgAu}_2\text{CO}$	0.71			
$\text{Au}_3\text{CO}$	0.99			
$\text{Ag}_3\text{CO}^-$	0.07	-	-	-
$\text{Ag}_2\text{AuCO}^-$	0.16	-	-	-
$\text{AgAu}_2\text{CO}^-$	0.17	-	-	-
$\text{Au}_3\text{CO}^-$	0.33	$0.28 \pm 0.04^a$	$0.46 \pm 0.05^a$	
$\text{Au}_3(\text{CO})_2^-$	0.26	+	+	$0.28 \pm 0.1$

A „+“ indicates that no binding energy determination was possible via RRKM analysis, although the reaction product has been observed experimentally, a “-” indicates that no adsorption products of CO to this clusters were detected under our experimental conditions. For all other cluster complexes (neutral clusters and  $\text{AgAu}_2^+$ ) no adsorption CO measurements of CO could be performed for experimental reasons. <sup>a</sup> Reference 113.



**Figure 4.3:** (a) Average number of adsorbed CO molecules after a reaction time of  $t_r = 0.5$  s as a function of the reaction temperature  $T_R$  for (a) the cationic cluster trimers,  $\text{Ag}_3^+$ ,  $\text{Ag}_2\text{Au}^+$ , and  $\text{Au}_3^+$ , and (b) for the anionic cluster trimers  $\text{Ag}_3^-$ ,  $\text{Ag}_2\text{Au}^-$ ,  $\text{AgAu}_2^-$ , and  $\text{Au}_3^-$ . Note that  $\text{Ag}_3^-$ ,  $\text{Ag}_2\text{Au}^-$ , and  $\text{AgAu}_2^-$  do not react with CO.

#### 4.2.2 Temperature dependent CO coverage

The experimentally obtained average number of adsorbed CO molecules as a function of the reaction temperature is shown in Figure 4.3 for all investigated cationic (Figure 4.3a) and anionic (Figure 4.3b) cluster trimers at a fixed reaction time of 500 ms. As can be seen from Figure 4.3a,  $\text{Au}_3^+$  rapidly reacted with three CO molecules already at room temperature (similar results have been obtained in a flow tube reactor experiment<sup>114</sup>) and adsorbed one more CO at 100 K. In contrast,  $\text{Ag}_3^+$  hardly reacted at all with CO at 300 K. Upon cooling, sequential adsorption of up to three CO molecules was observed.  $\text{Ag}_2\text{Au}^+$  exhibited an intermediate behavior between the gold and silver clusters.

In our ion trap measurements, no reaction products of  $\text{Au}_3^-$  with CO were detected at temperatures of 250 K and above.<sup>113,211</sup> The apparently weak binding of CO to  $\text{Au}_3^-$  is in agreement with earlier room temperature experiments, in which the size dependent reactivity of  $\text{Au}_n^-$  with CO was investigated and no gold anion carbonyl clusters were observed for  $n < 4$ .<sup>108,109,197</sup> Cooling of the rf-ion trap below 250 K lead to the formation of  $\text{Au}_3\text{CO}^-$  and at lower temperatures a maximum adsorption of two CO molecules was observed (Figure 4.3b).

$\text{Ag}_3^-$  as well as the binary silver-gold clusters  $\text{Ag}_2\text{Au}^-$  and  $\text{AgAu}_2^-$  were found to be non-reactive toward carbon monoxide over the whole available temperature range from 100 to 300 K (represented by the symbols -∇- in Figure 4.3b).<sup>110,198</sup>

### 4.3 Discussion

The aim of this discussion is to compare the trends in the experimental and theoretical CO binding energies to the binary silver-gold clusters as well as to illustrate the origin of the composition and charge state dependent reactivity.

No experimental binding energy data are hitherto available for the silver-gold binary trimers (only the CO binding energy to  $\text{Au}_3^-$  has been reported by our group earlier<sup>113</sup>). The previously predicted theoretical  $E_b$  values for  $\text{Au}_3\text{CO}^-$  (0.76 eV<sup>201</sup> and 0.96 eV<sup>212</sup>) are considerably higher than our RRKM and DFT data presented here (cf. Table 4.1). Notice, that in order to obtain accurate values for binding energies in the framework of DFT, a careful choice of the appropriate density functional as well as of the atomic basis sets and effective core potentials are needed to be made. With the proper choice of the functional and AO basis the expected errors of the binding energies should not be larger than 0.15 eV.<sup>213</sup> The theoretical value of 0.33 eV for the CO binding energy in  $\text{Au}_3\text{CO}^-$  that has been obtained in the present study is in much better agreement with the experimental value. In the case of the cationic carbonyl  $\text{Au}_3\text{CO}^+$ , our experimental RRKM data ( $\geq 1.36$  eV for the loose TS) and also the present calculated binding energy value (1.34 eV) agree well with the calculated value reported by Neumaier et al.<sup>111</sup> (1.36 eV), while the value reported by Wu et al.<sup>201</sup> (1.81 eV) seems to overestimate the binding energy of CO to the cationic gold cluster. For neutral species, only the theoretical values have been reported in the literature,<sup>207</sup> showing the general trend of increasing binding energies with increasing gold content.

A plot of the experimental and theoretical binding energies of one CO molecule to all investigated cationic, neutral and anionic triatomic clusters is shown in Figure 4.4. Only the experimental results obtained using the “loose” TS are displayed in Figure 4.4 because this TS represents the more realistic model for simple straight forward association reactions.<sup>113</sup> All of the experimental values are in good agreement with the theoretical data obtained in the current study. In general, as expected, the binding energies decrease from cationic to neutral to anionic species (cf. Figure 4.4 and Table 4.1).

The highest CO binding energy was obtained for the pure gold cluster cation  $\text{Au}_3^+$ . An



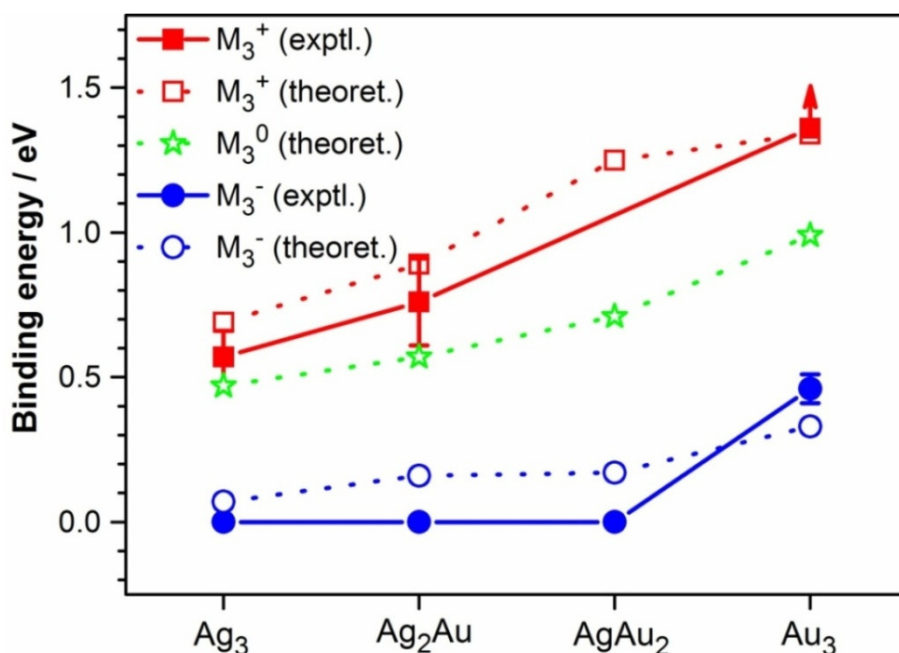


**Figure 4.4:** Plot of experimental (exptl.) and theoretical (theoret.) binding energies of CO to the cluster trimers as a function of the cluster charge and composition. For the cation and anion clusters the experimental binding energies obtained in this work by RRKM analysis employing a “loose” TS model are plotted. Lines are drawn to guide the eye.

increasing silver content decreased the CO binding energy, in accordance with previous observations,<sup>112,121</sup> as did a change in the charge state. For the cationic clusters the CO binding energy decreases almost linearly from  $\text{Au}_3^+$  to  $\text{Ag}_3^+$ , whereas for the anionic trimers only  $\text{Au}_3^-$  was observed to associate with CO at all.

The bonding of CO to the metal clusters of different composition can be qualitatively understood based on the energy differences between the valence orbitals of the different clusters. The CO molecule binds to metal clusters via an interplay between a charge donation from the  $\sigma^*$  orbitals of CO to the lowest unoccupied molecular orbital (LUMO) of the metal cluster and a  $\pi$  back-donation from the metal cluster d orbitals into the  $p\pi^*$  orbitals of CO.<sup>106,196,214</sup> The distinct reactive behavior of the gold clusters in contrast to the silver clusters can be generally attributed to relativistic effects present in gold. Qualitatively, the relativistic effects include the contraction and stabilization of the s and p shells, as well as an expansion and destabilization of the d atomic orbitals.<sup>208,215</sup> This latter is an indirect effect due to more efficient screening by the contracted s and p shells and leads to a narrowing of the s-d energy gap in Au compared to Ag. Exactly this effect manifested in the destabilization of the gold d orbitals would be expected to increase their availability for  $\pi$  back-donation in gold cluster association complexes resulting in the larger CO binding energies. In contrast, in silver clusters, the d orbitals are located energetically much deeper below the s orbitals than in gold and are thus unfavorable for a  $\pi$  back-donation.

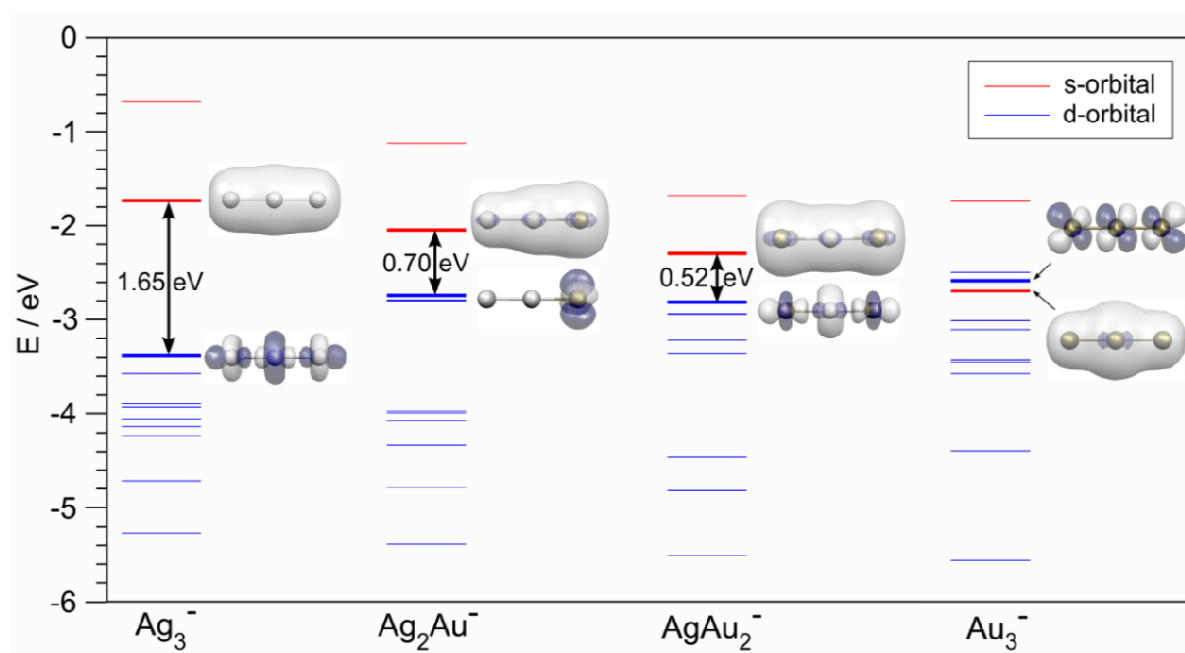


**Figure 4.5:** Schematic Kohn-Sham-MO energy diagrams for  $\text{Ag}_3^-$ ,  $\text{Ag}_2\text{Au}^-$ ,  $\text{AgAu}_2^-$  and  $\text{Au}_3^-$  showing the closing of the s-d energy gap with increasing gold content. The s-d energy gap is indicated by an arrow. Also depicted are the Kohn-Sham MOs corresponding to the respective s- and d-levels.

To quantitatively investigate this argument, the discrete energy levels of the negatively charged trimer clusters of different composition obtained in the present DFT study were compared. As can be seen from Figure 4.5, in the case of  $\text{Au}_3^-$  there is no s-d energy gap present and d orbitals lie even above the lowest s-type MO. By replacing only one Au atom by an Ag atom, the situation changes already dramatically and an s-d energy gap of 0.52 eV is created. By increasing the silver content the gap becomes larger, as expected (cf. Figure 4.5). In the case of the anionic trimers, thus apparently already one silver atom is sufficient to render the metal cluster d orbitals energetically unavailable for CO  $\pi$  back-donation. While the  $\pi$  back-donation depends on the energetic position of the d-orbitals which is determined by the composition for the silver-gold binary clusters, the charge state is assumed to be decisive for the contribution of  $\sigma$  donation in the CO bonding to the noble metal clusters. Electron donation from the  $\sigma$ -orbital of CO to the cluster LUMO will provide only a slightly attractive interaction in the case of anions,<sup>106</sup> which is however expected to increase considerably when going to the neutral or even cationic clusters. This explains qualitatively the observation reported in Figure 4.4 and Table 4.1 that the CO binding energies consistently decrease for all cluster compositions from positive to neutral to negative clusters. Thus, the cluster charge state may be used to coarse-tune the cluster chemical reactivity of the binary silver gold clusters whereas the composition might help to fine-tune chemical interaction.

Concerning the three C1 reactions of CO that have been introduced above (Equations 4.1), it is important to note that  $\text{O}_2$  represents an electron acceptor, whereas  $\text{H}_2$  and  $\text{H}_2\text{O}$  are



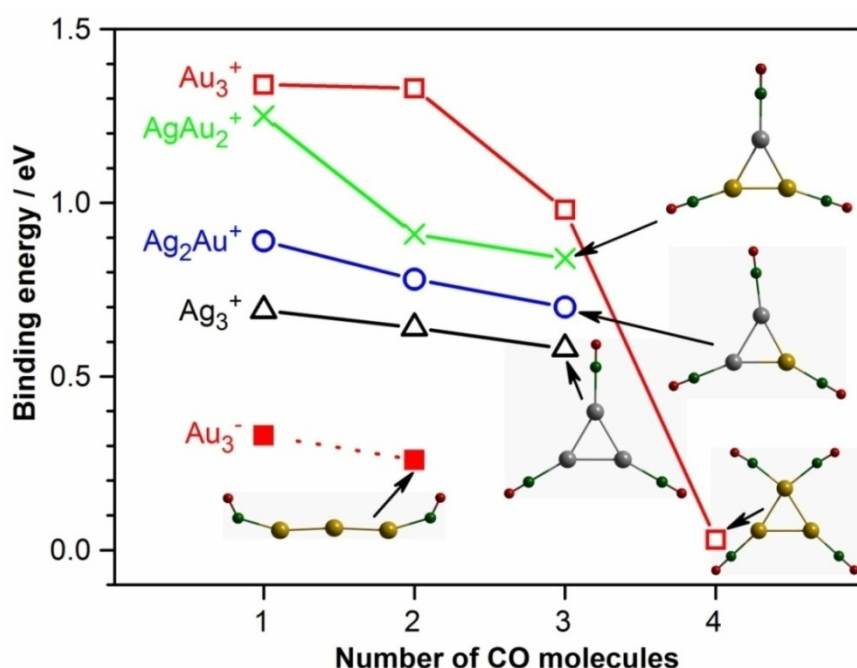


**Figure 4.6:** Plot of the calculated DFT binding energies as a function of the number of adsorbed CO molecules. The lines are drawn as guide to the eye. Also shown are the calculated lowest energy structures of selected carbonyl complexes. Yellow spheres: gold atoms; gray spheres: silver atoms; green spheres: carbon atoms; red spheres: oxygen atoms. More detailed structural information is given in the supplementary material.

generally regarded as electron donating ligands in the context of noble metal cluster binding.<sup>216</sup> The potential prediction of coadsorption effects of CO with these ligands is thus important to the investigation of potential cluster catalytic reactions.<sup>115,170,199</sup> Indeed, previous experiments, in which  $\text{Au}_3^-$  was exposed to a mixture of  $\text{O}_2$  and CO in the ion trap at 100 K demonstrated the importance of cooperative co-adsorption effects.<sup>211</sup> Unexpectedly, the coadsorption products  $\text{Au}_3(\text{CO})\text{O}_2^-$  and  $\text{Au}_3(\text{CO})(\text{O}_2)_2^-$  were observed. This is even more surprising as  $\text{O}_2$  did not react with bare  $\text{Au}_3^-$  clusters at any reaction temperature. The adsorption of the CO onto  $\text{Au}_3^-$  thus seemed to cooperatively modify the cluster complex electronic structure in a way that makes it able to react with the electron acceptor  $\text{O}_2$ .<sup>66,211</sup> In the case of  $\text{Au}_2^-$ , even a full thermal catalytic cycle of CO oxidation by molecular oxygen could be revealed.<sup>118,200,217</sup>

With molecular oxygen being an electron acceptor  $\text{Au}_3^+$  (such as all positively charged gold clusters<sup>115</sup>) was found to be completely non-reactive toward  $\text{O}_2$ . In addition, CO binds strongly to  $\text{Au}_3^+$  (see Table 4.1) rendering its reaction with coadsorbed molecules difficult. Indeed, the common presence of CO and  $\text{O}_2$  inside the ion trap did not change the initial carbonyl mass spectra, i.e., no coadsorption products could be identified for any reaction temperature or amounts of reactive gases.

In contrast, to bind and to activate the electron donor ligands  $\text{H}_2$  and  $\text{H}_2\text{O}$ , positively charged clusters are required<sup>115</sup> (in fact,  $\text{H}_2$  and  $\text{H}_2\text{O}$  do not bind at all to negatively charged gold clusters<sup>102,218</sup>). Yet, CO is strongly bound to  $\text{Au}_3^+$ , which might hamper the reactions (4.1b) and (4.1c) to proceed on this cluster ion. This impediment could probably be debarred by changing the cluster composition. An additional lowering of the CO binding energy is to be expected from charge donation of  $\text{H}_2$  or  $\text{H}_2\text{O}$  to the metal cations.<sup>115</sup> Future coadsorption experiments with CO in this laboratory will be directed along this line.

Figure 4.6 compares the computed binding energies for multiple CO adsorption onto pure and binary silver-gold cluster ions. The binding energy decreases only slightly with increasing number of CO ligands, except for the case of  $\text{Au}_3^+$  where the third and in particular the fourth CO binding energies are considerably reduced. This is well in accordance with the experimental observation that the addition of the fourth CO molecule to  $\text{Au}_3^+$  could only be detected at 100 K. Also in Figure 4.6, the lowest energy saturated carbonyl structures are displayed that have been obtained by the *ab initio* DFT calculations. The CO molecules were found to always bind in a  $\mu_1$ -atop position. In contrast to  $\text{Au}_3^+$  that formed a complex with four CO at cryogenic temperatures,  $\text{Au}_3(\text{CO})_4^+$ , the corresponding anion adsorbed at maximum two CO leading to  $\text{Au}_3(\text{CO})_2^-$ . All other trimer clusters that yielded carbonyl complexes adsorbed a maximum of three CO.

## 4.4 Conclusion

We presented a joint experimental and theoretical investigation of the charge state and composition dependent binding energies of CO to binary silver-gold clusters focusing on the most easily accessible multi-mode system with three atoms. Gas phase ion trap reaction kinetics and *ab initio* DFT calculations were able to reveal clear additive trends in the CO binding strength which provide a means to tune chemical reactivity by changing silver content and charge state in gold clusters.

## 4.5 Outlook

The implications of such reactivity tuning on selected reactions of CO catalyzed by small silver-gold clusters is discussed. In particular, it is proposed that the coadsorption and potential reaction of electron donor ligands (like  $\text{H}_2$  and  $\text{H}_2\text{O}$ ) with CO might be enabled through careful adjustment of the silver content of positively charged gold clusters in the clusters. Experiments and calculations are currently in progress in our laboratories to investigate such coadsorption reactions on binary silver-gold clusters.

## 4.6 Supplementary information

**Figure S1:** Plots of the experimental Gibbs free energy,  $\Delta G_T^0$ , vs. temperature for the CO adsorption reaction on (a)  $\text{Ag}_3^+$ , (b)  $\text{Ag}_2\text{Au}^+$ , and (c)  $\text{Au}_3^-$ .  $q$  denotes the number of adsorbed CO molecules. Solid lines are the calculated  $\Delta G_T^0$  vs. temperature for the investigated association reactions obtained by means of the statistical thermodynamic method.<sup>219</sup>

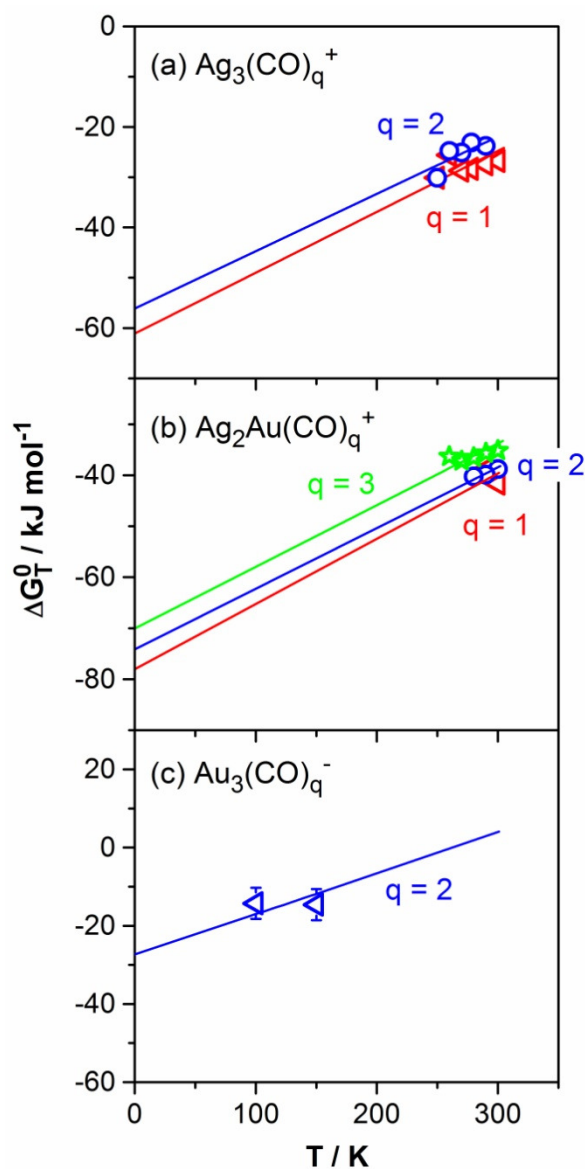
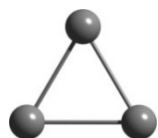


**Figure S2:** Energies (a.u.), coordinates (Å) and frequencies ( $\text{cm}^{-1}$ ) of the most stable isomers within 0.3 eV of  $\text{Ag}_n\text{Au}_m(\text{CO})_q^+$  ( $n+m = 3$ ,  $q = 0-4$ ) in singlet spin state.

**$\text{Ag}_3^+$**



$E = -440.838378965$

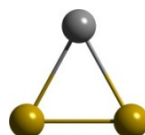
Coordinates:

	x	y	z
Ag	-0.357048	0.000000	-0.205732
Ag	1.014136	0.000000	2.167122
Ag	2.381276	0.000000	0.207190

Frequencies:

110.3356      111.6857      164.1771

**$\text{AgAu}_2^+$**



$E = -418.353952174$

Coordinates:

	x	y	z
Au	-0.208247	0.000000	0.053174
Au	0.957261	0.000000	2.326567
Ag	2.558738	0.000000	0.065541

Frequencies:

87.2938      116.7776      160.3363

**$\text{Ag}_2\text{Au}^+$**



$E = -429.600885488$

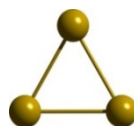
Coordinates:

	x	y	z
Au	0.234448	0.000000	0.334669
Ag	0.351613	0.000000	3.012856
Ag	2.710757	0.000000	1.360818

Frequencies:

79.6727      129.9845      165.8164

**$\text{Au}_3^+$**



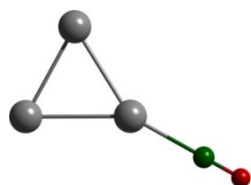
$E = -407.100228894$

Coordinates:

	x	y	z
Au	0.232558	0.000000	0.498635
Au	-0.004115	0.000000	3.205755
Au	2.459146	0.000000	2.059166

Frequencies:

98.2981      98.9347      156.7211

**$\text{Ag}_3\text{CO}^+$** 

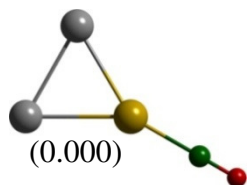
E= -554.220276717

Coordinates:

	x	y	z
Ag	-1.136606	-1.315513	0.900216
Ag	0.523794	0.758155	0.509673
Ag	-1.161610	-0.017548	-1.540420
C	-1.954853	0.225690	-3.593751
O	-2.355933	0.349216	-4.630748

Frequencies:

28.2008	36.0712	103.0574
114.3548	160.6334	201.5476
209.1907	226.5038	2286.8698

 **$\text{Ag}_2\text{AuCO}^+$** *Isomer I*

E= -542.990136108

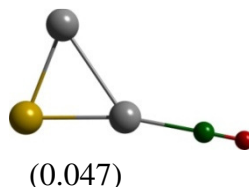
Coordinates:

	x	y	z
Ag	-1.767375	0.230987	1.097577
Ag	0.791037	-0.186296	0.314416
Au	-1.189974	0.000999	-1.575312
C	-1.796242	-0.017816	-3.559761
O	-2.122654	-0.027874	-4.631949

Frequencies:

33.4554	43.1129	106.0881
109.4072	162.7283	245.6494

268.0349      279.5954      2262.2698

*Isomer II*

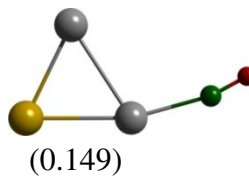
E= -542.988407307

Coordinates:

	x	y	z
Ag	-1.724583	0.361701	1.120228
Au	0.817024	0.266731	0.366714
Ag	-0.869441	-0.001426	-1.688784
C	-1.894079	-0.248943	-3.585715
O	-2.414129	-0.378063	-4.567472

Frequencies:

31.8395	40.1612	65.8390
127.8886	163.5638	226.2492
231.9626	253.9010	2289.4294

*Isomer III*

E= -542.984668338

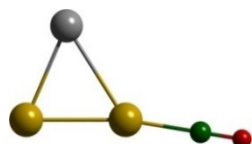
Coordinates:

	x	y	z
Ag	-1.568512	-0.000005	-0.783529
Au	0.801858	0.000033	0.412009
Ag	0.847118	-0.000021	-2.332766
C	-0.304992	-0.000019	-4.484668
O	-0.203952	0.000012	-5.481862

Frequencies:

40.5976	44.9619	83.9780
---------	---------	---------

111.9519    162.8577    200.7236  
224.0461    255.3955    2276.5555

**AgAu<sub>2</sub>CO<sup>+</sup>**

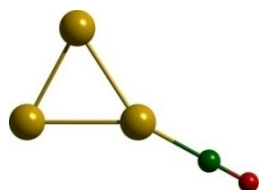
E= -531.756249406

Coordinates:

	x	y	z
Au	-1.144752	0.015441	-0.256036
Au	0.823119	0.031737	1.523504
Ag	1.669294	-0.067335	-1.014360
C	-2.846130	0.011246	-1.355571
O	-3.787649	0.008910	-1.964030

Frequencies:

45.0787	52.2683	73.0174
126.4373	163.4097	304.1659
314.4832	330.3973	2265.6477

**Au<sub>3</sub>CO<sup>+</sup>**

E= -520.506005335

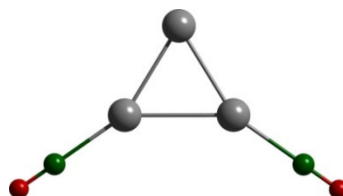
Coordinates:

	x	y	z
Au	-1.614820	0.000735	-0.246749
Au	0.997898	-0.000700	0.118564
Au	0.026455	0.000530	-2.478622
C	0.308026	0.000022	-4.477199
O	0.463946	-0.000588	-5.586809

Frequencies:

33.6865	49.7285	76.2215
---------	---------	---------

107.6652    158.7702    291.8490  
311.1096    334.7754    2269.7357

**Ag<sub>3</sub>(CO)<sub>2</sub><sup>+</sup>**

E= -667.600369843

Coordinates:

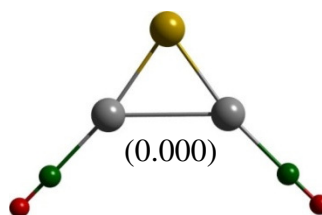
	x	y	z
Ag	-0.052303	0.276495	0.928679
Ag	0.070455	2.659756	-0.336474
Ag	-1.023704	0.593980	-1.689409
C	-2.007356	-0.415922	-3.397886
O	-2.513075	-0.920865	-4.259251
C	0.228245	-1.162767	2.588446
O	0.367949	-1.890857	3.426902

Frequencies:

22.1557	32.4130	33.5252
40.0113	97.8670	118.4026
151.4302	195.3651	200.4567
205.4664	209.4898	219.3838
229.5626	2280.5113	2282.8337

**Ag<sub>2</sub>Au(CO)<sub>2</sub><sup>+</sup>**

*Isomer I*



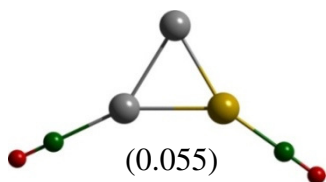
E= -656.375681617

Coordinates:

	x	y	z
Au	-1.848365	-2.830815	-0.093947
Ag	-0.418370	-0.948051	1.090997
Ag	-1.612925	-0.755965	-1.716241
C	-1.603241	0.753343	-3.258151
O	-1.600972	1.525078	-4.068391
C	0.769088	0.363982	2.326988
O	1.384996	1.032248	2.979751

Frequencies:

26.0080	38.7774	39.7685
40.8059	58.5363	131.5743
154.1888	230.0576	231.3449
233.8812	234.6545	255.9380
262.0595	2283.3397	2286.0069

*Isomer II*

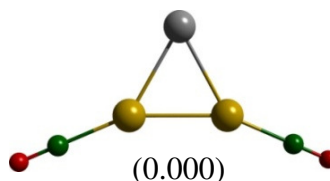
E= -656.373666728

Coordinates:

	x	y	z
Ag	0.047165	-0.100252	0.747982
Ag	1.664368	1.199447	-1.034296
Au	-0.732307	0.302706	-1.872442
C	-2.267901	-0.023477	-3.247584
O	-3.099625	-0.203863	-3.977854
C	-0.209387	-0.833127	2.797877
O	-0.332100	-1.201615	3.847324

Frequencies:

24.6552	36.6514	36.7704
45.0288	100.0765	115.5541
157.3506	212.1254	220.7291
234.5943	243.2580	264.1228
268.8826	2255.2435	2284.0997

**AgAu<sub>2</sub>(CO)<sub>2</sub><sup>+</sup>***Isomer I*

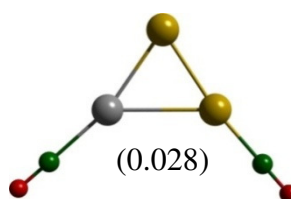
E= -645.146086620

Coordinates:

	x	y	z
Ag	-1.836936	-0.001420	-0.497721
Au	0.811134	0.000234	0.184878
Au	0.096020	0.000615	-2.432507
C	0.364331	0.001414	-4.487183
O	0.510404	0.001216	-5.598710
C	2.086843	-0.000304	1.817758
O	2.783007	-0.001761	2.696544

Frequencies:

29.1589	39.4968	43.1434
51.9142	105.2508	105.8189
156.7300	249.1318	264.8025
275.4319	287.3269	295.4714
297.3319	2255.8986	2263.6601

*Isomer II*

E= -645.145069624

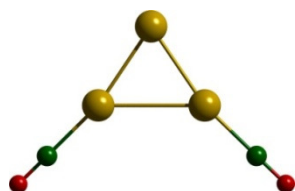
Coordinates:

	x	y	z
Au	1.334351	-0.005998	0.100302
Au	0.130607	-0.018328	2.438522
Ag	-1.621446	-0.003672	0.420395
C	-3.380676	0.005288	-0.828057

O	-4.300464	0.010411	-1.464768
C	2.492059	0.003221	-1.552837
O	3.138095	0.009078	-2.469651

Frequencies:

29.6488	40.1446	45.2289
52.1765	65.6502	126.0848
156.7293	232.0850	235.3043
255.2796	310.1555	318.7568
337.4773	2261.2164	2287.3628

 $\text{Au}_3(\text{CO})_2^+$ 

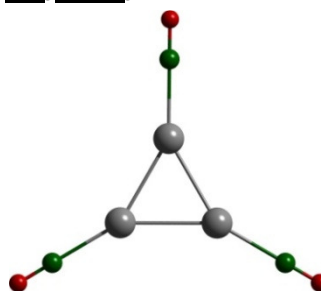
E= -633.911337468

Coordinates:

	x	y	z
Au	-1.572700	-1.272658	-0.022507
Au	0.286095	0.590885	0.295518
Au	-0.800235	0.675896	-2.120737
C	-1.366516	1.053702	-4.011813
O	-1.675980	1.273088	-5.066933
C	-2.889070	-2.785266	0.113004
O	-3.619082	-3.632712	0.190861

Frequencies:

38.1173	46.1453	50.2343
51.1310	60.7393	123.7471
156.9968	309.0858	312.7869
319.5651	322.5083	343.0250
347.3305	2261.9327	2268.4688

 $\text{Ag}_3(\text{CO})_3^+$ 

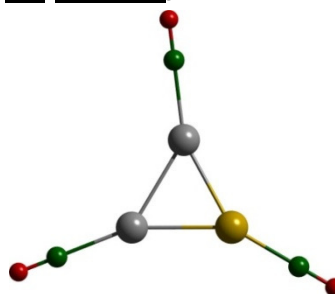
E= -780.978084054

Coordinates:

	x	y	z
Ag	-0.285283	-0.730399	1.194641
Ag	0.269280	1.875434	0.595116
Ag	-0.921446	0.270652	-1.265801
C	-1.788836	-0.032352	-3.291710
O	-2.228521	-0.189380	-4.309507
C	-0.247844	-2.424850	2.633445
O	-0.227816	-3.277622	3.358887
C	1.094303	3.848064	1.206657
O	1.510054	4.840126	1.518020

Frequencies:

18.7975	22.6032	26.6733
36.4526	40.5363	41.6942
111.5880	112.3080	140.5239
186.4249	188.0233	197.6310
199.1159	206.2979	207.2398
207.7627	209.6451	228.6041
2274.2543	2274.7871	2278.2185

 $\text{Ag}_2\text{Au}(\text{CO})_3^+$ 

E= -769.756008323

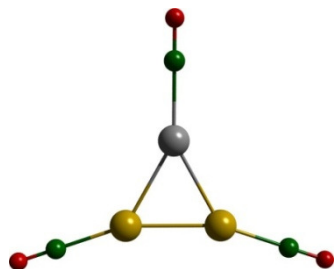


Coordinates:

	x	y	z
Ag	-0.044499	0.315556	0.940174
Au	0.108150	2.724997	-0.276684
Ag	-0.994516	0.667751	-1.641760
C	-1.957434	-0.394808	-3.295279
O	-2.453347	-0.938279	-4.139026
C	0.188352	-1.194832	2.507804
O	0.306704	-1.968774	3.307985
C	0.675057	4.759775	-0.213929
O	0.973164	5.840804	-0.182210

Frequencies:

25.6281	26.4607	29.1412
41.1563	43.4548	45.1809
104.7199	114.8092	145.6743
210.1102	212.3548	219.8941
225.1131	229.2006	237.5525
239.0437	253.8310	255.1642
2250.0891	2278.1174	2281.0427

AgAu<sub>2</sub>(CO)<sub>3</sub><sup>+</sup>

E= -758.532463972

Coordinates:

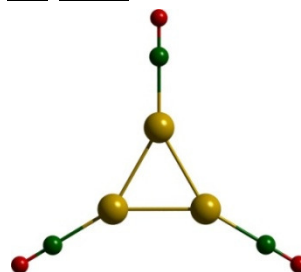
	x	y	z
Au	-0.179770	-0.291420	0.994030
Ag	0.084513	2.256353	-0.020997
Au	-1.053418	0.213073	-1.477696
C	-1.896809	-0.050082	-3.359482
O	-2.356239	-0.190368	-4.373053
C	0.266359	-1.300328	2.756448
O	0.505326	-1.843378	3.708456

C 0.715040 4.317004 0.175478

O 1.041156 5.382731 0.277107

Frequencies:

26.9984	32.6535	33.7579
44.1161	46.7655	52.9528
98.4946	112.2478	148.1493
224.4437	230.2790	246.2535
257.9712	263.7208	275.4362
289.9708	293.7621	302.1344
2250.1582	2257.9735	2283.1167

Au<sub>3</sub>(CO)<sub>3</sub><sup>+</sup>

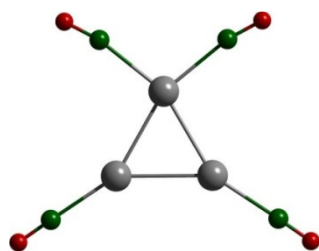
E= -747.304054835

Coordinates:

	x	y	z
Au	-0.224904	-0.786923	1.127358
Au	0.239843	1.860909	0.674542
Au	-0.930215	0.336277	-1.254070
C	-1.755688	0.145655	-3.122470
O	-2.206588	0.041979	-4.143861
C	-0.141702	-2.428770	2.352179
O	-0.111974	-3.323931	3.026749
C	0.954525	3.672208	1.316177
O	1.350594	4.662272	1.663144

Frequencies:

33.3075	34.6992	39.8455
47.6852	54.5965	54.7679
100.2303	100.8180	147.2627
267.8996	269.0718	292.4242
300.9870	310.4430	310.9913
314.1032	314.2056	318.9461
2256.5858	2257.0867	2267.7637

$\text{Ag}_3(\text{CO})_4^+$ 

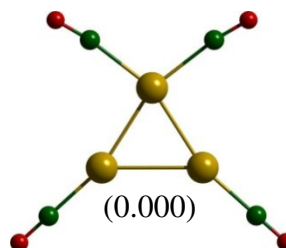
E= -894.339973621

Coordinates:

	x	y	z
Ag	-2.011683	-0.167934	0.219286
Ag	-0.125346	1.598353	-0.689459
Ag	-1.533221	0.065939	2.468009
C	-1.896705	-0.454645	-4.604340
O	-2.068050	-0.698656	-5.684217
C	-1.802263	0.237582	2.503143
O	-1.552015	0.576810	3.542703
C	1.440638	3.160402	-0.413441
O	2.229663	3.947589	-0.300351
C	-3.680504	-1.789707	0.143994
O	-4.456588	-2.559613	-0.107670

Frequencies:

11.2083	22.0400	22.9992
27.5090	35.7654	36.9239
40.3349	41.5950	98.8632
108.6267	135.8568	138.0025
138.3365	159.2620	168.8680
180.9769	186.0047	194.0484
199.5712	203.1291	207.4637
213.3938	220.7515	2248.8881
2255.7971	2269.2330	2272.1367

 $\text{Au}_3(\text{CO})_4^+$ *Isomer I*

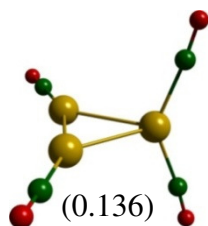
E= -860.661586940

Coordinates:

	x	y	z
C	0.442451	0.174042	-3.723364
O	-0.177806	0.184935	-4.657843
Au	1.446465	0.002422	-1.749444
C	3.383023	1.051037	-2.040908
O	4.389389	1.546374	-2.044868
Au	-0.518324	-1.376811	-0.548813
C	-2.243732	-2.375405	-0.130568
O	-3.195584	-2.923950	0.100873
Au	1.868867	-0.650865	0.819078
C	2.668189	-0.878691	2.679374
O	3.109911	-1.003732	3.703939

Frequencies:

21.3912	29.7532	37.3506
38.1379	44.8414	48.6462
53.2148	53.7644	76.5119
109.6020	147.7777	150.1847
178.7478	180.6951	227.8492
247.7195	265.8137	289.1563
304.3884	309.4896	311.1267
317.9310	323.2693	2241.9483
2245.0216	2249.6561	2258.9631

*Isomer II*

E= -860.656574306

Coordinates:

	x	y	z
Au	-1.657235	0.540285	-0.852151
Au	0.993885	0.633314	-0.997833
Au	-0.371192	-1.164160	-2.759905
C	-0.576956	-0.293197	-4.641665
O	-0.689823	0.269423	-5.607348
C	-0.188943	-3.086136	-1.974468
O	-0.084081	-4.076778	-1.455385
C	-3.621283	0.900806	-0.290020
O	-4.670028	1.122336	0.042482
C	2.976850	1.136117	-0.652685
O	4.036383	1.437691	-0.438345

Frequencies:

17.1459	28.8598	30.4292
38.8612	39.4170	45.3410
51.5966	52.8535	79.8499
84.3207	144.2854	219.3687
221.9198	239.7041	255.1827
270.8054	271.9204	292.4654
294.3081	296.4715	301.9068
325.1102	366.6168	2225.9590
2240.8019	2244.4495	2254.7206

**Figure S3:** Energies (a.u.), coordinates (Å) and frequencies ( $\text{cm}^{-1}$ ) of the most stable isomers within 0.3 eV of  $\text{Ag}_n\text{Au}_m(\text{CO})_q^-$  ( $n+m = 3$ ,  $q = 0-2$ ) in singlet spin state.

**Ag<sub>3</sub><sup>-</sup>**

E= -441.140638840

Coordinates:

	x	y	z
Ag	0.896356	0.000000	0.417741
Ag	-0.245753	0.000000	2.865213
Ag	2.036987	0.000000	-2.029709

Frequencies:

34.5288      103.2306      169.7269

**AgAu<sub>2</sub><sup>-</sup>**

E= -418.723818754

Coordinates:

	x	y	z
Ag	0.895833	0.000000	0.417734
Au	-0.231496	0.000000	2.835597
Au	2.023253	0.000000	-2.000087

Frequencies:

36.7658      90.3530      188.0273

**Ag<sub>2</sub>Au<sup>-</sup>**

E= -429.932485912

Coordinates:

	x	y	z
Ag	0.894422	0.000000	0.422138
Ag	-0.240275	0.000000	2.844676
Au	2.033443	0.000000	-2.013570

Frequencies:

36.5999      97.4099      178.2699

**Au<sub>3</sub><sup>-</sup>**

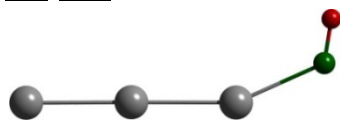
E= -407.491785972

Coordinates:

	x	y	z
Au	1.169490	0.000000	1.169121
Au	-0.709419	0.000000	3.048536
Au	3.048330	0.000000	-0.709257

Frequencies:

34.0938      102.0337      168.7532

**Ag<sub>3</sub>CO<sup>-</sup>**

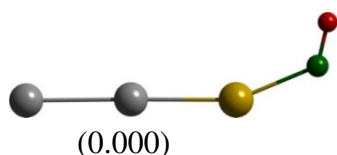
E= -554.499579914

Coordinates:

	x	y	z
Ag	-0.302710	-0.084822	0.162770
Ag	1.100184	0.269728	2.451033
Ag	-1.706510	-0.461513	-2.108628
C	-2.242898	-0.176183	-4.518305
O	-1.605998	0.452788	-5.229238

Frequencies:

15.5399	30.9970	40.1647
59.8677	67.6525	105.1481
169.8226	230.6499	2041.2571

**Ag<sub>2</sub>AuCO<sup>-</sup>***Isomer I*

(0.000)

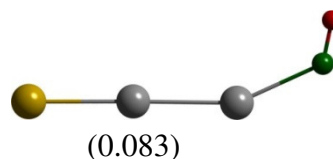
E= -543.294737891

Coordinates:

	x	y	z
Ag	0.440267	0.045718	0.782169
Ag	1.864045	0.281167	3.046484
Au	-0.954465	-0.183044	-1.510287
C	-2.777649	-0.177535	-2.856873
O	-3.858315	0.033694	-2.527987

Frequencies:

25.5359	34.4101	46.3621
94.8729	108.8806	156.9933
178.1874	298.7186	2006.2999

*Isomer II*

(0.083)

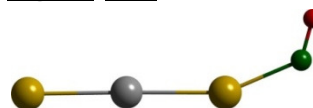
E= -543.291704758

Coordinates:

	x	y	z
Ag	-0.182078	0.143309	0.079478
Au	0.680114	-0.446163	2.563785
Ag	-1.029980	0.765831	-2.376880
C	-1.955236	0.284028	-4.565980
O	-2.270752	-0.747005	-4.942772

Frequencies:

17.6898	32.5488	42.3961
78.9281	88.9396	115.9223
179.2459	239.1828	2052.8721

**AgAu<sub>2</sub>CO<sup>-</sup>**

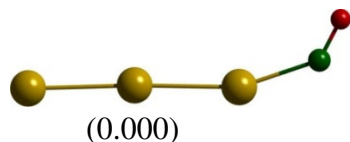
E= -532.086725742

Coordinates:

	x	y	z
Ag	-0.218885	0.000000	0.097688
Au	0.445666	0.000000	2.690087
Au	-0.839773	0.000000	-2.499684
C	-2.162350	0.000000	-4.301571
O	-3.309867	0.000000	-4.341549

Frequencies:

26.2011	35.1373	49.8291
88.4616	128.4676	172.5513
190.6191	303.7804	2016.8376

**Au<sub>3</sub>CO<sup>-</sup>***Isomer I*

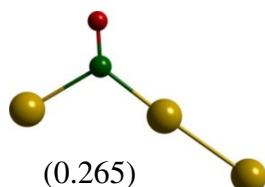
E= -520.860265598

Coordinates:

	x	y	z
Au	0.674979	0.000991	1.213442
Au	3.257848	-0.002659	1.935348
Au	-1.891640	0.004536	0.619681
C	-3.686652	0.001459	-0.512680
O	-3.961594	-0.004328	-1.627420

Frequencies:

25.5623	30.8788	55.0674
98.9330	160.9197	176.1354
228.4457	323.9060	2019.0921

*Isomer II*

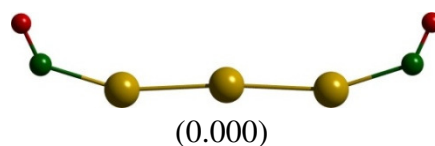
E= -520.850516464

Coordinates:

	x	y	z
Au	-1.362220	0.009825	1.019846
Au	1.254648	0.001126	1.389370
Au	4.416288	0.020531	-0.065796
C	3.285918	-0.007289	1.767394
O	3.892142	-0.024193	2.773190

Frequencies:

7.1473	46.2376	69.2232
143.4244	243.3179	293.3026
404.5993	576.8164	1857.0681

**Au<sub>3</sub>(CO)<sub>2</sub><sup>-</sup>***Isomer I*

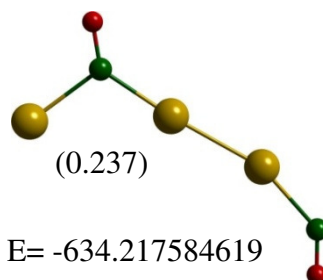
E= -634.226302433

Coordinates:

	x	y	z
Au	-0.391178	-0.284514	0.675206
Au	-2.097500	1.679634	0.113651
Au	1.464246	-2.088816	1.296655
O	-4.987167	2.292040	-0.673822
C	-3.936489	2.683582	-0.421212
O	2.098651	-5.079366	1.293807
C	2.435152	-4.006829	1.533532

Frequencies:

8.4043	21.0739	29.5202
40.9708	59.2683	98.9890
145.6918	152.8548	159.2660
210.7633	213.9827	301.0280
339.6056	1999.0856	2016.7547

*Isomer II*

E= -634.217584619

Coordinates:

	x	y	z
Au	-1.619232	0.182465	-0.311503
Au	-2.288692	0.406874	2.225527
Au	0.648856	-0.959744	-2.720537

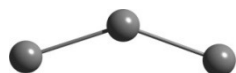
C	-1.223655	0.087671	-2.371280
O	-1.803033	0.479904	-3.312374
C	-2.256384	0.169191	4.352725
O	-1.604659	-0.366362	5.128003

Frequencies:

11.9140	21.0504	43.1162
45.6041	70.1281	142.4579
180.9574	218.6317	232.5026
270.0534	325.9941	386.8772
551.4502	1864.9405	2037.0472

**Figure S4:** Energies (a.u.), coordinates (Å) and frequencies ( $\text{cm}^{-1}$ ) of the most stable isomers within 0.3 eV of  $\text{Ag}_n\text{Au}_m(\text{CO})_q$  ( $n+m = 3$ ,  $q = 0-1$ ) in doublet spin state.

### **Ag<sub>3</sub>**



E= -441.055985111

Coordinates:

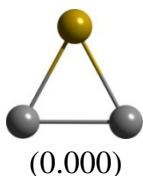
	x	y	z
Ag	0.754137	0.000000	0.754137
Ag	-0.412619	0.000000	3.166881
Ag	3.166881	0.000000	-0.412619

Frequencies:

14.4179      115.3688      158.6578

### **Ag<sub>2</sub>Au**

#### *Isomer I*



E= -429.833847427

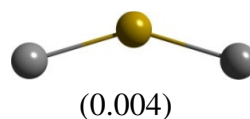
Coordinates:

	x	y	z
Ag	0.194950	0.000000	0.432490
Ag	0.171683	0.000000	3.097106
Au	2.640653	0.000000	1.785764

Frequencies:

60.9148      105.1755      164.6089

#### *Isomer II*



E= -429.833692800

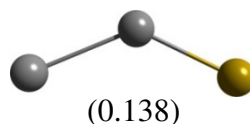
Coordinates:

	x	y	z
Au	0.776659	0.000000	0.776659
Ag	-0.427106	0.000000	3.158847
Ag	3.158847	0.000000	-0.427106

Frequencies:

15.9317      126.2680      151.4463

#### *Isomer III*



E= -429.828792339

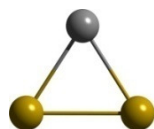
Coordinates:

	x	y	z
Ag	0.694459	0.000000	0.803968
Ag	-0.471390	0.000000	3.238359
Au	3.232031	0.000000	0.075301

Frequencies:

10.6732      117.2314      164.7048



**AgAu<sub>2</sub>***Isomer I*

(0.000)

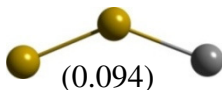
E= -418.603740524

Coordinates:

	x	y	z
Au	0.264312	0.000000	0.500160
Au	-0.245569	0.000000	3.366384
Ag	2.236413	0.000000	2.329446

Frequencies:

69.5672      102.2985      164.2984

*Isomer II*

(0.094)

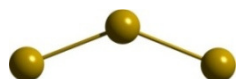
E= -418.600280148

Coordinates:

	x	y	z
Au	0.702856	0.000000	0.708552
Au	-0.343338	0.000000	3.144497
Ag	3.148882	0.000000	-0.344649

Frequencies:

17.2927      121.8020      153.2142

**Au<sub>3</sub>**

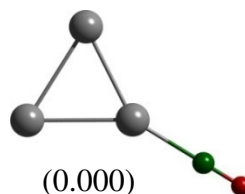
E= -407.364055257

Coordinates:

	x	y	z
Au	0.708133	0.000000	0.708152
Au	-0.337876	0.000000	3.138130
Au	3.138143	0.000000	-0.337882

Frequencies:

18.1937      113.9768      152.6913

**Ag<sub>3</sub>CO***Isomer I*

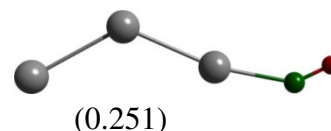
(0.000)

E= -554.429615816

Coordinates:

	x	y	z
Ag	-0.372658	0.008237	0.186325
Ag	1.522390	-0.000793	2.101117
Ag	2.414952	-0.008953	-0.439602
C	1.991206	-0.000848	4.177185
O	2.242963	0.002356	5.280133

Frequencies:

25.7445      36.2886      89.5572  
102.1377      155.2544      196.1403  
206.1930      259.8453      2128.8262*Isomer II*

(0.251)

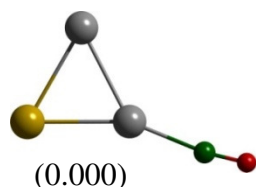
E= -554.420399424

Coordinates:

	x	y	z
Ag	0.477542	0.503717	-0.132653
Ag	0.237550	-0.294901	2.428503
Ag	-1.140940	-0.038646	-2.167266
C	-2.181013	-0.232269	-4.139687
O	-2.151072	0.062100	-5.231263

Frequencies:

10.5541	13.4949	34.1446
113.0258	118.1095	148.7011
173.2584	241.1073	2144.9487

**Ag<sub>2</sub>AuCO***Isomer I*

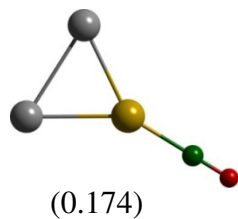
E= -543.211448549

Coordinates:

	x	y	z
Ag	-0.238850	0.622329	0.282122
Ag	1.705759	-0.066757	2.077199
Au	2.270828	-0.403357	-0.505256
C	2.024434	-0.099345	4.161042
O	2.036681	-0.052870	5.290051

Frequencies:

29.7559	38.7646	91.9757
102.2411	154.1228	214.2933
222.3367	276.6906	2150.7845

*Isomer II*

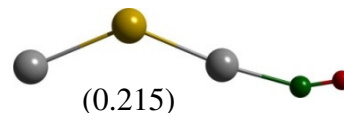
E= -543.205069545

Coordinates:

	x	y	z
Ag	-0.375204	-0.000147	0.239043
Au	1.537287	-0.000398	2.139287
Ag	2.435496	-0.000163	-0.401333
C	1.976521	0.000933	4.110354
O	2.224753	-0.000225	5.217806

Frequencies:

29.0968	39.8012	82.6213
83.9259	157.4996	217.5534
265.4454	326.9262	2118.4014

*Isomer III*

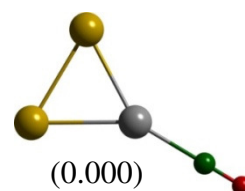
E= -543.203545498

Coordinates:

	x	y	z
Au	0.554438	-0.013978	-0.028490
Ag	2.473734	-0.012298	1.750177
Ag	0.433393	0.070295	-2.737715
C	4.168581	-0.029720	4.492197
O	3.856630	-0.014298	3.407837

Frequencies:

14.0117	17.7271	36.5207
118.7755	145.9695	151.8716
190.2542	268.1190	2171.6671

**AgAu<sub>2</sub>CO***Isomer I*

E= -531.986484767

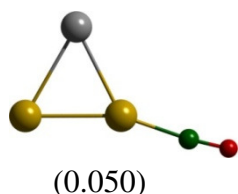
Coordinates:

	x	y	z
Au	0.236509	0.029497	-0.548987
Au	-0.405442	-0.061877	2.177713
Ag	2.159446	-0.000995	1.343819
C	4.199807	0.012531	1.825221
O	5.296456	0.020843	2.086238

Frequencies:

30.2238	42.0087	91.4552
97.1638	151.2162	231.3080
240.1684	280.1333	2190.4985

*Isomer II*



E= -531.984638364

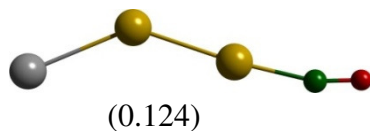
Coordinates:

	x	y	z
Au	-0.981969	0.000000	0.225313
Au	1.357480	0.000000	1.476507
Ag	1.271044	0.000000	-1.368883
C	-2.948147	0.000000	-0.081079
O	-4.044589	0.000000	-0.370070

Frequencies:

38.7808	46.8367	85.2835
88.7648	153.1424	271.9022
296.0986	359.2580	2138.7718

*Isomer III*



E= -531.981944615

Coordinates:

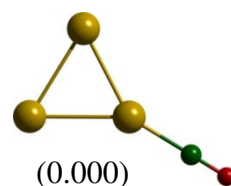
	x	y	z
Au	0.357081	0.341974	-0.132276
Ag	0.103962	-0.253487	2.514332
Au	-1.027727	0.048683	-2.319719
C	-1.956353	-0.095279	-4.104709
O	-2.234896	-0.041890	-5.199995

Frequencies:

16.6062	23.4793	35.5854
112.8169	152.3841	234.6946
255.8851	337.5362	2165.7178

**Au<sub>3</sub>CO**

*Isomer I*



E= -520.756898809

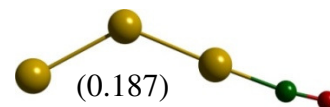
Coordinates:

	x	y	z
Au	-0.386286	-0.066097	0.499510
Au	2.235359	0.149164	1.153049
Au	1.616211	-0.172597	-1.465082
C	3.614367	0.379779	2.547822
O	4.406192	0.512758	3.345698

Frequencies:

34.0473	49.8887	82.4732
88.7855	148.1113	302.2429
316.2044	369.8294	2166.4910

*Isomer II*



E= -520.750013909

Coordinates:

	x	y	z
Au	-1.118329	0.125813	0.415066
Au	1.088030	-0.092830	1.941038
Au	-1.323309	0.030743	-2.174943
C	-1.562450	-0.027101	-4.164659
O	-1.841874	-0.036625	-5.258870

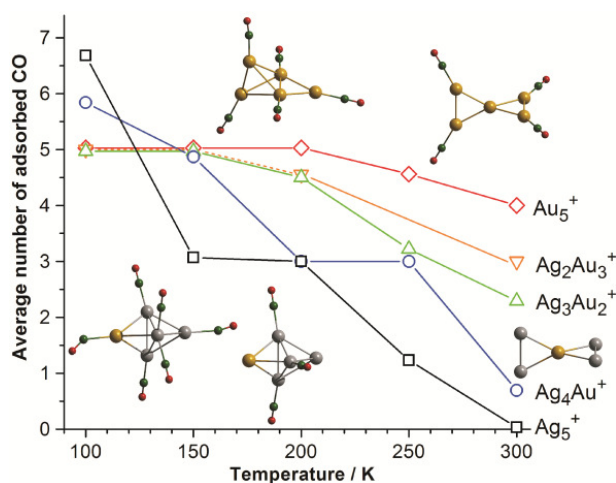
Frequencies:

15.9311	33.6126	36.8443
112.0514	156.2251	265.9027
272.8659	341.6063	2189.7337

# Composition dependent adsorption of multiple CO molecules on binary silver-gold clusters $\text{Ag}_n\text{Au}_m^+$ ( $n+m = 5$ )<sup>\*</sup>

The binding energies of multiple CO molecules to five-atom silver-gold cluster cations have been obtained employing temperature dependent gas phase ion trap measurements and *ab initio* calculations. The CO binding energies to  $\text{Ag}_n\text{Au}_m^+$  ( $n + m = 5$ ) decrease with increasing number of silver atoms. Most strikingly, after the adsorption of the fourth CO to  $\text{Au}_5^+$  and of the third CO to  $\text{Ag}_5^+$ , respectively, a pronounced decrease in the binding energies of further CO molecules was observed. This is related to a CO-induced structural transformation yielding more compact metal cluster geometries. First principles calculations revealed that the exact structure of the carbonyl complexes with multiple CO and the nature of the CO-induced structural transformation strongly depend on the composition of the metal cluster as well as on the number of adsorbed CO molecules.

## Graphical abstract<sup>\*</sup>



<sup>\*</sup> The contents of this chapter have been published in a contribution to *Physical Chemistry Chemical Physics*: D. M. Popolan, M. Nöbler, R. Mitrić, T. M. Bernhardt, V. Bonačić-Koutecký, "Composition dependent adsorption of multiple CO molecules on binary silver-gold clusters  $\text{Ag}_n\text{Au}_m^+$  ( $n+m = 5$ ): theory and experiment", **12**, 7865-7873 (2010).

## 5.1 Introduction

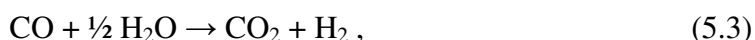
The activity of heterogeneous gold nano-particle catalysts in several important reactions of carbon monoxide such as the total combustion<sup>70,72,80,187,188</sup>



the syngas based methanol synthesis<sup>188</sup>



or the water gas shift reaction<sup>188</sup>



has attracted considerable attention in recent years. An important initial step in these reactions is the adsorption of CO on the catalyst. Quantitative information about the binding of carbon monoxide to isolated gold clusters as a function of the number of CO molecules, i.e., the CO coverage, can thus be of great value and assist the understanding of the overall reaction mechanisms. Although gas-phase studies of isolated clusters might never account for the precise mechanisms, energetics, and kinetics operating in applied catalysis, such investigations can provide a conceptual framework and an efficient tool to obtain direct insight into reactivity patterns, as stated in a recent review.<sup>120</sup>

A further interesting aspect of the investigation of free size-selected clusters is that their exact number and nature of atoms is known. In this respect, bimetallic silver-gold clusters offer the opportunity to tune the properties of the binary clusters in such a way to potentially increase their catalytic activity.<sup>206</sup>

Geometrical structures of free gold, silver, and of binary gold-silver cluster cations have been investigated previously with ion mobility mass spectrometry<sup>81,82,84</sup> and with ion trap electron diffraction<sup>85-87</sup> as well as via first principles calculations.<sup>81,82,84,93-97,99-101</sup>

The CO adsorption onto mass-selected free gold clusters was also investigated before by various groups.<sup>108,109,111,113,114,189-193,195,197,201,211,220,221</sup> Experimental binding energies of one and two CO molecules to  $\text{Au}_n^+$  have been obtained by a radiative association model study in an ion cyclotron resonance mass spectrometer.<sup>111</sup>

Considerably less is known about silver cluster carbonyls. Evidence for the existence of silver carbonyl clusters was first obtained from infrared spectra recorded in Ar matrix isolation studies.<sup>222-225</sup> Spectroscopy in ultracold CO droplets revealed that the growth of positively charged silver cluster carbonyls  $\text{Ag}_n(\text{CO})_q^+$  ( $n = 1-15$ ,  $q = 1-3$ ) leads to the formation of particularly stable complexes with a maximum of three CO ligands.<sup>226</sup>

Reactivity studies under single collision conditions indicated no reaction of  $\text{Ag}_4^+$  with CO.<sup>112</sup> Free, negatively charged silver clusters were found to be unreactive toward CO, too.<sup>106,113,198</sup> No binding energy values of CO to any silver clusters have been reported so far, neither experimentally, nor theoretically.

The adsorption of CO onto binary silver-gold clusters was investigated experimentally and theoretically.<sup>110,112,207,227</sup> However, no saturation coverage measurements were performed. A close relation between the adsorbate coverage, the adsorption energetics and the cluster structure had been pointed out before for pure gold and silver clusters.<sup>114,117</sup> We here investigate the details of this structure-reactivity relationship for the adsorption of multiple CO molecules on five-atom binary silver-gold clusters.

In this contribution, CO binding energies of metal cluster carbonyl complexes  $\text{Ag}_n\text{Au}_m^+$  ( $n + m = 5$ ) are presented as a function of the metal cluster composition and of the carbonyl complex size. Furthermore, based on the experimental binding energies and on first principles calculations a CO-induced structural transformation is revealed that strongly depends on the exact composition of the complexes.

## 5.2 Results and discussion

### 5.2.1 Temperature dependent CO coverage

Figure 5.1 displays the product ion mass spectra obtained for the reaction of  $\text{Au}_5^+$ ,  $\text{Ag}_3\text{Au}_2^+$ , and  $\text{Ag}_5^+$  with CO as a function of the reaction temperature  $T_R$  at a fixed reaction time of  $t_R = 0.1$  s. All clusters reacted with carbon monoxide in a sequential adsorption mechanism without fragmentation. However, the number of sequentially adsorbed CO molecules was strongly dependent on the composition as well as on the reaction temperature. With decreasing temperature, the number of adsorbed CO molecules increased for all investigated clusters.  $\text{Au}_5^+$  rapidly reacted with four CO molecules already at room temperature and adsorbed one more CO at temperatures lower than 250 K (Figure 5.1a). In contrast,  $\text{Ag}_5^+$  hardly reacted at all with CO at 300 K (Figure 5.1c). Upon cooling, the sequential adsorption of up to three CO molecules was observed. Three CO remained the saturation coverage over a wide temperature range until, below 150 K, further CO adsorption took place leading to a maximum coverage of seven at 100 K. The adsorption behavior of  $\text{Ag}_3\text{Au}_2^+$  displayed in Figure 5.1b was somewhat intermediate between the bare gold and silver clusters, respectively.

Starting from two and three CO at room temperature a saturation coverage of five, similar to  $\text{Au}_5^+$ , was reached at 100 K in this case. In order to obtain the temperature dependent CO coverage as a function of the cluster composition, all possible binary clus-

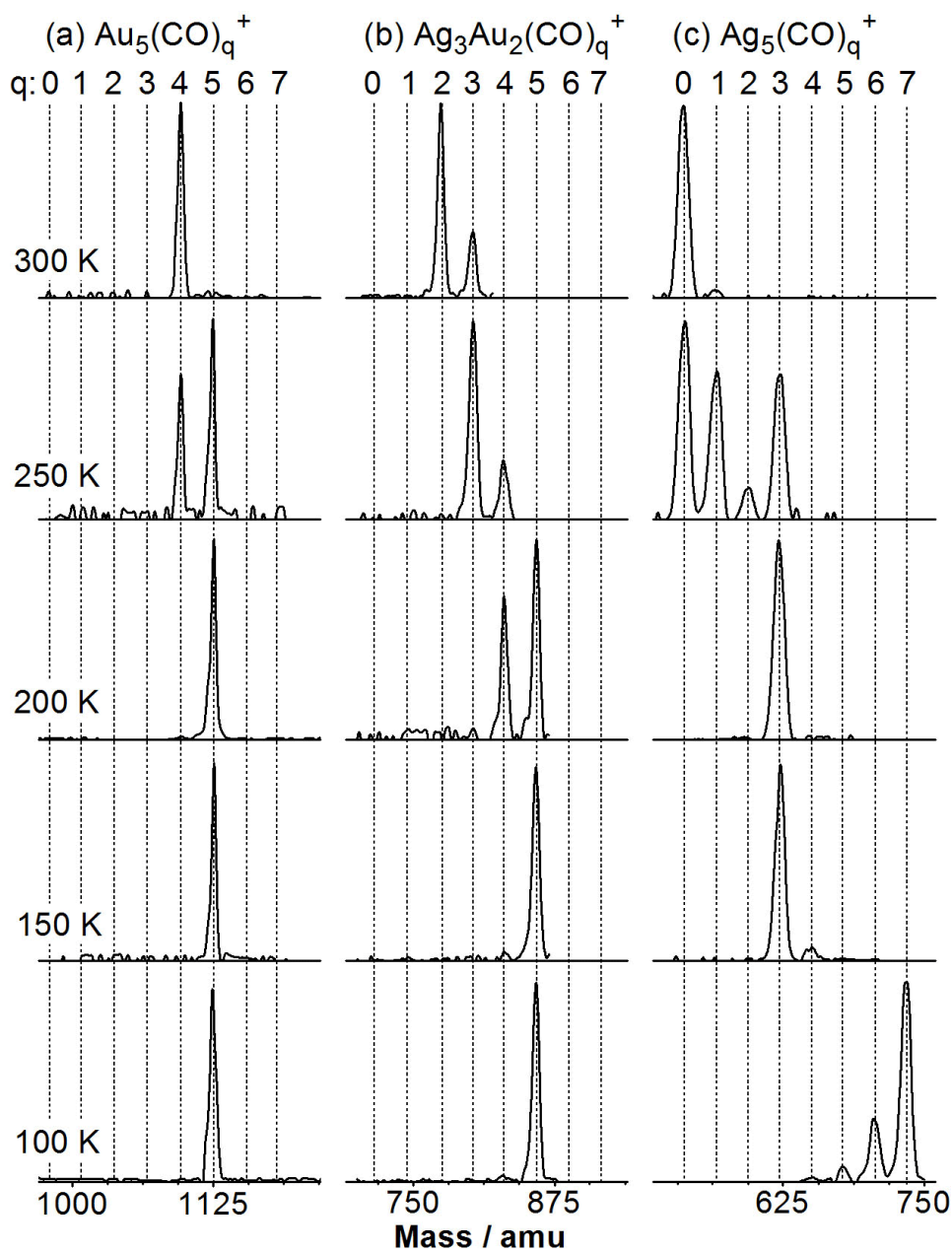


**Figure 5.1:** Product ion mass spectra recorded after a reaction time of  $t_R = 0.1$  s and at different reaction temperatures,  $T_R$ , as indicated, for (a)  $\text{Au}_5^+$ , (b)  $\text{Ag}_3\text{Au}_2^+$ , and (c)  $\text{Ag}_5^+$ . The ion trap was filled with 0.1 Pa CO and 1.0 Pa He.



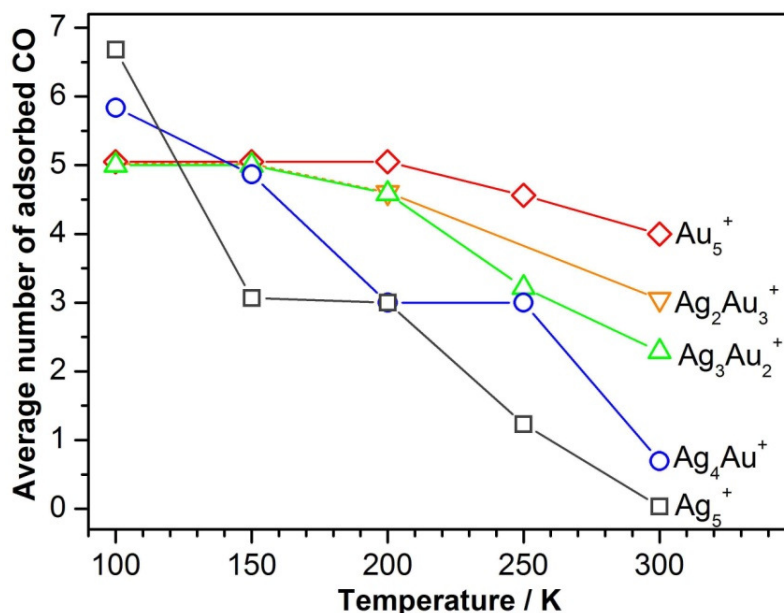


**Figure 5.2:** Average number of adsorbed CO molecules after a reaction time of  $t_R = 0.1$  s as a function of the reaction temperature,  $T_R$ , for all investigated clusters. Lines are drawn to guide the eye. The dashed line in the case of  $\text{Ag}_2\text{Au}_3^+$  indicates the expected trend although no data were obtained for 150 K.

ter combinations  $\text{Ag}_4\text{Au}^+$ ,  $\text{Ag}_3\text{Au}_2^+$ , and  $\text{Ag}_2\text{Au}_3^+$  (except  $\text{AgAu}_4^+$ , for experimental reasons) were studied. The results are summarized in Figure 5.2, where the average number of adsorbed CO molecules is plotted as a function of the reaction temperature for all investigated pentamers  $\text{Ag}_n\text{Au}_m^+$ . From Figure 5.2 it can be seen that the gold as well as the gold-rich binary clusters adsorbed multiple CO ligands already at 300 K and rather quickly reached the saturation coverage of five with decreasing temperature. In contrast, the average number of adsorbed CO did not exceed three for the silver pentamer unless the reaction temperature was lowered below 150 K. Actually, as can be seen from Figure 5.1c,  $\text{Ag}_5(\text{CO})_3^+$  was the sole carbonyl complex observed in this temperature range. A similar temperature dependent behavior as for the silver cluster was only observed for  $\text{Ag}_4\text{Au}^+$ . This cluster also exhibits the plateau at an average coverage of three CO in the graph in Figure 5.2 that reflects the particular stability of this complex.  $\text{Ag}_4\text{Au}^+$  was also the only cluster composition apart from  $\text{Ag}_5^+$  that adsorbed more than five CO molecules at cryogenic temperatures.

### 5.2.2 Experimental CO binding energies

To determine the binding energies of CO to the metal cluster cations, temperature dependent equilibrium methods were applied as described in Section 3.3. All data

obtained in the present investigation are displayed as plots of  $\Delta G_T^\circ$  versus temperature in Figure 5.3.

In Figure 5.3 the open symbols represent the experimental data whereas the solid lines are linear fits to these data to obtain the ordinate intercepts at  $T = 0$  K which represent the CO binding energies ( $\Delta H_0^\circ$ , see Section 3.3). In few cases, where it was only possible to obtain a  $\Delta G_T^\circ$  value at one single temperature, the entropy  $\Delta S_T^\circ$ , reflected by the slope of the linear fits, was assumed to be similar to the entropy of the reaction with one CO less. These cases are marked by dashed lines in Figure 5.3.

Most interestingly, the slope of the linear fits to the data in Figures 5.3b ( $\text{Ag}_4\text{Au}^+$ ) and 3c ( $\text{Ag}_5^+$ ) change their sign with the adsorption of the fourth CO ligand. This means, according to Equation (3.25), that the reaction entropy  $\Delta S_T^\circ$  becomes positive with the adsorption of more than three CO for  $\text{Ag}_4\text{Au}^+$  and  $\text{Ag}_5^+$  yielding entropically unfavorable complexes. This is in marked contrast to the case of  $\text{Ag}_3\text{Au}_2^+$  in Figure 5.3a. Although no temperature dependent  $\Delta G_T^\circ$  data could be obtained for the clusters with even higher gold content, the temperature dependent adsorption behavior displayed in Figure 5.2 indicates that the reactions of CO with  $\text{Ag}_2\text{Au}_3^+$  and  $\text{Au}_5^+$  are similar to those with  $\text{Ag}_3\text{Au}_2^+$ . Consequently,  $\text{Ag}_4\text{Au}^+$  and  $\text{Ag}_5^+$  must exhibit a very distinct carbonyl formation mechanism which is different from the gold-rich clusters.

This conclusion is supported by the resulting experimental binding energy data which are listed in Table 5.1. Whereas the binding energy of the first carbon monoxide molecule decreases continuously with increasing silver content in the clusters, the adsorption energies of multiple CO molecules are very different for the gold-rich and for the silver-rich complexes. Multiple CO molecules all exhibit similar binding energies around 0.3 to 0.5 eV in the case of  $\text{Ag}_3\text{Au}_2^+$ , but in the cases of  $\text{Ag}_4\text{Au}^+$  and  $\text{Ag}_5^+$  just three CO molecules are bound comparably strong whereas further CO are only very weakly adsorbed with binding energies less than 0.1 eV.

In the following we present the results of ab initio simulations in the DFT formalism which aim to elucidate the composition dependent adsorption behavior of CO onto the five-atom noble metal cluster cations.

### 5.2.3 Theoretical structures and binding energies

Lowest energy structures of all investigated cluster carbonyl complexes have been determined employing density functional theory at the B3LYP level. Binding energies for the sequentially adsorbed CO molecules were obtained from the total energy of the respective complexes according to

$$E_b(\text{X}_5 - \text{CO}(\text{CO})_{q-1}^+) = E(\text{X}_5(\text{CO})_q^+) - E(\text{X}_5(\text{CO})_{q-1}^+) - E(\text{CO}). \quad (5.4)$$

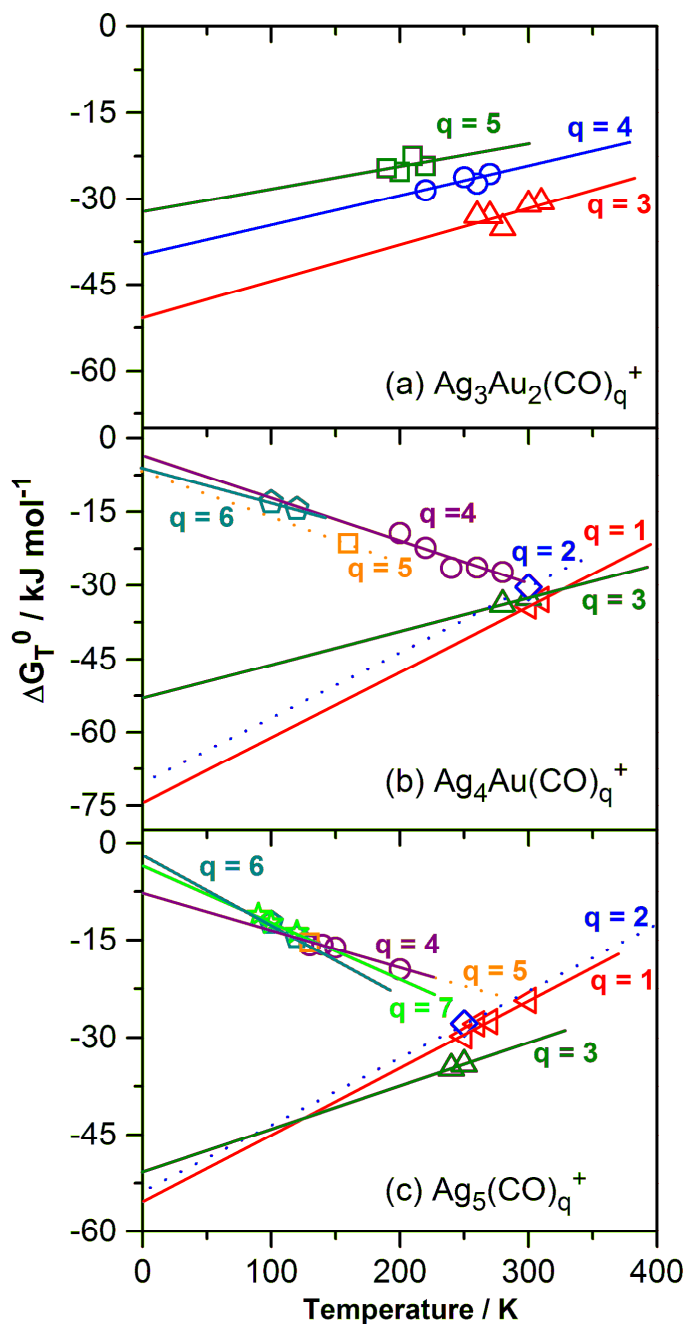


**Figure 5.3:** Plots of the Gibbs free energy,  $\Delta G_T^0$ , vs. temperature for the CO adsorption reactions on (a)  $\text{Ag}_3\text{Au}_2^+$ , (b)  $\text{Ag}_4\text{Au}^+$ , and (c)  $\text{Ag}_5^+$ .  $q$  denotes the number of adsorbed CO molecules. Solid lines represent linear extrapolations of the experimental data to obtain  $\Delta H_0^\circ$  values. Dashed lines are shown, if data were available for one temperature value only. In these cases the reaction entropy was assumed equal to be to the one of the  $(q-1)$  CO adsorption (see text for details).

The resulting calculated binding energy values are also included in Table 5.1.

In the following we will address the influence of the number of CO ligands on the structural properties of the clusters with a given composition in order to elucidate the origin of the adsorption properties. The structures of the pure gold complexes  $\text{Au}_5(\text{CO})_q^+$  shown in Figure 5.4 will be discussed first, followed by the discussion of the structures of the carbonyl complexes of the three investigated binary clusters displayed in Figure 5.5.

Finally, we will present the results obtained for  $\text{Ag}_5(\text{CO})_q^+$  (Figure 5.6) and in particular discuss the influence of different theoretical approaches on structures and binding energies.

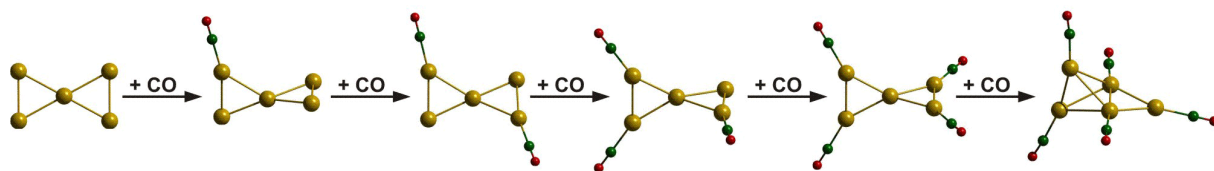
### 5.2.3.1 $\text{Au}_5(\text{CO})_q^+$ ( $q = 1-5$ )

Figure 5.4 shows the lowest energy structures of the  $\text{Au}_5(\text{CO})_q^+$  ( $q = 1-5$ ) cluster complexes. Note that all other isomers are at least 0.2 eV less stable.

The bare  $\text{Au}_5^+$  cluster was found to exhibit a planar, X-shaped structure of  $D_{2h}$  symmetry in agreement with a previous report.<sup>81</sup> The first CO binds to the planar structure of the  $\text{Au}_5^+$  cluster in a  $\mu_1$ -atop position leading to an out of plane structure as also previously proposed.<sup>111,114</sup>

Subsequently, all four corner gold atoms of  $\text{Au}_5^+$  are successively occupied by  $\mu_1$ -CO ligands. Upon adsorption of a fifth CO the geometric structure of the metal cluster is completely changed. The calculated lowest energy structure of  $\text{Au}_5(\text{CO})_5^+$  shown in Figure 5.4 can be described as a side capped tetrahedral type arrangement with one CO attached atop of each of the five gold atoms.

The corresponding sequential CO binding energy values are listed in Table 5.1. The calculated binding energy of the first CO amounts to 1.21 eV and is in quite good agreement with the experimental and theoretical literature values of 1.04 and 1.25 eV, respectively.<sup>111,112</sup> The binding energy of CO to bulk Au surfaces ( $0.55 \pm 0.05$  eV for  $\text{Au}(110)$ <sup>228</sup>) is only reached for clusters with more than 30 atoms.<sup>111</sup>



**Figure 5.4:** Calculated geometries of the  $\text{Au}_5(\text{CO})_q^+$  cluster complexes ( $q = 0-5$ ). Gold atoms are represented by yellow spheres, carbon atoms by green spheres, and oxygen atoms by red spheres. The depicted geometries have been obtained employing DFT at the B3LYP/TZVP level.

The binding energy of the second CO is similar to the first one and  $E_b$  only slightly decreases for the next two ligand molecules. However, with only 0.18 eV the fifth CO is much more weakly bound than the first four. This is in accordance with the experimental observation that a fifth CO ligand is only adsorbed at reduced temperatures (cf. Figures 5.1 and 5.2).

#### **5.2.3.2 $\text{Ag}_2\text{Au}_3(\text{CO})_q^+$ ( $q = 1-5$ )**

The lowest energy structures of the cationic bimetallic pentamers  $\text{Ag}_2\text{Au}_3^+$ ,  $\text{Ag}_3\text{Au}_2^+$ , and  $\text{Ag}_4\text{Au}^+$  all exhibit a twisted (non-planar) X-shaped structure as displayed in Figure 5.5. The structure calculated in the present work for  $\text{Ag}_2\text{Au}_3^+$  is similar to the previously reported geometry.<sup>84</sup>

The reaction of one CO molecule with the gold-rich bimetallic pentamers  $\text{AgAu}_4^+$  and  $\text{Ag}_2\text{Au}_3^+$  has been investigated experimentally as well as theoretically by Neumeier et al.<sup>112,227</sup> This group found the exclusive adsorption of the first CO atop of a peripheral (corner) gold atom. This is in agreement with our calculations for  $\text{Ag}_2\text{Au}_3^+$ . Also our calculated binding energy value for this case (0.84 eV) is in good agreement with the previous experimental (0.78 eV, cf. Table 5.1) and theoretical (0.9 eV) values.<sup>227</sup> The calculated binding energies of the first CO molecule decrease with increasing silver content in the clusters as is apparent from Table 5.1, in accordance with the previous investigations.<sup>112</sup>

As can be seen from Figure 5.5, our calculations indicate that the subsequent two CO molecules are adsorbed at silver corner atoms of the lowest energy structure of  $\text{Ag}_2\text{Au}_3^+$  with  $E_b$  values comparable to the first CO (see Table 5.1). For the binding of the fourth CO to the vacant Au corner atom of  $\text{Ag}_2\text{Au}_3^+$  an  $E_b$  value of 0.58 eV has been calculated. Upon adsorption of the fifth CO the side capped tetrahedral type arrangement is calculated to be the lowest energy structure; other structural isomers are at least 0.1 eV higher in energy. Therefore, a change in the geometry of the  $\text{Ag}_2\text{Au}_3^+$  cluster complex is predicted which goes along with a considerably smaller binding energy of 0.24 eV of the fifth CO in  $\text{Ag}_2\text{Au}_3(\text{CO})_5^+$  (see Table 5.1).

#### **5.2.3.3 $\text{Ag}_3\text{Au}_2(\text{CO})_q^+$ ( $q = 1-5$ )**

The cluster  $\text{Ag}_3\text{Au}_2^+$  and its carbonyl complexes have been investigated experimentally and theoretically here for the first time. The calculated lowest energy structure of the bare metal cluster is displayed in Figure 5.5 (middle row). In addition, two further isomers have been found that are close in energy to the shown structure of  $\text{Ag}_3\text{Au}_2^+$ . These are an X-shaped structure with a silver center atom, which is 0.044 eV higher in energy, and a trigonal bipyramidal structure with a central silver triangle, which is 0.054 eV less stable

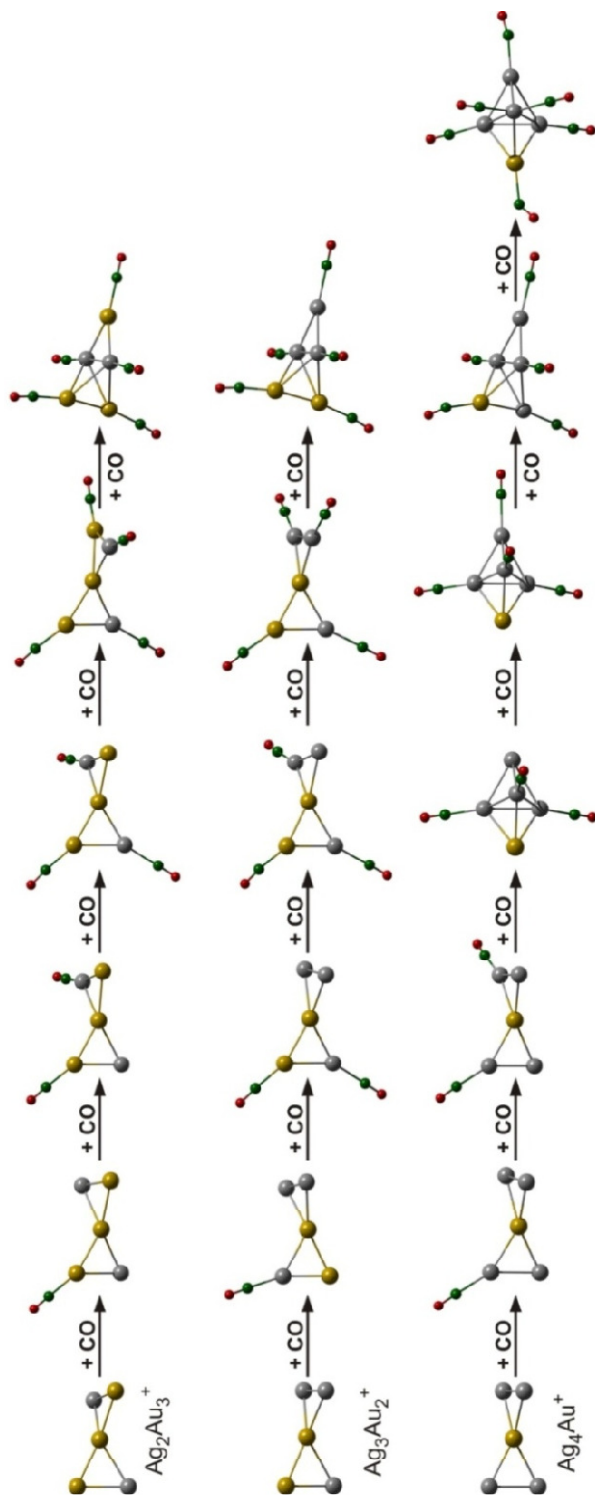


**Figure 5.5:** Computed structures of the binary silver-gold cluster carbonyls  $\text{Ag}_2\text{Au}_3(\text{CO})_q^+$  ( $q = 0-5$ ),  $\text{Ag}_3\text{Au}_2(\text{CO})_q^+$  ( $q = 0-5$ ), and  $\text{Ag}_4\text{Au}(\text{CO})_q^+$  ( $q = 0-6$ ) illustrating the sequential adsorption of carbon monoxide onto the lowest energy metal cluster isomer. Gold atoms are represented by yellow spheres, silver atoms by grey spheres, carbon atoms by green spheres, and oxygen atoms by red spheres. The depicted geometries have been obtained employing DFT at the B3LYP/TZVP level. Notice that for the sequential adsorption of CO the structures of complexes involving the lowest energy structure of the bare metal cluster are shown. Isomeric structures (generally within 0.1 eV) are given in the Supplementary Information.

than the structure depicted in Figure 5.5 (cf. also Supplementary Information, Figure S6). Other isomers of  $\text{Ag}_3\text{Au}_2^+$  are more than 0.2 eV less stable. The CO adsorption was studied on all of these structures, however, only the lowest energy isomer will be discussed in the following.

Interestingly, in contrast to  $\text{AgAu}_4^+$  and  $\text{Ag}_2\text{Au}_3^+$ , the first CO preferentially adsorbs atop of a corner silver instead of a gold atom in the case of  $\text{Ag}_3\text{Au}_2^+$ . The adsorption on a corner gold atom is, however, almost degenerate (+ 0.002 eV).

The general structural motifs of all the carbonyl clusters  $\text{Ag}_3\text{Au}_2(\text{CO})_q^+$  ( $q = 1-5$ ) are very similar to those of  $\text{Au}_5(\text{CO})_q^+$  (Figure 5.4) and  $\text{Ag}_2\text{Au}_3(\text{CO})_q^+$  (first row of Figure 5.5) with the same number  $q$  of CO ligands. Upon adsorption of the fifth CO the metal cluster structure changes from a X-shaped geometry to a side capped tetrahedral type arrangement.

Experimental binding energy values have been obtained for  $\text{Ag}_3\text{Au}_2(\text{CO})_q^+$  ( $q = 3-5$ ). These data are in very good agreement with the corresponding calculated CO binding energies (see Table 5.1).

#### **5.2.3.4 $\text{Ag}_4\text{Au}(\text{CO})_q^+$ ( $q = 1-6$ )**

Also for  $\text{Ag}_4\text{Au}^+$ , neither calculations nor experiments have been reported previously. The calculated lowest energy isomer of the metal cluster is the twisted X-shaped structure with a center gold atom (see Figure 5.5, bottom row). All other isomers are at least 0.13 eV less stable.

The calculated binding energies of the first three CO molecules of 0.62, 0.59, and 0.57 eV are in quite good agreement with the experimentally obtained values of 0.77, 0.73, and 0.55 eV, respectively (cf. Table 5.1). The calculated lowest energy structures of the complexes  $\text{Ag}_4\text{Au}(\text{CO})_q^+$  ( $q = 1-2$ ) predict a CO adsorption atop the corner silver atoms of the X-shaped structure for the first two CO. However, a striking structural transformation occurs upon adsorption of the third CO.

This structural transformation leads to a trigonal bipyramidal geometry as shown in Figure 5.5 ( $\text{Ag}_4\text{Au}(\text{CO})_3^+$ ). In this structure the three CO molecules are adsorbed atop the silver atoms at the trigonal center of the cluster. The isomer of  $\text{Ag}_4\text{Au}(\text{CO})_3^+$  closest in energy to the shown geometry is a twisted X-shaped complex structure which is 0.045 eV less stable.

The calculated binding energy of the fourth CO to the trigonal bipyramidal complex structure amounts to 0.31 eV (Table 5.1). This is notably less than the binding energies of the first three CO, however, the experimental results indicate an even weaker binding of the fourth CO of only 0.05 eV (see Table 5.1). This extremely weak and unfavorable binding interaction of the fourth (as well as of the fifth and sixth) CO measured experimentally is also reflected in the negative slopes of the Gibbs free energy

**Table 5.1:** Binding energies (in eV) of the  $q^{\text{th}}$  CO in the complexes  $\text{Ag}_n\text{Au}_m(\text{CO})_q^+$  for all investigated metal cluster cations. Experimental values (exptl.) are compared to theoretical data (calculated according to Equation (8)) obtained via the different methods as indicated (cf. also Section 2.2). The error of the experimental thermochemical equilibrium data is estimated to be within  $\pm 0.1$  eV.

Cluster	Complex	$\text{X}_5\text{CO}^+$	$\text{X}_5(\text{CO})_2^+$	$\text{X}_5(\text{CO})_3^+$	$\text{X}_5(\text{CO})_4^+$	$\text{X}_5(\text{CO})_5^+$	$\text{X}_5(\text{CO})_6^+$	$\text{X}_5(\text{CO})_7^+$
$\text{Au}_5^+$	exptl.	1.04 <sup>a</sup>						
	B3LYP	1.21	1.22	0.91	0.81	0.18		
$\text{Ag}_2\text{Au}_3^+$	exptl.	0.78 <sup>a</sup>						
	B3LYP	0.84	0.78	0.72	0.58	0.24		
$\text{Ag}_3\text{Au}_2^+$	exptl.							
	B3LYP	0.78	0.68	0.52	0.47	0.33		
$\text{Ag}_4\text{Au}^+$	exptl.	0.77	0.73	0.55	0.05	0.07	0.07	
	B3LYP	0.62	0.59	0.57	0.31	0.27	0.05	
$\text{Ag}_5^+$	exptl.	0.57	0.55	0.52	0.08	0.08	0.03	0.04
	B3LYP	0.56	0.54	0.46	0.43	0.17	0.09	0.13
	BP86	0.79	0.77	0.91	0.44	0.50		
	B3PW91	0.61	0.60	0.67	0.33	0.35	0.23	0.18
	CCSD	0.51	0.50	0.58	0.31			

<sup>a</sup>Taken from Reference 227.



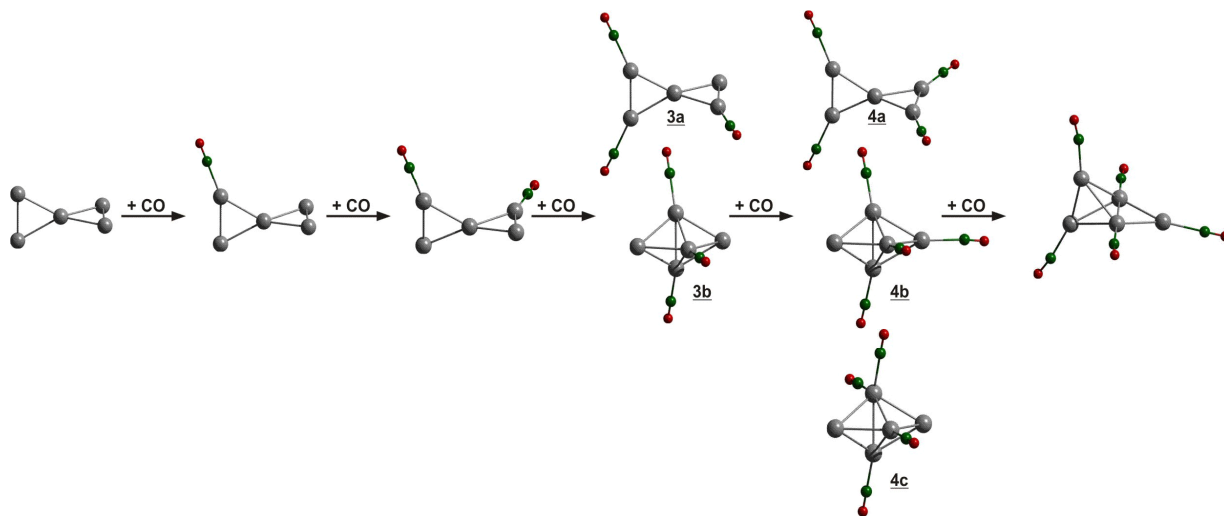


**Figure 5.6:** Ground state geometries of  $\text{Ag}_5(\text{CO})_q^+$  carbonyl complexes obtained by employing DFT with different functionals and basis sets as well as by using coupled cluster SD theory. Isomeric structures are shown for  $\text{Ag}_5(\text{CO})_3^+$  and  $\text{Ag}_5(\text{CO})_4^+$  where different theoretical approaches lead to different ground state geometries (see text for discussion). The corresponding CO binding energies obtained with the different methods are compared in Figure 5.7.

graphs for these adsorption reactions (cf. Figure 5.3b).

Apparently, however, the B3LYP calculations overestimate the weak binding energy of the fourth (0.31 eV) and fifth CO (0.27 eV) to  $\text{Ag}_4\text{Au}^+$ . The calculated binding energy of the sixth CO (0.05 eV) is again in good accord with the experimental value (0.06 eV). The lowest energy structures of  $\text{Ag}_4\text{Au}(\text{CO})_5^+$  and  $\text{Ag}_4\text{Au}(\text{CO})_6^+$  are shown in Figure 5.5. For both of these complexes, the side capped tetrahedral type arrangement and the trigonal bipyramidal geometry are, however, almost degenerate.

The observation that the B3LYP calculations apparently fail to accurately reproduce the surprisingly small experimental binding energies of the fourth and the fifth CO to the metal cluster  $\text{Ag}_4\text{Au}^+$ , whereas all other CO binding energies are in excellent agreement with the experimental data, is even more striking for the pure silver cluster carbonyls  $\text{Ag}_5(\text{CO})_q^+$  as will be discussed in the following section.

### 5.2.3.5 $\text{Ag}_5(\text{CO})_q^+$

The lowest energy isomer of  $\text{Ag}_5^+$  obtained in this work has the twisted X-shaped geometry displayed in Figure 5.6 independent of the employed theoretical method and in accordance with earlier calculations.<sup>99,117</sup>

No geometrical structures of silver cluster carbonyl complexes and no CO binding

energies to  $\text{Ag}_5^+$  (or any other silver cluster, except the atomic ion  $\text{Ag}^+$ )<sup>173</sup> have been reported so far, neither experimentally, nor theoretically. The binding energies for the first three CO molecules to  $\text{Ag}_5^+$  calculated here employing the B3LYP functional with the triple zeta basis set are in good agreement with the experimentally determined values (see Table 5.1). Yet, the calculated binding energy for the fourth CO in  $\text{Ag}_5(\text{CO})_4^+$  (0.43 eV) is considerably higher than the experimental result (0.08 eV). The theoretically obtained binding energies for the fifth to seventh CO ( $\text{Ag}_5(\text{CO})_q^+$ ,  $q = 5-7$ ) agree again quite well with the experimentally obtained data (all  $E_{b,\text{exptl.}} < 0.1$  eV for  $\text{Ag}_5(\text{CO})_q^+$ ,  $q > 3$ ).

The structures of the silver carbonyl complexes  $\text{Ag}_5(\text{CO})_q^+$  ( $q = 1-5$ ) calculated in the B3LYP formalism are depicted in Figure 5.6. For  $\text{Ag}_5(\text{CO})_2^+$ , an isomer with the two CO molecules adsorbed at adjacent corner site Ag atoms is only 0.06 eV higher in energy than the displayed structure. For  $\text{Ag}_5(\text{CO})_3^+$ , the shown isomers 3a and 3b are degenerate in energy. For  $\text{Ag}_5(\text{CO})_4^+$ , the B3LYP calculation gives 4a as ground state structure with all other isomers being more than 0.1 eV less stable. The side capped tetrahedral structure is preferred for  $\text{Ag}_5(\text{CO})_q^+$  with  $q = 5-7$ . In  $\text{Ag}_5(\text{CO})_6^+$  and  $\text{Ag}_5(\text{CO})_7^+$  (not shown in Figure 5.6) CO is also always bound in  $\mu_1$ -atop position, i.e., no bridged adsorption sites have been identified.

The calculated B3LYP binding energies for  $q = 1-5$  are graphically displayed together with the experimentally obtained binding energies in Figure 5.7a, which clearly illustrates that the binding energy of the fourth CO in  $\text{Ag}_5(\text{CO})_4^+$  is overestimated by the B3LYP calculations.

To elucidate the deviation of the otherwise very successful B3LYP theory from the experiment in the case of the binding energy of the weakly bound fourth CO in  $\text{Ag}_5(\text{CO})_4^+$  and to obtain more accurate theoretical  $E_b$  values, different DFT functionals and a coupled cluster approach have been employed to re-calculate the silver carbonyl complexes (cf. Section 3.4).

In Figure 5.7b the binding energy trend of the  $q^{\text{th}}$  CO in the lowest energy cluster complex structures of  $\text{Ag}_5(\text{CO})_q^+$  ( $q = 1-5$ ) are summarized as a function of the CO coverage for the various theoretical approaches other than B3LYP (see also Table 5.1 and Figure 5.6).

For the mono-carbonyl complex  $\text{Ag}_5(\text{CO})^+$  all theoretical methods yield the same lowest energy structure displayed in Figure 5.6. The theoretical binding energies of the first CO obtained with the different theoretical methods compare well with the experimental value of 0.57 eV with the exception of the CO binding energy calculated with the BP86 functional which is about 0.2 eV larger than all the other calculated values and the experimental value (see Table 5.1). Generally, the BP86 functional yields  $E_b$  values that are too high for all  $\text{Ag}_5(\text{CO})_q^+$  complexes. For comparison, the CO binding energy to a bulk silver surface amounts to  $0.28 \pm 0.02$  eV.<sup>229</sup>

The experimental binding energy of the second CO is similar to the first. All methods again result in the same geometry of the  $\text{Ag}_5(\text{CO})_2^+$  complex and the theoretical

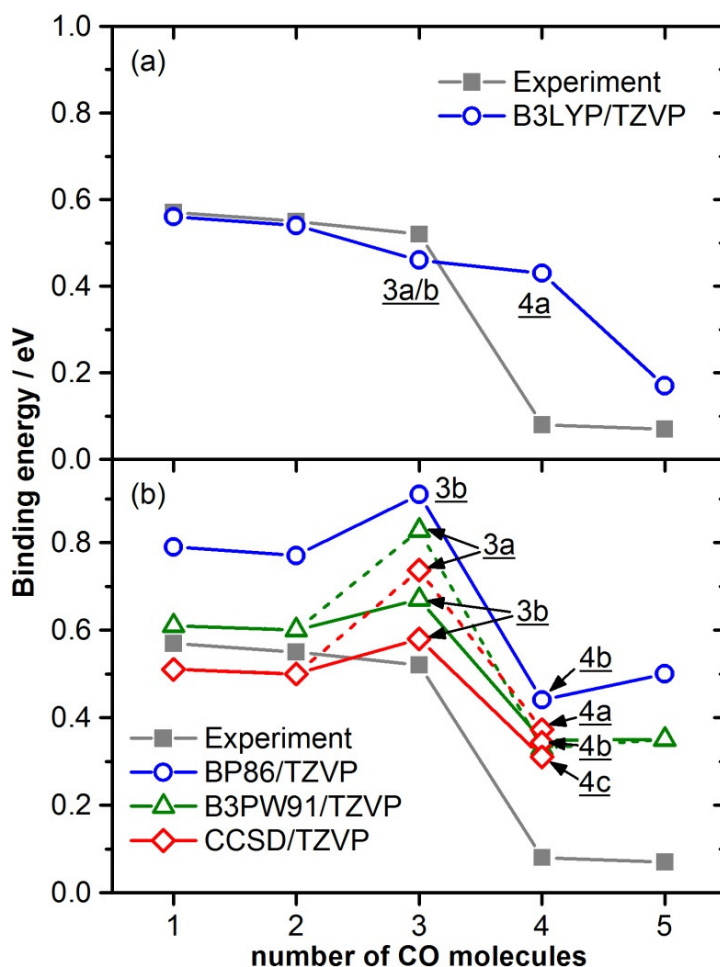


**Figure 5.7:** CO binding energies as a function of the number of CO molecules. The calculated values that have been obtained employing the different theoretical methods as indicated (open symbols) are compared to the experimentally deduced values (solid squares). Dashed lines in (b) indicate higher energy isomeric structures. The labels (3a-b, 4a-c) indicate that these data correspond to the respective structures shown in Figure 5.6.

binding energies (except the BP86 value) are in good agreement with the experimental value of 0.55 eV (cf. Table 5.1 and Figure 5.6).

The measured binding energy of the third CO in  $\text{Ag}_5(\text{CO})_3^+$  (0.52 eV) is very similar to the previous two CO binding energies. Most importantly, our calculations using all the different methods indicate a structural transformation of the  $\text{Ag}_5^+$  cluster with the adsorption of the third CO leading to the trigonal bipyramidal complex structure labeled 3b in Figure 5.6. Employing the B3LYP/TZVP functional this geometry is found to be almost degenerate (+0.005 eV) with the X-shaped structure 3a (Figure 5.6), but for all other methods the trigonal bipyramidal structure 3b is more than 0.15 eV lower in energy than structure 3a.

It is interesting to note that these latter methods (BP86, B3PW91, CCSD) also

predict an increase in the CO binding energy for the third CO compared to the previous two (see Table 5.1 and Figure 5.7b). And, strikingly, these methods yield the dramatic drop in the CO binding energy for the fourth CO that has been observed experimentally (Figure 5.7b) and that was not reproduced by the B3LYP method (Figure 5.7a).

Yet, the quantitative theoretical binding energies for the fourth CO in  $\text{Ag}_5(\text{CO})_4^+$  shown in Figure 5.7b are still larger than the experimental value of 0.08 eV. Comparing the different methods summarized in Figure 5.7b (and Table 5.1) it is apparent that the coupled cluster method yields the value closest to the experiment for the geometrical structure 4c of  $\text{Ag}_5(\text{CO})_4^+$  in Figure 5.6. Isomer 4b, also a trigonal bipyramidal structure, is very close in energy.

This leads to the conclusion that the very weak adsorption energies observed experimentally for the fourth CO in  $\text{Ag}_5(\text{CO})_4^+$  cannot be adequately reproduced by DFT based on the B3LYP functional. In addition, this method does indicate a possible transformation to a more compact trigonal bipyramidal geometry for  $\text{Ag}_5(\text{CO})_3^+$ , however, the X-shaped structure is still calculated to be almost degenerate in energy.

Only the coupled cluster SD method was found to unambiguously identify the trigonal bipyramidal structure as lowest energy isomer of  $\text{Ag}_5(\text{CO})_3^+$  and to yield the quantitative binding energy values closest to the experimental data (cf. Figures 5.6 and 5.7).

For larger numbers of CO ( $q > 4$ ) all theoretical methods favor the side-capped tetrahedral structure with (multiple)  $\mu_1$ -atop CO adsorption as major structural motif of  $\text{Ag}_5(\text{CO})_q^+$  ( $q = 5-7$ ).

## 5.3 Conclusions

A detailed joint experimental and theoretical investigation of the adsorption of multiple CO molecules onto binary silver-gold cluster cations reveals a strong dependence of the cluster complex geometry on the number of CO ligands as well as on the metal cluster composition. Sequential experimental CO binding energies have been obtained for several of the carbonyl complexes  $\text{Ag}_n\text{Au}_m(\text{CO})_q^+$  ( $n + m = 5$ ,  $q = 1-7$ ). These binding energies are generally in excellent agreement with the results of the DFT first principles calculations employing the B3LYP functional with the exception of  $\text{Ag}_4\text{Au}(\text{CO})_4^+$  and  $\text{Ag}_5(\text{CO})_4^+$ , where the unexpectedly weak bonding interaction of the fourth CO is better described by the more accurate wave function based CCSD calculation.

The temperature dependent CO coverage of the five-atom noble metal clusters (Figures 5.1 and 5.2), the deduced experimental binding energies (Table 5.1), as well as the calculated theoretical structures (Figures 5.4 to 5.6) conclusively support the occurrence of a major CO induced structural transformation to a more compact trigonal

bipyramidal metal cluster structure for  $\text{Ag}_5(\text{CO})_3^+$  (Structure 3b in Figure 5.6). Such a structural transformation has been proposed previously to occur for the adsorption of three ethylene ligands on  $\text{Ag}_5^+$ .<sup>117,230</sup> Our data clearly indicate that a similar geometric rearrangement is the explanation for the CO coverage dependent binding energies in the case of the silver-rich cluster complex  $\text{Ag}_4\text{Au}(\text{CO})_q^+$  ( $q = 1-6$ ) (Figure 5.4).

For the gold cluster carbonyls  $\text{Au}_5(\text{CO})_q^+$  and the binary silver-gold cluster carbonyls  $\text{Ag}_2\text{Au}_3(\text{CO})_q^+$  and  $\text{Ag}_3\text{Au}_2(\text{CO})_q^+$  ( $q = 1-5$ ) a structural transformation of the metal cluster complexes is proposed here to occur upon adsorption of the fifth CO molecule from the X-shaped to a side capped tetrahedral type arrangement. This observation is in excellent agreement with previous vibrational spectra of  $\text{Au}_5(\text{CO})_4^+$  and  $\text{Au}_5(\text{CO})_5^+$  the latter of which exhibits two different CO vibrational frequencies, whereas for  $\text{Au}_5(\text{CO})_4^+$  only a single absorption line is observed in the IR spectrum.<sup>114</sup>

The results obtained here for multiple CO adsorption on binary silver-gold clusters emphasize the previously described structural rigidity of gold clusters,<sup>231</sup> due to the presence of relativistic effects that support directional bonding. In contrast, silver clusters exhibit a much more viable structural fluxionality which is exerted in the present case in a pronounced structural transformation upon bonding of three CO which in turn strongly averts further CO adsorption.

These conceptual insights might have potential prospects for the design of binary metal cluster catalysts for reactions (5.1) to (5.3) where the steering of the bonding strength of multiple CO adsorbates might be highly desirable with respect to the availability of vacant adsorption sites and their reactivity in the metal catalyzed bimolecular reaction mechanisms.

## 5.4 Supporting information

### I. $\text{Ag}_2\text{Au}_3^+ + \text{CO}$

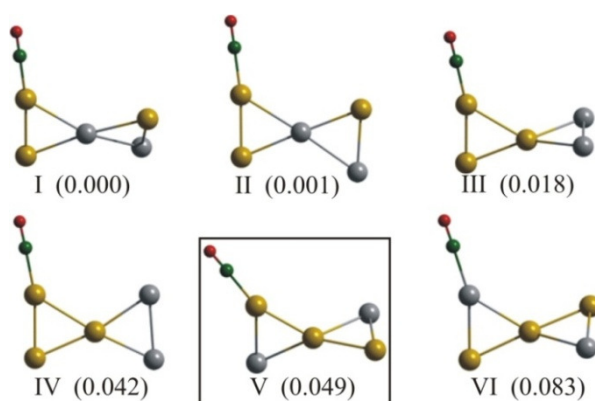


**Figure S1:** The lowest energy isomers of  $\text{Ag}_2\text{Au}_3\text{CO}^+$  within 0.1 eV obtained from DFT with B3LYP functional and TZVP atomic basis set. Notice that isomer V shown in window is used in Fig. 5 to illustrate the sequential adsorption of CO.

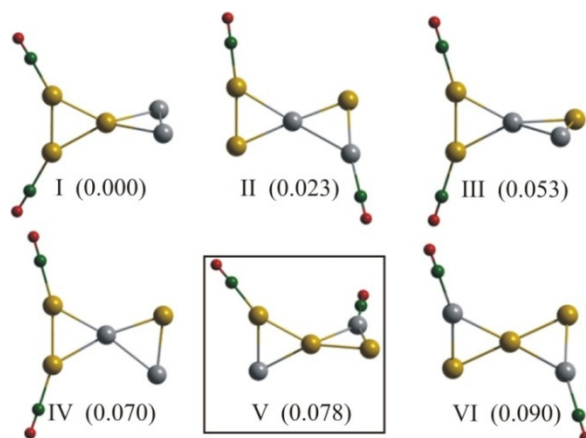


**Figure S2:** The lowest energy isomers of  $\text{Ag}_2\text{Au}_3(\text{CO})_2^+$  within 0.1 eV obtained from DFT with B3LYP functional and TZVP atomic basis set. Notice that isomer V shown in window is used in Fig. 5 to illustrate the sequential adsorption of CO.

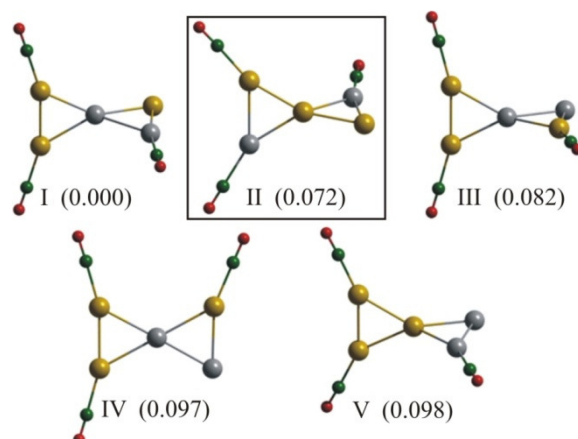


**Figure S3:** The lowest energy isomers of  $\text{Ag}_2\text{Au}_3(\text{CO})_3^+$  within 0.1 eV obtained from DFT with B3LYP functional and TZVP atomic basis set. Notice that isomer II shown in window is used in Fig. 5 to illustrate the sequential adsorption of CO.

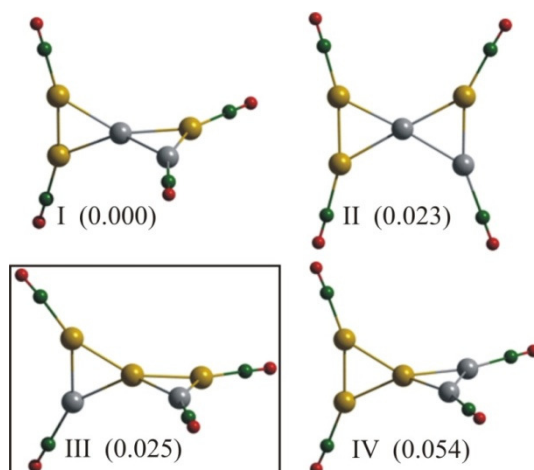


**Figure S4:** The lowest energy isomers of  $\text{Ag}_2\text{Au}_3(\text{CO})_4^+$  within 0.1 eV obtained from DFT with B3LYP functional and TZVP atomic basis set. Notice that isomer III shown in window is used in Fig. 5 to illustrate the sequential adsorption of CO.

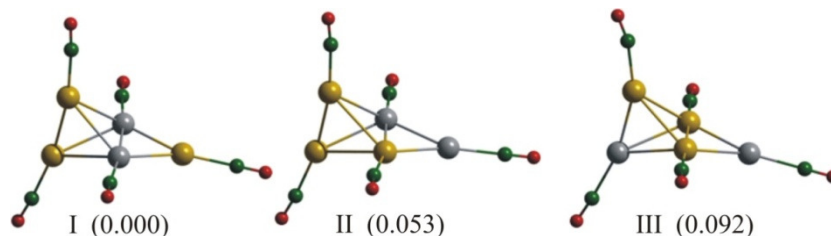


**Figure S5:** The lowest energy isomers of  $\text{Ag}_2\text{Au}_3(\text{CO})_5^+$  within 0.1 eV obtained from DFT with B3LYP functional and TZVP atomic basis set.

## II. $\text{Ag}_3\text{Au}_2^+ + \text{CO}$

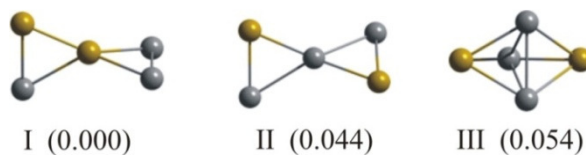


**Figure S6:** The lowest energy isomers of  $\text{Ag}_3\text{Au}_2^+$  obtained from DFT with B3LYP functional and TZVP atomic basis set. All other isomers are more than 0.2 eV less stable.

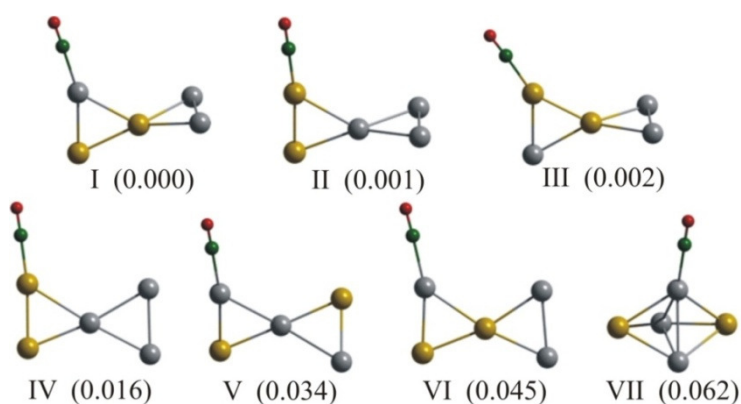


**Figure S7:** The lowest energy isomers of  $\text{Ag}_3\text{Au}_2\text{CO}^+$  within 0.1 eV obtained from DFT with B3LYP functional and TZVP atomic basis set.

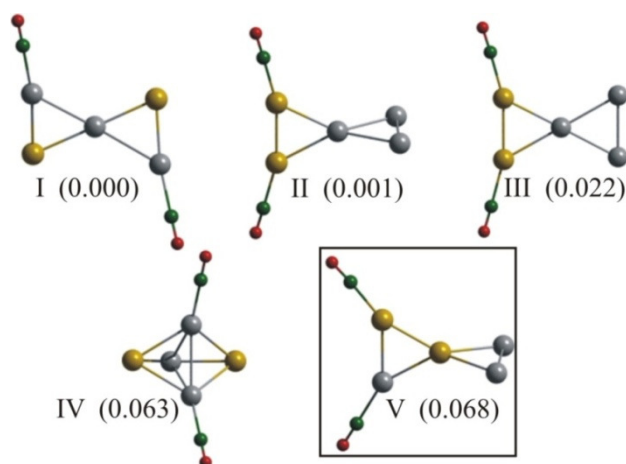


**Figure S8:** The lowest energy isomers of  $\text{Ag}_3\text{Au}_2(\text{CO})_2^+$  within 0.1 eV obtained from DFT with B3LYP functional and TZVP atomic basis set. Notice that isomer V shown in window is used in Fig. 5 to illustrate the sequential adsorption of CO.



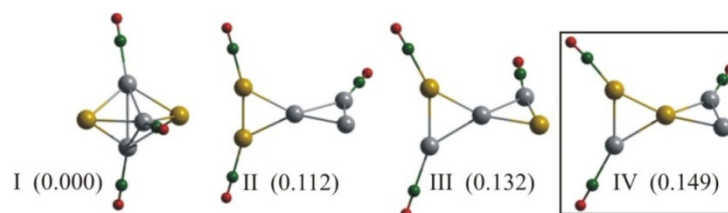


**Figure S9:** The lowest energy isomers of  $Ag_3Au_2(CO)_3^+$  within 0.15 eV obtained from DFT with B3LYP functional and TZVP atomic basis set. Notice that isomer IV shown in window is used in Fig. 5 to illustrate the sequential adsorption of CO.

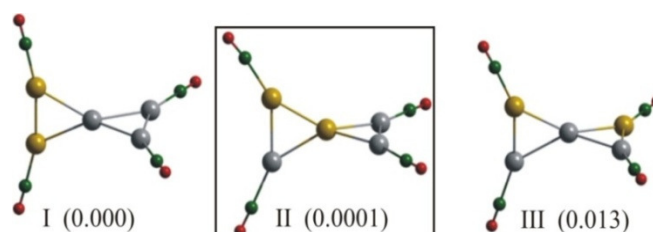


**Figure S10:** The lowest energy isomers of  $Ag_3Au_2(CO)_4^+$  within 0.1 eV obtained from DFT with B3LYP functional and TZVP atomic basis set. Notice that isomer II shown in window is used in Fig. 5 to illustrate the sequential adsorption of CO.

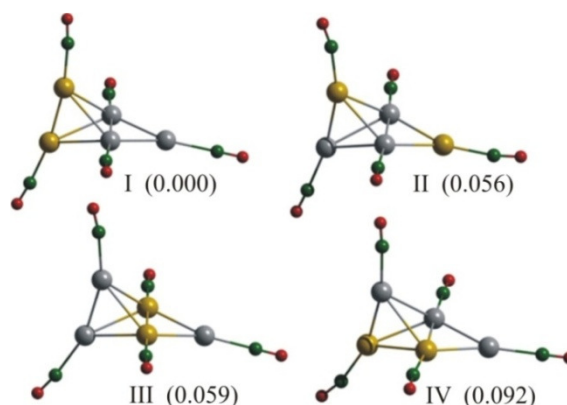


**Figure S11:** The lowest energy isomers of  $Ag_3Au_2(CO)_5^+$  within 0.1 eV obtained from DFT with B3LYP functional and TZVP atomic basis set.

### III. $\text{Ag}_4\text{Au}^+ + \text{CO}$

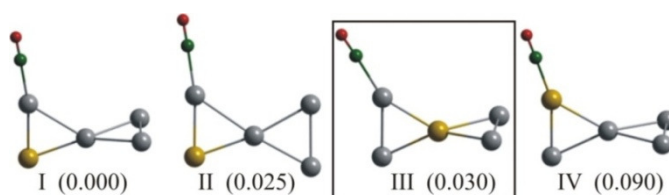


**Figure S12:** The lowest energy isomers of  $\text{Ag}_4\text{AuCO}^+$  within 0.1 eV obtained from DFT with B3LYP functional and TZVP atomic basis set. Notice that isomer III shown in window is used in Fig. 5 to illustrate the sequential adsorption of CO.

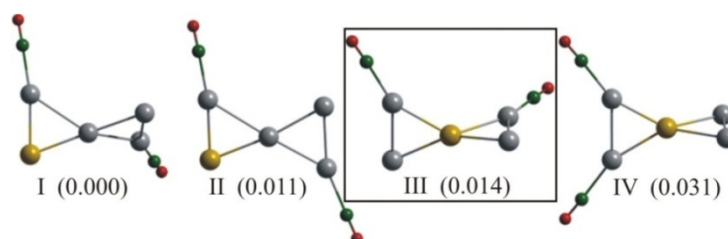


**Figure S13:** The lowest energy isomers of  $\text{Ag}_4\text{Au}(\text{CO})_2^+$  within 0.1 eV obtained from DFT with B3LYP functional and TZVP atomic basis set. Notice that isomer III shown in window is used in Fig. 5 to illustrate the sequential adsorption of CO.

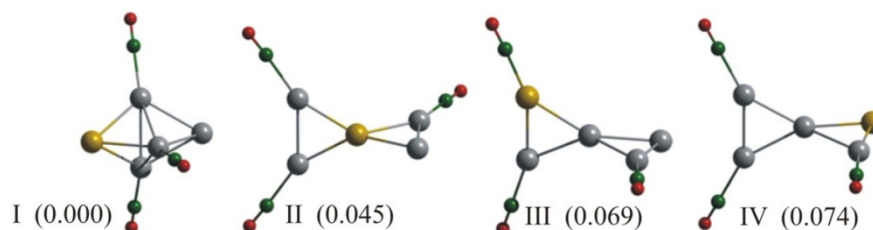


**Figure S14:** The lowest energy isomers of  $\text{Ag}_4\text{Au}(\text{CO})_3^+$  within 0.1 eV obtained from DFT with B3LYP functional and TZVP atomic basis set.

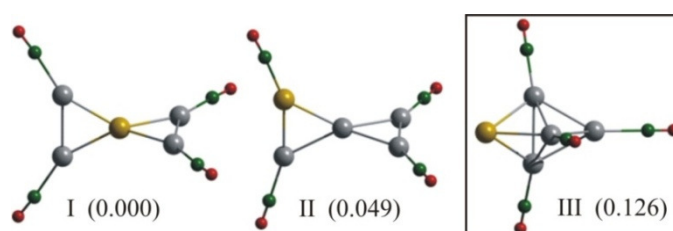


**Figure S15:** The lowest energy isomers of  $\text{Ag}_4\text{Au}(\text{CO})_4^+$  within 0.13 eV obtained from DFT with B3LYP functional and TZVP atomic basis set. Notice that isomer III shown in window is used in Fig. 5 to illustrate the sequential adsorption of CO.

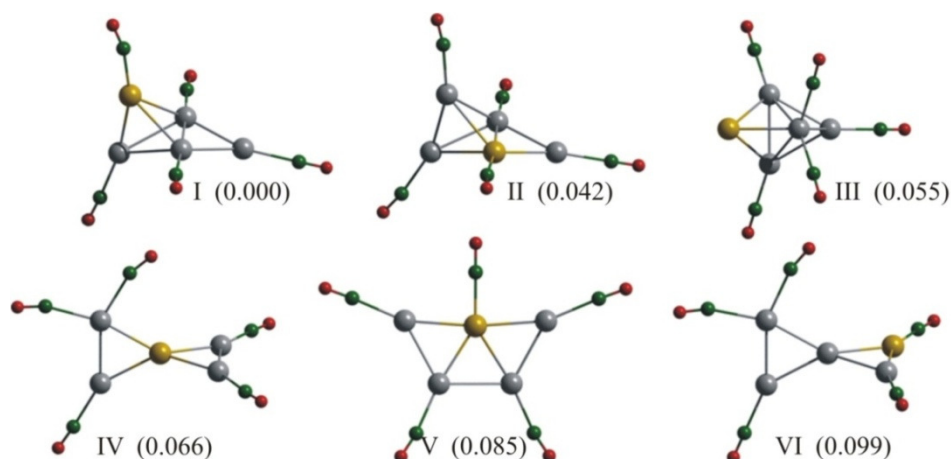


**Figure S16:** The lowest energy isomers of  $\text{Ag}_4\text{Au}(\text{CO})_5^+$  within 0.1 eV obtained from DFT with B3LYP functional and TZVP atomic basis set.

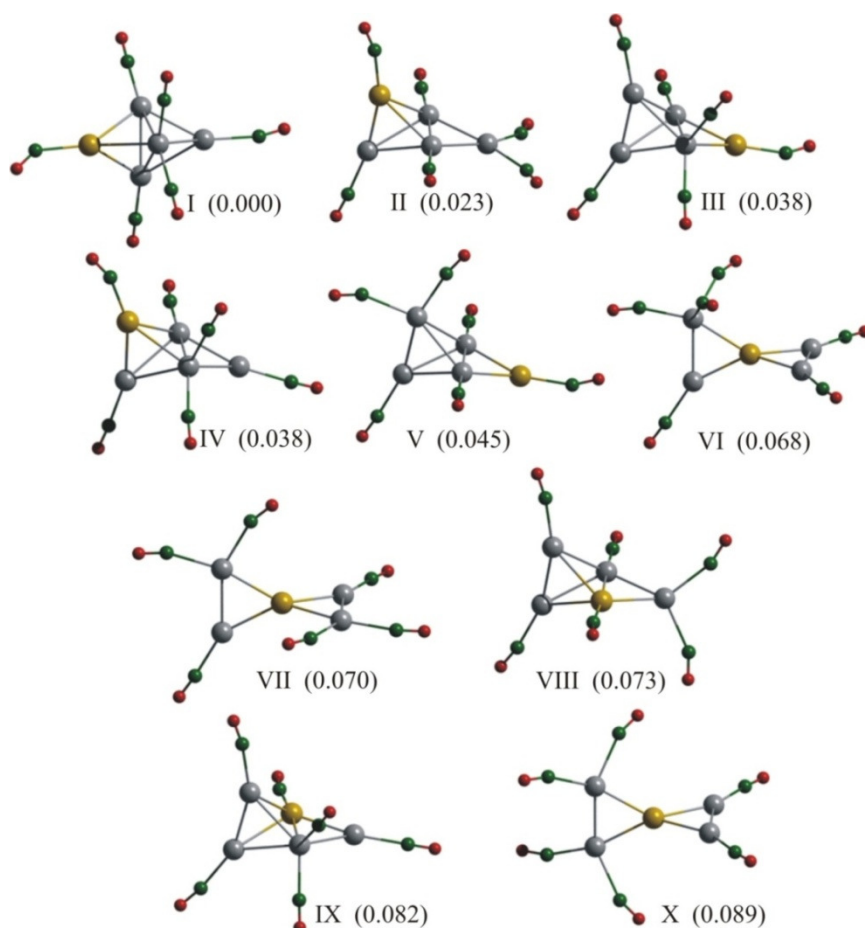


**Figure S17:** The lowest energy isomers of  $\text{Ag}_4\text{Au}(\text{CO})_6^+$  within 0.1 eV obtained from DFT with B3LYP functional and TZVP atomic basis set.



# 6

## Reactions of free $\text{Ag}_3^+$ clusters with $\text{N}_2\text{O}$ and mixtures of $\text{N}_2\text{O}$ and $\text{CO}^*$

---

*The gas-phase reactions of  $\text{Ag}_3^+$  clusters with  $\text{N}_2\text{O}$  were investigated under well defined reaction conditions in the octopole ion trap. The temperature was found to be a crucial parameter since different product channels could be activated for various reaction temperatures. At room temperature  $\text{Ag}_3^+$  did not react with  $\text{N}_2\text{O}$ , but at temperatures just below 270 K the formation of  $\text{Ag}_3\text{O}_x^+$  ( $x = 1-3$ ) products competed with the formation of  $\text{Ag}_3\text{O}_x(\text{N}_2\text{O}_2)_y^+$  ( $x, y = 1-3, x \geq y$ ) complexes. At 200 K only products corresponding to  $\text{Ag}_3(\text{N}_2\text{O})_n^+$  ( $n = 2, 3$ ) were observed. In order to reveal the reaction mechanism, detailed kinetic measurements were performed and the results are discussed in comparison to *ab initio* DFT calculations. In addition to  $\text{N}_2\text{O}$  also small, well defined amounts of  $\text{CO}$  were admitted to the ion trap. First evidence for a successful catalytic conversion  $\text{CO} + \text{N}_2\text{O} \rightarrow \text{CO}_2 + \text{N}_2$  is presented. Most interestingly, the catalytically active species were identified to be oxidized silver clusters  $\text{Ag}_3\text{O}_x^+$  ( $x = 1-3$ ). As a consequence, two different oxygen atom species are involved in the oxidation of carbon monoxide in this case. One oxygen atom, which is actively involved in the oxidation of  $\text{CO}$  and weakly attached to the  $\text{Ag}_3\text{O}_x^+$  complex which in turn contains a second kind of oxygen atom that is firmly bound to the silver atoms.*

---

\* Parts of this chapter have been accepted as a contribution to *Journal of Chemical Physics*: D. M. Popolan, T. M. Bernhardt, “CO oxidation by silver and gold cluster cations: Identification of different active oxygen species”.

## 6.1 Reactions of $\text{Ag}_3^+$ with nitrous oxide: Mass spectra and kinetics

### 6.1.1 Introduction

Nitrous oxide is a potential greenhouse gas and constitutes the main source of stratospheric  $\text{NO}_x$  contributing to ozone depletion.<sup>232-234</sup> This has stimulated a great interest in the development and understanding of its metal mediated decomposition, especially involving heterogeneous metal-catalyzed  $\text{N}_2\text{O}$  decomposition.<sup>235-242</sup> On the other hand,  $\text{N}_2\text{O}$  is a clean and highly selective oxygen donor for catalytic oxidation processes due to the low O-atom affinity of  $\text{N}_2$  ( $\text{OA}(\text{N}_2) = 40 \text{ kcal mol}^{-1}$ ).<sup>48,221</sup> Generally,  $\text{N}_2\text{O}$  is recognized as a poor ligand to transition-metals owing to its weak  $\sigma$ -donating and  $\pi$ -accepting capabilities. The reaction pathways leading to N-O bond activation and to the formation of the metal oxide and  $\text{N}_2$  were found to be quite exothermic.

The gas-phase reactions of metal atoms with nitrous oxide have been extensively studied employing a variety of experimental methods.<sup>237,242,243</sup> Theoretical treatments generally supported the end-on O coordination of  $\text{N}_2\text{O}$  to the metal atom with subsequent charge transfer (metal to  $\text{N}_2\text{O}$ ) and concomitant M-O-NN bending along the N-O bond scission pathway.<sup>96,244,245</sup> Some recent reviews summarize the latest literature reports in which the main research goal was to understand the reactivity of  $\text{N}_2\text{O}$  with metal centers in a variety of environments including the gas phase, solid supports, enzymes, and soluble complexes in solutions.<sup>246,247</sup>

The reactivity of neutral gas-phase Ag with  $\text{N}_2\text{O}$  as a function of temperature and pressure was reported by Campbell.<sup>236</sup> The room temperature reactions of atomic silver cations with  $\text{N}_2\text{O}$  had been investigated using an inductively coupled plasma/selected-ion flow tube tandem mass spectrometer by Böhme and coworkers.<sup>238,239</sup> Nothing is known so far concerning the reactions of gas-phase silver clusters with nitrous oxide.

Silver particle catalysts find important industrial applications in the partial oxidation of, e.g., ethylene or methanol.<sup>248</sup> However, also only few information is available concerning the oxidation reactions catalyzed by very small silver clusters.<sup>63,107,198,228,249</sup> Since the  $\text{Ag}_3^+$  cluster was found to be unreactive to  $\text{O}_2$  under our experimental conditions,<sup>121</sup> our approach to produce silver-oxides was through reaction with  $\text{N}_2\text{O}$ . Surprisingly, this reaction exhibited a very complicated temperature dependent reaction mechanism, especially in the temperature range between 270 and 230 K. Not only the silver-oxide formation, but also a competitive formation of  $\text{Ag}_3\text{O}_x(\text{N}_2\text{O}_2)_y^+$  ( $x, y = 1-3, x \geq y$ ) products was observed.

In the following, mass spectra and kinetic measurements are presented on the basis of which a reaction mechanism for the oxidation of triatomic silver cations with nitrous oxide will be proposed. The experimental results are then discussed in the context of the results obtained by DFT *ab initio* calculation.

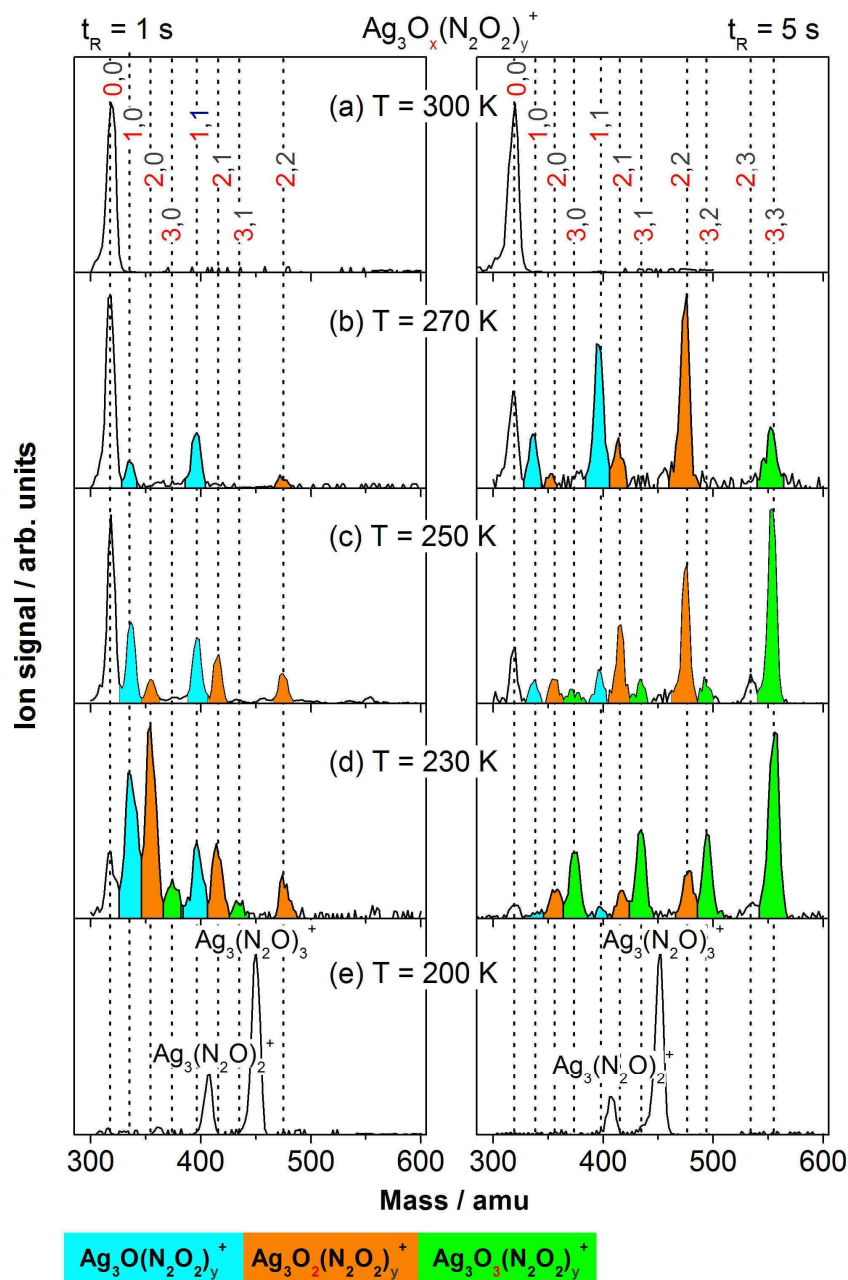


**Figure 6.1:** Product ion mass spectra obtained after the reaction of mass selected  $\text{Ag}_3^+$  with  $\text{N}_2\text{O}$  in the rf-ion trap for  $t_R = 1$  s (left column) and  $t_R = 5$  s (right column), respectively. The spectra were recorded at (a) 300 K, (b) 270 K, (c) 250 K, (d) 230 K, and (e) 200 K and well defined amount of He buffer gas ( $p(\text{He}) = 1$  Pa) and  $\text{N}_2\text{O}$  reactive gas ( $p(\text{N}_2\text{O}) = 0.1$  Pa). The mass peaks are labeled by (x,y) corresponding to complexes of the stoichiometry  $\text{Ag}_3\text{O}_x(\text{N}_2\text{O})_y^+$ .

### 6.1.2 Results and discussion

Product ion mass spectra for the reaction of mass-selected silver cluster  $\text{Ag}_3^+$  with  $\text{N}_2\text{O}$  recorded at different reaction temperatures (between 300 and 200 K) for two different reaction times ( $t_R = 1$  s (left hand side) and  $t_R = 5$  s (right hand side)) are depicted in Figure 6.1. As can be seen from Figure 6.1a no reaction products were formed at a temperature of 300 K and reaction times up to 5 s. Even for longer reaction times, i.e. up to 10 s, or higher quantities of  $\text{N}_2\text{O}$  (not shown here) no changes in the initially recorded mass spectra were observed. When the temperature was decreased to 270 K (Figure 6.1b), the formation of  $\text{Ag}_3\text{O}^+$  and  $\text{Ag}_3\text{O}(\text{N}_2\text{O}_2)^+$  could be measured already after 1 s reaction time. These reaction products must result from multiple  $\text{N}_2\text{O}$  adsorption correlated with the dissociation of the N-O bond of the  $\text{N}_2\text{O}$  molecules.

To our knowledge, this predominate formation of clusters containing equal amounts of  $\text{N}_2$  and  $\text{O}_2$  as in  $\text{Ag}_3\text{O}(\text{N}_2\text{O}_2)^+$  in addition to oxygen atoms, due to the reaction with  $\text{N}_2\text{O}$ , has not yet been reported. Of course, the experimental mass spectrometry investigation cannot determine the geometric structure of the  $\text{Ag}_3\text{O}(\text{N}_2\text{O}_2)^+$  complex. Nevertheless, several possible structures can be assumed for the  $\text{N}_2\text{-O}_2$  unit: (i) two separate NO molecules; (ii)  $(\text{NO})_2$ ; or (iii)  $\text{N}_2$  and  $\text{O}_2$  molecules independently bound to the cluster. Products with  $\text{Ag}_3\text{NONO}_2^+$  or  $\text{Ag}_3\text{N}_2\text{O}_3^+$  configurations could also not be excluded.

A close inspection of the mass spectra shown in Figure 6.1 for temperatures between 230 and 270 K reveals that only distinct product peaks appeared even for lower temperatures where more products are observed. Surprisingly enough, these peaks can all be grouped into sequences with similar mass differences that corresponded to the mass of a  $\text{N}_2\text{O}_2$  unit. Therefore, in Figure 6.1b-d these product peaks were color coded as follows: in blue  $\text{Ag}_3\text{O}^+$ , and  $\text{Ag}_3\text{O}(\text{N}_2\text{O}_2)^+$ ; in orange  $\text{Ag}_3\text{O}_2^+$ ,  $\text{Ag}_3\text{O}_2(\text{N}_2\text{O}_2)^+$ , and  $\text{Ag}_3\text{O}_2(\text{N}_2\text{O}_2)_2^+$  and in green those corresponding to  $\text{Ag}_3\text{O}_3^+$ ,  $\text{Ag}_3\text{O}_3(\text{N}_2\text{O}_2)^+$ ,  $\text{Ag}_3\text{O}_3(\text{N}_2\text{O}_2)_2^+$ , and  $\text{Ag}_3\text{O}_3(\text{N}_2\text{O}_2)_3^+$ . Also for convenience, in the following the  $\text{N}_2\text{-O}_2$  units will be denoted as  $(\text{N}_2\text{O}_2)$ .

At 270 K and a longer reaction time of 5 s, in addition to the initial reaction products, the formation of the new complexes  $\text{Ag}_3\text{O}_2^+$ ,  $\text{Ag}_3\text{O}_2(\text{N}_2\text{O}_2)^+$ ,  $\text{Ag}_3\text{O}_2(\text{N}_2\text{O}_2)_2^+$  (orange colored peaks), and  $\text{Ag}_3\text{O}_3(\text{N}_2\text{O}_2)_3^+$  were observed. As can be seen, even for a reaction time of 5 s considerable amounts of bare  $\text{Ag}_3^+$  were still present, the recorded mass spectra reflecting the poor reactivity of  $\text{Ag}_3^+$  towards nitrous oxide at this temperature.

When the temperature was decreased to 250 K (Figure 6.1c), the reaction products  $\text{Ag}_3\text{O}_2^+$ ,  $\text{Ag}_3\text{O}_2(\text{N}_2\text{O}_2)^+$ , and  $\text{Ag}_3\text{O}_2(\text{N}_2\text{O}_2)_2^+$  (orange colored peaks) were already present at a reaction time of 1 s. For a reaction time of 5 s (Figure 6.1c right) the  $\text{Ag}_3^+$  signal decreased considerably. Small amounts of the new products  $\text{Ag}_3\text{O}_3^+$ ,  $\text{Ag}_3\text{O}_3(\text{N}_2\text{O}_2)^+$ , and  $\text{Ag}_3\text{O}_3(\text{N}_2\text{O}_2)_2^+$  (green colored peaks) were measured in addition to the initially formed products. Most strikingly the  $\text{Ag}_3\text{O}_3(\text{N}_2\text{O}_2)_3^+$  peak strongly increased.

At 230 K, the intensity of the pure silver clusters again decreased and the formation of



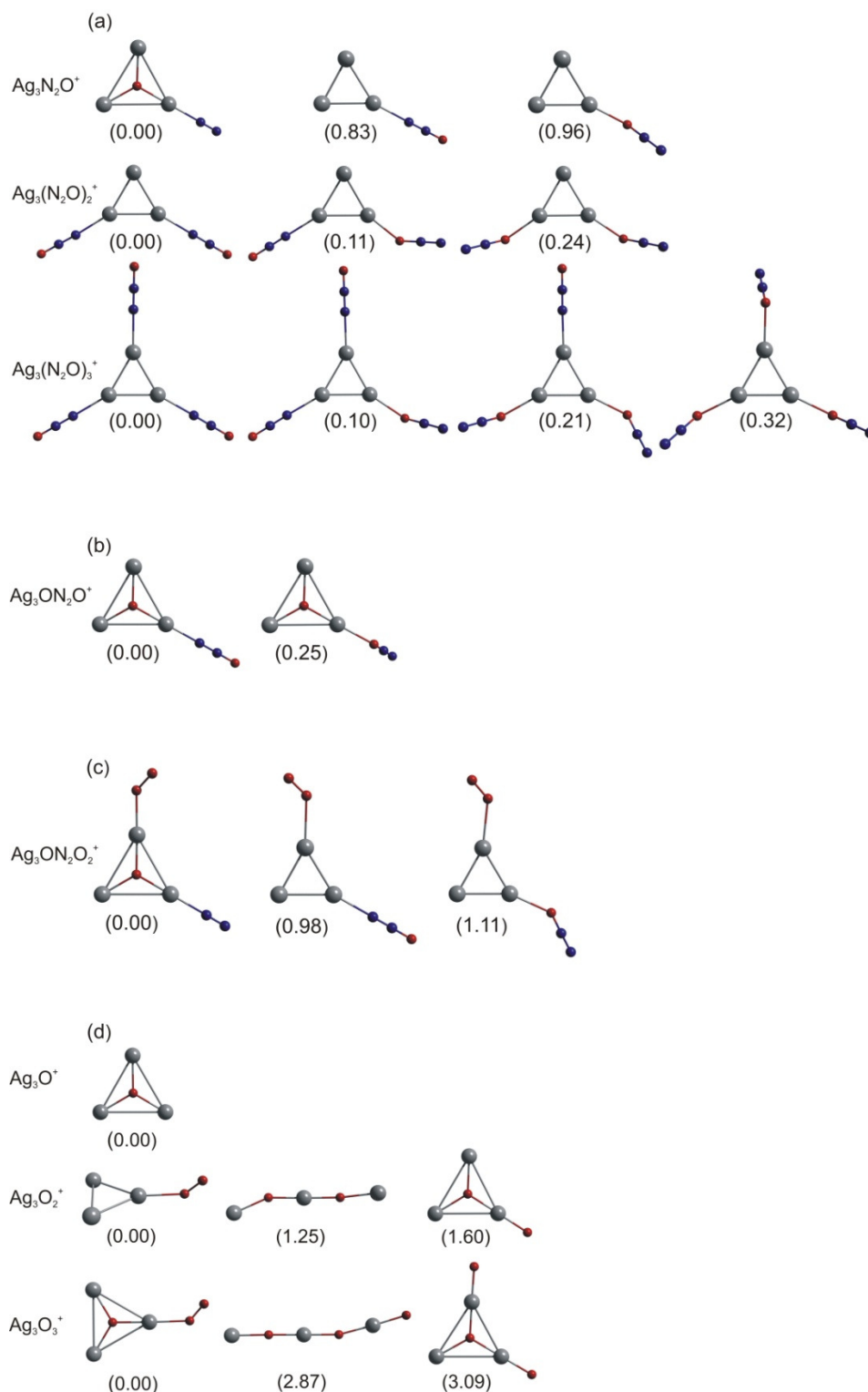


**Figure 6.2:** The lowest energy isomers of (a)  $\text{Ag}_3\text{O}_x^+$  ( $x = 1-3$ ) (b)  $\text{Ag}_3\text{ON}_2\text{O}^+$ , (c)  $\text{Ag}_3\text{O}(\text{N}_2\text{O}_2)^+$ , and (d)  $\text{Ag}_3(\text{N}_2\text{O})_x^+$  ( $x = 1-3$ ), obtained from DFT with B3LYP functional and TZVP atomic basis set by Bonačić-Koutecký et al..<sup>250</sup> Silver atoms are represented by the grey spheres, oxygen atoms by red sphere, and nitrogen atoms by blue spheres.

$\text{Ag}_3\text{O}_3^+$  was already observed at a reaction time of 1 s (Figure 6.1d). In addition to the silver-oxides  $\text{Ag}_3\text{O}_x^+$  ( $x = 1-3$ ), again only very distinct  $\text{Ag}_3\text{O}_x(\text{N}_2\text{O}_2)_y^+$  peaks were observed. The most intense product peaks at this temperature and at a reaction time of 5 s (Figure 6.1d right) corresponded to the green series, i.e.  $\text{Ag}_3\text{O}_3^+$ ,  $\text{Ag}_3\text{O}_3(\text{N}_2\text{O}_2)^+$ ,  $\text{Ag}_3\text{O}_3(\text{N}_2\text{O}_2)_2^+$ , and  $\text{Ag}_3\text{O}_3(\text{N}_2\text{O}_2)_3^+$ .

Finally, at 200 K (see Figure 6.1e) the product ion distribution completely changed. No  $\text{N}_2\text{O}$  dissociation occurred and the recorded reaction products corresponded to  $\text{Ag}_3(\text{N}_2\text{O})_2^+$  and  $\text{Ag}_3(\text{N}_2\text{O})_3^+$ , respectively. The  $\text{Ag}_3^+$  minimum energy structure is a planar equilateral triangle ( $D_{3h}$  symmetry)<sup>82,99,100,251</sup> with three electronically equivalent ‘corners’.<sup>82</sup> Thus, the maximum number of adsorbed  $\text{N}_2\text{O}$  molecules at 200 K equals the number of silver atoms, i.e. the number of corner sites in the corresponding ground state geometry. Figure 6.2a displays the calculated lowest energy structures of the  $\text{Ag}_3(\text{N}_2\text{O})_n^+$  ( $n = 1-3$ ) cluster complexes. As can be seen the saturated silver trimer structure corresponds to a stoichiometry with one  $\text{N}_2\text{O}$  molecule adsorbed at each Ag corner atom. The calculated lowest energy isomers of  $\text{Ag}_3\text{ONO}_2^+$  are displayed in Figure 6.2b.

Irrespective of the reaction temperature, reaction time or  $\text{N}_2\text{O}$  partial pressure no  $\text{Ag}_3^+$  reaction fragments were detected. Moreover, no evidence for the  $\text{Ag}_3\text{N}_2^+$  or  $\text{Ag}_3\text{NO}^+$  products formation was observed.

As discussed in Section 2.2, within the Lindemann model for low-pressure gas-phase kinetics, the negative temperature dependence of the  $\text{Ag}_3(\text{N}_2\text{O})_n^+$  ( $n = 2, 3$ ) reaction products observed in Figure 6.1 is indicative of a barrier-less reaction step. On the other hand, the  $\text{Ag}_3\text{O}_x^+$  and  $\text{AgO}_x(\text{N}_2\text{O}_2)_y^+$  product formation indicates an activation barrier for the dissociation of  $\text{N}_2\text{O}$ . Consequently, the molecular adsorption of  $\text{N}_2\text{O}$  on  $\text{Ag}_3^+$  clusters, in the temperature range between 270 and 230 K, results in sufficient heating of the clusters to promote the system over the barrier to dissociative adsorption.

The dissociation of  $\text{N}_2\text{O}$  on the metal clusters can be rationalized in terms of frontier orbital considerations:  $\text{N}_2\text{O}$  has sixteen valence electrons and the ground-state electron configuration is  $(1\sigma)^2(2\sigma)^2(3\sigma)^2(4\sigma)^2(5\sigma)^2(6\sigma)^2(1\pi)^4(7\sigma)^2(2\pi)^4(3\pi)^0$ .<sup>252</sup> From a chemical point of view,  $\text{N}_2\text{O}$  is generally viewed as a poor ligand to transition metals and the bonding scheme between a metal and nitrous oxide involves a synergetic  $\sigma$  donation from the  $7\sigma$  orbital of  $\text{N}_2\text{O}$  into an empty  $\sigma$ -symmetry orbital of the metal ion and  $\pi$  back-bonding from metal d orbitals into the  $3\pi^*$  orbital of  $\text{N}_2\text{O}$ .<sup>241,253</sup> Theoretical calculations show that metal cluster reactions with  $\text{N}_2\text{O}$  are initiated by charge transfer from the metal cluster into the  $\text{N}_2\text{O}$  empty  $3\pi$  (LUMO) orbital. This implies three essential consequences: (i) population of the  $\text{N}_2\text{O}$  LUMO destabilized both the N-N and N-O bonds because this orbital has antibonding character for these bonds; (ii) since the optimal structure of a negatively charged  $\text{N}_2\text{O}$  is band-shaped, the  $\text{N}_2\text{O}$  molecule starts to bend when electronic charge is donated to the molecule; and (iii) the  $3\pi$  orbital of the metal-oxygen bond starts to form from this charge transfer.<sup>245</sup>

In order to elucidate the mechanism of the investigated reaction, kinetic measurements

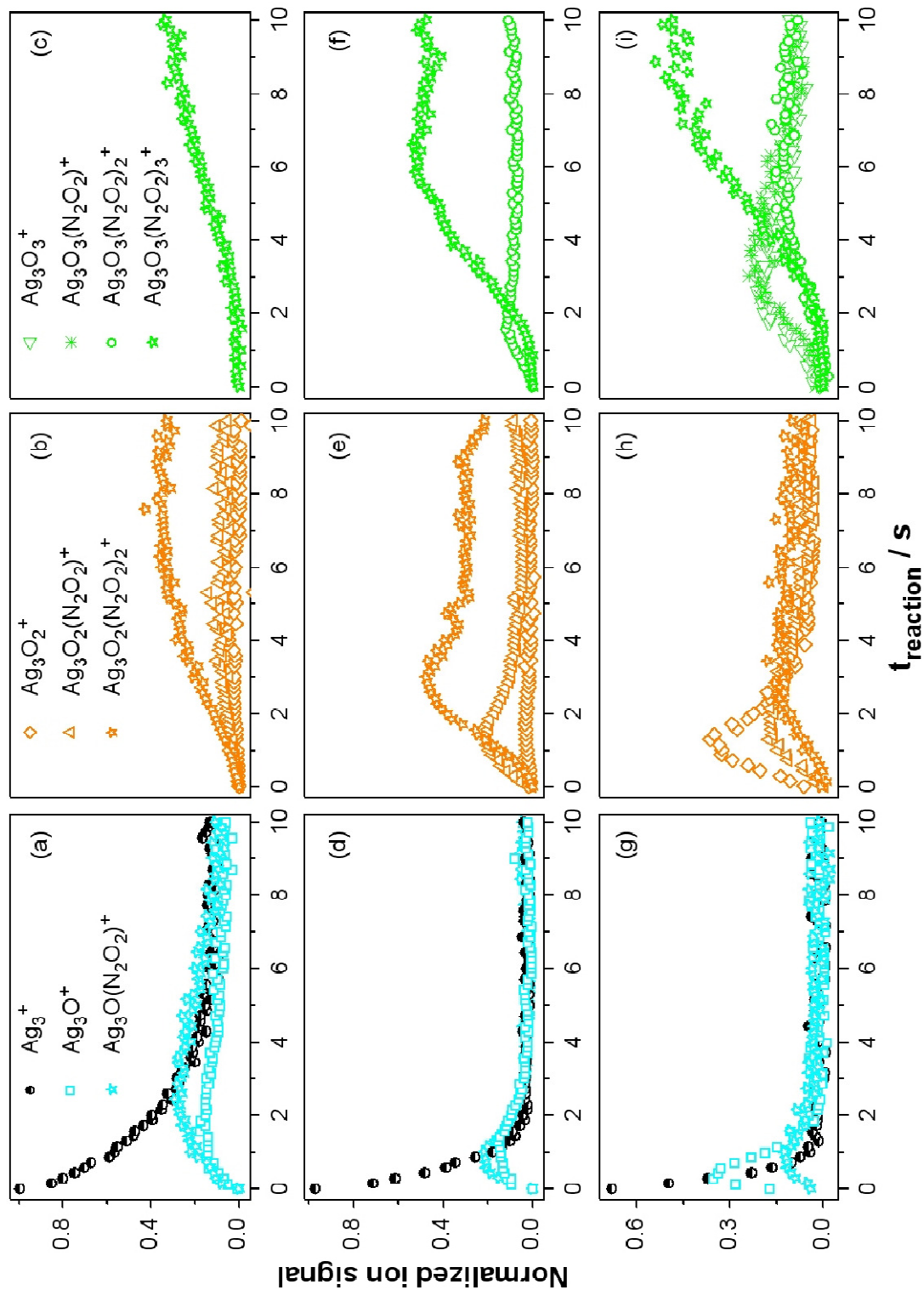


**Figure 6.3:** Product ion concentrations of the reaction  $\text{Ag}_3^+ + \text{N}_2\text{O}$  as a function of the reaction time  $t_R$  for: (a-c)  $T = 270$  K, (d-f)  $T = 250$  K and (g-i)  $T = 230$  K, respectively. The symbols represent the experimental data, normalized on the initial  $\text{Ag}_3^+$  concentration and on the total ion concentration in the trap. The partial pressure during the experiment were  $p(\text{He}) = 1$  Pa and  $p(\text{N}_2\text{O}) = 0.1$  Pa, respectively.

at temperatures between 270 and 230 K were performed. Figure 6.3 displays the product ion signals normalized on the initial  $\text{Ag}_3^+$  concentration and on the total ion concentration in the trap as a function of reaction time  $t_R$ . Because the reaction of  $\text{Ag}_3^+$  with  $\text{N}_2\text{O}$  generated a large number of intermediate reaction products, only for sake of clarity in Figure 6.3 the product kinetic traces are grouped according to the number of  $\text{O}_x$  atoms in the  $\text{Ag}_3\text{O}_x^+$  and  $\text{Ag}_3\text{O}_x(\text{N}_2\text{O}_2)_y^+$  cluster complexes. The same color coding as the one used in the Figure 6.1b-d was employed in Figure 6.3 as well. The kinetic traces of the bare  $\text{Ag}_3^+$  signals (Figure 6.3a, d, g) are shown in black.

The recorded kinetic curves presented in Figure 6.3 demonstrate that there are two different types of reaction products, i.e. intermediate and final products. In addition, different intermediate reaction products arise at different reaction times. For instance, the first intermediate products  $\text{Ag}_3\text{O}^+$  and  $\text{Ag}_3\text{O}(\text{N}_2\text{O}_2)^+$  that were observed, appear simultaneously (blue symbols in Figure 6.3a, d, g), while the  $\text{Ag}_3\text{O}_3^+$ ,  $\text{Ag}_3\text{O}_3(\text{N}_2\text{O}_2)^+$ ,  $\text{Ag}_3\text{O}_3(\text{N}_2\text{O}_2)_2^+$ , and  $\text{Ag}_3\text{O}_3(\text{N}_2\text{O}_2)_3^+$  (green symbols in Figure 6.3c, f, i) were monitored to appear at a considerable later reaction time. Nevertheless,  $\text{Ag}_3\text{O}_3(\text{N}_2\text{O}_2)_3^+$  was identified to be the final reaction product independent of the reaction temperature. Furthermore, some equilibrium reactions were also observed between the  $\text{Ag}_3\text{O}_3(\text{N}_2\text{O}_2)_3^+$  final product and  $\text{Ag}_3\text{O}_2(\text{N}_2\text{O}_2)_2^+$ ,  $\text{Ag}_3\text{O}_3^+$ ,  $\text{Ag}_3\text{O}_3(\text{N}_2\text{O}_2)^+$ , and  $\text{Ag}_3\text{O}_3(\text{N}_2\text{O}_2)_2^+$  intermediate products.

Possible reaction mechanisms were evaluated by fitting the integrated rate equation to

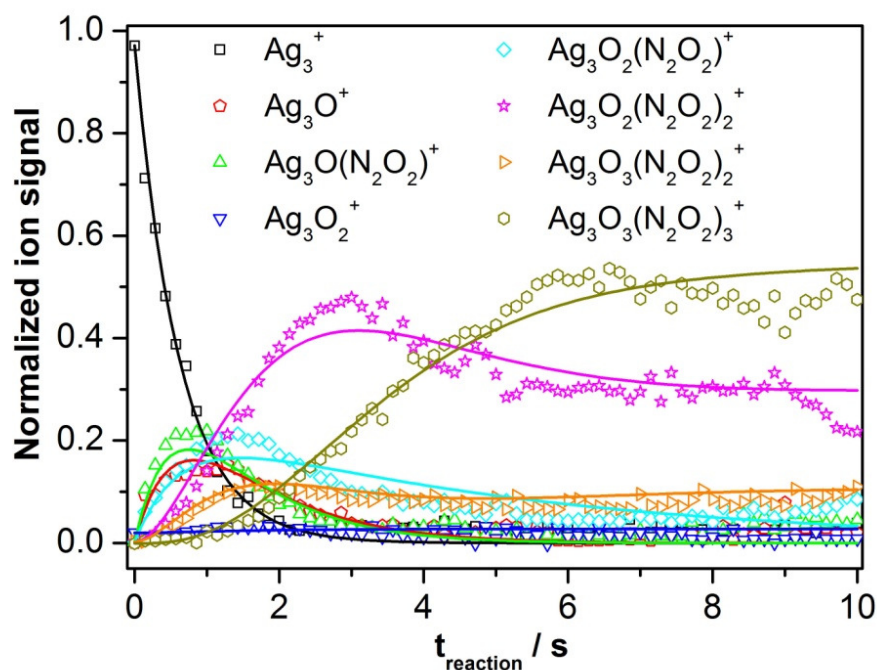


**Figure 6.4:** Product ion concentrations as a function of reaction time for a reaction temperature of 250 K. The solid lines were obtained by fitting the integrated rate equations of the proposed reaction mechanism displayed in Figure 6.5 to the experimental data.

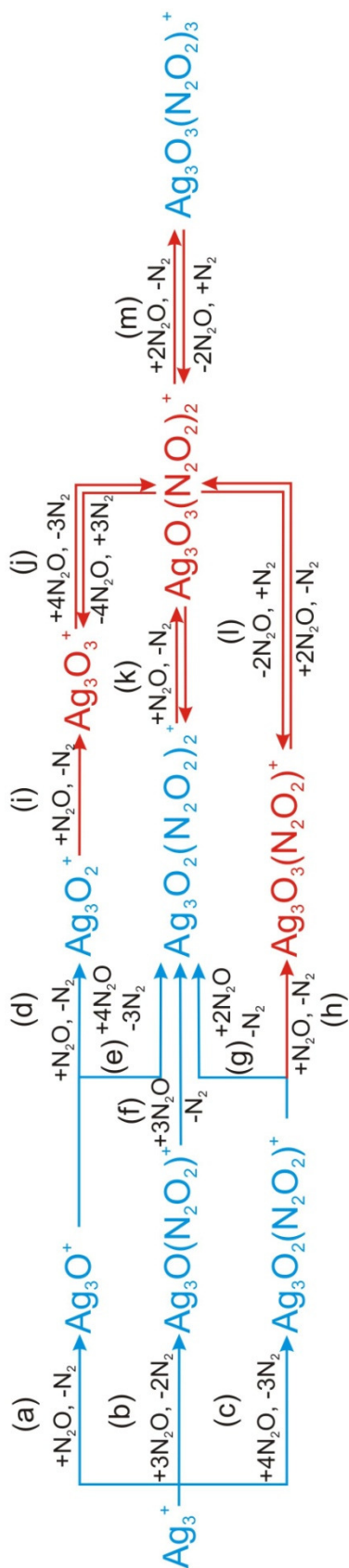


Figure 6.5: Proposed reaction mechanism of the reaction between  $\text{Ag}_3^+$  and  $\text{N}_2\text{O}$ .

the experimental kinetic data. The integration of the rate equation was performed numerically by using the fourth order Runge-Kutta algorithm as described in Section 2.2. Figure 6.4 displays a typical fit to the kinetic traces obtained for the reaction of  $\text{Ag}_3^+$  with nitrous oxide at 250 K. The reaction mechanism corresponding to the shown fit is displayed in Figure 6.5. This mechanism is based on the information presented above and includes the identified intermediates, final products, competing reaction steps, and equilibria. However, as this reaction involves a multitude of reaction intermediates the complete mechanism must be rather complicated. Therefore, it was not possible to unambiguously assign one reaction mechanism by fitting the data in this case. Variations in the basic reaction sequences of the mechanism resulted in almost the same fitting quality. For the temperature of 270 K some intermediate products, which were observed for a reaction temperature of 250 K and 230 K were not present in the recorded kinetic data. This could be attributed probably to the time scale of the present experiment. Therefore, in Figure 6.5 in blue colored were the products detected at a reaction temperature of 270 K, while in red colored were the products monitored just for lower temperatures, i.e. 250 K and 230 K. The same color code was used to indicate the reaction steps for different temperatures.

In the following, the proposed reaction steps were discussed in the context of structural information delivered by *ab initio* DFT calculations performed by Bonačić-Koutecký and coworkers.<sup>171,250</sup>

(i) The origin of the  $\text{Ag}_3\text{O}^+$  reaction product can be explained by means of dissociative adsorption reaction as described in Figure 6.5 step (a). This reaction led to the reduction of the corresponding nitrous oxide as well as the oxidation of  $\text{Ag}_3^+$  to  $\text{Ag}_3\text{O}^+$ . The calculated lowest energy geometry of  $\text{Ag}_3\text{O}^+$  (see Figure 6.2d) exhibited a tetrahedral structure with the oxygen atom displaced slightly off the center of the triangle formed by the three Ag atoms, similar to that reported by Bréchnac and coworkers.<sup>254</sup>

The formation of  $\text{Ag}_3\text{O}^+$  competed with the formation of the  $\text{Ag}_3\text{O}(\text{N}_2\text{O}_2)^+$  reaction product. The formation of  $\text{Ag}_3\text{O}(\text{N}_2\text{O}_2)^+$  must result from the dissociative adsorption of multiple  $\text{N}_2\text{O}$  molecules, as shown in Figure 6.5 step (b). The theoretical calculations performed in the group of Professor Bonačić-Koutecký predicted for the lowest energy geometry of  $\text{Ag}_3\text{O}(\text{N}_2\text{O}_2)^+$  a tetrahedral structure with one oxygen atom displaced slightly off the center of the triangle formed by the three Ag atoms and the oxygen and nitrogen molecularly adsorbed at two different corner silver atoms (see Figure 6.2c). Interesting to note is that all other calculated structural isomers, i.e. with nitrous oxide and oxygen molecularly adsorbed at two different corner silver atoms, are at least 0.98 eV higher in energy.

The best fit to the kinetic data indicated an additional reaction channel, in which  $\text{Ag}_3\text{O}_2(\text{N}_2\text{O}_2)^+$  formation competed with the generation of  $\text{Ag}_3\text{O}^+$  and  $\text{Ag}_3\text{O}(\text{N}_2\text{O}_2)^+$ . The  $\text{Ag}_3\text{O}_2(\text{N}_2\text{O}_2)^+$  formation was observed to be enhanced for temperatures lower than 270 K. Its formation could be explained by a dissociative adsorption reaction scenario, as described in Figure 6.5 step (c).

Depending on the reaction temperature one channel could be more probable than others. Thus, for reaction temperature of 270 K (see Figure 6.3, panels a and b) the channel corresponding to the  $\text{Ag}_3\text{O}(\text{N}_2\text{O}_2)^+$  product formation appeared to be favored. At this temperature, the  $\text{Ag}_3\text{O}(\text{N}_2\text{O}_2)^+$  product intensity was slightly higher than that of  $\text{Ag}_3\text{O}^+$  and  $\text{Ag}_3\text{O}_2(\text{N}_2\text{O}_2)^+$ , with a maximum around 2.5 s. The situation was changed by slightly decreasing the reaction temperature to 250 K (see Figure 6.3, panels d and e). The  $\text{Ag}_3\text{O}^+$ ,  $\text{Ag}_3\text{O}(\text{N}_2\text{O}_2)^+$ , and  $\text{Ag}_3\text{O}_2(\text{N}_2\text{O}_2)^+$  product maxima were shifted to shorter reaction time around 1 s while their formation probability was almost similar. Further decreasing the reaction temperature to 230 K seemed to visibly favor the  $\text{Ag}_3\text{O}^+$  product (see Figure 6.3, panels g and h).

(ii) The produced  $\text{Ag}_3\text{O}^+$  further reacted with the  $\text{N}_2\text{O}$  from the ion trap. Also here, two competitive reaction channels were identified corresponding to the  $\text{Ag}_3\text{O}_2^+$  and  $\text{Ag}_3\text{O}_2(\text{N}_2\text{O}_2)_2^+$  product formation. The  $\text{Ag}_3\text{O}_2^+$  product formation corresponded to a straightforward reaction, as described in Figure 6.5 steps (d) and (e).

In agreement with the theoretical calculations the formation of  $\text{Ag}_3\text{O}_2^+$  was found to be not very pronounced for reaction temperatures above 230 K, reflecting the very low binding energy of  $\text{O}_2$  to the  $\text{Ag}_3^+$  cluster. The theory predicted as energetically most favorable structure of  $\text{Ag}_3(\text{O}_2)^+$  an  $\text{Ag}_3^+$  with the  $\text{O}_2$  molecule attached to a corner Ag atom ( $E_b(\text{Ag}_3\text{O}_2^+) = 0.167$  eV). All other calculated isomers were found to be at least 1.2 eV less stable (see Figure 6.2d). Similar results were reported by Zhou and coworkers where the oxygen was found to be molecularly attached to a corner silver atom with  $E_b(\text{Ag}_3\text{O}_2^+) = 0.184$  eV.<sup>249</sup>

Subsequently,  $\text{Ag}_3\text{O}^+$  was the source of the formation of  $\text{Ag}_3\text{O}_2(\text{N}_2\text{O}_2)_2^+$  by means of a dissociative adsorption of  $\text{N}_2\text{O}$  molecule on  $\text{Ag}_3\text{O}^+$  complex according to Figure 6.5 step (e).

(iii) The origin of  $\text{Ag}_3\text{O}_3^+$  could be explained by a dissociative adsorption scenario as shown in Figure 6.5 step (i). Theoretical investigations predicted a tetrahedral structure with one oxygen atom displaced slightly off the center of the triangle formed by the three Ag atoms and an oxygen molecule attached to a corner Ag atom to be the lowest energy geometry of  $\text{Ag}_3\text{O}_3^+$ . As can be seen in Figure 6.2d, all other calculated isomers were found to be more than 2.8 eV higher in energy.

In conclusion, we did indeed successfully oxidize the  $\text{Ag}_3^+$  cluster by means of  $\text{N}_2\text{O}$  reaction. The experimental data obtained in this study clearly demonstrate that the  $\text{Ag}_3^+$  cluster initiate a very rich chemistry in its reaction with  $\text{N}_2\text{O}$ , which was strongly dependent on the reaction temperature. These studies provide for the first time insights into the nature of the chemical bond between  $\text{N}_2\text{O}$  and  $\text{Ag}_3^+$ , and describe the  $\text{N}_2\text{O}$  activation for N-O bond scission.

At room temperature,  $\text{Ag}_3^+$  was found not to bind  $\text{N}_2\text{O}$ . The  $\text{N}_2\text{O}$  dissociative adsorption observed in the temperature range between 270 and 230 K promoted two competitive reaction channels:  $\text{Ag}_3\text{O}_x^+$  ( $x = 1-3$ ) oxidation and  $\text{Ag}_3\text{O}_x(\text{N}_2\text{O}_2)_y^+$  ( $x, y = 1-3, x \geq y$ ) product

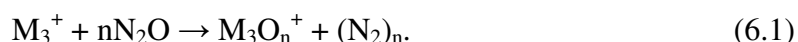
formation, respectively. For temperatures below 200 K, N<sub>2</sub>O adsorbed on Ag<sub>3</sub><sup>+</sup> cluster without dissociation and the maximum number of adsorbed N<sub>2</sub>O molecule corresponded to the number of Ag<sub>3</sub><sup>+</sup> adsorption sites.

## 6.2 Indication of two distinct kinds of oxygen atoms involved in the CO oxidation by silver clusters

The investigations were further extended by adding well defined amounts of CO into the trap in addition to N<sub>2</sub>O. For comparison, the reactions of Au<sub>3</sub><sup>+</sup> with N<sub>2</sub>O and N<sub>2</sub>O/CO were also investigated.

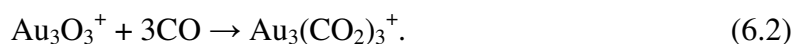
Before presenting the results for silver first the reactions of gold oxide cluster cations with CO were considered in order to be able to emphasize the pertinent differences of oxygen species in the corresponding oxidized silver clusters.

Figure 6.6a displays the product ion mass spectra obtained after the reaction of Au<sub>3</sub><sup>+</sup> with nitrous oxide. The most prominent peaks correspond to the gold oxides Au<sub>3</sub>O<sub>n</sub><sup>+</sup> (n = 2, 3). The proposed oxide formation mechanism can be written as (M = Au):



Furthermore, smaller peaks at larger masses could be assigned to multiple adsorption of a unit of stoichiometry (N<sub>2</sub>O<sub>2</sub>) onto the gold oxide clusters. However, only the gold oxide clusters were considered in the following.

When, in addition to N<sub>2</sub>O, CO was present in the ion trap the sole reaction product observed besides the carbonyl Au<sub>3</sub>(CO)<sub>3</sub><sup>+</sup> corresponded to the stoichiometry Au<sub>3</sub>(CO<sub>2</sub>)<sub>3</sub><sup>+</sup>, as can be seen from Figure 6.6b. This was a strong indication that each oxygen atom in the final oxidation product Au<sub>3</sub>O<sub>3</sub><sup>+</sup> reacted with one CO molecule to produce CO<sub>2</sub> according to Equation 6.2:



A similar reaction mechanism of CO oxidation by gold oxide clusters has been observed by Castleman and coworkers.<sup>255</sup>

As already shown in Section 6.1 the reaction of silver cluster cations Ag<sub>3</sub><sup>+</sup> with N<sub>2</sub>O also led to the oxidation of the metal clusters yielding the oxides Ag<sub>3</sub>O<sub>n</sub><sup>+</sup> (n = 1-3) (Figure 6.6c) according to Equation 6.1 (M = Ag). Additional products in the mass spectrum in Figure 6.6c corresponding to the adsorption of multiple (N<sub>2</sub>O<sub>2</sub>) units were again not considered here.



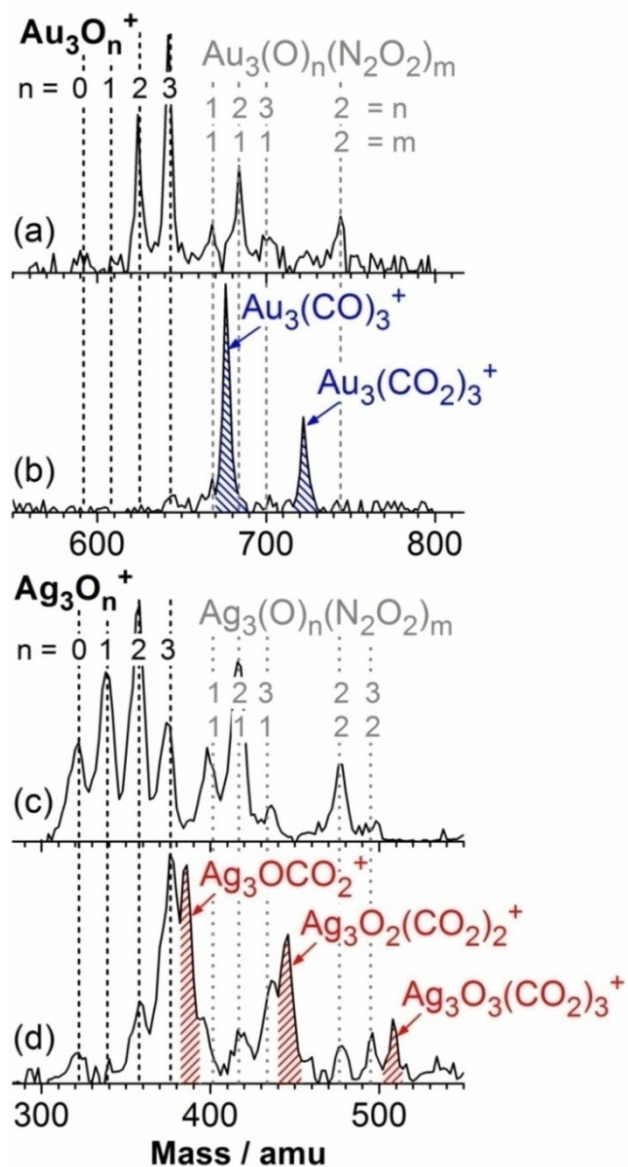
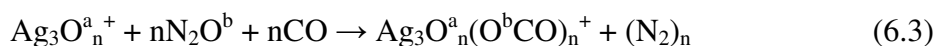


**Figure 6.6:** Product ion mass spectra obtained after trapping of  $\text{Au}_3^+$  and  $\text{Ag}_3^+$ , respectively, inside the octopole ion trap pre-filled with 1 Pa of helium buffer gas and defined quantities of reactant gases: (a)  $p(\text{N}_2\text{O}) = 0.09$  Pa; (b)  $p(\text{N}_2\text{O}) = 0.09$  Pa,  $p(\text{CO}) = 0.05$  Pa; (c)  $p(\text{N}_2\text{O}) = 0.12$  Pa, (d)  $p(\text{N}_2\text{O}) = 0.12$  Pa,  $p(\text{CO}) = 0.05$  Pa. In (a) and (b) the reaction time was  $t_R = 0.5$  s, the temperature 300 K; in (c) and (d)  $t_R = 1$  s,  $T = 230$  K.

The reaction of the silver oxide clusters with CO (Figure 6.6d), however, led to very different products than in the case of the gold oxide clusters. The new mass signals in Figure 6.5d could be assigned to the product stoichiometries  $\text{Ag}_3\text{O}_n(\text{CO}_2)_n^+$  ( $n = 1-3$ ). The proposed explanation of this observation was that CO apparently does not react with the oxygen atoms in  $\text{Ag}_3\text{O}_n^+$  to produce  $\text{CO}_2$ , but rather with an additional  $\text{N}_2\text{O}$  because the products contain an additional oxygen atom per  $\text{CO}_2$  compared to the gold clusters (cf. Figures 6.5b and 6.5d). This is reflected in Equation 6.3:



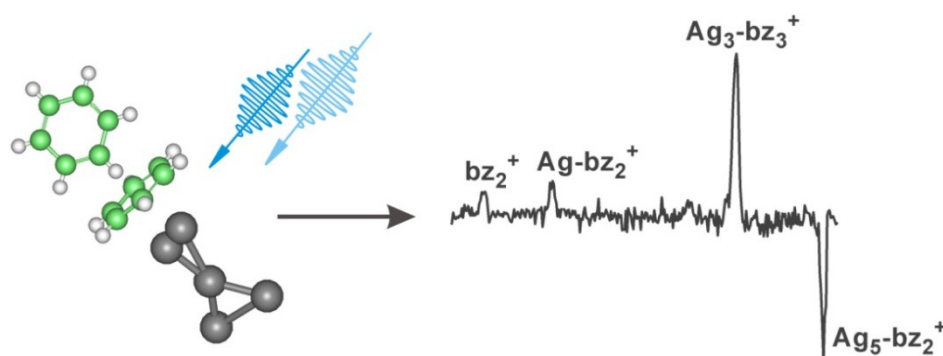
The two distinct kinds of oxygen involved in the oxidation of carbon monoxide by the silver clusters were labeled  $\text{O}^a$  and  $\text{O}^b$ , respectively, in Equation 6.3. The species  $\text{O}^a$  does not directly react with CO but served as an adsorption site for an additional  $\text{N}_2\text{O}$  molecule containing the oxygen species  $\text{O}^b$  that is subsequently able to react with CO. This assignment of the reaction site was based on the observation that only stoichiometries with equal numbers of O and  $\text{CO}_2$  in  $\text{Ag}_3\text{O}_n(\text{CO}_2)_n^+$  were detected.

Hence, the catalytically active species in the CO oxidation reaction was the gold cluster  $\text{Au}_3^+$  itself. However, in the case of silver, the catalytically active species were the silver oxide clusters  $\text{Ag}_3\text{O}_n^+$ . No CO oxidation was observed without previous formation of  $\text{Ag}_3\text{O}_n^+$ . The two different kinds of oxygen atoms identified in the silver oxide catalyst cluster model investigated in the present study might be compared to bulk silver oxidation catalysts, which are also characterized by the presence of several different oxygen species. In particular, the catalytically active surface  $\gamma$ -oxygen was found to be always connected to a sub-surface, strongly bound  $\beta$ -oxygen atom.<sup>256,257</sup> Theoretical calculations are still in progress in order to elucidate the mechanism behind the observed CO oxidation reactions.

# Formation and femtosecond photodissociation of $\text{Ag}_n^+$ and $\text{Au}_n^+$ complexes with benzene and carbon monoxide\*

*The reaction of free, size selected gold and silver cluster cations  $\text{Ag}_n^+$  and  $\text{Au}_n^+$  ( $n = 3,5$ ) with  $\text{C}_6\text{H}_6$  as well as with a mixture of  $\text{C}_6\text{H}_6$  and  $\text{CO}$  were investigated in the radio frequency ion trap under multiple collision condition. While benzene was found to react with all investigated metal clusters exhibiting size dependent adsorbate coverages, the coadsorption of  $\text{C}_6\text{H}_6$  and  $\text{CO}$  was only observed on the gold clusters. Photodissociation experiments at 353 and 393 nm, respectively, provided indications for charge transfer induced fragmentation in the case of the silver cluster-benzene complexes. In particular, for  $\text{Ag}_5(\text{C}_6\text{H}_6)_2^+$  the femtosecond time resolved fragmentation dynamics could be measured.*

## Graphical abstract\*



\* The contents of this chapter have been published in a contribution to *Chemical Physics Letters*: D. M. Popolan, T. M. Bernhardt, "Formation and femtosecond photodissociation of  $\text{Ag}_n^+$  and  $\text{Au}_n^+$  complexes with benzene and carbon monoxide", **470**, 44-48 (2009).

## 7.1 Introduction

Free, gas-phase complexes containing metal cluster centers and organic ligand molecules provide good model systems for the investigation of fundamental organometallic bonding interactions without any substrate or solvent influence.<sup>214</sup> In addition, mass-selected clusters offer the opportunity to study the influence of size effects on the complex properties. Cluster size effects are, e.g., very important with respect to the chemical and catalytic properties of metal nano-clusters.<sup>258</sup> In this regard coinage metal clusters have attracted particular interest in recent years due to their unexpected size dependent reactive behavior which in many cases completely differs from that of the bulk.<sup>110,259</sup>

Besides the cluster size, the charge state of the metal clusters was found to present a key factor in catalytic activity.<sup>60,118</sup> The idea of the gas-phase experiment presented in this contribution is to induce a change in the charge state of the metal cluster by electron transfer from one ligand (here benzene) via photoexcitation. As a consequence, the changed charge state of the metal cluster will result in a different chemical reactivity that might activate the cluster itself or coadsorbed molecules on the cluster to further react in the ion trap, in which the clusters are stored. Employing femtosecond (fs) lasers for photoexcitation, the dynamics following this photoinduced chemical activation can now be resolved in real time via pump-probe mass spectrometry, detecting the emerging reaction products. From the thus obtained molecular dynamics insight into the details of the cluster bonding and reaction mechanisms can be obtained.<sup>260</sup>

In the present contribution we focus our interest on the interaction of small gold and silver cluster cations with benzene and mixtures of benzene with carbon monoxide. The benzene-metal interaction is representative for aromatic  $\pi$ -bonding and has attracted particular interest recently due to the unexpected sandwich structure formation in transition metal cluster-benzene complexes.<sup>261</sup>

The photo-induced charge-transfer (CT) reaction in positively charged silver cluster-benzene complexes has been reported previously.<sup>262-264</sup> The CT induced fragmentation yielding neutral silver clusters and positively charged benzene was found to exhibit pronounced cluster size and wavelength dependencies. The interaction of benzene with  $\text{Ag}^+$  and  $\text{Au}^+$  was also previously investigated by means of collision induced fragmentation.<sup>265-267</sup>

As a second ligand molecule to be potentially activated by the photoinduced electron transfer we investigated the coadsorption of CO. Of particular future interest would be the reaction of activated CO with  $\text{O}_2$  in the ion trap, because whereas cationic gold and silver clusters do not promote the catalytic CO oxidation, neutral and negatively charged clusters of these elements have been observed previously to efficiently catalyze the transformation of CO to  $\text{CO}_2$ .<sup>66,118,222</sup>

In the present investigations we did indeed observe the coadsorption of CO and benzene on gold cluster cations. The photoinduced charge transfer was, however, only detected

for silver-benzene complexes at the wavelengths available in the present setup. Nevertheless, for the largest silver cluster complex investigated it was even possible to resolve the femtosecond dynamics following charge transfer excitation leading to new reaction products via reactive interaction with the molecules in the ion trap

## 7.2 Results and discussion

### 7.2.1 Reactions of silver and gold cluster cations with $\text{C}_6\text{H}_6$ and $\text{C}_6\text{H}_6/\text{CO}$

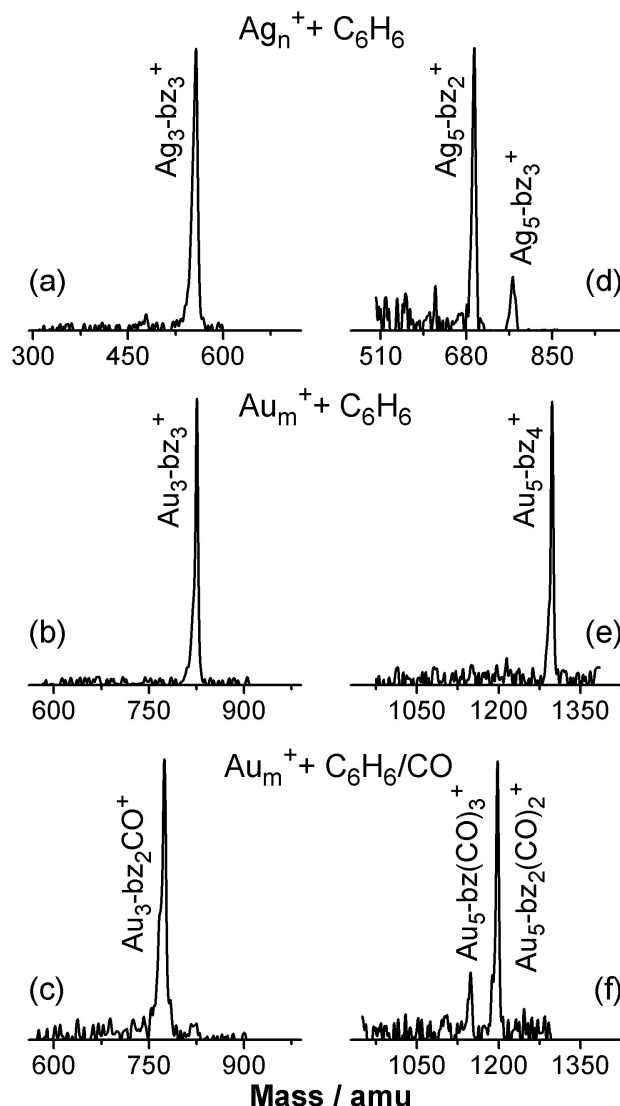
The silver and gold dimer cations undergo fragmentation in the ion trap upon reaction with benzene (for convenience abbreviated as ‘-bz’ in the following). Therefore, we focused our investigations on the trimer and pentamer cations, which are also most abundant in our cluster ion distribution generated by the cluster source (see Figure 3.2).

Figure 7.1 displays the product mass spectra for the reaction of  $\text{Ag}_n^+$  and  $\text{Au}_m^+$  ( $n, m = 3, 5$ ) in the presence of benzene and a mixture of  $\text{C}_6\text{H}_6$  with CO, respectively, under similar reaction conditions.

Product ion mass spectra obtained after the reaction of the trimers  $\text{Ag}_3^+$  and  $\text{Au}_3^+$  with solely benzene as reactive gas in the ion trap are depicted in Figures 7.1a and b. Both,  $\text{Ag}_3^+$  and  $\text{Au}_3^+$ , are found to adsorb three benzene molecules each, which appear to represent the saturated coverages, since the mass spectra do not change at higher concentrations of benzene and at longer reaction times. The geometries of the gold and silver trimer cations have been reported to be equilateral triangles.<sup>81,82</sup> DFT calculations furthermore predict that all atoms in the trimers are electronically equivalent carrying equal amounts of partial positive charge.<sup>268</sup> In this context our experimental results therefore suggest that both complexes,  $\text{Au}_3\text{-bz}_3^+$  and  $\text{Ag}_3\text{-bz}_3^+$ , assume structures in which one benzene molecule is attached to each metal atom in the cluster.

The mass spectrum in Figure 7.1c shows the reaction product of  $\text{Au}_3^+$  when benzene and CO are simultaneously present in the ion trap. The single product complex  $\text{Au}_3\text{-bz}_2\text{CO}^+$  indicates that CO competes with benzene for the available adsorption sites. This competitive coadsorption effect will be discussed below for the pentamer reactions. No coadsorption was observed for  $\text{Ag}_3^+$  clusters, independent of CO partial pressure and reaction time.

Figure 7.1d and e show the product mass spectra recorded for  $\text{Ag}_5^+$  and  $\text{Au}_5^+$  in the presence of benzene only. Similar to the trimers, also  $\text{Ag}_5^+$  and  $\text{Au}_5^+$  react with benzene without fragmentation, but the number of adsorbed  $\text{C}_6\text{H}_6$  molecules differs for silver and gold. In the case of  $\text{Ag}_5^+$ , already trace amounts of  $\text{C}_6\text{H}_6$  lead to the formation of  $\text{Ag}_5\text{-bz}_2^+$  (not shown). Even at the largest possible benzene pressures this complex remains the major product with only very small amounts of  $\text{Ag}_5\text{-bz}_3^+$  appearing, as can be seen from Figure 7.1d. In



**Figure 7.1:** Product ion mass spectra obtained after reaction ( $t_R = 200$  ms) of  $Ag_{3,5}^+$  and  $Au_{3,5}^+$  with  $C_6H_6$  and  $C_6H_6/CO$  ( $p_{He} = 1$  Pa; (a)-(d)  $p_{bz} = 0.1$  Pa; (e)-(f)  $p_{bz} = p_{CO} = 0.1$  Pa). Note that no other reaction products are observed even after 10 s trapping period or higher reactant partial pressure.

contrast, four  $C_6H_6$  molecules represent the saturation coverage of the gold pentamers ( $Au_5-bz_4^+$  in Figure 7.1e).

Ion mobility measurements and DFT calculations confirm for the bare  $Ag_5^+$  cluster an X-shaped geometry ( $D_{2d}$  symmetry) with four equivalent corners carrying the positive charge and a central atom with basically no charge.<sup>82</sup> The observation of  $Ag_5-bz_2^+$  as major adsorption complex stoichiometry appears quite surprising, because for other ligand molecules  $Ag_5X_3^+$  ( $X = C_2H_4$ ,<sup>117</sup>  $C_3H_6$ ,<sup>230</sup>  $CO$ <sup>121</sup>) was reported to be of particular intensity and stability due to a ligand induced change to a bipyramidal  $Ag_5^+$  structure. Hence, no conclusive suggestion for the silver pentamer complex structure can be deduced from the presented adsorption

data.

The bare cluster geometry of  $\text{Au}_5^+$  is also an X-shaped configuration ( $\text{D}_{2h}^{81}$ ) with four electronically equivalent corner sites and a fifth “central atom” appearing essentially neutral and not being considered to be a binding site. Here four benzene ligand molecules are observed (Figure 7.1e) which are potentially attached to the corner atoms of the X-shaped  $\text{Au}_5^+$  structure.<sup>114</sup>

In the next step, a controlled amount of both, CO and  $\text{C}_6\text{H}_6$  were admitted into the trap. Similar to the trimers, exclusively the gold cluster exhibits coadsorption of  $\text{C}_6\text{H}_6$  and CO. The competitive substitution reaction mechanism is confirmed by pressure dependent reactivity measurements. At a CO partial pressure of 0.1 Pa in the octopole ion trap together with  $\text{C}_6\text{H}_6$  traces only, the formation of an  $\text{Au}_5\text{-bz}(\text{CO})_3^+$  complex is observed. Increasing the  $\text{C}_6\text{H}_6$  pressure to 0.1 Pa leads to the formation of the final product  $\text{Au}_5\text{-bz}_2(\text{CO})_2^+$ . Even for higher  $\text{C}_6\text{H}_6$  partial pressures no further competitive substitution is observed and no more than four ligands are detected even at a residence time inside the trap of  $t_R = 10$  s.

In summary, the trimer and pentamer cluster cations of silver and gold were all found to exhibit strong reactivity toward benzene in our ion trap experiment at room temperature. However, the most prominent pentamer complex stoichiometries differ for gold and silver. Most interestingly, the pronounced abundance of  $\text{Ag}_5\text{-bz}_2^+$  with two benzene molecules adsorbed has not been observed for any other ligand molecule investigated so far (including CO,<sup>121</sup>  $\text{CH}_4$ ,<sup>117</sup>  $\text{C}_2\text{H}_4$ ,<sup>117</sup> and  $\text{C}_3\text{H}_6$ <sup>230</sup>).

The reactivity of gold clusters toward carbon monoxide is known to be considerably larger than that of the silver clusters.<sup>121,227</sup> This is considered to be due to the strong relativistic effects in gold that lead to a decrease in s-d orbital splitting making the d-derived cluster orbitals available for  $\pi^*$  back-donation (Dewar-Chatt-Duncanson complexation model<sup>269</sup>). This is apparently also the reason why coadsorption of benzene and CO is only observed for the gold cluster cations.<sup>221</sup>

## 7.2.2 Photodissociation spectroscopy of $\pi$ -complexes: $\text{Ag}_3\text{bz}_3^+$ and $\text{Ag}_5\text{bz}_2^+$

Employing fs-laser pulses, the possible photoinduced dissociation reaction channels of the cluster complexes presented above were investigated. Photodissociation products were only observed for  $\text{Ag}_3\text{-bz}_3^+$  and  $\text{Ag}_5\text{-bz}_2^+$ . Because our experiment aims to eventually detect the fs time resolved CT induced reaction dynamics of the complexes we used wavelengths of 353 nm, which is known to excite silver-bz complexes to a CT state,<sup>262-264</sup> and 393 nm, which enables multi-photon ionization of neutral silver clusters,<sup>270,271</sup> in the pump-probe configuration.

Figure 7.2a shows the photodissociation difference spectrum of the  $\text{Ag}_3\text{-bz}_3^+$  complex for the dissociation wavelength of 353 nm. The difference spectrum is obtained by subtracting the product mass spectrum measured after a defined storage time of  $t_R = 5$  s from the mass spectrum recorded after the same storage time, but with laser irradiation during ion trapping

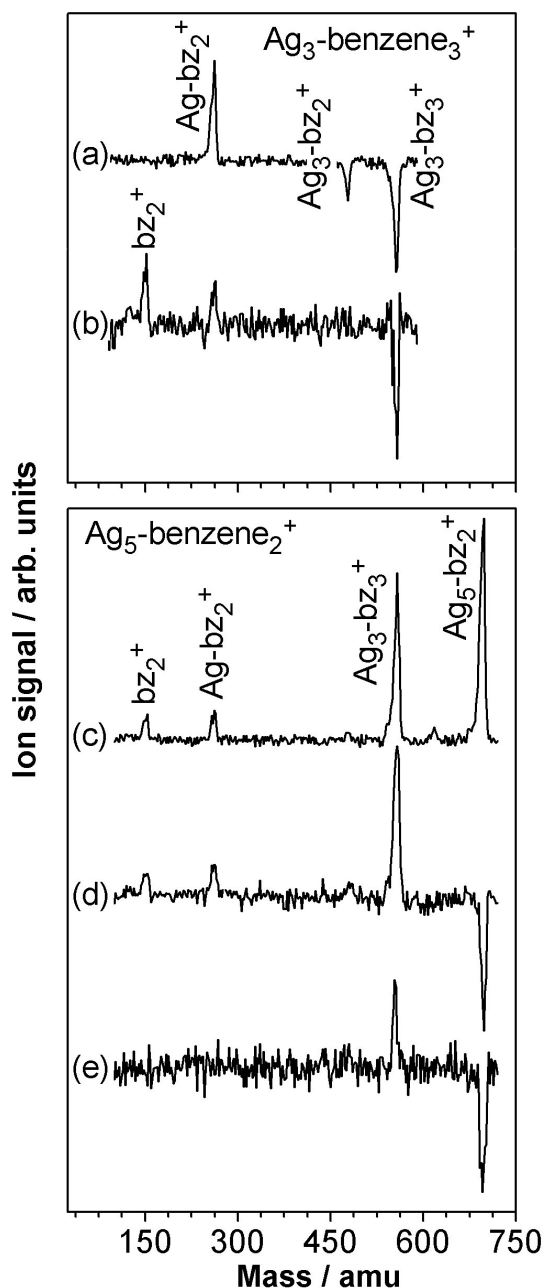


**Figure 7.2:** Upper frame: Photodissociation mass spectra of the  $\text{Ag}_3\text{-bz}_3^+$  complex: (a) Photodissociation difference spectrum at 353 nm (with minor amounts of  $\text{Ag}_3\text{-bz}_2^+$  also present in the ion trap); (b) under irradiation with both laser beams (353 nm and 393 nm). Lower frame: Photodissociation mass spectra of the  $\text{Ag}_5\text{-bz}_2^+$  complex: (c) Depleted mass spectrum under irradiation with 353 nm and 393 nm at zero time delay between both laser pulses; (d) photodissociation difference spectrum at 353/393 nm and zero time delay; (e) difference mass spectrum between the depleted mass spectra recorded at 0 and at 2 ps pump-probe delay time.



(depleted spectrum). In this particular experiment, a small amount of  $\text{Ag}_3\text{-bz}_2^+$  was trapped in addition to  $\text{Ag}_3\text{-bz}_3^+$ . Nevertheless, the only photofragment detected is  $\text{Ag-bz}_2^+$  (see Figure 7.2a).

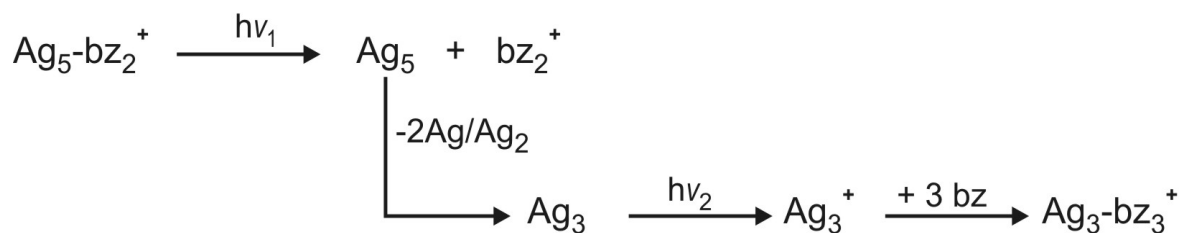
The next trace (Figure 7.2b) depicts the  $\text{Ag}_3\text{-bz}_3^+$  photodissociation difference mass spectrum obtained when both laser pulse wavelengths (353 and 393 nm) are present (time delayed by 2 ps). In this case the new complexes  $\text{Ag-bz}_2^+$  and  $\text{bz}_2^+$  are formed upon photodissociation. The formation of a benzene dimer product ion is quite surprising and indicates the occurrence of a CT photoreaction induced by irradiation with 393 nm. The benzene dimer appearance might also be thought to be in contradiction with the above assumed complex structure exhibiting one benzene molecule attached to each silver atom of the trimer. The product  $\text{Ag-bz}_2^+$  might either be formed via direct photodissociation of  $\text{Ag}_3\text{-bz}_3^+$  or by reaction of  $\text{Ag}_2^+$  or  $\text{Ag}^+$  fragments with benzene present in the ion trap ( $\text{Ag-bz}_2^+$  is the single dissociation product occurring upon reaction of  $\text{Ag}_2^+$  with benzene). Yet, no pump-probe delay time dependent mass-signals could be observed for  $\text{Ag}_3\text{-bz}_3^+$ .

Figure 7.2c presents the photodissociation mass spectrum of the  $\text{Ag}_5\text{-bz}_2^+$  complex. In this case the product mass spectrum without laser, which is similar to the mass spectrum shown in Figure 7.1d, has not yet been subtracted from this depleted mass spectrum. Both wavelengths, 353 and 393 nm, at zero time delay between the two pulses, were employed for irradiation. All signals with a mass smaller than  $\text{Ag}_5\text{-bz}_2^+$  are due to photofragmentation. The abundance of  $\text{Ag}_5\text{-bz}_3^+$  is smaller than 5% and does not change during irradiation (no difference signal).

The photodissociation difference mass spectrum obtained from Figure 7.2c is displayed in Figure 7.2d. As can be seen, the three photofragments  $\text{bz}_2^+$ ,  $\text{Ag-bz}_2^+$ , and  $\text{Ag}_3\text{-bz}_3^+$  are detected. The appearance of the benzene dimer cation again indicates the photoinduced CT dissociation. However, it also sheds light on the surprising stability of  $\text{Ag}_5\text{-bz}_2^+$  in contrast to other  $\text{Ag}_5^+$  complexes, which generally exhibit enhanced stability with three ligand molecules (cf. discussion above). The assumption of an  $\text{Ag}_5\text{-bz}_2^+$  complex structure involving a benzene dimer unit would be in accordance with both, the formation of  $\text{Ag}_5\text{-bz}_2^+$  as preferred reaction product of  $\text{Ag}_5^+$  in the ion trap and the appearance of  $\text{bz}_2^+$  upon CT photodissociation. The binding energy of the free benzene dimer cation is comparably large (0.663 eV<sup>272</sup>) and even the neutral  $\text{bz}_2$  is bound by 0.1 eV,<sup>273</sup> supporting a potential benzene dimerization on the silver cluster. Also, note that no  $\text{bz}^+$  monomer photoproducts are observed, nor for  $\text{Ag}_5\text{-bz}_2^+$  neither for  $\text{Ag}_3\text{-bz}_3^+$ .

The formation pathways of the  $\text{Ag-bz}_2^+$  fragment observed in Figure 7.2d might be similar as in the case of the  $\text{Ag}_3\text{-bz}_3^+$  photodissociation (see above).

Delaying the pump (353 nm) and probe (393 nm) laser pulses by 2 ps reveals that the fragment  $\text{Ag}_3\text{-bz}_3^+$  is the only product ion exhibiting a time dependent intensity change. This is apparent from Figure 7.2e, which shows the difference mass spectrum between the photodissociation (depleted) mass spectra recorded at zero delay time (Figure 7.2c) and at 2 ps



Scheme 7.1

pump-probe delay time.

In the following we will give a preliminary discussion of the origin of the time delayed appearance of the  $\text{Ag}_3\text{-bz}_3^+$  pump-probe signal from the photodissociation of  $\text{Ag}_5\text{-bz}_2^+$ . We suggest that the dissociative CT excitation (pump) leads to the formation of  $\text{bz}_2^+$  and a neutral  $\text{Ag}_5$  cluster. Subsequently, the neutral  $\text{Ag}_5$  separates from  $\text{bz}_2^+$  and undergoes structural rearrangement eventually leading to dissociation to form  $\text{Ag}_3$  and  $\text{Ag}_2$  or  $2\text{Ag}$ .  $\text{Ag}_3$  is then preferably ionized (probe) because it is the only silver cluster amenable to two photon ionization at our laser wavelengths due to its comparably low ionization potential ( $\text{IP}(\text{Ag}_3) = 6.2 \text{ eV}$ ;  $\text{IP}(\text{Ag}_2) = 7.65 \text{ eV}$ ;  $\text{IP}(\text{Ag}) = 7.58 \text{ eV}^{274,275}$ ). The  $\text{Ag}_3^+$  photoproduct further reacts with the benzene present in the ion trap to form  $\text{Ag}_3\text{-bz}_3^+$  during the trapping period of 5 s. This mechanism is supported by the previous observation that neutral  $\text{Ag}_5$  generated by electron detachment from the anion,  $\text{Ag}_5^-$ , is also found to decompose leading to the predominant occurrence of  $\text{Ag}_3^+$  in the subsequent ionization step.<sup>276,277</sup> Scheme 7.1 summarizes the proposed photoinduced charge transfer reaction scenario.

### 7.2.3 Femtosecond time resolved fragmentation dynamics

By systematic variation of the pump-probe delay time it was possible to resolve the ultrafast photodissociation dynamics in the case of the  $\text{Ag}_5\text{-bz}_2^+$  complex. Figure 7.3 displays the transient ion signal intensities for the decaying  $\text{Ag}_5\text{-bz}_2^+$  (Figure 7.3a) and the emerging  $\text{Ag}_3\text{-bz}_3^+$  (Figure 7.3b). Starting at  $t = 0 \text{ ps}$ , the  $\text{Ag}_5\text{-bz}_2^+$  signal exhibits exponential decays with a time constant  $\tau_1 = 0.1 \text{ ps}$  for the 393 nm pump and 353 nm probe configuration (positive delay times) and with a time constant  $\tau_2 = 0.5 \text{ ps}$  for the 353 nm pump and 393 nm probe configuration (negative time delays), respectively. Within the model of Scheme 7.1, these decays reflect the escape of the wavepacket initially prepared on the  $\text{Ag}_5^0 \cdots \text{bz}_2^+$  CT potential energy surface from the Franck-Condon region of the  $\text{Ag}_5$  ionization. Once ionized by the probe pulse,  $\text{Ag}_5^+$  will react with benzene again to yield  $\text{Ag}_5\text{-bz}_2^+$ . This ion reaction takes place on a time scale of milliseconds and is thus not perceptible in the fs transients displayed in Figure 7.3.

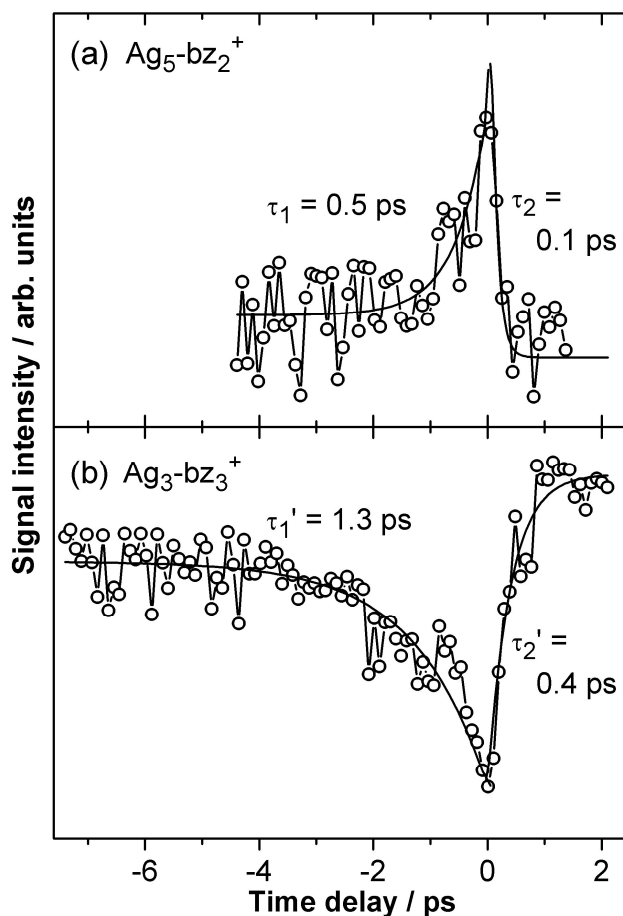


**Figure 7.3:** Femtosecond time dependent signal intensity of (a)  $\text{Ag}_5\text{-bz}_2^+$  and of (b)  $\text{Ag}_3\text{-bz}_3^+$ . The open circles represent the experimental data while the solid lines correspond to the best fits of exponentials convoluted with a Gaussian cross correlation yielding the indicated time constants (see text for more details).

The  $\text{Ag}_3\text{-bz}_3^+$  product must also be formed by reaction of an initial photoproduct with the benzene in the ion trap. The mechanism proposed in Schema 7.1 involves the separation from  $\text{bz}_2^+$ , the geometric rearrangement and eventually the dissociation of  $\text{Ag}_5$  generated by the initial CT excitation. The time delayed probe pulse will thus ionize the  $\text{Ag}_3$  fragments formed in this process to yield  $\text{Ag}_3^+$ . Therefore, the fs dynamics reflected by the exponentially rising signal of  $\text{Ag}_3\text{-bz}_3^+$  must originate from the motion of the wavepacket as it reaches the Franck-Condon window for the ionization of  $\text{Ag}_3$  at the respective probe laser wavelengths. These time constants have been deduced by fitting exponential growth models to the data in Figure 7.3b to be  $\tau_1' = 0.4$  ps for the 393 nm pump and 353 nm probe configuration (positive delay times) and  $\tau_2' = 1.3$  ps for the 353 nm pump and 393 nm probe configuration (negative time delays), respectively.

These time scales of geometric rearrangement and dissociation of neutral  $\text{Ag}_5$  compare very well with the dynamics measured previously in the abovementioned NeNePo (negative-

to-neutral-to-positive) fs pump-probe experiment in which the  $\text{Ag}_5$  was prepared by electron detachment from the anion.<sup>276</sup>

## 7.3 Conclusions

A new experimental concept has been proposed to investigate the reaction dynamics of metal cluster complexes based on gas phase ion trap and fs pump-probe techniques. In this concept photo-induced electron transfer (CT excitation) from a benzene ligand adsorbed on a positively charged metal cluster induces neutralization of the metal cluster resulting in a change of the reactivity of the cluster or of other ligands coadsorbed on the cluster. The respective reaction dynamics is probed by time delayed product ionization.

First experiments presented here show that (i) silver and gold cluster cations of different sizes ( $\text{Ag}_{3,5}^+$ ,  $\text{Au}_{3,5}^+$ ) react with benzene in a rf octopole ion trap setup under multiple collision conditions leading to size and element dependent adsorbate coverages. (ii) Also the coadsorption of  $\text{C}_6\text{H}_6$  and a second ligand molecule (here carbon monoxide) is observed in the case of the gold clusters ( $\text{Au}_{3,5}^+$ ). (iii) Photodissociation experiments performed at laser wavelengths of 353 nm and 393 nm indeed indicate the presence of the CT excitation mechanism for  $\text{Ag}_3\text{-bz}_3^+$  and  $\text{Ag}_5\text{-bz}_2^+$  leading to  $\text{bz}_2^+$  photoproducts. Finally, (iv) the fs time resolved signal intensities of the  $\text{Ag}_5\text{-bz}_2^+$  and  $\text{Ag}_3\text{-bz}_3^+$  photoproducts provide insight into the CT induced reaction dynamics and are interpreted in terms of the separation of the neutralized  $\text{Ag}_5$  from  $\text{bz}_2^+$ , its geometric rearrangement and its dissociation to yield  $\text{Ag}_3$ , which is subsequently ionized.  $\text{Ag}_3^+$  further reacts with benzene in the ion trap to form the observed final product  $\text{Ag}_3\text{-bz}_3^+$ .

## Interaction of gold and silver cluster cations with CH<sub>3</sub>Br: Thermal and photoinduced reaction pathways\*

---

*The reactions of free, size selected Au<sub>n</sub><sup>+</sup> (n = 1 - 3, 5, 7) and Ag<sub>3</sub><sup>+</sup> clusters with CH<sub>3</sub>Br as well as the photodissociation of the resulting complexes at 266 nm were studied in the radio frequency ion trap under multiple collision condition. CH<sub>3</sub>Br was found to interact more strongly with the gold clusters than with the silver clusters. All investigated metal clusters exhibited characteristic size dependent adsorbate coverages. Furthermore, the successive loss of methyl radicals was identified as a major thermal reaction channel of the adsorbed CH<sub>3</sub>Br molecules. Photodissociation experiments were performed with the product complexes of the trimer clusters and revealed the strongly preferred lightinduced fragmentation of Au<sub>3</sub>Br<sub>3</sub><sup>+</sup> and Ag<sub>3</sub>Br<sub>3</sub><sup>+</sup>, respectively, over any other thermal reaction products. However, whereas in the case of the gold cluster complexes the bare Au<sub>3</sub><sup>+</sup> was exclusively re-formed through laser irradiation, considerable photoinduced metal cluster fragmentation occurred in the case of Ag<sub>3</sub>Br<sub>3</sub><sup>+</sup>.*

---

\* The contents of this chapter have been accepted as a contribution to *The European Physical Journal D*: D. M. Popolan, T. M. Bernhardt, "Interaction of gold and silver cluster cations with CH<sub>3</sub>Br: Thermal and photoinduced reaction pathways".

## 8.1 Introduction

Gas-phase studies of free metal clusters provide an ideal means to assess the elementary processes of bond-making and bond-breaking that are potentially involved in reactions catalyzed by metal particles, while avoiding complications due to solvent or substrate effects. Although such investigations might certainly never account for the precise mechanisms operative in applied catalysis, gas-phase studies can provide a conceptual framework and an efficient tool to obtain direct insight into reactivity patterns.<sup>120</sup> Moreover, by increasing the cluster size atom by atom, important knowledge about the transition from the chemistry of single atoms to that of nanoparticles can be achieved.<sup>278</sup>

Methyl halogenides have been considered as precursors in a highly selective methanol synthesis via catalytic hydrolysis.<sup>279</sup> In this respect, the reactions of free gold cluster cations with  $\text{CH}_3\text{Cl}$  and  $\text{H}_2\text{O}$  were recently investigated in this laboratory.<sup>280</sup> In the present contribution, these studies were extended to the interaction of small gold and silver cluster cations with  $\text{CH}_3\text{Br}$ . In addition, the lightinduced fragmentation of the resulting reaction products was probed employing femtosecond (fs)-laser excitation.

The adsorption and photodissociation of methyl bromide molecules on magnesia supported gold clusters had been recently investigated in this laboratory as well<sup>127,281</sup> and the present study aims to provide data for a direct comparison of the gas-phase and surface results.

The gas phase reactions of the atomic noble metal ions  $\text{Au}^+$  and  $\text{Ag}^+$  with methyl bromide were studied by various groups before,<sup>153,282-284</sup> but no investigations of the reactions of  $\text{CH}_3\text{Br}$  with  $\text{Au}_n^+$  and  $\text{Ag}_n^+$  ( $n > 1$ ) cluster cations have been reported so far.

The results presented here reveal a strongly cluster size dependent methyl bromide adsorption coverage and extensive methyl elimination reactions succeeding the molecular  $\text{CH}_3\text{Br}$  adsorption. Most strikingly, a highly selective photodissociation behavior was observed in which preferably the bromine-rich thermal reaction products were depleted through laser irradiation. In the case of  $\text{Au}_3^+$  this lead to a lightinduced re-formation of the bare gold cluster cation which could further react with residual  $\text{CH}_3\text{Br}$  in the ion trap establishing a photocatalytic methyl radical elimination mechanism.

## 8.2 Results and Discussion

### 8.2.1 Thermal reactions of $\text{Au}_n^+$ ( $n=1-3, 5, 7$ ) clusters with $\text{CH}_3\text{Br}$

The reaction behavior of small cationic gold clusters  $\text{Au}_2^+$ ,  $\text{Au}_3^+$ ,  $\text{Au}_5^+$ , and  $\text{Au}_7^+$  with methyl bromide was investigated experimentally here for the first time. No theoretical studies on the methyl bromide adsorption on free gold atoms or clusters have been reported so far as well. Only for the case of the atomic ion  $\text{Au}^+$  the reactions with  $\text{CH}_3\text{Br}$  have been investigated experimentally previously.<sup>282-284</sup>

A mass spectrum showing the reaction products of  $\text{Au}^+$  with  $\text{CH}_3\text{Br}$  obtained in our ion trap experiment at room temperature is displayed in Figure 8.1a.  $\text{Au}^+$  adsorbed a maximum of two  $\text{CH}_3\text{Br}$  molecules, which however subsequently dissociated on the gold ion under the loss of  $\text{CH}_3$  radicals. The resulting product peaks of  $\text{Au}(\text{CH}_3\text{Br})\text{Br}^+$  and  $\text{AuBr}_2^+$  are consequently observed in the mass spectrum in Figure 8.1a. In addition, two products resulting from an apparent dehydrogenation reaction are detected:  $\text{AuC}_2\text{H}_4(\text{CH}_3\text{Br})^+$  and the corresponding methyl elimination product  $\text{AuC}_2\text{H}_4\text{Br}^+$ .

These results are in very good agreement with the earlier investigations of the gas phase reaction of  $\text{Au}^+$  with  $\text{CH}_3\text{Br}$ , in which also the formation of  $\text{Au}(\text{CH}_3\text{Br})_2^+$  and  $\text{AuC}_2\text{H}_4(\text{CH}_3\text{Br})^+$  as well as the methyl elimination reactions had been observed.<sup>282-284</sup>

Figure 8.1b displays the reaction products of  $\text{Au}_2^+$ . The gold dimer is the only cluster size which completely fragmented in the presence of  $\text{CH}_3\text{Br}$ . Furthermore, the formed  $\text{Au}(\text{CH}_3\text{Br})_2^+$  fragment also successively forfeited the  $\text{CH}_3$  radicals.

The product mass spectra of  $\text{Au}_3^+$  are displayed in Figure 8.1c and (as a function of the reaction time) in Figure 8.1f-j. For the shortest investigated reaction time of 10 ms (Figure 8.1c and f), the predominant mass peak corresponds to  $\text{Au}_3(\text{CH}_3\text{Br})_3^+$  and additionally only a small  $\text{Au}_3(\text{CH}_3\text{Br})_2\text{Br}^+$  signal was observed. The fact that no product complexes with less than the maximum  $\text{CH}_3\text{Br}$  coverage of three molecules were observed even at the shortest reaction time indicates that the adsorption of the first methyl bromide molecule is the rate determining step in the sequential adsorption reaction.<sup>113</sup> At a reaction time of 100 ms (Figure 8.1g) the  $\text{Au}_3(\text{CH}_3\text{Br})_2\text{Br}^+$  concentration was slightly increased and a small contribution from  $\text{Au}_3(\text{CH}_3\text{Br})\text{Br}_2^+$  was observed. The intensities of the methyl elimination products successively increased with reaction time (Figures 8.1h-j) eventually yielding  $\text{Au}_3\text{Br}_3^+$  as major product at  $t_R = 5$  s.

The observation of the adsorption of a maximum of three ligands ( $\text{CH}_3\text{Br}$  or  $\text{Br}$ ) is in accordance with the minimum energy structure of  $\text{Au}_3^+$  which is a planar equilateral triangle ( $D_{3h}$  symmetry) with three electronically equivalent corners each presenting one adsorption site.<sup>81,268,285</sup> Since the bromide atom exhibits the largest electronegativity in  $\text{CH}_3\text{Br}$ , it can be assumed that methyl bromide coordinates to the cluster cations through the bromide atom.

In addition to the methyl bromide adsorption and methyl radical elimination product complexes, the emergence of a product peak assigned to  $\text{Au}_3(\text{C}_2\text{H}_4)_3\text{CH}_3\text{Br}^+$  was detected for reaction times longer than 500 ms. A  $\text{C}_2\text{H}_4$  ligand results apparently from multiple dehydrogenation steps similar to those observed in the case of the reactions of the atomic ion  $\text{Au}^+$  (cf. Figure 8.1a).

The investigations were extended to  $\text{Au}_5^+$  and  $\text{Au}_7^+$ . The corresponding product mass spectra are depicted in Figure 8.1d and e. In both cases a maximum adsorption of four  $\text{CH}_3\text{Br}$  molecules was observed at room temperature even for longer reaction times (not shown here). A saturation coverage of four ligands is nicely in accordance with the geometry of the  $\text{Au}_5^+$  cluster which is an X-shaped configuration ( $D_{2h}$  symmetry<sup>82,121</sup>) with four electronically equivalent corner atoms as binding sites. In contrast,  $\text{Au}_7^+$  exhibits a hexagon structure,<sup>81</sup>

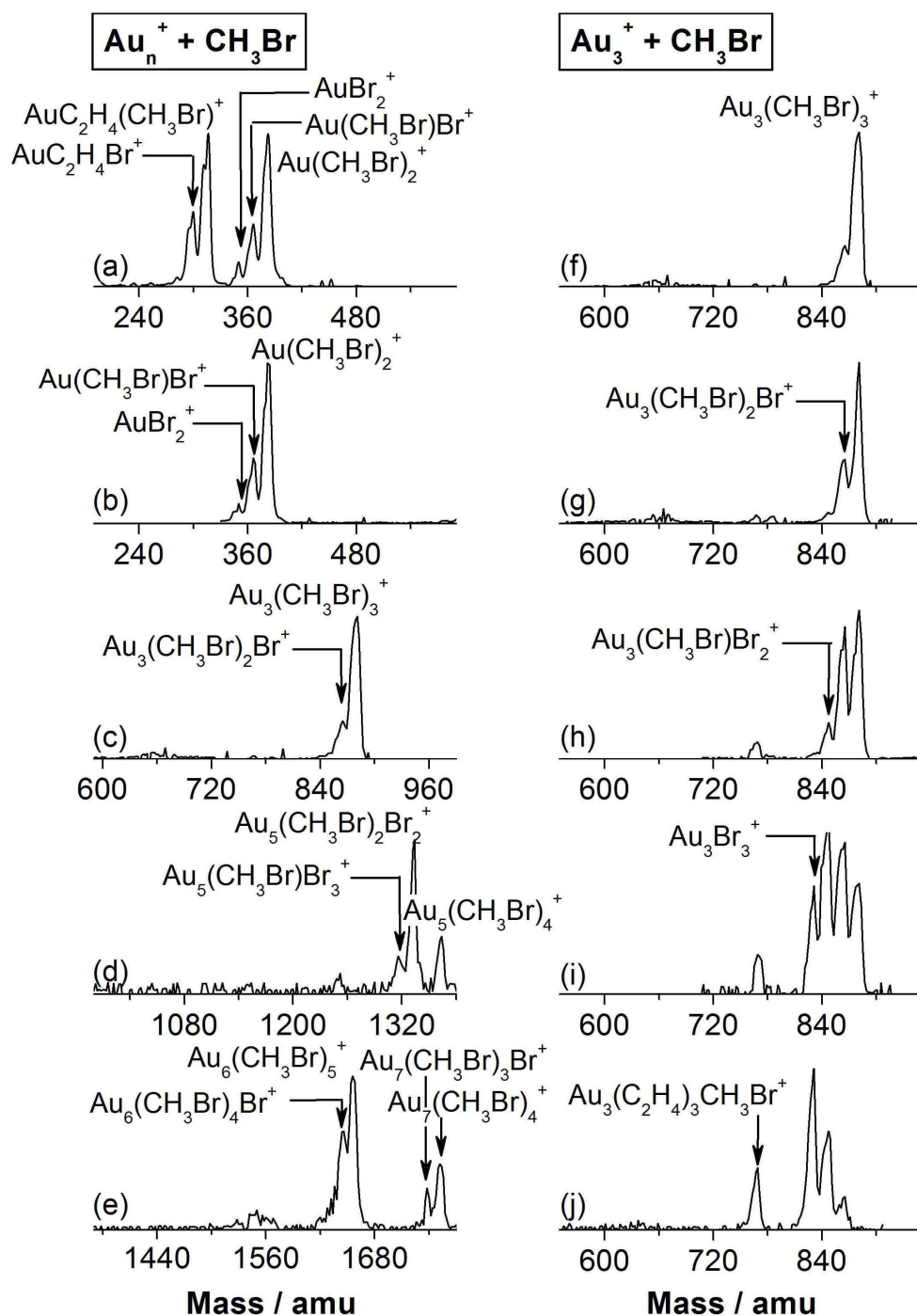


**Figure 8.1:** Product ion mass spectra of the reaction of (a)-(e)  $\text{Au}_n^+$  ( $n = 1-3, 5, 7$ ) with  $\text{CH}_3\text{Br}$  ( $t_R = 10$  ms), (f)-(j)  $\text{Au}_3^+$  with  $\text{CH}_3\text{Br}$  after different reaction times between 10 ms and 5 s (300 K,  $p(\text{He}) = 1$  Pa,  $p(\text{CH}_3\text{Br}) = 0.1$  Pa)



which would suggest a maximum saturation coverage of six ligands. This indicates that lower reaction temperatures might be required in this case to reach the maximal possible number of ligand molecules.<sup>121</sup> Analogous to  $\text{Au}_3^+$ , a successive elimination of the  $\text{CH}_3$  radical from the adsorbed  $\text{CH}_3\text{Br}$  molecules with increasing reaction time was observed for  $\text{Au}_5^+$  and  $\text{Au}_7^+$ . This methyl elimination was accompanied by the partial fragmentation of the metal cluster for  $\text{Au}_7^+$  (see Figure 8.1e).

### 8.2.2 Photodissociation of $\text{Au}_3(\text{CH}_3\text{Br})_n\text{Br}_{3-n}^+$ ( $n = 1-3$ ) product complexes

Figure 8.2a shows again the product mass spectrum obtained after 5 s from the reaction of  $\text{Au}_3^+$  with  $\text{CH}_3\text{Br}$  under thermal reaction conditions (300 K). The dominant mass peak corresponds to  $\text{Au}_3\text{Br}_3^+$ . In the photodissociation experiments the reaction mixture in the ion trap was irradiated with 266 nm laser pulses at a repetition rate of 1 kHz during the whole reaction

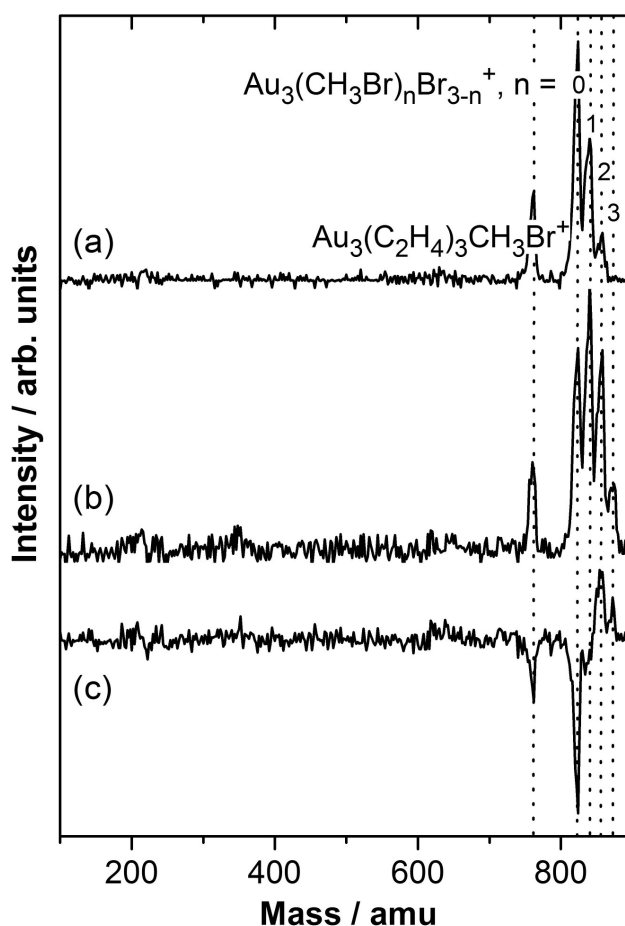


**Figure 8.2:** Photodissociation of  $\text{Au}_3(\text{CH}_3\text{Br})_n\text{Br}_{3-n}^+$  ( $n = 1-3$ ) product complexes. (a) Thermal reaction products of  $\text{Au}_3^+$  after 5 s reaction time (300 K,  $p(\text{CH}_3\text{Br}) = 0.1$  Pa). (b) Product ion mass spectrum obtained under similar reaction conditions after 5 s laser irradiation (266 nm). (c) Difference spectrum (b-a).

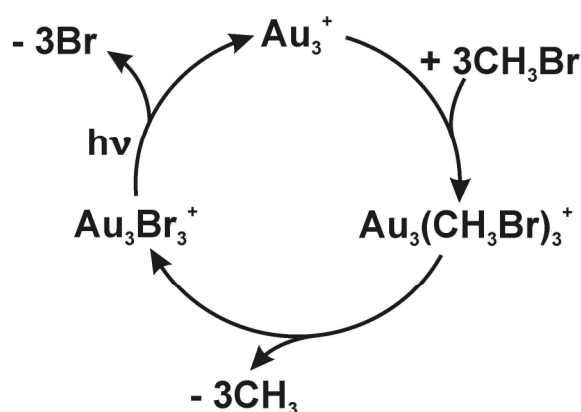


**Figure 8.3:** Proposed mechanism for the photocatalytic methyl elimination reaction.

time of 5 s. Subsequently, the mass spectrum depicted in Figure 8.2b was recorded. It can be observed that the relative intensity of the methyl elimination products have changed considerably. Most strikingly, the complex  $\text{Au}_3(\text{CH}_3\text{Br})_3^+$ , which is absent in the mass spectrum of Figure 8.2a, is re-formed during irradiation as can be seen from Figure 8.2b.

The selective interaction of the laser light with some molecular complexes in the ion trap is even more apparent from the photodissociation difference spectrum shown in Figure 8.2c which clearly demonstrates the preferred photoinduced depletion of  $\text{Au}_3\text{Br}_3^+$  over all other thermal reaction products. Also the product  $\text{Au}_3(\text{C}_2\text{H}_4)_3\text{CH}_3\text{Br}^+$  and to a small extent  $\text{Au}_3(\text{CH}_3\text{Br})\text{Br}_2^+$  are depleted. In contrast, the concentrations of  $\text{Au}_3(\text{CH}_3\text{Br})_2\text{Br}^+$  and  $\text{Au}_3(\text{CH}_3\text{Br})_3^+$  increase due to laser irradiation.

These observations in conjunction with the fact that no further fragmentation products are observed in the mass spectra of Figure 8.2 lead to the conclusion that the preferred light-induced decomposition of  $\text{Au}_3\text{Br}_3^+$  must result in the re-formation of the bare  $\text{Au}_3^+$  cluster. The gold trimer cation is in turn able to react again with the residual  $\text{CH}_3\text{Br}$  in the ion trap. As a consequence, the relative concentration of the adsorption products before methyl elimination is increased as observed in the mass spectra of Figure 8.2b in comparison to Figure 8.2a. This mechanism is summarized in the “photocatalytic” reaction cycle displayed in Figure 8.3 and presents a versatile methyl radical source which might be used in future experiments to methylate coadsorbed ligand molecules.

### 8.2.3 Thermal reaction of $\text{Ag}_3^+$ with $\text{CH}_3\text{Br}$

Compared to gold, the silver clusters were found to be less reactive toward methyl bromide. Figure 8.4 displays the product ion mass spectra for the reaction of  $\text{Ag}_3^+$  with methyl bromide recorded at a reaction time of 5 s and different reaction temperatures from 300 K to 230 K. At 300 K (Figure 8.4a) almost no reaction products were observed. At lower temperatures (Figure 8.4b and c) the sequential adsorption of  $\text{CH}_3\text{Br}$  molecules was detected. As a consequence

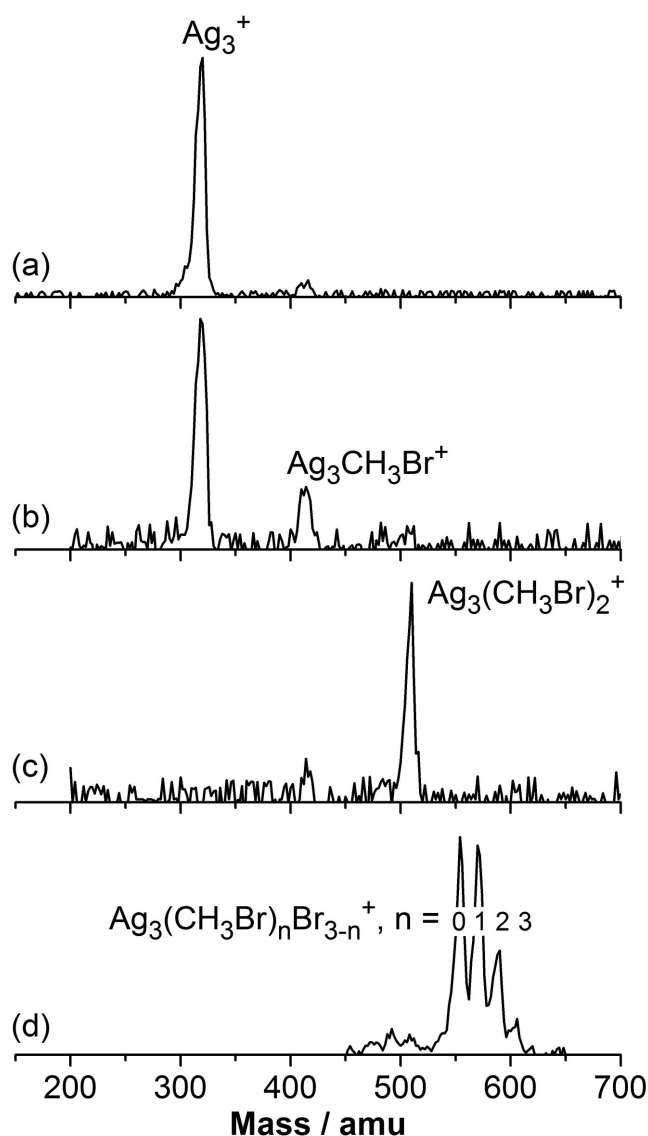


**Figure 8.4:** Product ion mass spectra of the reaction of  $\text{Ag}_3^+$  with  $\text{CH}_3\text{Br}$  at various reaction temperatures: (a) 300 K, (b) 250 K, (c) 240 K, and (d) 230 K ( $p(\text{He}) = 1 \text{ Pa}$ ,  $p(\text{CH}_3\text{Br}) = 0.1 \text{ Pa}$ ,  $t_R = 5 \text{ s}$ ).

of the smaller reactivity of the silver clusters toward  $\text{CH}_3\text{Br}$  compared to gold, the maximum coverage of three  $\text{CH}_3\text{Br}$  was only reached at 230 K (Figure 8.4d). Subsequently, similar to the behavior of  $\text{CH}_3\text{Br}$  adsorbed on the gold trimer clusters, the C-Br bond of the adsorbed molecules broke progressively, such that for 5 s reaction time the  $\text{Ag}_3\text{Br}_3^+$  product exhibited the highest intensity in the recorded mass spectrum in Figure 8.4d. However, no dehydrogenation products were observed in the case of  $\text{Ag}_3^+$ .

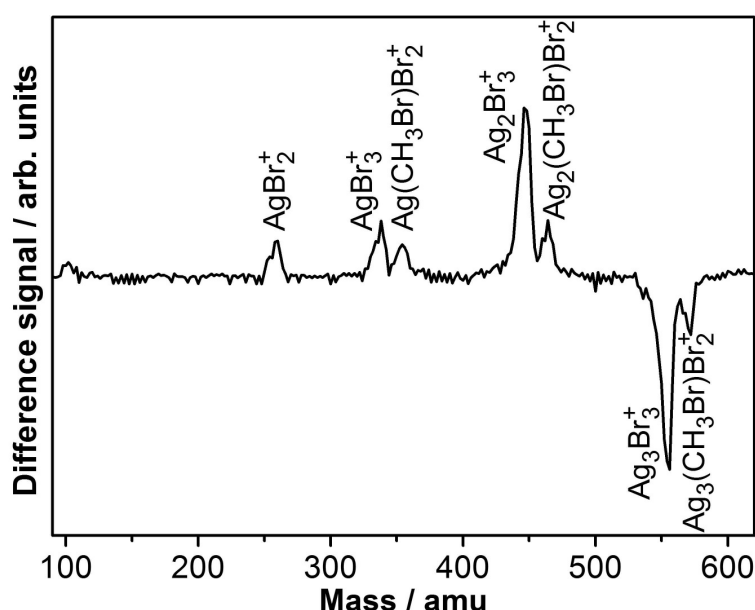


**Figure 8.5:** Photodissociation mass spectrum of the  $\text{Ag}_3(\text{CH}_3\text{Br})_n\text{Br}_{3-n}^+$  ( $n = 1-3$ ) product complexes at a laser wavelength of 266 nm (230 K,  $t_R = 5$  s,  $p(\text{CH}_3\text{Br}) = 0.1$  Pa)

#### 8.2.4 Photodissociation of $\text{Ag}_3(\text{CH}_3\text{Br})_n\text{Br}_{3-n}^+$ ( $n = 1-3$ ) product complexes

Also in the case of the silver trimer reactions, the photoinduced dissociation of the reaction products was investigated. Figure 8.5 shows the photodissociation difference mass spectrum which resulted from the subtraction of the thermal product mass spectrum (5 s reaction time) from the reaction product spectrum obtained with laser irradiation (266 nm, also 5 s reaction time). This difference spectrum clearly shows the preferred chromophoric properties of the product  $\text{Ag}_3\text{Br}_3^+$  compared to all other reaction products. However, the depletion of  $\text{Ag}_3\text{Br}_3^+$  (and to a minor extent of  $\text{Ag}_3(\text{CH}_3\text{Br})\text{Br}_2^+$ ) was accompanied by a considerable metal cluster fragmentation as indicated by the various product peaks at lower masses in Figure 8.5. This observation is in agreement with previous photodissociation and metastable fragmentation studies on silver bromide cluster cations.<sup>286-288</sup>

### 8.3 Summary and comparison to the supported clusters data

The experiments presented in this chapter showed that  $\text{Au}_n^+$  ( $n = 1-3, 5, 7$ ) and  $\text{Ag}_3^+$  react with methyl bromide in an rf octopole ion trap under multiple collision conditions leading to size dependent  $\text{CH}_3\text{Br}$  coverages. Under thermal conditions the successive loss of methyl radicals was identified as major adsorbate reaction channel. Interestingly, these gas phase results, namely that methyl bromide decomposed on small gold clusters, provide an explanation why no molecular  $\text{CH}_3\text{Br}$  desorption was observed in previous temperature programmed desorption experiments (TPD) of  $\text{CH}_3\text{Br}$  on magnesia supported gold clusters, if the cluster size did

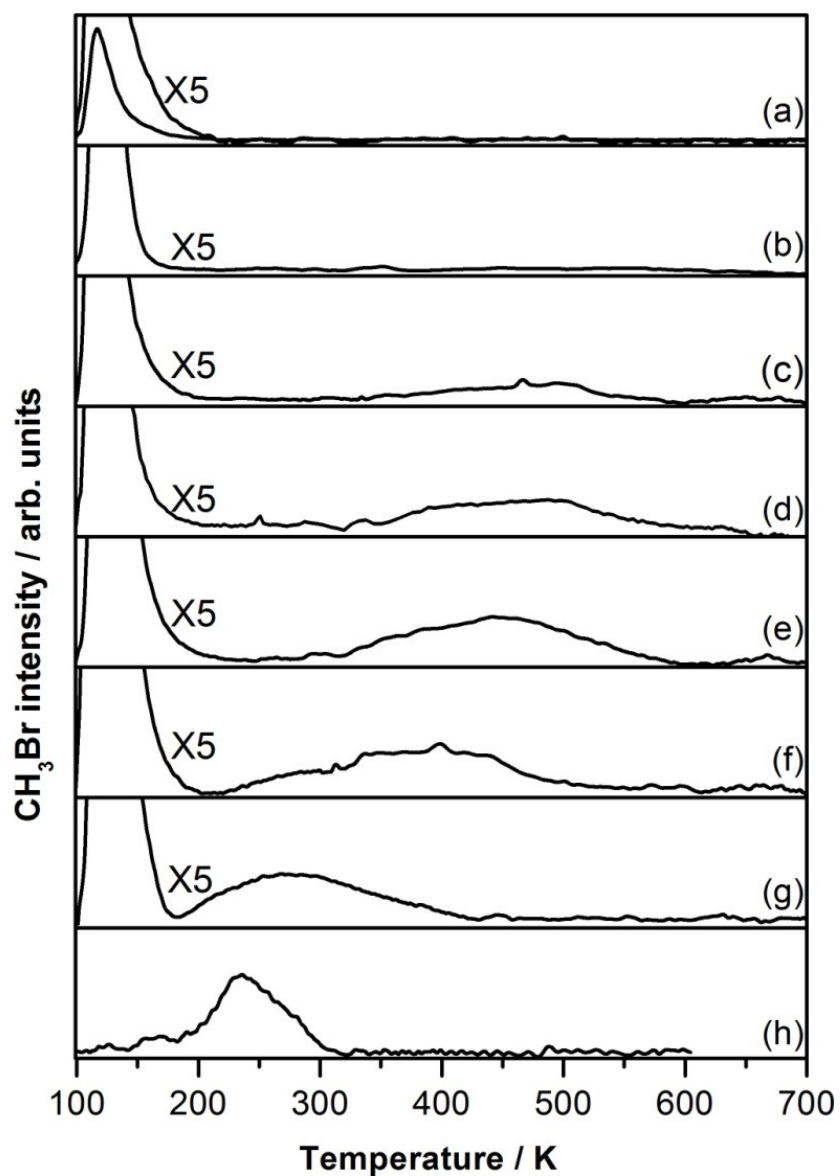


**Figure 8.6:** TPD spectra of  $\text{CH}_3\text{Br}$  from (a) bare 10 ML MgO on Mo(100); (b-g) MgO supported gold nano-particles generated by depositing different gold coverages ((b) 0.07 ML Au; (c) 0.1 ML Au; (d) 0.13 ML Au; (e) 0.45 ML Au; (f) 1 ML Au; (g) 3 ML Au) and (h) 10 ML gold film on Mo(100). The spectra were obtained with a heating rate of 2 K/s. The numbers indicated at the spectra represent the  $\text{CH}_3\text{Br}$  exposure in units of Langmuir (L).<sup>127</sup>

not exceed a certain value corresponding to an Au coverage above 0.07 ML.<sup>127,281</sup> Figure 8.6b-g displays the CH<sub>3</sub>Br TPD spectra recorded from magnesia supported gold clusters. For comparison the TPD spectrum recorded from a gold surface is presented as well (Figure 8.6h). A single desorption peak below 180 K originates from CH<sub>3</sub>Br molecular desorption from the bare magnesia surface (see Figure 8.1a-g). A second desorption peak above 200 K was detected just on magnesia surfaces prepared with gold nanoparticles (see Figure 8.6c-g). Thus, this second peak, which also shifts with the gold coverage and hence with the gold particle size was attributed to CH<sub>3</sub>Br molecular desorption from Au nanoparticles. For the lowest gold coverage of 0.07 ML, where small 2D Au clusters are expected on the magnesia surface,<sup>127,289,290</sup> no molecular CH<sub>3</sub>Br desorption from the gold clusters is detected, but just the peak below 180 K is observed (see Figure 8.6b). From the gas phase observation of dissociative CH<sub>3</sub>Br adsorption on very small gold clusters it can be proposed that the CH<sub>3</sub>Br molecules also strongly interact with the smallest gold clusters on the surface, leading to CH<sub>3</sub>Br dissociation in these cases (0.07 ML Au).

The photodissociation of the product complexes of the silver and gold trimer clusters in the ion trap revealed a strongly preferred lightinduced fragmentation of Au<sub>3</sub>Br<sub>3</sub><sup>+</sup> and Ag<sub>3</sub>Br<sub>3</sub><sup>+</sup>. In the case of the gold trimer complexes, the metal cluster Au<sub>3</sub><sup>+</sup> was even re-formed without fragmentation, which leads to the formulation of a photocatalytic reaction cycle in which methyl radicals are thermally liberated followed by the lightinduced abstraction of the remaining bromine atoms.

## Conclusions and outlook

---

In the present investigations, the reaction kinetics and fs-photodissociation of small noble metal clusters-molecule complexes in the gas-phase were explored. These investigations were motivated by the significant role played by small particles in catalytic processes and especially by gold nanoparticles in the low-temperature combustion of carbon monoxide. Although gas-phase studies are simplified systems, such experiments are important in order to determine reactivity patterns and general concepts that are relevant to the analysis of catalytic reaction mechanisms.

The experimental approach employed in the presented studies relies on the storage of mass-selected pure and binary silver-gold cluster ions in an octopole ion trap. The tandem quadrupole/octopole mass spectrometer arrangement allowed the investigation of the reactivity of the metal clusters towards different reactive gases (CO, N<sub>2</sub>O, C<sub>6</sub>H<sub>6</sub>, CH<sub>3</sub>Br) under thermodynamically well defined conditions. The fs-photodissociation dynamics of cluster-adsorbate complexes was investigated by means of a femtosecond laser system.

By applying RRKM analysis or thermodynamic equilibrium methods, the binding energy of the CO ligand to pure and binary silver-gold cluster trimers were calculated from the measured reaction rate constants or/and equilibrium constants, respectively. The binding energies of the first CO molecule to the trimer clusters was found to increase with increasing gold content in the cluster composition and with changing charge from negative to positive. The gas-phase investigations in conjunction with *ab initio* DFT calculations performed in the group of Prof. V. Bonačić-Koutecký enabled us to reveal clear additive trends in the CO binding strength which provide a means to tune chemical reactivity by changing silver content and charge state in the binary silver-gold clusters. The implication of such reactivity tuning on selected reactions of CO catalyzed by small silver-gold clusters was discussed. In particular, the coadsorption and potential reaction of electron donor ligand as H<sub>2</sub> and H<sub>2</sub>O with CO was proposed to be carefully adjusted through silver content of positively charged gold clusters in the clusters.

The investigations were further extended to binary silver-gold cluster pentamers. Similar to the trimer case, the CO binding energies to  $\text{Ag}_n\text{Au}_m^+$  ( $n+m = 5$ ) decrease with increasing number of silver atoms in the bimetallic clusters. The adsorption of multiple CO molecules onto binary silver-gold cations revealed a strong dependence of the cluster complex geometry on the number of CO ligands as well as on the metal cluster composition. The experimental binding energies for sequential adsorption obtained by means of thermodynamic equilibrium methods were found to be generally in excellent agreement with the results of the DFT first principle calculations performed in the group of Prof. V. Bonačić-Koutecký. The theoretical binding energies were obtained employing the B3LYP functional with the exception of  $\text{Ag}_4\text{Au}(\text{CO})_4^+$  and  $\text{Ag}_5(\text{CO})_4^+$ , where the unexpectedly weak bonding interaction of the fourth CO is better described by the more accurate wave function based CCSD calculation. The results obtained for multiple CO adsorption on binary silver-gold clusters revealed the rigidity of gold clusters, due to the presence of relativistic effects that support directional bonding. In contrast, silver clusters exhibited a much more viable structural fluxionality which is exerted in the present case in a pronounced structural transformation upon bonding of three CO which in turn strongly averts further CO adsorption.

Since one of the primary goal of these investigations was to study the catalytic properties of cationic clusters for CO oxidation reaction, the reactivity of positively charged gold and silver clusters in the presence of a well defined mixture of nitrous oxide and carbon monoxide was measured. Silver as well as gold were found to be completely inert in reaction with oxygen under our experimental conditions and no coadsorption products were observed when both  $\text{O}_2$  and CO were present in the trap. Therefore, the approach to produce metal oxide used in the present work was through reaction with  $\text{N}_2\text{O}$ . In addition to the metal-oxide formation, a competitive channel corresponding to the formation of  $\text{M}_3\text{O}_x(\text{N}_2\text{O}_2)_y^+$  ( $\text{M} = \text{Ag}, \text{Au}$ ;  $x, y = 1-3, x \geq y$ ) products was observed. Evidence for a successful CO oxidation on silver and gold trimers were observed. In the future, the combination of the experimental results with *ab initio* theoretical simulations will be important for defining and evaluating catalytic factors, as well as for understanding of the energetics of the reaction steps involved in the catalytic cycle, or the structure of the reaction intermediates.

In a further set of experiments, a new experimental concept has been proposed to investigate the reaction dynamics of metal clusters complexes. In this concept photoinduced electron transfer (CT excitation) from a benzene ligand adsorbed on a positively charged metal cluster induces neutralization of the metal cluster resulting in a change of the reactivity of the clusters towards ligands coadsorbed on the clusters. The reactive reaction dynamics was probed by time delayed product ionization. Silver and gold cluster cations of different sizes ( $\text{Ag}_{3,5}^+, \text{Au}_{3,5}^+$ ) reacted with benzene leading to size and element dependent adsorbate coverages. The coadsorption of  $\text{C}_6\text{H}_6$  and a second ligand molecule, CO in this case, was observed for the investigated gold clusters ( $\text{Au}_{3,5}^+$ ). Photodissociation experiments performed at laser wavelengths of 353 and 393 nm revealed the presence of CT excitation mechanism for  $\text{Ag}_3$ -



$\text{bz}_3^+$  and  $\text{Ag}_5\text{-bz}_2^+$  leading to  $\text{bz}_2^+$  products. For  $\text{Ag}_5\text{-bz}_2^+$  it was even possible to measure the femtosecond time resolved fragmentation dynamics. The fs time resolved signal intensities of the  $\text{Ag}_5\text{-bz}_2^+$  and  $\text{Ag}_3\text{-bz}_2^+$  products provide insight into the CT induced reaction dynamics and are interpreted in terms of the separation of the neutralized  $\text{Ag}_5$  from  $\text{bz}_2^+$ , its geometric rearrangement, and its dissociation to yield  $\text{Ag}_3$ , which was subsequently ionized, and further reacted with benzene in the ion trap to form the final product  $\text{Ag}_3\text{-bz}_3^+$ .

Further investigations will aim to identify additional coadsorption products of the cluster-organic molecule systems that exhibit CT induced photoreactions and are potentially interesting candidates for catalytically relevant reactions to be investigated in the ion trap. Of particular future interest would be the reaction of activated  $\text{O}_2$  with CO, because whereas cationic gold and silver clusters do not promote the catalytic CO oxidation, neutral and negatively charge clusters of those elements have been previously observed to efficiently catalyze the transformation of CO to  $\text{CO}_2$ .

As photochemical model system the gas-phase interaction between  $\text{CH}_3\text{Br}$  and  $\text{Au}_n^+$  ( $n = 1, 2, 3, 5, 7$ ) was investigated. The gas-phase investigations revealed that methyl bromide molecularly adsorbed on  $\text{Au}_3^+$  and sequentially forfeited the  $\text{CH}_3$  radical with increasing the reaction time. A similar trend was found for all investigated gold cluster sizes up to seven atoms per cluster. These studies were important to the understanding of  $\text{CH}_3\text{Br}$  adsorbed on supported gold clusters on magnesia ultrathin films. Based on the surface results and the present gas-phase observations, it seems reasonable to assume that Au atoms and small Au cluster consisting of just few atoms supported on a magnesia surface induce a dissociation of the C-Br bond of the adsorbed  $\text{CH}_3\text{Br}$  molecules. Consequently, neither  $\text{CH}_3^+$  transient signal nor  $\text{CH}_3\text{Br}$  thermal desorption was observed from thin magnesia films covered with less than 0.06 ML Au.

In conclusion, there is no doubt that a new catalytic chemistry emerges in the non-scalable size regime where reactivity and selectivity can be influenced in a distinct way by adding or removing single atoms and by changing the electronic charge state and the composition of the clusters. The experiments performed in the present work allow a detailed insight into charge and composition dependent reactivity as well as into coadsorption phenomena which are extremely important in order to conceptionally understand the catalytic relevant reactions. In particular with respect to photo reaction and/or coadsorption reactions, future experiments with two sequential ion traps (for reaction and for photodissociation) might be helpful to unambiguously reveal the photodissociation pathways of the metal cluster-molecule complexes.



# Zusammenfassung

Das Ziel der vorliegenden Arbeit war es, die Chemie freier, massenselektierter Gold, Silber und binärer Ag-Au Cluster in Abhängigkeit von ihrer Größe und Zusammensetzung zu untersuchen.

Kürzlich wurde gezeigt, dass Cluster dieser Art unerwartete größenabhängige katalytische Aktivität aufweisen, wenn sie sich auf metalloxidischen Oberflächen befinden. Diese Beobachtungen warfen Fragen bezüglich der intrinsischen Eigenschaften dieser Cluster und bezüglich ihres Verhaltens gegenüber katalytisch relevanten Liganden auf.

Im Rahmen dieser Dissertation werden die oben angeführten Fragestellungen von zwei Seiten angegangen: (i) durch Reaktivitätsmessungen massenselektierter  $\text{Ag}_n^+$ ,  $\text{Au}_m^+$  und  $\text{Ag}_n\text{Au}_m^+$  Nanocluster in der Gasphase unter definierten Reaktionsbedingungen und (ii) durch Untersuchung der durch einen Femtosekunden-Laser induzierten Photodissoziation der gebildeten Komplexe.

Temperaturabhängige Reaktivitätsmessungen wurden durchgeführt, um die Bindungsenergien von Kohlenstoffmonooxid an dreiatomige, binäre Ag-Au Cluster-Kationen und Anionen zu untersuchen. Es wurde gezeigt, dass die Bindungsenergien des ersten CO-Moleküls an Cluster-Trimere mit zunehmendem Goldanteil und mit einem Ladungswechsel von negativ zu positiv ansteigen. Demzufolge kann die Reaktivität binärer Cluster höchst sensitiv beeinflusst werden durch Veränderungen des Ladungszustandes oder des Ag-Au Verhältnisses. Auch die Adsorption von mehreren CO-Molekülen an die o.g. Cluster wurde untersucht. Es stellte sich heraus, dass die maximale Anzahl an adsorbierten CO-Molekülen insbesondere von der Ladung des Clusters und dessen Zusammensetzung abhängt. Bei kryogenen Temperaturen bildete das kationische  $\text{Au}_3$ -Cluster einen Carbonylkomplex der Form  $\text{Au}_3(\text{CO})_4^+$  aus, wohingegen sich nur maximal zwei CO-Moleküle an das anionische Pendant anlagerten und zu  $\text{Au}_3(\text{CO})_2^-$  führten. Während alle anderen kationischen Trimer-Cluster drei CO-Moleküle adsorbierten, waren die entsprechenden anionischen Cluster unter den gegebenen experimentellen Bedingungen gegenüber der Adsorption von CO inert.

Die experimentellen Messungen wurden auf die Untersuchung größerer Cluster ausgedehnt. Temperaturabhängige Gleichgewichtsmethoden wurden angewendet, um die Bindungsenergien der sequentiellen Adsorption von CO an fünfatomige Ag-Au Cluster-Kationen zu untersuchen. Es zeigte sich, dass die CO-Bindungsenergien an  $\text{Ag}_n\text{Au}_m^+$  ( $n+m=5$ ) Cluster mit zunehmender Anzahl an Ag-Atomen abnehmen. Besonders auffällig war die deutliche Herabsetzung der Bindungsenergien der weiteren CO-Moleküle nach der Adsorption des vierten CO-Moleküls an  $\text{Au}_5^+$  beziehungsweise des dritten CO-Moleküls an  $\text{Ag}_5^+$ . Im Einklang mit theoretischen Simulationen konnte gezeigt werden, dass diese Beobachtung durch eine CO-induzierte strukturelle Transformation erklärt werden kann, welche zu einer kompakteren Anordnungen der Metallcluster führt. Die Berechnungen der Strukturen sämtlicher untersuchter Systeme wurden von Professor Vlasta Bonačić-Koutecký und ihren Mitarbeitern unter

Verwendung von Dichtefunktionaltheorie (DFT) durchgeführt.

Während sich herausstellte, dass unter den gegebenen experimentellen Bedingungen Gold- und Silber-Kationen völlig inert gegenüber molekularem Sauerstoff sind, war es möglich metalloxidische Cluster durch Reaktion mit Distickstoffmonoxid ( $\text{N}_2\text{O}$ ) herzustellen. Insbesondere wurde die Reaktion des dreiatomigen Silber-Kationclusters mit  $\text{N}_2\text{O}$  detailliert untersucht, welche einen komplizierten, temperaturabhängigen Reaktionsmechanismus aufweist. Der Reaktionsmechanismus offenbart sich in einem Temperaturbereich von 270 und 230 K durch zunehmende Reaktivität mit abnehmender Temperatur und durch zwei unerwartete Fragmentierungskanäle. Ein experimenteller Hinweis für das Auftreten eines vollständigen katalytischen CO Oxidationszyklus induziert durch Silber- und Goldoxide, konnte durch die Reaktion mit  $\text{N}_2\text{O}$  gefunden werden. In der vorliegenden Arbeit wurde ein derartiger katalytischer Zyklus für Silberoxid-Cluster zum ersten Mal beschrieben.

Darüber hinaus wurden die Reaktionen größenselektierter Gold- und Silber-Kationen  $\text{Ag}_n^+$  und  $\text{Au}_n^+$  ( $n = 3, 5$ ) mit Benzol ( $\text{C}_6\text{H}_6$ ) und mit Gemischen von  $\text{C}_6\text{H}_6$  und CO untersucht. Während es sich zeigte, dass Benzol mit sämtlichen untersuchten Metallclustern reagiert und von der Clustergröße abhängige Adsorbatbedeckungen aufweist, wurde hingegen die Koadsorption von  $\text{C}_6\text{H}_6$  und CO nur auf den untersuchten Goldclustern beobachtet. Experimente zur Photodissoziation bei 353 beziehungsweise 393 nm an Silberclustern liefern Hinweise auf Fragmentierung induziert durch Ladungsverschiebung. Insbesondere konnten für  $\text{Ag}_5(\text{C}_6\text{H}_6)^+$  die in Fragmentierungsgeschwindigkeiten auf der Femtosekunden Zeitskala gemessen werden. Wie in dieser Arbeit gezeigt, könnte die vom Ladungszustand abhängige Reaktivität möglicher Koadsorbate von  $\text{C}_6\text{H}_6$  an kleinen Edelmetallclustern ein neuer, vielversprechender Weg zur Untersuchung von Reaktionen in Echtzeit an Metallclustern sein, die durch eine Laser-induzierte Ladungsverschiebung initiiert werden.

In einer abschließenden Messreihe wurden die Reaktionen von kationischen Goldclustern mit  $\text{CH}_3\text{Br}$  in der Gasphase direkt mit denen von Metalloxid-geträgerten Au-Clustern verglichen. Die Messungen wurden in demselben Messaufbau durchgeführt. Obwohl generell Ergebnisse von Untersuchungen in der Gasphase nicht unmittelbar auf Untersuchungen auf Oberflächen übertragen werden können, lieferte dieser direkte Vergleich jedoch wertvolle Hinweise, um Reaktionen, die an sich auf einer Oberfläche befindlichen Au-Clustern ablaufend, aufzuklären.

# Bibliography

- (1) R. P. Feynman, *Engineering and Science XXIII*, no.5 (1960).
- (2) R. S. Berry and H. Haberland, *Clusters of Atoms and Molecules I*, Ed. H. Haberland (Springer-Verlag, Berlin; New York, 1994).
- (3) U. Kreibig and M. Vollmer, *Optical Properties of Metal Clusters* (Springer-Verlag, Berlin, 1995).
- (4) J. Jortner, *Z. Phys. D* 24, 247 (1992).
- (5) M. Moskovits, *Metal Clusters* (Wiley, New York, 1986).
- (6) M. M. Kappes, *Chem. Rev.* 88, 369 (1988).
- (7) R. A. J. O' Hair and G. N. Khairallah, *J. Cluster Sci.* 15, 331 (2004).
- (8) G. Mie, *Ann. Phys.* 25, 377 (1908).
- (9) W. A. de Heer, W. D. Knight, M. Y. Chou and M. L. Cohen, *Solid State Physics* 40, 93 (1987).
- (10) J. Kowalski, T. Stehlin, F. Träger and M. Vollmer, *Phase Transitions* 24-26, 737 (1990).
- (11) V. Kresin, *Phys. Rep.* 220, 1 (1992).
- (12) W. A. de Heer, *Rev. Mod. Phys.* 65, 611 (1993).
- (13) M. Brack, *Rev. Mod. Phys.* 65, 677 (1993).
- (14) G. C. Papavassiliou, *Prog. Solid State Chem.* 12, 185 (1979).
- (15) J. A. A. J. Perenboom, P. Wyder and F. Meyer, *Phys. Rep.* 78, 171 (1981).
- (16) U. Kreibig and L. Genzel, *Surf. Sci.* 156, 678 (1985).
- (17) W. P. Halperin, *Rev. Mod. Phys.* 58, 533 (1986).
- (18) U. Kreibig and L. Genzel, *Contribution of Clusters Physics to Material Science and Technology: From Isolated Clusters to Aggregated Materials*, Ed. J. Davenas and P. M. Rabette (Nijhoff, Dordrecht, 1986).
- (19) M. L. Mandich, W. D. Reents and V. E. Bondybey, *Atomic and Molecular Clusters* Ed. R. E. Bernstein (Elsevier, Amsterdam, 1990).
- (20) A. Herrmann, M. Hofmann, S. Leutwyler, E. Schumacher and L. Wöste, *Chem. Phys. Lett.* 62, 216 (1979).

- (21) W. D. Knight, K. Clemenger, W. de Heer, W. A. Saunders, M. Y. Chou and M. L. Cohen, *Phys. Rev. Lett.* 52, 2141 (1984).
- (22) U. Heiz, A. Vayloyan and E. Schumacher, *Rev. Sci. Instrum.* 68, 3718 (1997).
- (23) D. Rayane, P. Melinon, B. Tribollet, B. Chabaud, A. Hoareau and M. Broyer, *J. Chem. Phys.* 91, 3100 (1989).
- (24) W. Schulze, B. Winter and I. Goldenfeld, *Phys. Rev. B* 38, 2937 (1988).
- (25) H. G. Limberger and T. P. Martin, *J. Phys. Chem.* 90, 2979 (1988).
- (26) K. Sattler, J. Mühlbach and E. Recknagel, *Phys. Rev. Lett.* 45, 821 (1980).
- (27) V. E. Bondybey and J. H. English, *J. Chem. Phys.* 76, 2165 (1982).
- (28) S. J. Riley, E. K. Parks, C. R. Mao, L. G. Pobo and S. Wexler, *J. Phys. Chem.* 86, 3911 (1982).
- (29) R. E. Smalley, *Laser Chem.* 2, 167 (1983).
- (30) H. R. Siekmann, C. Luder, J. Fachrmann, H. O. Lutz and K. H. Maiwes-Broer, *Z. Phys. D* 20, 417 (1991).
- (31) B. Keiser, T. M. Bernhardt, B. Stegemann, J. Opiz and K. Rademann, *Phys. Rev. Lett.* 83, 2918 (1999).
- (32) T. M. Bernhardt, B. Keiser and K. Rademann, *Phys. Chem. Chem. Phys.* 4, 1192 (2002).
- (33) W. Begemann, S. Deihöfer, K. H. Maiwes-Broer and H. O. Lutz, *Z. Phys. D* 3, 183 (1986).
- (34) W. Begemann, K. H. Maiwes-Broer and H. O. Lutz, *Phys. Rev. Lett.* 56, 2248 (1986).
- (35) P. Fayet, J. P. Wolf and L. Wöste, *Phys. Rev. B* 33, 6792 (1986).
- (36) N. D. Bhaskar, R. P. Frueholz, C. M. Klimcak and R. A. Cook, *Phys. Rev. B* 36, 4418 (1987).
- (37) Y. Saito, K. Minami, T. Ishida and T. Noda, *Z. Phys. D* 11, 87 (1989).
- (38) P. Sudraud, C. Collinex and J. van der Walle, *J. Phys. D* 13, L203 (1979).
- (39) A. Wagner and T. M. Hall, *J. Vac. Sci. Technol.* 16, 1871 (1979).
- (40) W. A. Saunders and S. Fredrigo, *Chem. Phys. Lett.* 156, 14 (1989).
- (41) K. M. Ervin, *Int. Rev. Phys. Chem.* 20, 127 (2001).

- (42) E. K. Parks, G. C. Nieman, K. P. Kerns and S. J. Riley, *J. Chem. Phys.* 107, 1861 (1997).
- (43) R. E. Leuchtner, A. C. Harms and A. W. C. Jr, *J. Chem. Phys.* 92, 6527 (1990).
- (44) B. Kaiser, T. M. Bernhardt, M. Kinne, K. Rademann and A. Heidenreich, *J. Chem. Phys.* 110, 1437 (1999).
- (45) M. Kinne, T. M. Bernhardt, B. Kaiser and K. Rademann, *Z. Phys. D* 40, 105 (1997).
- (46) S. J. Riley, *Nanostruct. Mater.* 1, 155 (1992).
- (47) M. Andersson, J. L. Persson and A. Rosen, *J. Phys. Chem.* 100, 12222 (1996).
- (48) M. M. Kappes and R. A. Staley, *J. Am. Chem. Soc.* 103, 1286 (1981).
- (49) J. L. Elkind, F. D. Weiss, J. M. Alford, R. T. Laaksonen and R. E. Smalley, *J. Chem. Phys.* 88, 5215 (1988).
- (50) M. P. Irion and A. Selinger, *Chem. Phys. Lett.* 158, 145 (1989).
- (51) M. P. Irion, A. Selinger and R. Wendel, *Int. J. Mass Spectrom. Ion proc.* 96, 27 (1990).
- (52) C. Berg, T. Schindler, G. Niedner-Schatteburg and V. E. Bondybey, *J. Chem. Phys.* 102, 4870 (1995).
- (53) G. Dietrich, S. Krückenberg, K. Lützenkirchen, L. Schweikhard and C. Walther, *J. Chem. Phys.* 112, 752 (2000).
- (54) H. Hess, S. Kwiet, L. Socaciu, S. Wolf, T. Leisner and L. Wöste, *Appl. Phys. B* 71, 337 (2000).
- (55) K. Koszinowski, D. Schröder and H. Schwarz, *J. Chem. Phys.* 107, 4999 (2003).
- (56) D. C. Parent and S. L. Anderson, *Chem. Rev.* 92, 1541 (1992).
- (57) D. Gerlich, *State-Selected and State-to-State Ion-Molecule Reaction Dynamics, Part 1: Experiment* Ed. C.-Y. Ng and M. Baer (Wiley, New York, 1992).
- (58) P. Fayet and L. Wöste, *Surf. Sci.* 156, 135 (1985).
- (59) H. Häkkinen, S. Abbet, A. Sanchez, U. Heiz and U. Landman, *Angew. Chem. Int. Ed.* 42, 1297 (2003).
- (60) B. Yoon, H. Häkkinen, U. Landman, A. S. Wörz, J.-M. Antonietti, S. Abbet, K. Judai and U. Heitz, *Science* 307, 403 (2005).

- (61) K. Christmann, *Introduction to Surface Physical Chemistry, Topics in Physical Chemistry* (Springer-Verlag, Berlin, 1991).
- (62) G. A. Somorjai, *Introduction to Surface Chemistry and Catalysis* (John Wiley and Sons, New York, 1994).
- (63) J. Hagen, L. D. Socaciu, J. Le Roux, D. Popolan, T. M. Bernhardt, L. Wöste, R. Mitrić, H. Noack and V. Bonačić-Koutecký, *J. Am. Chem. Soc.* **126**, 3442 (2004).
- (64) K. Koszinowski, D. Schröder and H. Schwarz, *Chem. Phys. Chem.* **4**, 1233 (2003).
- (65) K. Koszinowski, D. Schröder and H. Schwarz, *J. Am. Chem. Soc.* **125**, 3676 (2003).
- (66) W. T. Wallace and R. L. Whetten, *J. Am. Chem. Soc.* **124**, 7499 (2002).
- (67) A. H. Zewail, *Femtosecond Chemistry* Ed. J. Manz and L. Wöste (VCH, Weinheim, 1995).
- (68) A. H. Zewail, *J. Phys. Chem. A* **104**, 5660 (2000).
- (69) A. H. Zewail, *Femtochemistry* Ed. F. C. de Schryver, S. de Feyter and G. Schweitzer (Wiley-VCH, Weinheim, 2001).
- (70) M. Haruta, *Catal. Today* **36**, 153 (1997).
- (71) B. Hammer and J. K. Nørskov, *Nature* **376**, 238 (1995).
- (72) M. Valden, X. Lai and D. W. Goodman, *Science* **281**, 1647 (1998).
- (73) M. Haruta and M. Date, *Appl. Catal. A* **222**, 427 (2001).
- (74) N. Lopez and J. K. Nørskov, *J. Am. Chem. Soc.* **124**, 11262 (2002).
- (75) N. Lopez, T. V. W. Janssens, B. S. Clausen, Y. Xu, M. Mavrikakis, T. Bligaard and J. K. Nørskov, *J. Catal.* **223**, 232 (2004).
- (76) R. Meyer, C. Lemire, S. K. Shaikhutdinov and H. J. Freund, *Gold Bull.* **32**, 72 (2004).
- (77) D. J. Sajkowski and M. Boudart, *Catal. Rev. - Sci. Eng.* **29**, 325 (1987).
- (78) J. G. Serafin, A. C. Liu and S. R. Seyedmonir, *J. Mol. Catal. A: Chemical* **131**, 157 (1998).
- (79) A. L. de Oliveira, A. Wolf and F. Schüth, *Catal. Lett.* **73**, 157 (2001).
- (80) A. Sanchez, S. Abbet, U. Heiz, W. D. Schneider, H. Hakkinen, R. N. Barnett and U. Landman, *J. Phys. Chem. A* **103**, 9573 (1999).
- (81) S. Gilb, P. Weis, F. Furche, R. Ahlrichs and M. M. Kappes, *J. Chem. Phys.* **116**, 4094 (2002).



- 
- (82) P. Weis, T. Bierweiler, S. Gilb and M. M. Kappes, *Chem. Phys. Lett.* 355, 355 (2002).
- (83) F. Furche, R. Ahlrichs, P. Weis, C. Jacob, S. Gilb, T. Bierweiler and M. M. Kappes, *J. Chem. Phys.* 117, 6982 (2002).
- (84) P. Weis, O. Welz, E. Vollmer and M. M. Kappes, *J. Chem. Phys.* 120, 677 (2004).
- (85) M. N. Blom, D. Schooss, J. Stairs and M. M. Kappes, *J. Chem. Phys.* 124, 244308 (2006).
- (86) X. Xing, R. M. Danell, I. L. Garzon, K. Michaelian, N. M. Blom, M. M. Burns and J. H. Parks, *Phys. Rev. B: Condens. Matter* 72, 081405 (2005).
- (87) X. Xing, B. Yoon, U. Landman and J. H. Parks, *Phys. Rev. B: Condens. Matter* 74, 165423 (2006).
- (88) K. J. Taylor, C. L. Pettiette-Hall, O. Cheshnovsky and R. E. Smalley, *J. Chem. Phys.* 96, 3319 (1992).
- (89) J. Ho, K. M. Ervin and W. C. Lineberger, *J. Chem. Phys.* 93, 6987 (1990).
- (90) G. Ganteför, H. Handschuh, H. Moeller, C.-Y. Cha, P. Bechthold and W. Eberhardt, *Surf. Rev. Lett.* 3, 399 (1996).
- (91) G. Ganteför, D. Cox and A. Kaldor, *J. Chem. Phys.* 96, 4102 (1992).
- (92) R. Rousseau and D. Marx, *J. Chem. Phys.* 112, 761 (2000).
- (93) K. Balasubramanian and P. Y. Feng, *Chem. Phys. Lett.* 159, 452 (1989).
- (94) H. Partidge, C. W. Bauschlicher and S. R. Langhoff, *Chem. Phys. Lett.* 175, 531 (1990).
- (95) R. Wesendrup, T. Hunt and P. Schwerdtfeger, *J. Chem. Phys.* 112, 9356 (2000).
- (96) F. Remacle and E. S. Kryachko, *J. Chem. Phys.* 122, 044304 (2005).
- (97) A. V. Walker, *J. Chem. Phys.* 122, 094310 (2005).
- (98) V. E. Matulis, O. A. Ivashkevich and V. S. Gurin, *J. Mol. Struct. (Theochem)* 291, 664 (2003).
- (99) V. Bonačić-Koutecký, L. Češpiva, P. Fantucci and J. Koutecký, *J. Chem. Phys.* 98, 7981 (1993).
- (100) J. Yoon, K. S. Kim and K. K. Baek, *J. Chem. Phys.* 112, 9335 (2000).
- (101) V. Bonačić-Koutecký, J. Burda, R. Mitrić, M. Ge, G. Zampella and P. Fantucci, *J. Chem. Phys.* 117, 3120 (2002).

- (102) D. M. Cox, R. Brickman, K. Creegan and A. Kaldor, *Z. Phys. D* 19, 353 (1991).
- (103) B. E. Salisbury, W. T. Wallace and R. L. Whetten, *Chem. Phys.* 262, 131 (2000).
- (104) D. Stolcic, M. Fischer, G. Ganteför, Y. Kim, Q. Sun and P. Jena, *J. Am. Chem. Soc.* 125, 2848 (2003).
- (105) T. M. Bernhardt, L. D. Socaciu-Siebert, J. Hagen and L. Wöste, *Appl. Catal. A* 291, 170 (2005).
- (106) T. H. Lee and K. M. Ervin, *J. Phys. Chem.* 98, 10023 (1994).
- (107) M. J. Manard, P. R. Kemper and M. T. Bowers, *Int. J. Mass Spectrom.* 228, 865 (2003).
- (108) W. T. Wallace and R. L. Whetten, *J. Phys. Chem. B* 104, 10964 (2000).
- (109) W. T. Wallace and R. L. Whetten, *Eur. Phys. J. D* 16, 123 (2001).
- (110) T. M. Bernhardt, *Int. J. Mass Spectrom.* 243, 1 (2005).
- (111) M. Neumaier, F. Weigend, O. Hampe and M. M. Kappes, *J. Chem. Phys.* 122, 104702 (2005).
- (112) M. Neumaier, F. Weigend, O. Hampe and M. M. Kappes, *J. Chem. Phys.* 125, 104308 (2006).
- (113) T. M. Bernhardt, J. Hagen, S. M. Lang, D. M. Popolan, L. D. Socaciu-Siebert and L. Wöste, *J. Phys. Chem. A* 113, 2724 (2009).
- (114) A. Fielicke, G. von Helden, G. Meijer, D. B. Pedersen, B. Simard and D. M. Rayner, *J. Am. Chem. Soc.* 127, 8416 (2005).
- (115) S. M. Lang, T. M. Bernhardt, R. N. Barnett, B. Yoon and U. Landmann, *J. Am. Chem. Soc.* 131, 8939 (2009).
- (116) D. M. Cox, R. O. Brickman, K. Creegan and A. Kaldor, *Mater. Res. Soc. Symp. Proc.* 206, 43 (1991).
- (117) M. J. Manard, P. R. Kemper and M. T. Bowers, *J. Am. Chem. Soc.* 127, 9994 (2005).
- (118) L. D. Socaciu, J. Hagen, T. M. Bernhardt, L. Wöste, U. Heiz, H. Häkkinen and U. Landman, *J. Am. Chem. Soc.* 125, 10437 (2003).
- (119) S. M. Lang, T. M. Bernhardt, R. N. Barnett and U. Landmann, *Angew. Chem. Int. Ed.* 49, 980 (2010).
- (120) D. K. Böhme and H. Schwarz, *Angew. Chem. Int. Ed.* 44, 2336 (2005).

- 
- (121) D. M. Popolan, M. Nöbler, R. Mitrić, T. M. Bernhardt and V. Bonačić-Koutecký, *Phys. Chem. Chem. Phys.* **12**, 7865 (2010).
- (122) A. H. Zewail, *Femtochemistry: Ultrafast Dynamics of the Chemical Bond* (World Scientific, Singapore, 1994).
- (123) M. E. Vaida. Master Thesis, (Free University of Berlin, Berlin, 2004).
- (124) R. Keller, F. Nöhmayer, P. Spädtke and M. H. Schönenberg, *Vacuum* **34**, 31 (1984).
- (125) D. A. Dahl, *SIMION 3D Version 7.0 User`s Manual* (EG&G Indaho Inc., 2000).
- (126) D. A. Dahl, *Int. J. Mass Spectrom.* **200**, 3 (2000).
- (127) M. E. Vaida. PhD Thesis, (University of Ulm, Ulm, 2010).
- (128) T. Leisner. Habilitation Thesis, (Free University of Berlin, Berlin, 1998).
- (129) L. Hanley, S. A. Ruatta and S. L. Anderson, *J. Chem. Phys.* **87**, 260 (1987).
- (130) B. Krämer. Diploma Thesis, (Freie Universität Berlin, Berlin, 1993).
- (131) F. Rouessac and A. Rouessac, *Chemical Analysis* (John Wiley & Sons, Chichester, 2007).
- (132) H. Hess. PhD Thesis, (Free University of Berlin, Berlin, 1999).
- (133) J. Westergren, H. Grönbeck, S.-G. Kim and D. Tománek, *J. Chem. Phys.* **107**, 3071 (1997).
- (134) J. Westergren, H. Grönbeck, A. Rosén and S. Nordholm, *J. Chem. Phys.* **109**, 9848 (1998).
- (135) J. P. Hobson, *J. Vac. Sci. Technol.* **6**, 257 (1969).
- (136) O. Reynolds, *Philos. Trans. R. Soc. London* **10**, 727 (1879).
- (137) J. C. Maxwell, *Philos. Trans. R. Soc. London* **170**, 231 (1879).
- (138) G. Lorient and T. Moran, *Rev. Sci. Instr.* **46**, 140 (1975).
- (139) R. C. Bell, K. A. Zemski, D. R. Justes and A. W. Castleman, *J. Chem. Phys.* **114**, 798 (2001).
- (140) T. A. Miller, *J. Phys. Chem.* **67**, 1359 (1963).
- (141) Y. Wu, *J. Chem. Phys.* **48**, 889 (1968).
- (142) P. H. Carr, *Vacuum* **14**, 37 (1964).

- (143) J. P. Hobson, *J. Vac. Sci. Technol.* 7, 351 (1970).
- (144) P. F. Moulton, *Opt. News* 8, 9 (1982).
- (145) P. F. Moulton, *J. Opt. Soc. Am. B* 3, 125 (1986).
- (146) J.-C. Diels and W. Rudolph, *Ultrashort Laser Pulse Phenomena. Fundamentals, Techniques, and Applications on a Femtosecond Time Scale* (Academic Press, 1996).
- (147) C. Rullière, *Femtosecond Laser Pulses. Principles and Experiments* (Springer Verlag, Berlin-Heidelberg, 1998).
- (148) G. A. Mourou, C. P. J. Barty and M. D. Perry, *Phys. Today* 51, 22 (1998).
- (149) W. T. Silfvast, *Laser Fundamentals* (Cambridge University Press, Cambridge, 1996).
- (150) L. D. Socaciu, J. Hagen, U. Heiz, T. M. Bernhardt, T. Leisner and L. Wöste, *Chem. Phys. Lett.* 340, 282 (2001).
- (151) E. Schumacher. DETMECH - Chemical Reaction Kinetics Software; University of Bern 2003.
- (152) J. I. Steinfeld, J. S. Francisco and W. L. Hase, *Chemical Kinetics and Dynamics* (Prentice-Hall Inc., New Jersey, 1999).
- (153) A. W. Castleman, K. G. Weil, S. W. Sigsworth, R. E. Leuchtner and R. G. Keesee, *J. Chem. Phys.* 86, 3829 (1987).
- (154) P. Langevin, *Ann. Chem. Phys.* 5, 245 (1905).
- (155) T. Su and W. J. Chesnavich, *J. Chem. Phys.* 76, 5183 (1982).
- (156) T. Su, *J. Chem. Phys.* 89, 5355 (1988).
- (157) G. Gioumousis and D. P. Stevenson, *J. Chem. Phys.* 29, 294 (1958).
- (158) R. A. Marcus, *J. Chem. Phys.* 20, 359 (1952).
- (159) K. A. Holbrook, M. J. Pilling and S. H. Robertson, *Unimolecular Reactions, 2nd* (John Wiley & Sons Ltd., Chichester, U.K., 1996).
- (160) W. L. Hase, *Modern theoretical chemistry, dynamics of molecular collisions, Part B* Ed. W. H. Miller (Plenum, New York, 1976).
- (161) D. M. Cox, K. C. Reichmann, D. J. Trevor and A. J. Kaldor, *J. Chem. Phys.* 88, 111 (1988).
- (162) L. Drahos and K. Vékey, *J. Mass Spectrom.* 36, 237 (2001).
- (163) R. A. Marcus, *J. Chem. Phys.* 43, 2658 (1965).

- 
- (164) Y. Shi, V. A. Spasov and K. M. Ervin, *J. Chem. Phys.* 111, 938 (1999).
- (165) T. Baer and P. M. Mayer, *J. Am. Soc. Mass Spectrom.* 8, 103 (1997).
- (166) V. A. Spasov, T. H. Lee, J. P. Maberry and K. M. Ervin, *J. Chem. Phys.* 110, 5208 (1999).
- (167) M. F. Jarrold and J. E. Bower, *J. Chem. Phys.* 87, 5728 (1987).
- (168) R. G. Keesee and A. W. Castlemann, *J. Phys. Chem. Ref. Data* 15, 1011 (1986).
- (169) A. F. Kemper, M.-T. Hsu and M. T. Bowers, *J. Phys. Chem.* 95, 10600 (1991).
- (170) S. M. Lang and T. M. Bernhardt, *J. Chem. Phys.* 131, 024310 (2009).
- (171) M. Nößler. PhD Thesis, (Humboldt University of Berlin, Berlin, 2011).
- (172) A. D. Becke, *J. Chem. Phys.* 38, 3098 (1988).
- (173) A. D. Becke, *J. Chem. Phys.* 98, 5648 (1993).
- (174) C. Lee, W. Yang and R. G. Parr, *Phys. Rev. B: Condens. Matter* 37, 785 (1988).
- (175) B. Miehlich, A. Savin, H. Stoll and H. Preuss, *Chem. Phys. Lett.* 157, 200 (1989).
- (176) K. Eichkorn, F. Weigend, O. Treutler and R. Aldrichs, *Theor. Chim. Acta* 97, 119 (1997).
- (177) D. Andrea, U. Haeussermann, M. Dolg, H. Stoll and H. Preuss, *Theor. Chim. Acta* 77, 123 (1990).
- (178) A. Schäfer, H. Huber and R. Ahlrichs, *J. Chem. Phys.* 100, 5829 (1996).
- (179) J. P. Perdew, *Phys. Rev. B: Condens. Matter* 33, 8822 (1986).
- (180) J. P. Perdew, *Electronic Structure of Solids '91* Ed. P. Ziesche and H. Eschrig (Akademie Verlag, Berlin, 1991).
- (181) J. P. Perdew, J. A. Chevary, S. H. Vosko, K. A. Jackson, M. R. Pederson, D. J. Singh and C. Fiolhais, *Phys. Rev. B: Condens. Matter* 46, 6671 (1992).
- (182) J. P. Perdew, J. A. Chevary, S. H. Vosko, K. A. Jackson, M. R. Pederson, D. J. Singh and C. Fiolhais, *Phys. Rev. B: Condens. Matter* 48, 4978 (1993).
- (183) J. P. Perdew, K. Burke and Y. Wang, *Phys. Rev. B: Condens. Matter* 54, 16533 (1996).
- (184) K. Burke and J. P. Perdew, *Electronic Density Functional Theory: Recent Progress and New Directions* Ed. J. F. Dobson, G. Vignale and M. P. Das (Plenum, 1998).

- (185) D. R. Lide, *Handbook of Chemistry and Physics* (CRC Pres, Inc., Florida, 2000).
- (186) M. E. Vaida and T. M. Bernhardt, *Rev. Sci. Instr.* **81**, 104103 (2010).
- (187) A. A. Herzing, C. J. Kiely, A. F. Carley, P. Landon and G. J. Hutchings, *Science* **321**, 1331 (2008).
- (188) G. C. Bond, C. Louis and D. T. Thomson, *Catalysis by gold* (Imperial College Press, London, 2006).
- (189) J. Hagen, L. D. Socaciu, U. Heiz, T. M. Bernhardt and L. Wöste, *Eur. J. Phys. D* **24**, 327 (2003).
- (190) N. Veldeman, P. Lievens and M. Andersson, *J. Phys. Chem. A* **109**, 11793 (2005).
- (191) A. Fielicke, G. von Helden, G. Meijer, B. Simard and D. M. Rayner, *J. Phys. Chem. B* **109**, 23935 (2005).
- (192) H.-J. Zhai, B. Kiran, B. Dai, J. Li and L.-S. Wang, *J. Am. Chem. Soc.* **127**, 12098 (2005).
- (193) H.-J. Zhai and L.-S. Wang, *J. Chem. Phys.* **122**, 051101 (2005).
- (194) H.-J. Zhai, L.-L. Pan, B. Dai, B. Kiran, J. Li and L.-S. Wang, *J. Phys. Chem. C* **112**, 11920 (2008).
- (195) J. Velasquez, B. Njegic, M. S. Gordon and M. A. Duncan, *J. Phys. Chem. A* **112**, 1907 (2008).
- (196) L. Lian, P. A. Hackett and D. M. Rayner, *J. Chem. Phys.* **99**, 2583 (1993).
- (197) I. Balteanu, O. P. Balaj, B. S. Fox, M. K. Beyer, Z. Bastl and V. E. Bondybey, *Phys. Chem. Chem. Phys.* **5**, 1213 (2003).
- (198) L. D. Socaciu, J. Hagen, L. Le Roux, D. Popolan, T. M. Bernhardt, L. Wöste and S. Vajda, *J. Chem. Phys.* **120**, 2078 (2004).
- (199) D. M. Popolan and T. M. Bernhardt, *Chem. Phys. Lett.* **470**, 44 (2009).
- (200) H. Häkkinen and U. Landman, *J. Am. Chem. Soc.* **123**, 9704 (2001).
- (201) X. Wu, L. Senapati, S. K. Nayak, A. Selloni and M. Hajaligol, *J. Chem. Phys.* **117**, 4010 (2002).
- (202) R. Mitrić, C. Bürgel, J. Burda, V. Bonačić-Koutecký and P. Fantucci, *Eur. Phys. J. D* **24**, 41 (2003).
- (203) N. S. Phala, G. Klatt and E. van Steen, *Chem. Phys. Lett.* **395**, 33 (2004).

- 
- (204) A. Prestianni, A. Martorana, F. Labat, I. Ciofini and C. Adamo, *J. Phys. Chem. B* **110**, 12240 (2006).
- (205) P. Schwerdtfeger, M. Lein, R. P. Krawczyk and C. R. Jacob, *J. Chem. Phys.* **128**, 124302 (2008).
- (206) R. Ferrando, J. Jellinek and R. L. Johnston, *Chem. Rev.* **108**, 845 (2008).
- (207) A. M. Joshi, M. H. Tucker, W. N. Delgass and K. T. Thomson, *J. Chem. Phys.* **125**, 194707 (2006).
- (208) H. Schwarz, *Angew. Chem. Int. Ed.* **42**, 4442 (2003).
- (209) F. Meyer, Y.-M. Chen and P. B. Armentrout, *J. Am. Chem. Soc.* **117**, 4071 (2002).
- (210) A. Wang, Y.-P. Hsieh, Y. F. Chen and C.-Y. Mou, *J. Catal.* **237**, 197 (2005).
- (211) J. Hagen, L. D. Socaciu, M. Elijazyfer, U. Heiz, T. M. Bernhardt and L. Wöste, *Phys. Chem. Chem. Phys.* **4**, 1707 (2002).
- (212) D. W. Yuan and Z. Zeng, *J. Chem. Phys.* **120**, 6574 (2004).
- (213) L. A. Curtiss, K. Raghavachari, P. C. Redfern and J. A. Pople, *J. Chem. Phys.* **106**, 1063 (1997).
- (214) C. Elschenbroich and A. Salzer, *Organometallics* (VCH: Weinheim, Germany, 1989).
- (215) P. Pyykkö, *Angew. Chem. Int. Ed.* **43**, 4412 (2004).
- (216) G. J. Kubas, *Chem. Rev.* **107**, 4152 (2007).
- (217) M. L. Kimble, N. A. Moore, G. E. Johnson, J. A. W. Castleman, C. Bürgel, R. Mitrić and V. Bonačić-Koutecký, *J. Chem. Phys.* **125**, 204311 (2006).
- (218) W. T. Wallace, R. B. Wyrwas, T. L. Whetten, R. Mitrić and V. Bonačić-Koutecký, *J. Am. Chem. Soc.* **125**, 8408 (2003).
- (219) I. Fleischer. Diploma Thesis, (University of Ulm, Ulm, 2011).
- (220) M. A. Nygren, P. E. M. Siegnahn, C. Jin, T. Guo and R. E. Smalley, *J. Chem. Phys.* **95**, 6181 (1991).
- (221) D. Schröder, J. Hrušák, R. H. Hertwig, W. Koch, P. Schwerdtfeger and H. Schwarz, *Organometallics* **14**, 312 (1995).
- (222) H. Huber, D. McIntosh and G. A. Ozin, *Inorganic Chemistry* **16**, 975 (1977).
- (223) H. Huber and G. A. Ozin, *Inorg. Chem.* **16**, 64 (1977).

- (224) F. W. Froben, I. Rabin, M. Ritz and W. Schulze, *Z. Phys. D: At. Mol. Clusters* 38, 355 (1996).
- (225) L. Jiang and Q. Xu, *J. Phys. Chem. A* 110, 11488 (2006).
- (226) I. Rabin and W. Schulze, *J. Phys. Chem. B* 108, 14575 (2004).
- (227) M. Neumaier, F. Weigend, O. Hampe and M. M. Kappes, *Faraday Discuss.* 138, 393 (2008).
- (228) J. M. Goufried, K. J. Schmidt, S. L. M. Schroeder and K. Christmann, *Surf. Sci.* 536, 206 (2003).
- (229) G. McElhiney, H. Papp and J. Pritchard, *Surf. Sci.* 54, 617 (1976).
- (230) M. J. Manard, P. R. Kemper and M. T. Bowers, *Int. J. Mass Spectrom.* 249, 252 (2006).
- (231) R. Mitrić, C. Bürgel and V. Bonačić-Koutecký, *Proc. Natl. Acad. Sci. U.S.A.* 104, 10314 (2007).
- (232) M. Prather, *Science* 279, 1339 (1998).
- (233) A. R. Ravishankara, J. S. Daniel and R. W. Portmann, *Science* 326, 123 (2009).
- (234) M. Dameris, *Angew. Chem. Int. Ed.* 49, 489 (2010).
- (235) M. L. Campbell, E. J. Kölsch and K. L. Hooper, *J. Phys. Chem. A* 104, 11147 (2000).
- (236) M. Bronstrup, D. Schröder, I. Kretzschmar, H. Schwarz and J. N. Harvey, *J. Am. Chem. Soc.* 123, 142 (2000).
- (237) M. L. Campbell, *J. Phys. Chem. A* 107, 3048 (2003).
- (238) V. Blagojevic, M. J. Y. Jarvis, E. Flaim, G. K. Koyanagi, V. V. Lavrov and D. K. Bohme, *Angew. Chem. Int. Ed.* 42, 4923 (2003).
- (239) V. V. Lavrov, V. Blagojevic, G. K. Koyanagi, G. Orlova and D. K. Bohme, *J. Phys. Chem. A* 108, 5610 (2004).
- (240) O. P. Balaj, I. Balteanu, T. T. J. Roßteuscher, M. K. Beyer and V. E. Bondybey, *Angew. Chem. Int. Ed.* 43, 6519 (2004).
- (241) C. Luo, W. Fa and J. Dong, *J. Chem. Phys.* 125, 084707 (2006).
- (242) S. M. Hamilton, W. S. Hopkins, D. J. Harding, T. R. Walsh, P. Gruene, M. Haertel, A. Fielicke, G. Meijer and S. R. Meckenzie, *J. Am. Chem. Soc.* 132, 1448 (2010).
- (243) A. S. Narayan, M. P. Futerko and A. J. Fontijn, *J. Phys. Chem.* 96, 290 (1992).



- 
- (244) A. Delabie, C. Vinckier, M. Flock and K. Pierloot, *J. Phys. Chem. A* **105**, 5479 (2001).
- (245) A. Stirling, *J. Am. Chem. Soc.* **124**, 4058 (2002).
- (246) D.-H. Lee, B. Mondal and K. D. Karlin, *Activation of Small Molecules: Organometallic and Bioinorganic Perspectives* Ed. W. B. Tolman (Wiley-VCH, Weinheim, 2006).
- (247) W. B. Tolman, *Angew. Chem. Int. Ed.* **49**, 1018 (2010).
- (248) B. C. Gates, *Catalytic Chemistry* (John Wiley & Sons Inc., New York, Singapore, 1992).
- (249) J. Zhou, Z.-H. Li, W.-N. Wang and K.-N. Fan, *Chem. Phys. Lett.* **421**, 488 (2006).
- (250) V. Bonačić-Koutecký, Private communication
- (251) V. Bonačić-Koutecký, M. Boiron, J. Pittner, P. Fantucci and J. Koutecký, *Eur. J. Phys. D* **9**, 183 (1999).
- (252) D. F.-T. Tuan and R. Hoffmann, *Inorg. Chem.* **24**, 871 (1985).
- (253) Y. Wang and X. G. Gong, *J. Chem. Phys.* **125**, 124703 (2006).
- (254) M. Schmidt, P. Cahuzac and C. Bréchnignac, *J. Chem. Phys.* **118** (2003).
- (255) G. E. Johnson, N. M. Reilly, E. C. Tyo and A. W. Castleman, *J. Phys. Chem. C* **112**, 9730 (2008).
- (256) B. Pettinger, X. Bao, I. Wilcock, M. Muhler, R. Schlögl and G. Ertl, *Angew. Chem.* **106**, 113 (1994).
- (257) D. S. Su, T. Jacob, T. W. Hansen, D. Wang, R. Schlögl, B. Freitag and S. Kujawa, *Angew. Chem. Int. Ed.* **47**, 5005 (2008).
- (258) D. P. Woodruff, *Atomic Clusters: From Gas Phase to Deposited, The Chemical Physics of Solid Surfaces* **12** (Elsevier, Amsterdam, 2007).
- (259) U. Heiz and U. Landman, *Nanocatalysis* Berlin, 2007).
- (260) V. Bonačić-Koutecký, R. Mitrić, T. M. Bernhardt, L. Wöste and J. Jortner, *Adv. Chem. Phys.* **132**, 179 (2006).
- (261) A. Nakajima and K. Kaya, *J. Phys. Chem. A* **104**, 176 (2000).
- (262) K. F. Willey, P. Y. Cheng, M. B. Bishop and M. D. Duncan, *J. Am. Chem. Soc.* **113**, 4721 (1991).
- (263) K. F. Willey, P. Y. Cheng, C. D. Pearce and M. D. Duncan, *J. Phys. Chem. A* **94**, 4769 (1990).

- (264) K. F. Willey, C. S. Yeh, D. L. Robbins and M. D. Duncan, *J. Phys. Chem.* 96, 9106 (1992).
- (265) Y.-M. Chen and P. B. Armentrout, *Chem. Phys. Lett.* 210, 123 (1993).
- (266) S. Afzaal and B. S. Freiser, *Chem. Phys. Lett.* 218, 254 (1994).
- (267) D. Schröder, R. Brown, P. Schwerdtfeger and H. Schwarz, *Int. J. Mass Spectrom.* 203, 155 (2000).
- (268) S. K. Buratto, T. M. Bowers, H. Metiu, M. Manard, X. Tong, L. Benz, P. Kemper and S. Chretien, *Atomic Clusters: From Gas Phase to Deposited, The Chemical Physics of Solid Surfaces* Ed. D. P. Woodruff, Vol. 12 (Elsevier, Amsterdam, 2007).
- (269) G. Frenking and N. Fröhlich, *Chem. Rev.* 100, 717 (2000).
- (270) S. Wolf, G. Sommerer, S. Rutz, E. Schreiber, T. Leisner, L. Wöste and R. S. Berry, *Phys. Rev. Lett.* 74, 4177 (1995).
- (271) T. Leisner, S. Vajda, S. Wolf, L. Wöste and R. S. Berry, *J. Chem. Phys.* 111, 1017 (1999).
- (272) J. T. Snodgrass, R. C. Dunbar and M. T. Bowers, *J. Phys. Chem.* 94, 3649 (1990).
- (273) J. R. Grover, E. A. Walters and E. T. Hui, *J. Phys. Chem.* 91, 3233 (1987).
- (274) V. Beutel, G. L. Bahle, M. Kuhn and W. Demtröder, *Chem. Phys. Lett.* 185, 313 (1991).
- (275) C. Jackschath, I. Rabin and W. Schulze, *Z. Phys. D* 22, 517 (1992).
- (276) T. Leisner, S. Rutz, G. Sommerer, S. Vajda, S. Wolf, E. Schreiber and L. Wöste, *Fast Elementary Processes in Chemical and Biological Systems* Ed. A. Tramer (AIP Press, Woodbury, New York, 1996).
- (277) L. Wöste, *Z. Phys. D* 196, 1 (1996).
- (278) T. M. Bernhardt, U. Heiz and U. Landman, *Chemical and catalytic properties of size-selected free and deposited clusters*, Nanocatalysis, Ed. U. Heiz and U. Landman (Springer Verlag, Berlin, 2007).
- (279) G. A. Olah, A. Goeppert and G. K. S. Prakash, *Beyond Oil and Gas: The Methanol Economy* (Wiley-VCH, Weinheim, 2006).
- (280) S. M. Lang and T. M. Bernhardt, *Int. J. Mass Spectrom.* 286, 39 (2009).
- (281) M. E. Vaida, T. Gleitsmann, R. Tchitnga and T. M. Bernhardt, *Phys. Status Solidi B* 247, 1139 (2010).

- (282) A. K. Chowdhury and C. L. Wilkins, *J. Am. Chem. Soc.* **109**, 5336 (1987).
- (283) J. R. Brown, P. Schwerdtfeger, D. Schröder and H. Schwarz, *J. Am. Soc. Mass Spectrom.* **13**, 485 (2002).
- (284) W. S. Taylor, J. C. May and A. S. Lasater, *J. Phys. Chem. A* **107**, 2209 (2003).
- (285) D. M. Popolan, M. Nöbler, R. Mitrić, T. M. Bernhardt and V. Bonačić-Koutecký, *J. Phys. Chem. A*, submitted.
- (286) J.-M. L' Hermite, F. Rabilloud, L. Marcou and P. Labastie, *Eur. J. Phys. D* **14**, 323 (2001).
- (287) J.-M. L' Hermite, F. Rabilloud, P. Labastie and F. Spiegelman, *Eur. J. Phys. D* **16**, 77 (2001).
- (288) F. Rabilloud, F. Spiegelman, J.-M. L. Hermite and P. Labastie, *J. Chem. Phys.* **114**, 289 (2001).
- (289) M. Sterrer, T. Risse, M. Heyde, H.-P. Rust and H. J. Freund, *Phys. Rev. Lett.* **98**, 206103 (2007).
- (290) M. Yulikov, M. Sterrer, T. Risse and H. J. Freund, *Surf. Sci.* **603**, 1622 (2009).

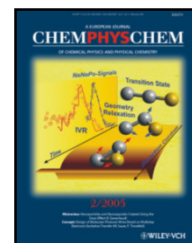


# List of publications

1. Denisia M. Popolan, Thorsten M. Bernhardt, Melanie Nöbler, Roland Mitrić, Vlasta Bonačić-Koutecký, *Temperature dependent reactivity of silver and gold cluster cations with  $N_2O$* , Int. J. Mass. Spectrom., **in preparation**.
2. Mihai E. Vaida, Tobias Gleitsmann, Denisia M. Popolan, Sandra M. Lang, G. Stibenz, B. Stegemann, L. Wöste, Thorsten M. Bernhardt, *Novel apparatus for femtosecond reaction dynamics studies on mass-selected free and deposited metal clusters*, Rev. Sci. Instrum., **in preparation**.
3. Thorsten M. Bernhardt, Jan Hagen, Henry Heß, Thomas Leisner, Denisia M. Popolan, Liana D. Socaciu-Siebert, Ludger Wöste, *Temperature dependent femtosecond NeNe-Po spectroscopy: Nuclear dynamics in noble metal trimers  $Ag_3$ ,  $Ag_2Au$ , and  $Au_3$* , J. Atom. Mol. Opt. Phys, **in preparation**.
4. Denisia M. Popolan, Mihai E. Vaida, Thorsten M. Bernhardt, *Ion trap meets surface science: The adsorption and photoreaction of  $CH_3Br$  free and supported gold clusters*, Chem. Phys. Lett., Topical Review, **in preparation**.
5. Denisia M. Popolan, Thorsten M. Bernhardt, *CO oxidation by silver and gold cluster cations: Identification of different active oxygen species*, J. Chem. Phys., **accepted for publication**.
6. Denisia M. Popolan, Melanie Nöbler, Roland Mitrić, Vlasta Bonačić-Koutecký, Thorsten M. Bernhardt, *Tuning cluster reactivity by charge state and composition: Experimental and theoretical investigation of CO binding energy to  $Ag_nAu_m^{+/-}$  ( $n+m = 3$ )*, J. Phys. Chem. A, **in press**.
7. Denisia M. Popolan, Thorsten M. Bernhardt, *Interaction of gold and silver cluster cations with  $CH_3Br$ : Thermal and photoinduced reaction pathway*, Eur. Phys. J. D, **in press**.
8. Denisia M. Popolan, Melanie Nöbler, Roland Mitrić, Thorsten M. Bernhardt, Vlasta Bonačić-Koutecký, *Composition dependent adsorption of multiple CO molecules on binary silver-gold clusters  $Ag_nAu_m^+$  ( $n+m = 5$ ): Theory and experiment*, Phys. Chem. Chem. Phys., **12**, 7865 (2010). **Selected as journal front cover**.
9. Thorsten M. Bernhardt, Jan Hagen, Sandra M. Lang, Denisia M. Popolan, Liana D. Socaciu-Siebert, Ludger Wöste, *Binding energies of  $O_2$  and CO to small anionic noble*



- metal clusters from temperature dependent reaction kinetics measurements, J. Phys. Chem. A **113**, 2724 (2009).
10. Denisia M. Popolan, Thorsten M. Bernhardt, *Formation and femtosecond photodissociation of  $Au_n^+$  and  $Ag_n^+$  complexes with benzene and carbonyl monoxide*, Chem. Phys. Lett. **470**, 44 (2009). **Selected as editor's choice** (see Chem. Phys. Lett. **474**, 239 (2009)).
11. Jan Hagen, Liana D. Socaciu-Siebert, Jerome Le Roux, Denisia Popolan, Stefan Vajda, Thorsten M. Bernhardt, Ludger Wöste, *Charge transfer initiated nitroxyl chemistry on free clusters anions  $Ag_{2.5}^-$ : Size effects and magic complexes*, Int. J. Mass. Spectrom. **262**, 152 (2007).
12. Sandra M. Lang, Denisia M. Popolan, Thorsten M. Bernhardt, *Chemical reactivity and catalytic properties of size-selected gas phase metal clusters*, in "The chemical physics of solid surfaces (Vol. 12): Atomic clusters: From gas phase to deposited", edited by D. P. Woodruff, Elsevier (2007).
13. Liana D. Socaciu-Siebert, Jan Hagen, Jerome Le Roux, Denisia Popolan, Mihai Vaida, Stefan Vajda, Thorsten M. Bernhardt, Ludger Wöste, *Ultrafast nuclear dynamics induced by photodetachment of  $Ag_2^-$  and  $Ag_2O_2^-$ : Oxygen desorption from a molecular silver surface*, Phys. Chem. Chem. Phys. **7**, 2706 (2005).
14. Thorsten M. Bernhardt, Jan Hagen, Liana D. Socaciu, Roland Mitrić, A. Heidenreich, Jerome Le Roux, Denisia Popolan, Mihai Vaida, Ludger Wöste, Vlasta Bonačić-Koutecký, Joshua Jortner, *Femtosecond time-resolved geometry relaxation and ultrafast intramolecular energy redistribution in  $Ag_2Au$* , Chem. Phys. Chem. **6**, 243 (2005). **Selected as journal front cover.**
15. Thorsten M. Bernhardt, Liana D. Socaciu, Jan Hagen, Denisia Popolan, Jerome Le Roux, Uli Heiz, Ludger Wöste, *Catalysis with small free noble metal clusters*, in "Clusters and Nano-Assemblies", eds. Puru Jena, S. N. Khanna, B. K. Rao, World Scientific, Singapore (2005).
16. Jan Hagen, Liana D. Socaciu, Jerome Le Roux, Denisia Popolan, Thorsten M. Bernhardt, Ludger Wöste, Roland Mitrić, Holger Noack, Vlasta Bonačić-Koutecký, *Cooperative effects in the activation of molecular oxygen by anionic silver clusters*, J. Am. Chem. Soc. **126**, 3442 (2004).



17. Liana D. Socaciu, Jan Hagen, Jerome Le Roux, Denisia Popolan, Thorsten M. Bernhardt, Ludger Wöste, Stefan Vajda, *Strongly cluster size dependent reaction behaviour of CO with O<sub>2</sub> on free silver clusters anions*, J. Chem. Phys. **120**, 2078 (2004)





# Poster and oral contributions

- **DPG – Frühjahrstagung**, Berlin (March 2005):  
D. M. Popolan, J. Hagen, L. D. Socaciu, M. E. Vaida, B. Schmidt, T. M. Bernhardt, and L. Wöste, *Influence of Size and Composition on the Reaction Kinetics of Binary Gold-Silver Cluster Anions in an RF-Ion Trap*
- **International Workshop on Ultrafast Time-Resolved Soft X-Ray Science**, Berlin-Zeuthen (April 2005):  
D. M. Popolan, S. M. Lang, J. Hagen, L. D. Socaciu-Siebert, M. E. Vaida, B. Schmidt, T. M. Bernhardt, and L. Wöste, *Structural Dynamics and Reaction Kinetics of Small Bimetallic Silver-Gold Clusters*
- **International Workshop on Ultrafast Time-Resolved Soft X-Ray Science**, Berlin-Zeuthen (April 2005):  
B. Schmidt, D. M. Popolan, S. M. Lang, T. M. Bernhardt, and L. Wöste, *Optimal Control of Metal Cluster Reactions by Modulated Ultra-Broadband Laser Pulses*
- **Cluster Meeting 2005 CNF-Symposium: Clusters as Molecular Nanostructures**, Bad Herrenalb (September 2005):  
S. M. Lang, D. M. Popolan, J. Hagen, L. D. Socaciu-Siebert, S. Vajda, T. M. Bernhardt, and L. Wöste, *Reactions of Mass Selected Silver Clusters*
- **9. Deutsche Physikerinnen-Tagung**, Darmstadt (October 2005):  
D. M. Popolan, S. M. Lang, J. Hagen, L. D. Socaciu-Siebert, M. E. Vaida, B. Schmidt, T. M. Bernhardt, and L. Wöste, *Structural Dynamics and Temperature Dependent NeNePo Spectroscopy of Small Bimetallic Silver-Gold Clusters*
- **9. Deutsche Physikerinnen-Tagung**, Darmstadt (October 2005):  
S. M. Lang, D. M. Popolan, J. Hagen, L. D. Socaciu-Siebert, S. Vajda, T. M. Bernhardt, and L. Wöste, *Reactions of Mass Selected Silver Clusters*
- **DPG – Frühjahrstagung**, Frankfurt/Main (March 2006):  
D. M. Popolan, S. M. Lang, J. Hagen, L. D. Socaciu-Siebert, L. Wöste and T. M. Bernhardt, *Size Effects and Reactive Behavior of Small Mass-Selected Silver Clusters in the Presence of NO and CO*
- **Bunsentagung**, Erlangen (May 2006):  
D. M. Popolan, S. M. Lang, and T. M. Bernhardt, *Catalytic Reactions of Levitated Metal Nanoclusters*

- **ISSPIC XIII – International Symposium on Small Particles and Inorganic Clusters**, Göteborg, Sweden (July 2006):  
D. M. Popolan, S. M. Lang, T. M. Bernhardt, J. Hagen, L. D. Socaciu-Siebert, and L. Wöste, *Ultrafast Nuclear Dynamics and Reaction Kinetics of Small Silver Clusters*
- **ISSPIC XIII – International Symposium on Small Particles and Inorganic Clusters**, Göteborg, Sweden (July 2006):  
S. M. Lang, D. M. Popolan, and T. M. Bernhardt, *Reaction Behavior of Small Mass-Selected Noble Metal Clusters in the Gas Phase*
- **S<sup>3</sup>C – Symposium on Size Selected Clusters**, Brand, Austria (March 2007):  
D. M. Popolan, M. Vaida, and T. M. Bernhardt, *The Effect of Gold Doping on the Reactivity of Free Silver Clusters: Comparison of Ag<sub>3</sub><sup>+</sup> and Ag<sub>2</sub>Au<sup>+</sup>*
- **DPG – Frühjahrstagung**, Düsseldorf (March 2007):  
D. M. Popolan, M. Vaida, and T. M. Bernhardt, *The Effect of Gold Doping on the Reactivity of Free Silver Clusters: Comparison of Ag<sub>3</sub><sup>+</sup> and Ag<sub>2</sub>Au<sup>+</sup>*
- **Summer School – Structural Dynamics. Methods and Applications**, Vilamoura, Portugal (June 2008):  
D. M. Popolan, and T. M. Bernhardt, *Real Time Photochemistry Investigation on Mass-Selected Ion-Organic Molecule Cluster Complexes of Silver*
- **DPG – Frühjahrstagung**, Berlin (March 2008)  
D. M. Popolan, and T. M. Bernhardt, *Structural Fluxionality in the CO Adsorption on Pure and Binary Silver-Gold Clusters Ag<sub>n</sub>Au<sub>m</sub><sup>+</sup>*. **Oral presentation**
- **ISSPIC XIV – International Symposium on Small Particles and Inorganic Clusters**, Valladolid, Spain (September 2008):  
D. M. Popolan, and T. M. Bernhardt, *Reaction Kinetics and Real Time Charge-Transfer Investigation on Mass-Selected Ion-Molecule Ag<sub>n</sub>Au<sub>m</sub> Cluster Complexes*
- **UCP – International Workshop on Ultrafast Chemical Physics**, Glasgow, Scotland (October 2008):  
D. M. Popolan, and T. M. Bernhardt, *Ultrafast Photoinduced Reaction Dynamics of Mass Selected Silver Cluster Ion-Organic Molecule Complexes*
- **S<sup>3</sup>C – Symposium on Size Selected Clusters**, Brand, Austria (March 2009):  
D. M. Popolan, and T. M. Bernhardt, *Size and Composition Dependent Kinetics and*

*Real Time Charge-Transfer Dynamics of Noble Metal Clusters Complexes*

- **FEMTO IX – Femtochemistry, Femtobiology and Femtophysics - Frontiers in Ultrafast Science and Technology**, Beijing, China (August 2009):  
D. M. Popolan, and T. M. Bernhardt, *Femtosecond Photodissociation Dynamics of  $\text{Ag}_n^+$  and  $\text{Au}_n^+$  Complexes with Small Organic Molecules*
- **Bunsen Colloquium – Microscopic Views on Interface Phenomena - From Surface Science to Fuel Cell Catalysis**, Reisenburg Castle, Günzburg (December 2009):  
D. M. Popolan, and T. M. Bernhardt, *Size and Composition Dependent Reaction Kinetics and Femtosecond Photodissociation Dynamics of Noble Metal Clusters Complexes*
- **ISSPIC XV – International Symposium on Small Particles and Inorganic Clusters**, Oaxaca, Mexico (September 2010):  
D. M. Popolan, and T. M. Bernhardt, *Reactions of Small Noble Metal Clusters with CO and  $\text{N}_2\text{O}$ : Implications for Selective CO Oxidation*
- **German-French Colloquium – French-German Research: 50 Years in the Light of the Laser**, Berlin (November 2010):  
D. M. Popolan, and T. M. Bernhardt, *Femtosecond Photodissociation Dynamics of  $\text{Ag}_n^+$  and  $\text{Au}_n^+$  Complexes with Small Organic Molecules*



# Curriculum Vitae

## PERSONAL DATA

Name	Denisia Maria Popolan
Born	09.03.1978 in Brad, Romania
Marital Status	Single
Nationality	Rumanian



## EDUCATION

1984 - 1992	Elementary school - "Școala Generală Nr. 2" Crișcior, Romania
1992 - 1996	High-school - "Liceul Teoretic Avram Iancu", Brad, Romania
06/1996	Graduation: High-school Diploma "Diplomă de Bacalaureat"

## ACADEMIC STUDIES

10/1998 - 07/2002	Studies of physics West University of Timișoara, Timișoara, Romania
07/2002	Graduation: Diploma Physics, "Diplomă de Licență"
10/2002 - 07/2004	Master studies West University of Timișoara, Timișoara, Romania Free University of Berlin, Berlin, Germany
07/2004	Graduation: Master of Science, "Diplomă de Master"
10/2004 - 04/2006	PhD studies in the group of Prof. Dr. Ludger Wöste Physics Department, Free University of Berlin, Berlin, Germany
Since 04/2006	PhD studies in the group of Prof. Dr. Thorsten M. Bernhardt Institute of Surface Chemistry and Catalysis, University of Ulm, Ulm, Germany

## TEACHING EXPERIENCE

2003 - 2004	Physics tutor. Preparation of physics experiments for students at Free University of Berlin, Berlin, Germany
2006 - 2009	Physical chemistry teaching assistant at University of Ulm, Ulm, Germany

## SCHOLARSHIPS AND AWARDS

10/2002 - 08/2003	ERASMUS scholarship for master studies at the Free University of Berlin, Berlin, Germany
10/2003 - 08/2004	EMSPS (European Mobility Scheme for Physics Students) scho- larship for master studies at the Free University of Berlin, Berlin, Germany
10/2004 - 08/2005	DAAD scholarship for PhD studies at the Free University of Ber- lin, Berlin, Germany
08/2009	Best Poster Award at the 9 <sup>th</sup> International Conference on <i>Femto- chemistry, Femtobiology and Femtophysics - Frontiers in Ultrafast Science and Technology</i> , Beijing, China



# Acknowledgments

It seems to be an impossible task to adequately express gratitude for the last years of learning, training, mentoring, support, encouragements, friendship, and fun to so many mentors, colleagues, friends, and family. In the next I will attempt to mention a few.

This thesis was completed at the “Institut für Experimentalphysik” at the Freie Universität Berlin and the “Institut für Oberflächenchemie und Katalyse” at the Universität Ulm.

Firstly, I would like to express my sincere gratitude to Prof. Dr. **Ludger Wöste** for giving me the possibility to start my PhD in his group and to discover the fascinating worlds of clusters and femtosecond laser spectroscopy.

To my supervisor Prof. Dr. **Thorsten M. Bernhardt** I am deeply thankful for giving me the possibility to continue my PhD in his research group in Ulm. I am also grateful for the effort he has made to instruct me and help me learn both the science itself and also how to be a scientist. His great optimism gave me always the power to go on. I will never forget his words in the critical moments in the lab, when nothing works as scheduled: “*Es hilft nichts außer weiter machen!*” I would also like to thank him for giving me the opportunity to take part at many national and international conferences and hence to be in contact with many excellent scientists in the field of femtochemistry and cluster science. Nevertheless, I would like to thank him for the careful reading and improvement of the present work.

I am deeply grateful for the excellent and fruitful collaboration with the theoretical group of Prof. Dr. **Vlasta Bonačić-Koutecký** and especially to **Melanie Nößler** who performed the theoretical work discussed in this thesis.

I am very indebted to Prof. Dr. **Michael D. Morse** for the advices concerning the fabrication of the silver-gold alloy targets used for all experiments presented in this thesis and to Prof. Dr. **Ernst Schumacher** for suggestions concerning the DETMECH program.

I am also very thankful to **DAAD** (Deutsche Akademische Austausch Dienst) for the financial support during the first year of my PhD studies.

I wish to thank my colleagues **Sandra, Tobias, Robert** and **Bruno** for being good friends and wonderful colleges. Thanks to my colleges the PhD period was not only a hard working period but also a good fun period. Out trips, our parties with culinary highlights and the afternoon beer meetings will make this time unforgettable.

I am also thankful to **Yvonne**, who shared with me more than three years the same office, for the nice atmosphere and for the countless times she helped me with the german language. Thanks Yvonne, my German language becomes a little better.

I also would like to thank Prof. Dr. **Jürgen Behm** and to entire **IOK institute** for the warm and friendly atmosphere. In this context, special thanks also to **Thomas Häring** and **Gerd Bräth** for their technical support.

My stay in Ulm was definitively nicer due to my friends **Manuela** and **Alina**. I would like to thank **Manuela** not only for spending time in order to help me to find a flat, but also for the countless time when we explore the Ulm and its neighborhoods by bike, which I really

enjoy it.

To **Alina** I am very thankful for the relaxing shopping tours and the evening jogging rounds which kept my body and soul fit but emptied my purse.

Further, I would like to express my gratitude to a very special person in my life, **Georgeta Circo**, who “contaminates” me with the physics virus. She was always convinced that I have good chances to become a good physicist.

*Stimată Doamnă Circo, vă mulțumesc pentru că m-ați susținut și m-ați îndrumat pe un drum pe care eu, probabil, din proprie inițiativă nu l-aș fi urmat! Nu voi putea uita niciodată cuvintele dumnevoastră din acea dupămasă de primăvară care, definitiv, mi-au influențat pentru totdeauna viața: “Deni, de ce nu te înscri la fizică?”*

Finally, I express my gratitude and love to my family. My parents, **Dumitru & Maria Popolan** have been a steady source of advice, support and encouragements throughout my studies. They have always encouraged me to work hard and to stretch my abilities. Unfortunately few months ago my mommy passed away, God decided to take her to him. This thesis is dedicated to her memory as gratitude for being the most wonderful mommy in the world. I love you mommy, and I miss you so much.

To my sister **Pușa**, my brother **Sergiu** and my brother in law **Sorin** I am also grateful for their support and encouragement. To my niece **Eliza (Lizuca)** I am also thankful for being a constant source of good-humor. For Eliza is still unclear why I must go so far away from home in order to study while in her kindergarten “her school” still are same free places.

*Dragii mei, tati, Puși, Sergiu, Sorin și Eliza, vă mulțumesc din suflet pentru ca mi-ați stat mereu aproape și prin încurajările voastre mi-ați dat tărie să pot merge înainte și să duc la bun sfârșit această lucrare.*

Last but not least, I would like to thank **Mihai** for staying by my side in the good as well as the bad moments during my PhD studies. He always believed in me and in my force to solve the problems, probably more than I even did myself. His great experimental support during the photodissociation experiments is also grateful acknowledged.

*Dragă Mihai, îți mulțumesc pentru răbdarea ta, pentru faptul că mi-ai stat mereu aproape, ai crezut în mine, m-ai înțeles și ai avut mereu o încurajare și un șervețel pregătit în momentele mai grele în care lacrimile mi-au umplut ochii. Datorită ție în ultimii ani nu a fost timp de plictiseală, iar viața mea a devenit, cu siguranță, mult mai frumoasă și mai interesantă.*



# Erklärung

Hiermit erkläre ich, Denisia Maria Popolan, dass ich die vorliegende Dissertation selbständig verfasst habe. Ich habe keine anderen als die angegebenen Quellen und Hilfsmittel benutzt und habe wörtliche oder sinngemäße Zitate als solche gekennzeichnet.

Ulm, den \_\_\_\_\_

Denisia Maria Popolan

